ABSTRACT

MODELING EDGE EFFECTS OF MESA DIODES FOR SILICON PHOTOVOLTAICS

by
Jesse S. Appel

A mesa diode has been modeled and its performance under dark and illuminated conditions has been simulated using a commercial finite element software package. These simulations have led to a determination of the self-consistent solution to the continuity equations for electrons and holes using the steady-state drift-diffusion model for carrier dynamics coupled with electric potential determined from Poisson's equation. The purpose of these simulations has been to determine the influence of edge conditions on the overall performance of mesa diodes under dark and illuminated conditions.

Mesa diode arrays are fabricated on crystalline silicon solar cells. They are an array of small area solar cells that are electrically isolated from one another. They can be probed to spatially measure the current density vs. voltage curves under dark and illuminated conditions. The underlying models of bulk and surface recombination mechanisms have been well established for crystalline silicon based semiconductor devices such as the mesa diode. However, the combination of these phenomena that occur during the simulation of the operation of the mesa diode results in a unique edge effect that can significantly change the overall performance of the mesa diode. In particular, the simulations performed show that the space charge region becomes extended along the vertical edge of the mesa diode due to the fixed positive surface charge. At the intersection of the vertical edge and step, a strong electric field is

produced because it has a small convex radius of curvature. Depending on the sharpness of this intersection, the entire device can become significantly shunted. Simulations have been performed with a sharp corner and a smooth curve at the intersection of the vertical edge and the step. The use of a smooth curved transition results in significantly lower dark current density vs. voltage and a greater open circuit voltage and fill factor under illumination. Yet, even with a curved transition, the space charge region can extend approximately 100 microns into a 199.5 micron thick mesa diode, and have a bulk recombination rate that is two orders of magnitude greater than the rest of the device at low forward biases.

MODELING EDGE EFFECTS OF MESA DIODES FOR SILICON PHOTOVOLTAICS

by
Jesse S. Appel

Dissertation
Submitted to the Faculty of
New Jersey Institute of Technology
in Partial Fulfillment of the Requirements for the Degree of
Doctor of Philosophy in Materials Science and Engineering

Interdisciplinary Program in Materials Science and Engineering

August 2008

APPROVAL PAGE

MODELING EDGE EFFECTS OF MESA DIODES FOR SILICON PHOTOVOLTAICS

Jesse S. Appel

Dr. Nuggehalli M. Ravindra, Dissertation Advisor — Date
Professor of Physics, New Jersey Institute of Technology

Dr. Bhushan Sopori, Dissertation Co-Advisor — Date
Principal Engineer, National Center for Photovoltaics,
National Renewable Energy Laboratory, Golden, CO

Dr. Trevor A. Tyson, Committee Member — Date
Professor of Physics, New Jersey Institute of Technology

Dr. Anthony T. Fiory, Committee Member — Date
Research Professor of Physics, New Jersey Institute of Technology

---

Dr. Tao Zhou, Committee Member — Date
Assistant Professor of Physics, New Jersey Institute of Technology

---

Dr. Sufian Abedrabbo, Committee Member — Date
Assistant Professor of Physics, University of Jordan

BIOGRAPHICAL SKETCH

Author: Jesse S. Appel

Degree: Doctor of Philosophy

Date: August 2008

Undergraduate and Graduate Education:

- Doctor of Philosophy in Materials Science and Engineering
  New Jersey Institute of Technology, Newark, NJ, 2008

- Master of Science in Materials Science and Engineering
  New Jersey Institute of Technology, Newark, NJ, 2002

- Bachelor of Engineering in Mechanical Engineering
  The Cooper Union for the Advancement of Science and Art, New York, NY 1997

Major: Materials Science and Engineering

Presentations and Publications:

Jesse Appel, Bhushan Sopori, N.M. Ravindra. *A Note on Edge Passivation Mechanisms of N/P Mesa Diodes Through Modeling.* 18th Workshop on Crystalline Silicon Solar Cells and Modules: Materials and Processes. Vail, USA (2008).

Jesse S. Appel et al. *Characterization of Solar Cell Substrates Using the Diode Array Technique.* To be published in a special issue of TMS Journal of Electronic Materials (2008).

B. Sopori, P. Rupnowski, J. Appel, V. Mehta, C. Li, and S. Johnston. *Wafer Preparation and Iodine-Ethanol Passivation Procedure for Reproducible Minority-Carrier Lifetime Measurement.* 33rd IEEE Photovoltaic Specialists Conference, San Diego, USA (2008).

For Victoria and Quintin

ACKNOWLEDGMENT

I would like to acknowledge my advisors Dr. Nuggehalli Ravindra from the New Jersey Institute of Technology and Dr. Bhushan Sopori from the National Renewable Energy Laboratory in Golden, Colorado. Dr. Ravindra provided excellent guidance and encouragement throughout my entire time enrolled in the doctoral program, and I greatly appreciated it. Dr. Sopori is an outstanding teacher who helped me understand and develop the skills necessary to perform independent scientific research. The most important thing I learned from Dr. Sopori is that the process of investigating is just as important as the end goal of the research itself, and I greatly appreciated his guidance while performing my dissertation.

I would like to thank Dr. Przemyslaw (Peter) Rupnowski for all of our discussions regarding finite element analysis.

I would also like to thank Dr. Trevor Tyson, Dr. Anthony Fiory, and Dr. Tao Zhou from NJIT, and Dr. Sufian Abedrabbo from the University of Jordan for serving on my dissertation committee.

In addition to the guidance and encouragement I received from my advisors and committee members, I would like to thank my parents, Philip and Harriet Appel, who have supported me since day one.

Lastly, I would not have been able to complete my dissertation without the support and love of my wife, Victoria, and the inspiration of our son, Quintin.

TABLE OF CONTENTS

TABLE OF CONTENTS
(Continued)

TABLE OF CONTENTS
(Continued)

LIST OF FIGURES

LIST OF FIGURES
(Continued)

LIST OF FIGURES
(Continued)

LIST OF FIGURES
(Continued)

LIST OF FIGURES
(Continued)

LIST OF FIGURES
(Continued)

LIST OF FIGURES
(Continued)

LIST OF SYMBOLS

A_f^{-1}	Jacobian matrix
BSF	Back surface field
CdTe	Cadmium Telluride
CIGS	Copper Indium Gallium Diselenide
CVD	Chemical vapor deposition
c	Concentration
cm	centimeter
cn	Electron concentration for calculation by COMSOL Multiphysics
cp	Hole concentration for calculation by COMSOL Multiphysics
D	Diffusion coefficient
D_n	Electron diffusion coefficient
D_p	Hole diffusion coefficient
$D_{it}(E)$	Density of interface states as a function of energy level
DLTS	Deep level transient spectroscopy
$\vec{E}$	Electric field
E_C	Energy level of conduction band
E_i	Intrinsic energy level
E_I	Intrinsic energy level
E_t	Energy level of a recombination center
E_V	Energy level of the valence band

EBIC	Electron beam induced current
f	Distribution function
f	Probability that an energy level is occupied
f_0	Equilibrium distribution function
FB	Forward bias
FF	Fill Factor
G	Electron – hole pair generation rate
$G_{PV\ OPTICS}$	Generation rate profile curve-fit from PVOPTICS software
GaAs	Gallium Arsenide
I	Electric current
J	Electric current density
J_n	Electron current density
J_p	Hole current density
J_{sc}	Short – circuit current density
k	Boltzmann's constant
k_B	Boltzmann's constant
L	Minority carrier diffusion length
LBIC	Light beam induced current
MACD	Maximum achievable current density
MOS	Metal oxide semiconductor
m	meter
m^*	Effective mass

mA	milliamp
mW	milliwatt
n	Electron concentration
$\hat{n}$	Outward pointing unit normal vector
N	Doping profile
N	Electron or hole current (boundary condition)
N_0	Recombination rate (boundary condition)
N_A	Number of acceptors
N_D	Number of donors
n_i	Intrinsic carrier concentration
n_init	Electron concentration at a metal contact
N_{it}	Number of interface states
nm	nanometer
n_s	Electron concentration at the surface of an oxide or nitride
N_t	Number of recombination centers
p	Hole concentration
PCD	Photoconductance decay
PDE	Partial differential equation
PERL	Passivated emitter, rear locally – diffused cell
p_init	Hole concentration at a metal contact
p_s	Hole concentration at the surface of an oxide or nitride
q	Magnitude of a single electric charge

R	Reaction rate
r_n	Residual of electron concentration
r_p	Residual of hole concentration
r_V	Residual of electric potential
r_{ec}	Electron capture rate
r_{ee}	Electron emission rate
r_{hc}	Hole capture rate
r_{he}	Hole emission rate
Si	Silicon
SiO_2	Silicon dioxide
SiO_x	Silicon oxide (non-stoichiometric)
s_{n0}	Electron surface recombination velocity parameter
s_{p0}	Hole surface recombination velocity parameter
SPV	Surface photovoltage
s_r	Effective surface recombination velocity
SRH	Shockley – Reed – Hall
t	Time
T	Temperature
$\vec{u}$	Velocity for calculation by COMSOL Multiphysics
U	Recombination rate
U_s	Surface recombination rate

U_{SRH}	Bulk recombination rate using Shockley – Reed – Hall equation
V	volts
V	Electric potential
$\vec{v}$	Velocity
V_D	Electric potential at the drain
V_G	Electric potential at the gate
V_init	Electric potential at a metal contact
V_{OC}	Open circuit voltage
V_T	Electric potential threshold
v_{th}	Thermal velocity
$< v_x^2 >$	Average velocity squared
$V2$	Electric potential for calculation by COMSOL Multiphysics
XBIC	X-Ray beam induced current
x_n	Initial guess for iteration
x_{n+1}	Iteration value after initial guess
XTEM	Cross – sectional transmission electron microscopy
$\vec{\alpha}$	Acceleration
Δn_s	Change in surface concentration of electrons from equilibrium
Δn_p	Change in surface concentration of holes from equilibrium
ε_0	Permittivity of free space
ε_r	Relative permittivity

λ	Damping factor
μ_n	Electron mobility
μ_p	Hole mobility
μPCD	Microwave photoconductance decay
ρ	Charge distribution
σ_n	Electron capture cross – section
σ_p	Hole capture cross – section
$\sigma_n(E)$	Electron capture cross – section as a function of energy level
$\sigma_p(E)$	Hole capture cross – section as a function of energy level
τ	Minority carrier lifetime
τ_c	Relaxation time
τ_{n0}	Electron minority carrier lifetime parameter
τ_{p0}	Hole minority carrier lifetime parameter
ϕ	Electric potential
ψ	Placeholder variable
Ω	ohm

CHAPTER 1

INTRODUCTION

1.1 Energy Production in the Future

The demand for energy increases as populations increase and new technologies and innovations emerge. In the future, new sources of energy will need to be developed in order for existing economies to expand and new economies to develop. As the demand for energy increases, the price also rises. This makes it possible for alternative sources of energy to be developed in addition to traditional energy sources because they are economically viable [1-4]. More importantly, as worldwide energy demand increases, all sources of energy will need to be produced at greater capacity. This situation makes the use of renewable energy sources more attractive from an economic perspective since the "fuel" used to develop power is no longer a commodity, but a freely available resource such as biomass, wind, and sunlight. However, it should be noted that energy input is still required to make the conversion system. Furthermore, renewable energy sources will be needed since they are environmentally sustainable, which is important for a world where pollution and environmental degradation from using conventional energy sources poses significant threats to the health of all mankind.

According to the United States Department of Energy's Annual Energy Review (AER) 2006 [5], electricity produced by coal, nuclear power, and natural gas accounts for almost 90% of the total electricity produced in the United States as shown in Figure 1.1.

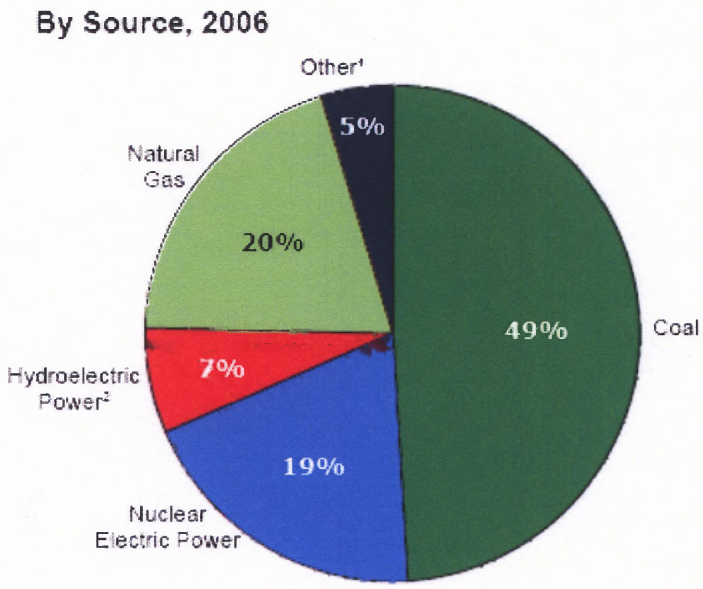

Figure 1.1 US electricity generation (all sectors) [5].

The consumption of these three fuels to generate electricity has also increased significantly over the last 20 years as shown in Figure 1.2. In addition, the price of coal

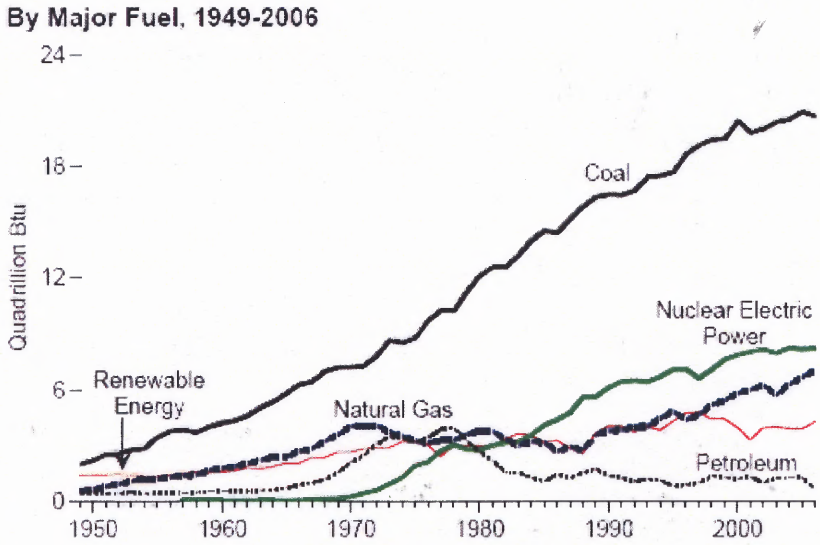

Figure 1.2 US electricity generation by fuel source [5].

has started to increase since 2003, the price of natural gas has increased since 1995, and uranium oxide fuel prices have increased since 2001. The price increases for these fuels are shown in Figure 1.3.

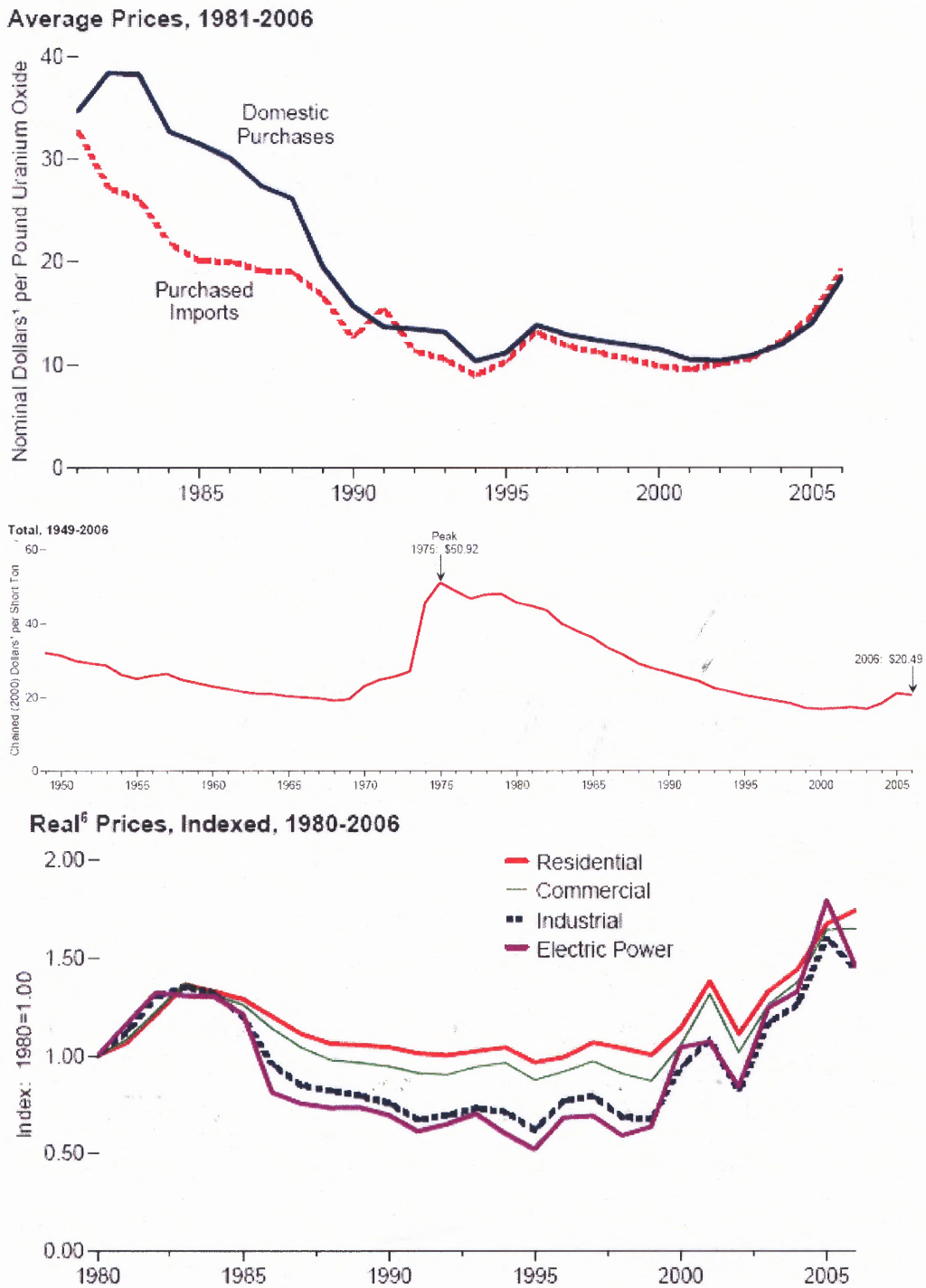

Figure 1.3 Price history for uranium oxide, coal, and natural gas [5].

Also, the total energy consumption from all sources of energy has increased or remained relatively constant since the early 1980's, and this trend is expected to continue into the future with results forecasted to 2030 as shown in Figure 1.4. Although this

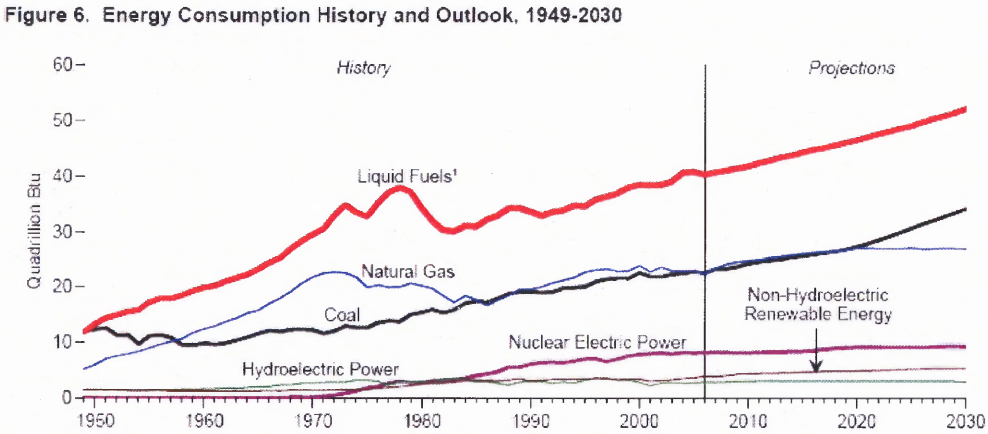

Figure 1.4 Timeline of consumption of energy in the United States [5].

would suggest higher electricity prices as well as higher energy prices in general, photovoltaics is one technology where the prices are actually going down. In particular, the cost of a photovoltaic module in 2005 is almost half of its cost in 1991, and this probably does not account for the increase in efficiency of the newer photovoltaic modules. What is more revealing is that the total number photovoltaic modules shipped for installation has increased by more than a factor of ten in the period of 1982-2005, and has doubled in the period of 2002-2005. The price history of photovoltaic cells and modules as well as the number of photovoltaic installation are shown in Figure 1.5 and Figure 1.6, respectively.

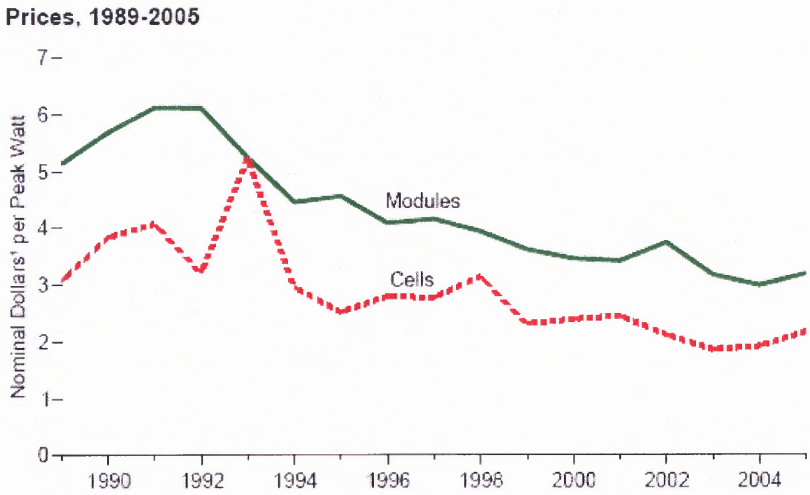

Figure 1.5 Prices of photovoltaic modules and cells 1989-2005 [5].

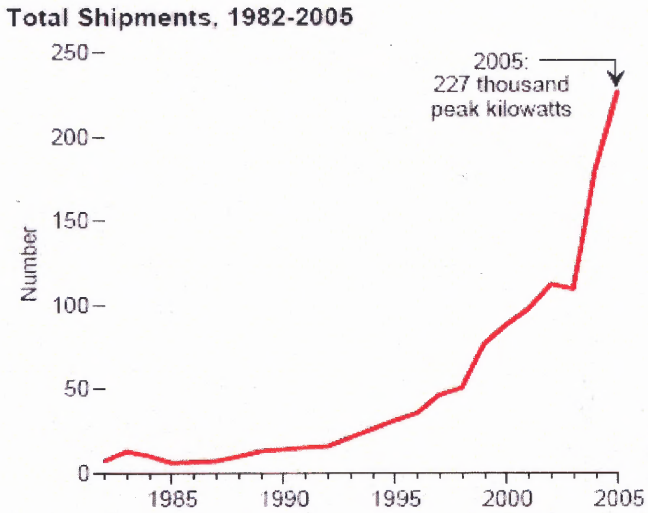

Figure 1.6 Total shipment of photovoltaic systems 1982-2005 [5].

The growth rate would have been more dramatic if not for recent shortages in silicon feedstock, which is used to make a majority of photovoltaic cells. However, the silicon feedstock shortage has led to many important developments in the silicon-based photovoltaic industry and contributed to its growth, and allowed the thin films photovoltaic manufacturers to mature by introducing commercially successful products [6-9].

Although the relatively recent commercial success of photovoltaic-based electricity generation is impressive, and the current trends look promising for this energy source in the future, the advances in cost and efficiency for photovoltaics need to continue to ensure photovoltaics remains a long term viable energy source. This is especially important when comparing energy generated from photovoltaic sources to that generated by all other sources. In particular, renewable energy accounted for 7% of the total energy generated in the United States in 2006, of which only 1% was generated by photovoltaics. The photovoltaic industry is working on many technologies that will continue to reduce the cost and increase the efficiency of photovoltaic cells and modules. Furthermore, a wide range of companies, universities, and researchers that work in fields related to photovoltaics have been developing a variety of products, tools, and materials so that photovoltaic energy production will continue to become cheaper and more efficient [10-13].

Investigating materials, characterization tools, processing technologies, and other scientific and engineering problems confronting the photovoltaics industry is more than an academic exercise. Performing research in this field is of paramount importance to furthering the development and implementation of energy from photovoltaics. In addition to developing solar cells from an economic standpoint, power generation from this source has been touted as an environmentally responsible energy source as well as a strategic source for energy independence. However, these goals will probably not be realized unless photovoltaics can compete economically on a similar scale to that of traditional energy sources [14].

The remainder of this chapter will include an introduction to typical solar cell operation and fabrication, followed by a brief review of some methods for mapping solar parameters and underlying wafer properties, then a discussion of mesa diode arrays, and conclude with an outline of the rest of the dissertation.

1.2 Introduction to Solar Cells

1.2.1 Solid State Theory

Solar cells are large area semiconductor diodes. They make use of the photoelectric effect to generate excess charged carriers that can be collected for power generation. Incoming photons emitted by the Sun that have energy greater than semiconductor's bandgap are absorbed in the semiconductor and will excite an electron located in the valence band to the conduction band. The excited electron leaves an unoccupied energy level in the valence band [15]. This process is shown in Figure 1.7 [16].

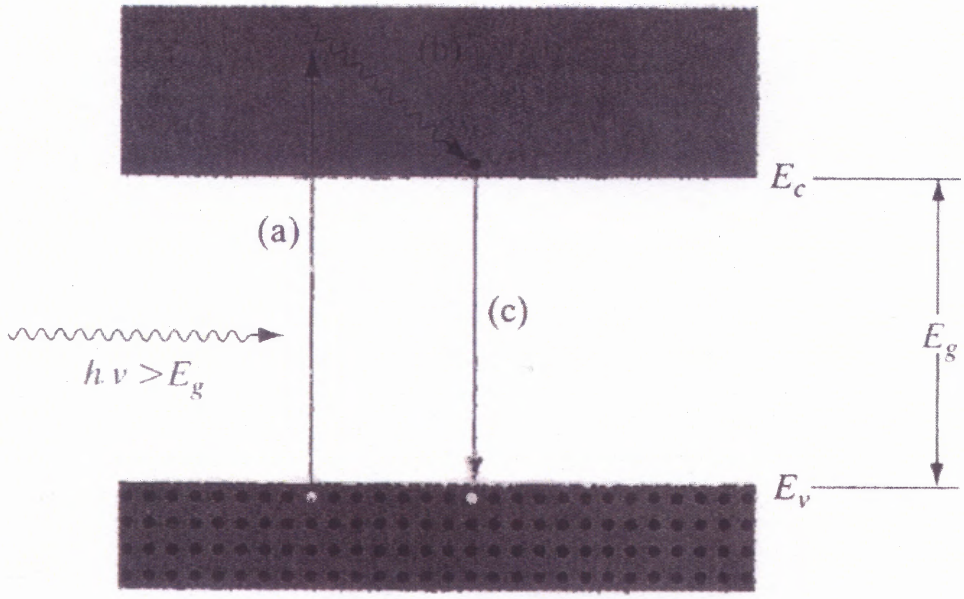

Figure 1.7 Semiconductor band diagram showing the absorption of a photon(a), settling to the lowest available conduction band energy level(b), and electron – hole recombination(c) [16].

This unoccupied energy level and the reduction of electron concentration in this state leads to the concept of a hole, which can be treated as an electron with a charge that is equal in magnitude but with a positive charge. Although a hole is essentially the absence of an electronic charge carrier, it can be treated as a discrete physical particle. It has an effective mass, diffusion coefficient, mobility, concentration level, and charge [17]. Therefore, when a photon of sufficient energy is absorbed by a semiconductor, from an electronic device standpoint, an electron – hole pair is generated.

The simplest driving force to separate electron-hole pairs is an electric field produced by the formation of a junction. Without a driving force, electrons and holes would move primarily via diffusion processes because of concentration gradients [17]. In order to derive useful energy from photogenerated carriers the electrons and holes must be separately and collected at different contacts. In most silicon solar cells, a single

junction is used and is made as close to the location of maximum electron – hole pair generation [18].

In standard crystalline silicon solar cell technology [18], an n-p junction is formed by diffusing a boron-doped base wafer with phosphorus. The resulting phosphorus doped layer is approximately 0.5 microns thick at the surface of the silicon wafer. Boron doping generates an energy level just above the valence band in the silicon bandgap, while phosphorus generates an energy level just below the conduction band in the silicon bandgap. At room temperature, electrons can be easily excited from the valence band to boron level and from the phosphorus level to the conduction band. Therefore, the boron doped region will have an excess hole concentration at room temperature, and is known as a p-type material. The phosphorus doped region will have an excess electron concentration at room temperature, and is known as an n-type material. However, at the junction between the phosphorus and boron doped regions, the positive phosphorus ion cores and the negative boron ion cores generate a large electric field that forces excess mobile electrons and holes out of this area, and is known as the depletion region, since it is depleted of mobile electronic charges [19]. A schematic of a junction, showing the depletion region, the electrostatic potential throughout the device, and the band diagram including the equilibrium Fermi level is shown in Figure 1.8.

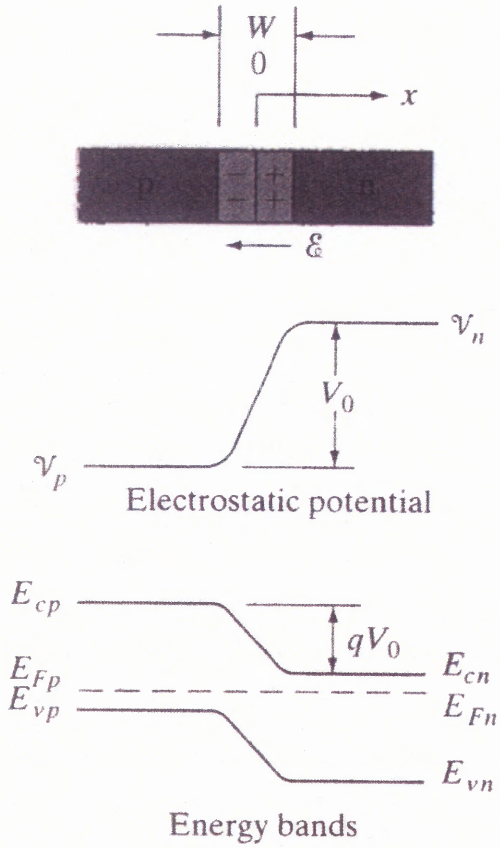

Figure 1.8 Semiconductor junction showing the depletion region, electrostatic potential spatially, and band diagram with equilibrium Fermi level [17].

If this material is illuminated, excess electrons and holes will be separated due to the built-in electric field produced by the junction [20]. The charge flow of electrons and holes due to the electric field is the drift current and dominates the charge flow near the junction. In regions away from the junction, the electric field strength becomes almost negligible and charge flow of electrons and holes is primarily a diffusion process that is largely dominated by concentration gradients. The drift-diffusion currents for electrons and holes adequately describe the primary transport mechanisms in a typical n-p junction solar cell [21]. The drift diffusion equations for electrons and holes are shown in Equations (1.1) and (1.2), respectively. Using the steady – state continuity equations, the

$$J_n = -q\, n\, \mu_n \nabla\phi + q\, D_n \nabla n \tag{1.1}$$

$$J_p = -q\, p\, \mu_p \nabla\phi - q\, D_p \nabla p \tag{1.2}$$

electron and hole currents can be related to the generation and recombination of excess carriers. This is shown in Equations (1.3) and (1.4) [21].

$$-\nabla \cdot J_n = q(G - U) \tag{1.3}$$

$$\nabla \cdot J_p = q(G - U) \tag{1.4}$$

1.2.2 Generation and Recombination

As previously stated, excess electron-hole pairs are generated by incident photons. The generation rate as a function of depth is dependent on many factors, some of which are the absorption coefficient and intensity of the photon flux spectrum, as well as surface texturing and the use of antireflective coatings [22, 23]. Physically, recombination is the process when an electron from the conduction band loses energy and occupies a state in the valence band [24]. Alternatively, it can be described as a hole from the valence band that gains energy and occupies a state in the conduction band. For an electronic device, an electron and a hole that occupy the same energy level at the same time recombine and reduce the concentration of both species by an equivalent amount.

Recombination of electrons and holes occurs in the bulk and at the surfaces of semiconductor materials. Bulk recombination primarily occurs through radiative, Auger, and recombination centers via energy levels inside the bandgap of the semiconductor [24]. The dominant bulk mechanisms will depend on the nature of the semiconductors that are used to make the solar cell and their operating conditions. For example, bulk recombination in typical crystalline silicon material occurs via recombination centers

except at high injection levels where Auger dominates. Surface recombination can occur at a semiconductor's free surface, an interface with a dissimilar material, or at a grain boundary of the same type of semiconductor.

1.2.2.1 Bulk Recombination. The following briefly describes bulk recombination processes. In radiative recombination, an electron from the conduction band loses energy and moves to an unoccupied state in the valence band. The energy loss results in the emission of a photon [25]. This recombination mechanism is more common for direct bandgap semiconductors such as gallium-arsenide (GaAs). Auger recombination is similar to radiative recombination except that energy loss is transferred to a secondary electron that becomes excited and then decays back to its original state by emitting phonons [25]. Recombination due to recombination centers via an energy level inside the bandgap is a two-stage process outlined separately by Hall [26] and, Shockley and Reed [27]. Available energy levels in the semiconductor bandgap are a result of defects, such as impurity atoms. An excited electron in the conduction band loses energy and moves to a defect level in the bandgap, which is followed by another step where it loses energy and recombines with a hole in the valence band [28, 29]. These recombination mechanisms, as shown in Figure 1.9, can occur simultaneously, and their effects are additive.

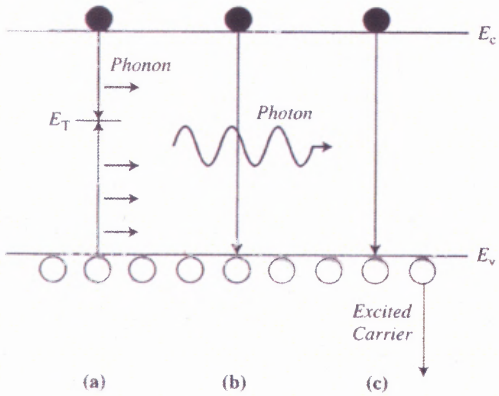

Fig. 7.2 Recombination mechanisms: (a) SRH, (b) radiative, and (c) Auger.

Figure 1.9 Band diagram depiction of bulk recombination mechanisms [25].

1.2.2.2 Surface Recombination. Surface recombination occurs at planar discontinuities in a semiconductor. As an example, in microelectronics, a thermally grown oxide on a silicon surface is a standard processing technique for applications such as the formation of a gate insulator. By adjusting the growth conditions, the number of interface states that arise in the semiconductor bandgap can be minimized. The recombination process that takes place due to interface states is similar to the bulk mechanism of recombination centers located at energy levels in the bandgap as previously described [30-32]. This is illustrated in Figure 1.10. In silicon solar cells

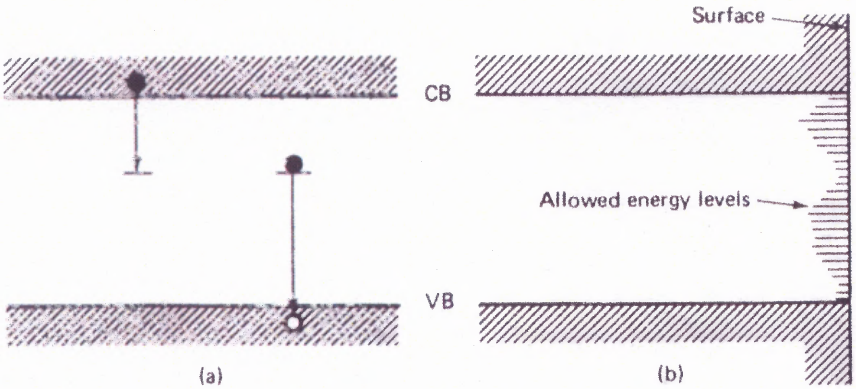

Figure 3.12. (a) Two-step recombination process via a trapping level within the forbidden gap of a semiconductor. (b) Surface states lying within the forbidden gap at the surface of a semiconductor.

Figure 1.10 Band diagram depiction of surface recombination caused by interface states between the semiconductor and the passivating material [21].

surface recombination occurs at the interface between silicon and the passivating hydrogenated silicon nitride layer [33, 34]. The dissimilar materials produce interface states in the bandgap and recombination occurs via these states, which is similar to bulk recombination via recombination centers. Recombination also occurs at grain boundaries [35, 36]. This mechanism can be particularly important if the base material is microcrystalline, such as thin film silicon. Grain boundary recombination can also become important in cast multicrystalline silicon material. Multicrystalline silicon is a common material used for making solar cells. Typically, grain sizes are macroscopic and range from a millimeter to a few centimeters. Although the number of grains on a 4-½"x4-½" wafer can be measured in the tens to hundreds, recombination at the grain boundaries can be significant if there a large number of impurities or metallic precipitates, which would be even worse. Also, a high degree crystalline disorder in adjacent grains can lead to a higher grain boundary recombination rate since this will generate interfacial states that would not exist in a more periodic crystalline grain.

1.2.3 Solar Cell Operation

If the electron-hole pair generation profile and recombination mechanisms are known, the continuity equations can be solved simultaneously to obtain the electron and hole concentration profiles. However, the continuity equations are coupled via the electric potential. Therefore, Poisson's equation, which relates the electric potential to the charge distribution in the device, is required to completely describe the system [37]. It is shown in Equation (1.5).

$$-\nabla \cdot \varepsilon_0 \varepsilon_r \nabla V = \rho \tag{1.5}$$

It should be noted that in many cases, the electron and hole concentrations are estimated using an exponential function, which is based on the Boltzmann approximation to the Fermi-Dirac distribution for electrons and holes. They are a function of electric potential, the Fermi level shift for electrons, and the Fermi level shift for holes [38]. The band diagram showing the Fermi level shift for electrons and holes is shown in Figure 1.11. The continuity equations for electrons and holes can be rewritten in terms of quasi-

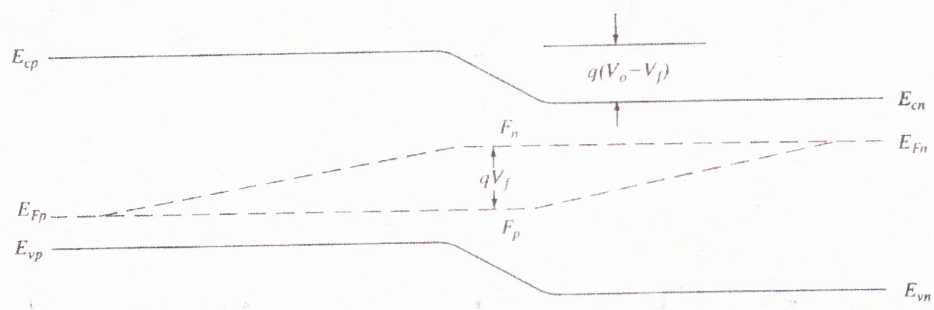

Figure 1.11 Band diagram of a forward biased semiconductor including Fermi level shifts for holes and electrons [19].

Fermi levels. Therefore, the coupled continuity equations, with Poisson's equation can be solved for electrical potential, electron quasi-Fermi level, and hole quasi-Fermi level.

Classically, this is known as Gummel's method [39], and has been used and adapted to solve a wide range of semiconductor device problems, including n-p junction solar cells.

The operation of an n-p semiconductor junction device also describes the fundamental operating principles of solar cells. The junction is used as the driving force to separate electrons and holes when they are illuminated. In some high efficiency concentrator solar cells, multiple junctions are used, with each one designed to capture a specific spectral band of incoming sunlight, but the operation of each junction is the same as that of a single junction solar cell [40, 11]. This brings up interesting technological challenges that face the solar cell industry. The two most important questions that face the solar cell industry are how can one make existing solar cells more efficient while reducing the cost, and what new materials or processing methods can be used to achieve better efficiency, lower cost, or both [11].

1.2.4 Solar Cell Fabrication

Currently, most solar cells are made from crystalline silicon, either by a quickly pulled, impurity rich, Czochralski single crystal or cast multicrystalline silicon [11]. The ingots grown by these methods have to be sliced into thin wafers before they are processed into solar cells and assembled to make photovoltaic modules. The following describes the typical processing steps for making a crystalline silicon photovoltaic cell. First, a p-type wafer is etched to remove saw damage. Next, the wafer is subjected to a diffusion process, which generates a thin n layer near the surface of the p-type wafer. In most cases the base p-type wafer consists of boron as the dopant, and the diffused n-type region consists of phosphorus as the dopant. A silicon nitride antireflective coating is deposited on the front side on top of the n-type layer. The front and back contacts are

applied by using the screen printing technique. The front contact is a grid structure of busbars and fingers made of a silver paste. It covers the minimal amount of area, while minimizing the series resistance. The rear contact is made from an aluminum paste and covers the entire backside of the wafer except for a thin layer around the edge. Both contacts are fired at the same time in an infrared furnace. During firing, the paste dissolves the silicon nitride and then forms an Ohmic contact with the silicon wafer. A schematic of a completed solar cell is shown in Figure 1.12. In addition to the steps previously outlined, Figure 1.12 represents an exaggerated depiction of surface texturing, shown as pyramids, on the top and bottom of the solar cell. This is done to enhance light trapping, which produces internal reflections of the incident photons, thereby increasing the cell efficiency.

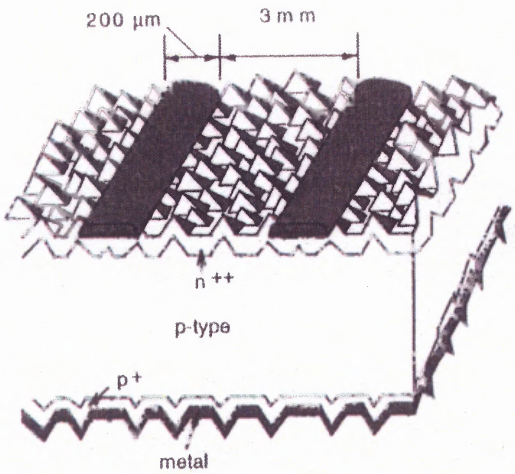

Figure 11.1: Screen printed crystalline silicon solar cell (not to scale).

Figure 1.12 Completed crystalline silicon solar cell with surface texturing [18].

Although the description of the processing steps for making typical crystalline silicon solar cells appears straightforward, the development of these processes has taken many years to implement. This is because in order to make an affordable solar cell with

reasonably good efficiency, each process has to serve more than one function. For example, during phosphorus diffusion for the formation of an n-type layer, a simultaneous impurity segregation process known as gettering also occurs, and some of the metallic impurity atoms in the material are moved to the emitter making them less electrically active and increasing the device's efficiency [41]. Another example is the use of silicon nitride as an antireflective coating on the top surface of the photovoltaic cell [33, 34]. The silicon nitride coating also acts as a surface passivation layer, which can significantly reduce the amount of carriers lost to surface recombination. Another example is the firing of the back contact. Not only does this occur while simultaneously firing the front contact, but aluminum in the aluminum paste also forms an alloy with the p-type silicon at the back surface. Being a group III element, aluminum itself is a p-type dopant and increases the dopant concentration in the surface region to about five to ten microns. This effect is very important since this region of increased dopant concentration acts a carrier reflector, which reduces the surface recombination velocity at the back contact, thereby increasing the solar cell efficiency [42]. In addition to creating the back surface field, the back aluminum layer is also an effective gettering layer during the firing process. Therefore, it can also reduce the bulk impurity levels, thereby reducing the bulk recombination rate, which will increase solar cell efficiency. It should be noted that many of these combinations are beneficial, but they have not been optimized, and further cost reduction and efficiency gains could be realized. In particular, front contact formation and hydrogen passivation of impurities and defects is an active area of research.

Significant improvements in crystalline silicon solar cell technology have helped reduce the cost, while improving the efficiency. However, the main drawback to standard crystalline silicon solar cell technology is that wafers need to be diced from the ingot, processed into solar cells, and then assembled into modules. In order to minimize the impact of these drawbacks, manufacturers have made wafers thinner and larger. Currently, for solar cell applications, crystalline silicon wafers are between 180 – 220 microns thick with dimensions of 4-½"x4-½", and 6"x6" will soon be the new standard. This doesn't eliminate the problem, and leads to more wafer breakage, which is another area of active investigation [43].

The alternative method to sawing wafers and assembling solar cells into panels is thin film photovoltaics. The main reasons for using thin film is to utilize direct bandgap materials. Making a solar panel using a thin film semiconductor with a direct bandgap does not require as much material as an indirect bandgap material such as crystalline silicon. There are a variety of materials that are used to make thin film solar cells/panels. Ones that are made using polycrystalline silicon, CdTe, and CIGS (copper indium gallium diselenide) are processed using chemical vapor deposition (CVD) and newer inkjet technologies. Both CdTe and CIGS based solar systems are commercially available products. Ribbon silicon can be produced by the string ribbon method and the cast ribbon method. Other technologies involve depositing hydrogenated amorphous silicon and crystalline silicon on glass. Research in the field of thin film photovoltaics is currently quite extensive because of the potential cost savings and the recent success of CdTe, CIGS, and ribbon silicon based systems [11].

Ongoing investigation in crystalline silicon based and thin film photovoltaic systems are focused on improving the efficiency, while reducing the cost. Characterization techniques are vital to ensure that this continues. The following section briefly describes some characterization methods that are used in the photovoltaics industry.

1.3 Characterizing and Mapping Solar Cell Properties

1.3.1 Introduction

Many of the techniques used to measure and characterize solar cell properties were adapted from ones used by the microelectronics industry. The parameter that is most useful for describing how well a solar cell will perform is the minority carrier diffusion length, which is the average distance the minority electronic carrier will travel before recombining with a majority electronic carrier [44]. A material with a long minority carrier diffusion length will have less bulk recombination and the photogenerated carriers will have a higher probability of making it to the contacts, where they can be collected and used to generate electric power. Conversely, a material with a short minority carrier diffusion length will have more bulk recombination, which leads to less carriers that will be collected at the contacts thus yielding a lower device efficiency. The minority carrier lifetime, τ, is related to the minority carrier diffusion length, L, via a straightforward relationship using the minority carrier diffusion coefficient, D, as shown in Equation

$$L = \sqrt{D\tau} \tag{1.6}$$

(1.6). τ is currently the most widely used parameter for characterizing crystalline silicon solar cells [44].

Historically, the minority carrier diffusion length was used to characterize solar cell material, in particular crystalline silicon. This was done because this parameter was measured extensively in the silicon microelectronics industry, and was transferred to the photovoltaics industry. Researchers in the photovoltaics community tend to use minority carrier lifetime as a parameter to determine the quality of the underlying semiconductor since techniques have been developed to measure the minority carrier lifetime as a function of incident photon flux, known as injection level. However, both parameters are useful for characterizing solar cells [44].

Minority carrier diffusion length and lifetime can be measured on semiconductor material that does not have a junction. Additional information can be ascertained after a junction has been formed on a solar cell that has been processed to a varying degree of completion [45]. One of the main techniques is to direct a laser beam or an electron beam on to part of the solar cell and measure the photogenerated current. This is known as LBIC (Light Beam Induced Current) or EBIC (Electron Beam Induced Current) [46]. Recently, some researchers have used x-rays, and this is known as XBIC, and it improves the scanning resolution and allows for other analyses, such as impurity composition [47].

Measurement of the minority carrier diffusion length and lifetime, as well as the LBIC and EBIC are important not only because of the parameters they determine, but also because the measurement systems can be used to scan a sample with very good resolution. This is particularly important for multicrystalline silicon based solar cells. With this type of material, a small poorly performing region can significantly degrade the overall efficiency of the entire solar cell [48]. The next section describes the primary methods used to determine the aforementioned parameters.

1.3.2 Diffusion Length Measurements

Minority carrier diffusion length can be measured using the surface photovoltage (SPV) technique. A space charge region is formed at the surface of the semiconductor because of surface states. The SPV measurement device generates a surface photovoltage in a semiconductor by the following process [49]. A collimated light source passes through a bandpass filter, and chopper, and then is focused on the semiconductor sample. Above the sample is a transparent insulator with a transparent conductor on top of the insulator. Using the chopped light source, which is assumed to be monochromatic due to the filter, and a lock-in amplifier the surface photovoltage can be measured. The surface photovoltage is a result of photogenerated carriers diffusing toward the space charge region at the top of the wafer while the back of the wafer is grounded. A schematic of a setup that is used to perform scanning diffusion length measurement using the surface photovoltage technique is shown in Figure 1.13.

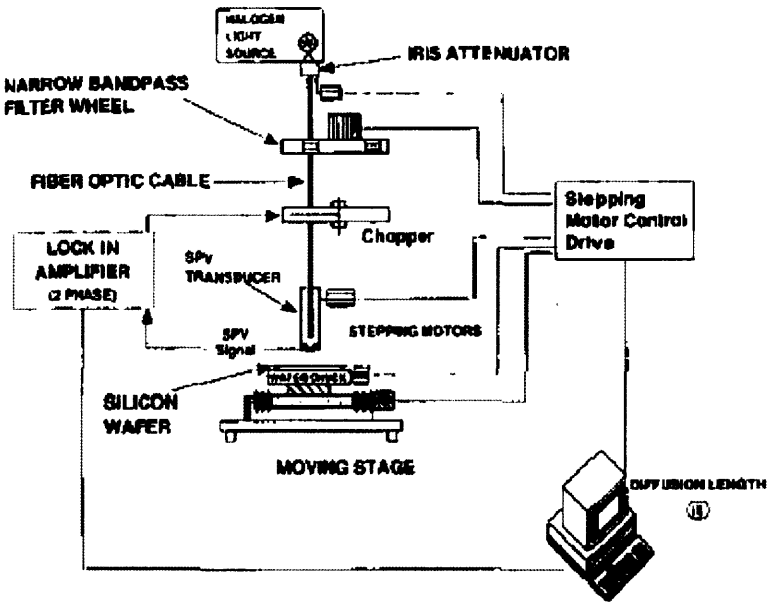

Figure 3. Schematic of the computerised apparatus for SPV mapping.

Figure 1.13 Diagram for making spatially resolved diffusion length measurements [49].

The surface photovoltage is a function of photon flux, sample reflection coefficient, sample absorption, diffusion length, and surface recombination velocity. By measuring the photon flux required to keep the SPV constant at different incident wavelengths, a plot of light the inverse of the absorption coefficient versus the photon flux can be drawn. The minority carrier diffusion length is found by determining the x-intercept of a linear regression through the experimental points. Typically this measurement is made by either keeping the photon flux or SPV constant. An example of a diffusion length calculation is shown in Figure 1.14. It should be noted that this

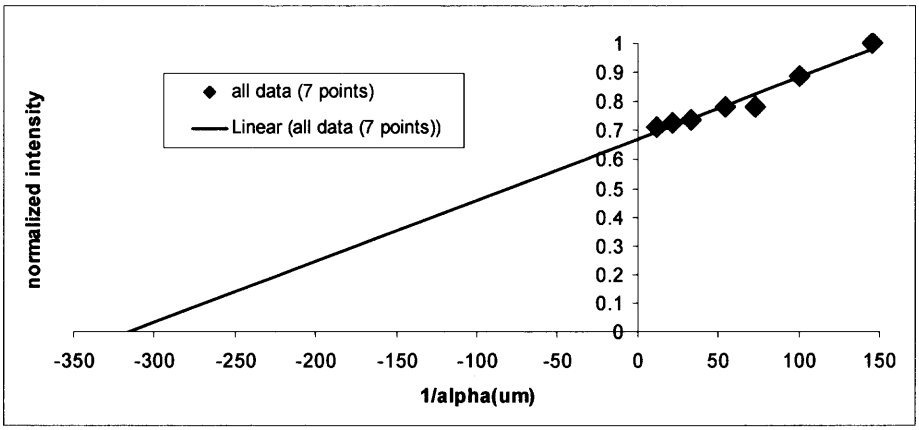

Figure 1.14 Diffusion length measurement using constant SPV (p-Si 14.68 Ω-cm).

measurement assumes that the thickness of the wafer is three to four times greater than the minority carrier diffusion length. As the wafer thickness approaches the minority carrier diffusion length, the influence of the surface recombination velocity cannot be ignored and needs to be accounted for in the determination of the minority carrier diffusion length [50, 51]. The main advantages of this method are that sample preparation is minimal and it is a steady-state measurement. Furthermore, measurements

can be made on a sample with a junction. The only difference is the space charge region is a result of the junction rather than the surface states.

1.3.3 Lifetime Measurements

For solar cell materials, the minority carrier lifetimes are primarily measured using two techniques. One is photoconductance [52, 53] and the other photoluminescence [54-56]. Both techniques use an illumination source, typically a laser, to generate electron-hole pairs in the semiconductor sample. In the photoconductance measurement, the excess photogenerated carriers increase the conductivity of the sample [57]. After the illumination source is removed, the excess photogenerated carriers recombine via one or more mechanisms previously described and the conductivity of the sample returns to its equilibrium value. The conductivity is monitored by directing a periodic microwave laser beam on the back of the sample [52]. A conductivity change can be observed as a reflected microwave beam. Typically, the decay of reflected microwave power is used to determine the minority carrier lifetime. However, one can also use the phase shift of the reflected microwave to determine the minority carrier lifetime [58]. A block diagram of the microwave photoconductance decay (PCD) measurement setup is shown in Figure 1.15.

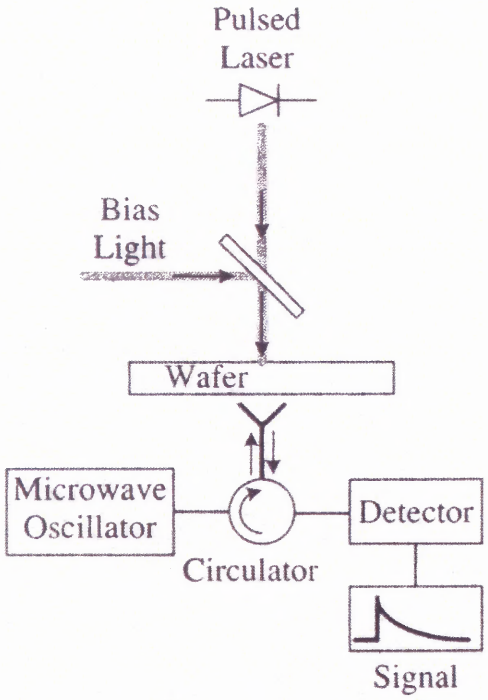

Figure 1.15 Diagram of the microwave PCD measurement setup [24].

In the photoluminescence measurement, the radiative decay is measured [54]. After the illuminated source is removed, the radiative recombination process emits photons that are absorbed by a detector. The decay rate of the photoluminescence signal can be used to determine the minority carrier lifetime. The setup for photoluminescence measurements is shown in Figure 1.16. Since both PCD and PL techniques use lasers to

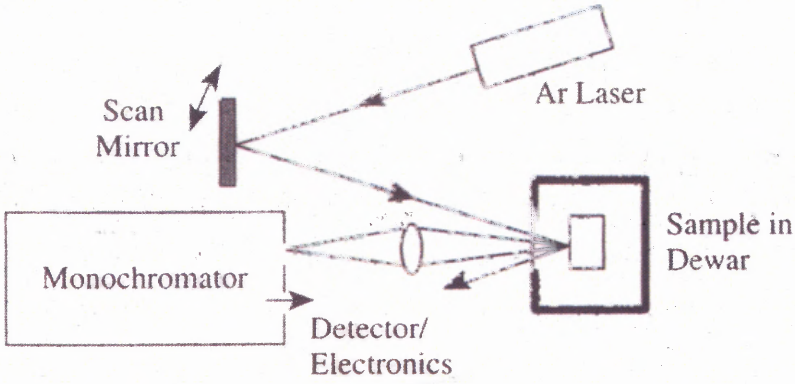

Fig. 10.27 Schematic photoluminescence arrangement.

Figure 1.16 Diagram of PL measurement setup [46].

illuminate the sample, both are used extensively for mapping wafers.

1.3.4 LBIC and EBIC Measurements

In addition to surface photovoltage (SPV), photoconductance decay (PCD), and photoluminescence (PL) measurements, LBIC and EBIC measurements are used to measure the minority carrier diffusion length and lifetime as well as the output power as a function of constant input power. LBIC and EBIC scans can also be used to identify impurities [59].

1.3.5 I-V Measurements Using Mesa Diodes

The scanning techniques previously discussed can be used to spatially determine the minority carrier diffusion length and lifetime. They have been extended to find impurity concentrations. LBIC measurements of a wafer with a junction, or a completed solar cell, are used to determine the power output, but only at the intensity and frequency of the laser used for illumination. A significant amount of useful information can be obtained by measuring the current versus voltage characteristics of the solar cell under dark and illuminated conditions [45]. Simply probing different locations on a solar cell does not accurately determine the local current versus voltage characteristics. Localized measurements of the current versus voltage can be made using an array of small diodes (by photovoltaic industry standards), which are edge passivated mesas [45]. They are fabricated on single or multicrystalline silicon substrates. The most important aspect of the mesa diode arrays is they are the only way to make localized illuminated measurements of the open circuit voltage and fill factor. These are two of the most useful

parameters in determining losses in a solar cell. Therefore, characterizing a solar cell using mesa diode arrays is a valuable tool that can be viewed as a process monitor for silicon crystal growth and subsequent formation of the substrate and the effectiveness of the steps for processing the silicon wafer into a completed solar cell.

Although using diode arrays as a characterization technique is not widely used in the solar cell industry, it is not uncommon to see them used in research, such as measuring impurity concentration measurements via deep level transient spectroscopy (DLTS) [60]. Furthermore, mesa diode arrays have been used to measure the effectiveness of backside hydrogen implantation [61] and the effects of dislocation density in multicrystalline silicon on the dark current [45]. Also, Schottky and junction diodes have been used to investigate a wide range of phenomena in the microelectronics industry for many decades [62]. The primary difference is that the diodes made using microelectronics grade silicon are comprised of a cleaner material and active electronic devices can be incorporated to minimize the edge effects in the device. This is not an option when using solar grade silicon because constructing an active device will likely alter the material that is being investigated to a point where the measurements would not correlate to the solar cell performance. The following section briefly describes how mesa diodes used for crystalline silicon solar cell characterization address edge effects and the importance of modeling them.

1.4 Edge Effects in Mesa Diodes

In microelectronics, edge effects were some of the most important and earliest problems investigated. Fast switching planar Schottky diodes were studied, and it was determined

that using a guard ring, which is an additional concentric diode with an appropriate bias, can almost result in ideal diode characteristics of the main device. Grove et al. studied charge and interface state distributions at silicon and oxide interfaces [30, 31]. Shockley et al. studied surface charges at the interface of silicon dioxide at n – p silicon junctions [63]. Early work by these groups and others led to the exploitation of edge effects to produce metal – oxide – semiconductor (MOS) transistors [64].

For silicon diodes whose surfaces are adjacent to a thermally grown silicon dioxide passivation layer, the oxide needs to have a low degree of disorder, which reduces the interface charge and interface state density. Furthermore, the oxide should have few impurities and crystallographic defects. These are the requirements for an oxide to passivate a silicon surface [45].

It is not feasible to grow a thermal oxide of high enough quality without significantly altering the diffused n region at the top of a typical crystalline silicon solar cell. Therefore, the mesa diodes arrays are passivated with a hydrogenated oxide grown from a chemical etch. The mesa diodes are delineated and have their surfaces passivated by the specially formulated chemical etchant. Chapter 2 will present a detailed description of how this etch passivates the surface of the mesa diodes. This etch produces a clean Si-SiO_x interface of low interface states, and additionally provides hydrogen for edge passivation. Therefore, when a mesa diode is probed under dark and illuminated conditions, the current versus voltage characteristics are representative of the bulk diode.

Although the passivating chemical oxide performs well, a detailed understanding of its limitations is not known. In order to determine such limitations, the edge effects

need to be modeled and incorporated as boundary conditions for solving the continuity equations for electrons and holes coupled with Poisson's equation. Then, how these parameters affect the operation of the mesa diode can be determined. Modeling the edge effects of the mesa diode and incorporating them into a complete electronic model of a diode is the primary objective of this dissertation.

1.5 Dissertation Outline

Characterizing crystalline silicon wafers and completed solar cells is very important for identifying problems with various crystal growth techniques and solar cell processing methods. Currently, there are commercially available characterization tools that perform measurements to determine the minority carrier diffusion length and lifetime as well as the light beam induced current (LBIC). These are all valuable techniques especially since they can be used to scan an entire wafer.

Mesa diode arrays are currently the only way to obtain spatially resolved measurements of the open circuit voltage and fill factor. In order to fabricate these devices, a special chemical etch is used to delineate and passivate the diodes. The main purpose of this dissertation is to incorporate the edge effects of surface charge and interface states at the silicon – oxide interface into the drift – diffusion model of a semiconductor device, and understand the influence edge effects have on the operation of a mesa diode.

Chapter 2 will discuss edge losses in semiconductor diodes. Chapter 3 will discuss the theoretical basis for modeling the entire diode including the edge effects. Furthermore, an explanation of how the problem can be cast numerically and the solution

procedure will be provided. Chapter 4 will discuss the results of simulating the operation of a small sample diode and a mesa diode. A discussion of mesa diode simulations that indicate an edge shunting mechanism that had not been previously considered will be described in detail. Chapter 5 will discuss conclusions of the simulations and proposals for future work.

CHAPTER 2

EDGE LOSS IN SEMICONDUCTOR DIODES

2.1 Introduction

Characterizing silicon substrates used for manufacturing photovoltaic cells has always been important and this field has grown significantly over the past few years. As commercial solar cells have become more efficient, investigating the limitations of current materials and processes becomes more imperative if efficiencies are to further increase. Historically, characterization techniques and electronic measurements, such as photoconductance decay (PCD) [57] and current vs. voltage measurements under a solar simulator, have provides data with respect to large area samples and have been used to estimate the performance of an entire cell. Complementary characterization techniques and electronic measurements, such as surface photovoltage (SPV) [49], light beam induced current (LBIC) [59], photoluminescence (PL) [54], microwave photoconductance decay (PCD) [52], and a wide range of scanning microscopy techniques can be used to map material properties and electronic characteristics of the underlying substrate locally. As a comparison of large area measurements and scanning measurements, a PCD measurement using an rf bridge to obtain the minority carrier lifetime of a p-type single crystal silicon wafer is shown in Figure 2.1, while a 4"x4" LBIC map of a completed multicrystalline based silicon solar cell is shown in Figure 2.2.

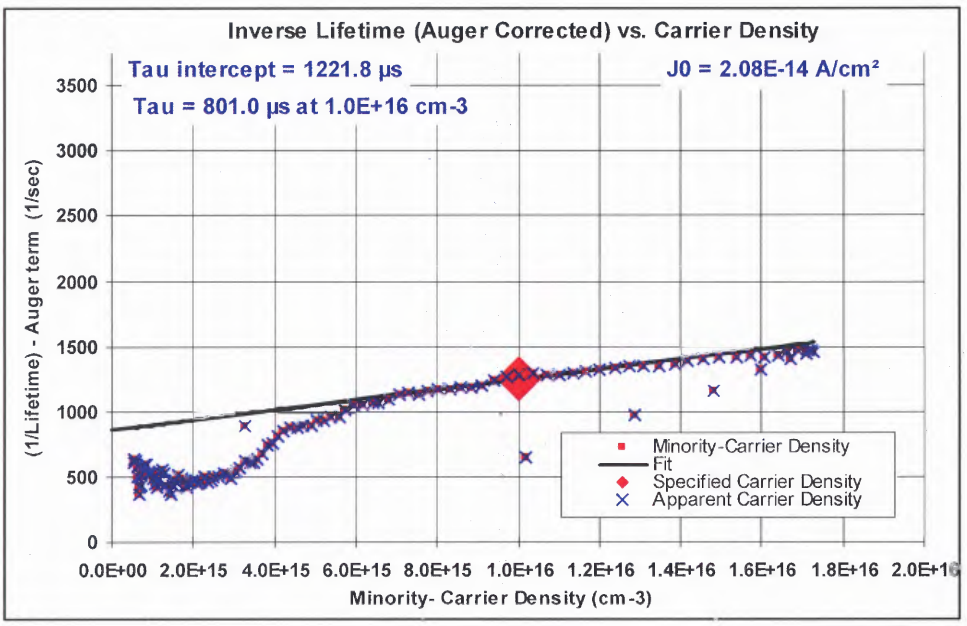

Figure 2.1 Minority carrier lifetime as a function of injection level for a p-type single crystal silicon wafer.

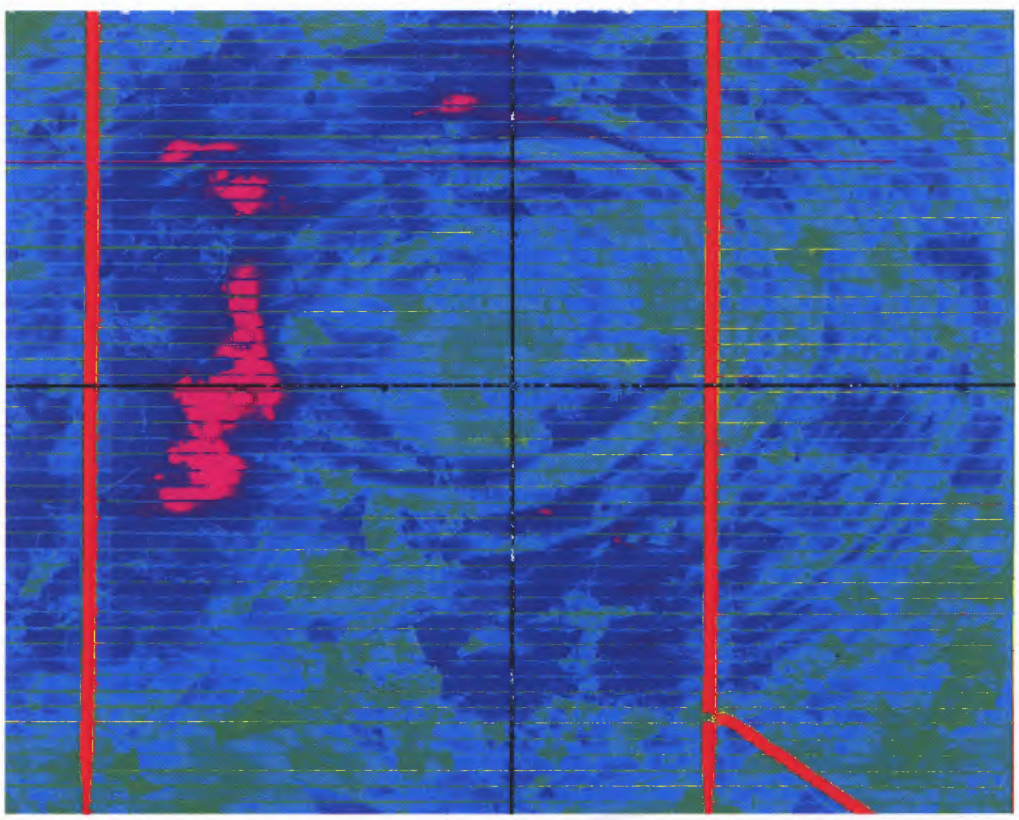

Figure 2.2 LBIC map of a completed multicrystalline silicon based solar cell.

It is also very useful to be able to perform measurements, such as current vs. voltage, locally on a substrate. Electronic devices, such as diodes, are a highly effective way to make spatially resolved measurements on a large area silicon substrate [45]. Similar approaches of characterizing substrates are routinely done in the microelectronics industry. However, solar material has different requirements than a microelectronics device. In particular, a solar diode needs to be tested under dark and illuminated conditions, while a microelectronics device usually operates under dark conditions only. Also, solar cells are fabricated on multicrystalline and single crystal silicon material, while microelectronics devices are fabricated on single crystal material. Furthermore, microelectronics devices were primarily made to test their performance, while devices made for solar cell studies were primarily made to characterize the underlying material. This is a subtle, yet fundamental difference between microelectronics and solar devices.

In order to fabricate diodes on solar grade silicon material, existing principles of operating fast switching Schottky diodes and wet chemistry have been employed. Unlike planar semiconductor diodes for microelectronics, guard rings cannot be used to minimize edge losses along the perimeter of the diode. However, it has been found that Schottky diodes that are fabricated on low resistivity substrates (<76 ohm-cm), have a mesa geometry, and are greater than 10 mm in diameter, have greatly reduced edge loss in both the forward and reverse bias even without the use of a guard ring [65]. Using a specialized chemical etch that has been derived from the Sopori etch, simultaneous formation of the mesa structure using a photolithography mask and a surface passivating hydrogenated silicon oxide are formed [45]. Furthermore, the chemical etch can be used on multicrystalline silicon substrates because it is isotropic, and it does not contain any

metallic constituents, which can increase edge losses since they act as carrier recombination centers. In the past, mesa diode arrays have been used to determine the effect of dislocation density on the local current vs. voltage characteristics of an underlying substrate [45]. Also, they have been used to analyze the effect of hydrogen implanted from the backside of a silicon solar cell [61].

Recent developments in gettering metallic precipitates from multicrystalline silicon substrates have prompted a renewed interest in using mesa diode arrays [48]. Gettering dissolved impurities from silicon substrates has been studied in both the microelectronics and solar industries for decades, and a number of successful techniques can be used remove or relocate these impurities, especially for single crystal microelectronics grade material [66, 67]. However, removing metallic precipitates located at dislocation clusters for solar grade multicrystalline silicon material continues to be a major problem [68]. A XTEM image of precipitates trapped at a dislocation cluster

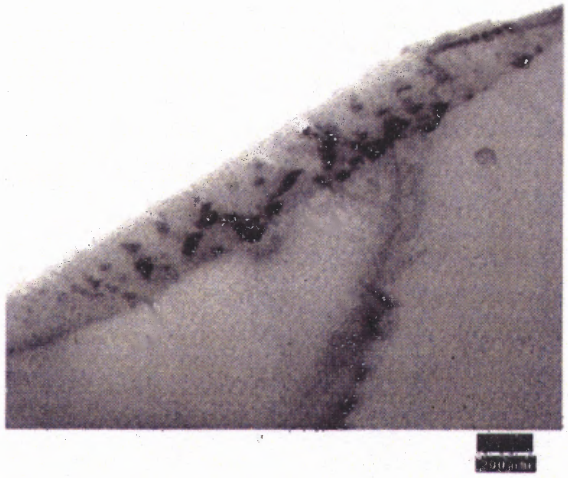

Figure 2.3 XTEM image of a defect cluster showing metallic precipitates [48].

is shown in Figure 2.3. It is only expected to become more acute as the solar industry moves toward using cheaper and impurity rich material [8]. Furthermore, these

precipitates have been identified as one of the leading causes of efficiency loss in multicrystalline silicon based solar cells [69]. Consequently, removing precipitates from dislocation clusters would significantly increase the overall efficiency of the solar cell.

Using mesa diode arrays to characterize local electronic properties is an excellent way to measure the effectiveness of new gettering processes. Current vs. voltage measurements made on mesa diodes under illuminated conditions is the only practical way to determine the open circuit voltage and fill factor locally on a large multicrystalline silicon solar cell. Although the fabrication of sidewall passivated mesa diodes is understood, a complete physical model of what occurs at the edge of this device and how these processes relate to measured device parameters is required. Understanding the amount of edge loss that occurs in a mesa diode is essential for determining its effect on the measurements made using the mesa diode.

2.2 Si-SiO_2 Interface

2.2.1 Increase in Dark Current

The interface between silicon and its oxide has been studied extensively for many decades. Understanding how charge is transported and recombines in this region is vital to the design of metal – oxide – silicon (MOS) devices [64]. Thermally grown silicon dioxide directly results in two mechanisms that increase edge loss in a semiconductor diode. They are the formation of a positive charge next to the oxide and interface states at the silicon-oxide interface. Both are a result of discontinuities in the form of free or dangling bonds at the silicon-oxide interface [30, 31]. Free bonds that occur at the interface have been shown to have a fixed positive charge for both n-type and p-type

silicon [30]. Also, the free bonds that occur at discontinuities at the interface between the oxide and silicon generate available energy levels in the bandgap of silicon. An illustration of the band diagram of p-type silicon terminated next to a silicon dioxide layer is shown in Figure 2.4. It shows the band bending that occurs at the oxide surface, interface states due to lattice mismatch, fixed positive charge due to the abrupt change and incomplete oxidation at the interface, and possible fixed and mobile charges due to defects and impurities.

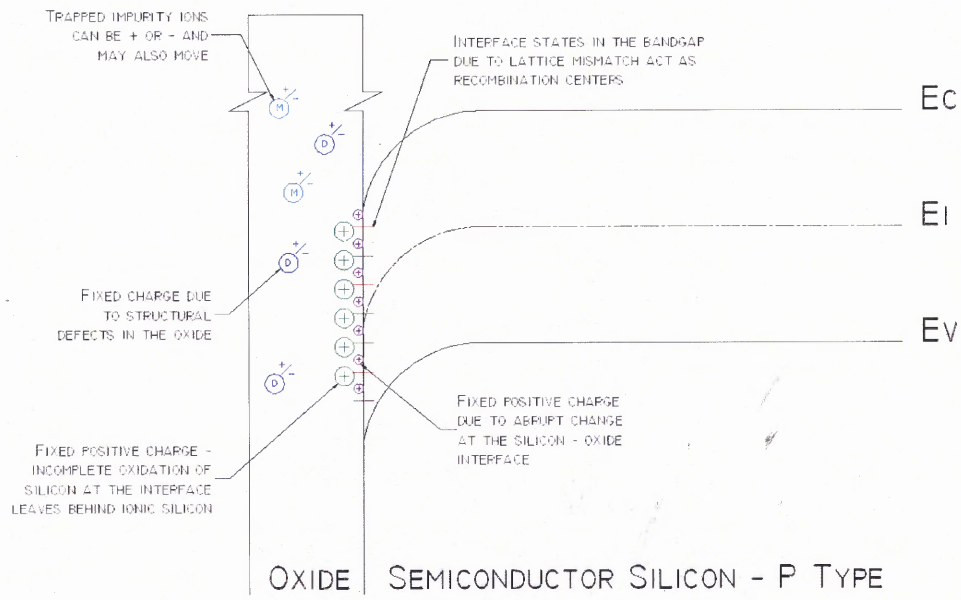

Figure 2.4 Band diagram of p-type silicon next to an oxide layer.

The fixed positive charge at the interface causes a depletion region in a p-type material for low charge densities and will produce an inversion layer at moderate to large charge densities, even for a semiconductor diode with no bias. When this region becomes depleted it acts as a variable voltage resistive shunt. When this region becomes strongly inverted the surface recombination rate decreases since the region adjacent to the oxide layer will be n-type, and the surface recombination will limited by the number of

holes, which are the minority carriers in the inverted region. This is illustrated in Figure 2.5. This topic will be fully analyzed in Chapter 4. In a MOS transistor, a bias applied to

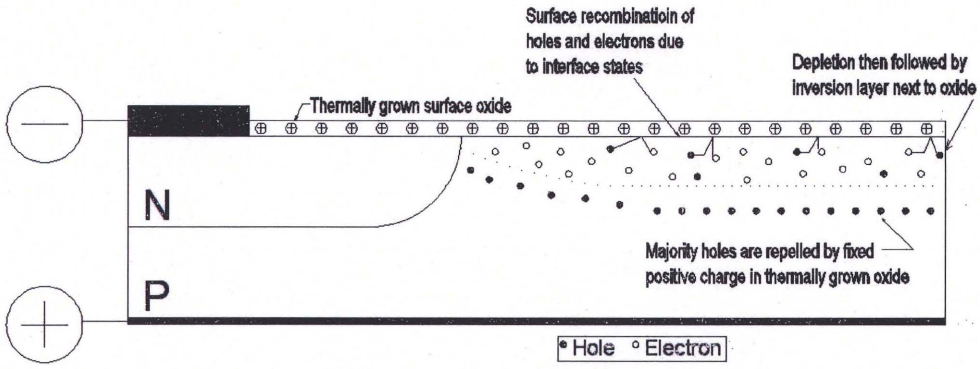

Figure 2.5 NP junction covered by thermally grown oxide.

the metal gate can generate this inversion channel and a current can flow from the source to the drain. Therefore, the inversion process at the silicon – oxide interface is used in an advantageous way to produce an electronic switch [31]. The formation of an n channel in MOS transistors occurs when the appropriate gate bias is applied as shown in Figure 2.6.

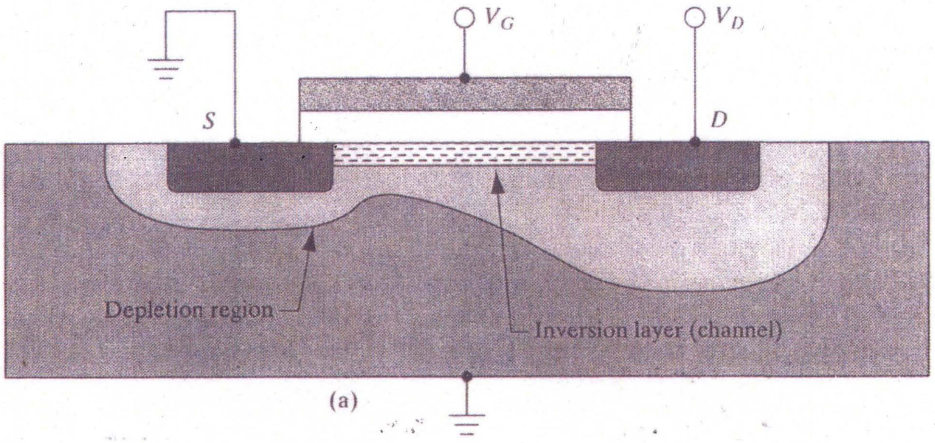

Figure 2.6 MOS transistor – n inversion layer forms $V_G > V_T$ and $V_D < (V_G - V_T)$ [64].

However, in a semiconductor diode, excessive charge at the silicon – oxide interface that results in a highly depleted or inverted region can act as a current sink and increase the

recombination rate in this region. The interface region behaves as a resistive shunt that allows charges to recombine adjacent to the edge of the diode. An exaggerated illustration of this phenomenon in a mesa diode is shown in Figure 2.7.

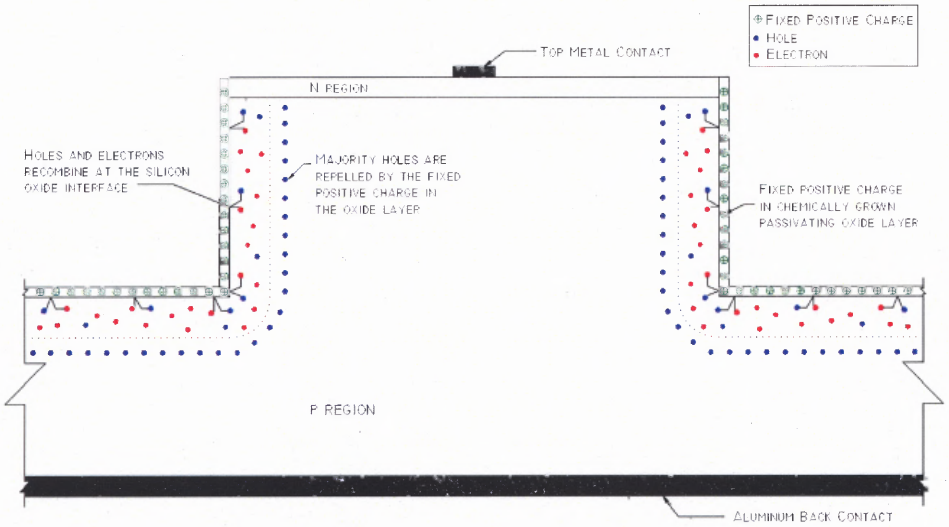

Figure 2.7 Development of a resistive shunt along the edge of an n-p mesa diode.

The interface states that produce energy levels in the bandgap of silicon also contribute to the increased dark current of a forward biased diode. The surface recombination rate of electrons and holes at the silicon – oxide interface is dependent on the available energy levels in the bandgap, which are associated with the interface states that arise from discontinuities at the interface. Furthermore, the surface recombination velocity is directly proportional to the number of interface states. Consequently, a more disordered interface will result in a greater number of interface states, which increases the surface recombination velocity and surface recombination rate, and ultimately results in an increase in the forward dark current.

2.2.2 Additional Interface Effects

In the previous section, two phenomenological aspects of the silicon-oxide interface that increase the dark current were discussed. They were the development of a positive charge at the interface and the formation of interface states in the silicon bandgap, which increases the surface recombination velocity. Both directly affect the dark current vs. voltage characteristics. Although these two aspects are particularly important, other physical phenomena occur at or adjacent to the silicon-oxide interface and also effect the operation of a diode.

A disorganized silicon – oxide interface effects the transport of electrons and holes in this region as well [30]. The disruption of the lattice at the interfacial region causes scattering of mobile charged carriers, such as holes and electrons. This scattering process leads to a significant reduction of the mobility of electrons and holes [30, 70]. The reduction of mobility does not directly affect the surface recombination process. However, since it affects the process by which electrons and holes reach the surface, it can be considered as indirectly altering the surface recombination rate.

During the formation of the surface oxide, by thermal or chemical processes, some of the silicon from the base wafer is used to form the silicon oxide surface. Since the oxide is formed on a doped silicon surface, the dopant ions are also consumed. Dopant atoms trapped in the oxide layer can still become ionized [71]. Carriers generated by dopants trapped in the oxide layer can lead to additional edge losses in a semiconductor diode. Carriers can become delocalized and act as a resistive shunt. Also, delocalized carriers leave behind ionized dopants, which can change the potential distribution in the interfacial space charge region, increase the density of interface states,

and act as a resistive shunt via ionic conduction. Furthermore, during thermal oxidation of a doped silicon substrate, the silicon dioxide layer can getter dopant atoms since they are more soluble in the oxide layer than the silicon layer [38]. This gettering effect alters the fixed dopant ion distribution in the region adjacent to the silicon – oxide interface. This can be seen in a comprehensive study of PERL type solar cells study done by Robinson et al. and is reproduced in Figure 2.8. The difference in doping levels between

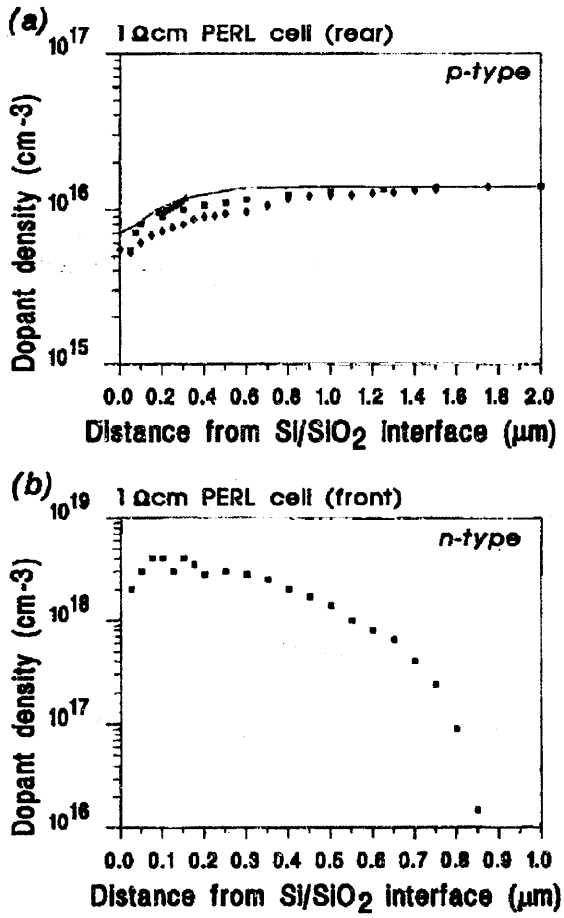

Figure 2.8 Dopant distribution next to a thermally grown oxide [38].

the bulk silicon substrate and the region next to silicon – oxide interface can be as great as one order of magnitude. This leads to a variable Fermi level, which can significantly alter the electric potential and the carrier distributions in this region.

The silicon – oxide interface significantly alters the band structure of silicon, which affects all aspects of carrier dynamics and potential distribution in this region. Consequently, as the size of the electronic device becomes smaller or the interface becomes more disorganized, the electronic effects that occur in the interfacial region become more significant and could even dominate the entire operation of the device.

2.3 Edge Effects in Semiconductor Diodes – A Historical Perspective

Historically, the edge effect in a semiconductor diode system was studied using a reversed biased Schottky diode [65, 72-74]. The original problem was that these diodes initially had soft breakdown current vs. voltage curves, and they did not achieve their maximum theoretical breakdown voltage. Consequently, this problem needed to be solved in order for Schottky diodes to be used for fast switching devices. Furthermore, the fundamental problem of parasitic edge effects in silicon p-n junctions covered by a thermal oxide was studied and can be considered a precursor to the edge effects documented in Schottky diodes [63, 75]. In either case, when reverse biasing a Schottky or p-n junction diode, an inversion layer forms at the oxide interface as a result of its inherent positive charge. Therefore, as the diode is further reversed biased, a diode with an opposite emitter collector is induced at the oxide interface and eventually the current in the field induced edge diode dominates the actual physical device resulting in avalanche breakdown.

Although most of the work regarding edge effects was performed on reversed biased diodes, the edge effect does occur in forward biased diodes as well [76]. Wall described a fanout effect that occurs in a forward biased diode when carriers move away

from the area directly under the metal part of a Schottky diode and are trapped at some distance under the neighboring oxide. This results in a significant amount of noise in the current vs. voltage signal and results in a tremendous edge density of carriers for especially small diodes. A detailed analytic solution of the edge effects of Schottky diodes for reverse and forward bias was developed by Willis [77]. In his paper, he also shows that as the diode radius is reduced, the forward edge leakage increases which is most likely a result of increased tunneling probably since it primarily occurs at low forward bias voltages. This may also be explained by the dominance of edge recombination current at low applied voltages.

2.4 Mitigating Edge Losses in Semiconductor Diodes

The edge effect in semiconductor diode devices such as switches and power devices is well understood and can be virtually eliminated using straightforward processing steps [62, 65, 78]. The most common method is to diffuse a guard ring around the edge of the diode and apply bias to the ring to control the space charge region at the edge. This method has been investigated in detail for Schottky and junction diodes, and the results of both are shown in Figure 2.9 and Figure 2.10. Slightly more elaborate steps can be taken

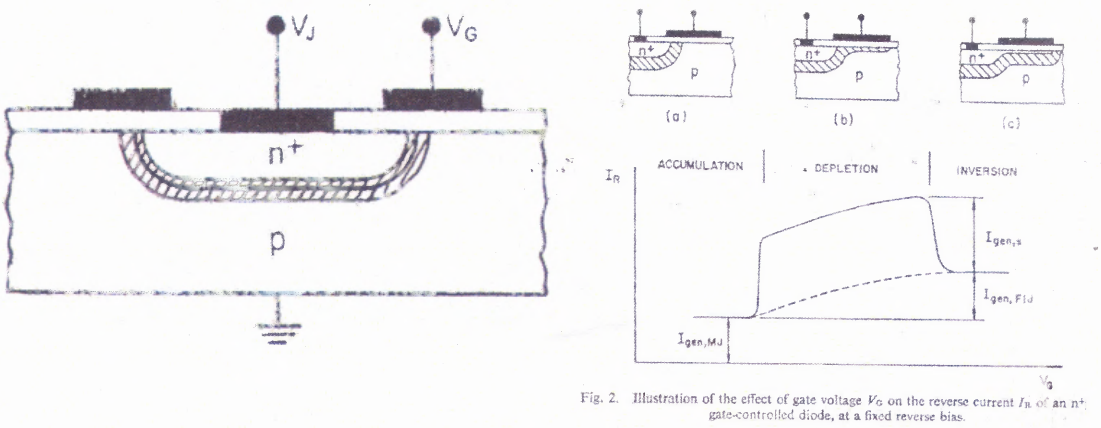

Figure 2.9 Use of a guard ring for an n^+p diode to control the space charge region [31].

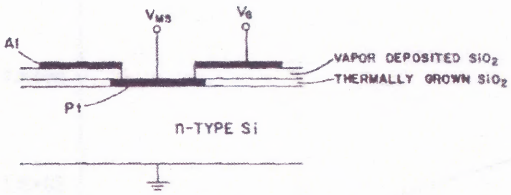

FIG. 1. The gate-controlled diode structure used in this work.

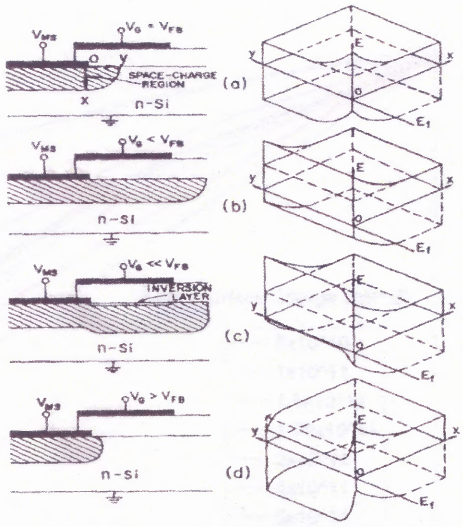

FIG. 2. Space-charge region (cross-hatched area) of the gate-controlled M–S diode and three dimensional band diagram of the M–S contact corner region. (a) Surface at flat-band condition, (b) Surface depletion, (c) Surface inversion, (d) Surface accumulation.

Figure 2.10 Use of a guard ring for a Schottky diode to control the space charge region [73].

to obtain almost ideal current vs. voltage characteristics for Schottky diodes such as using a double guard ring [79]. One important aspect of the guard ring analysis performed by Tove et al. was that for Schottky diodes made on wafers with bulk resistivity of 76 Ω-cm or less, the guard ring had little, if any, effect. In addition, for the low resistivity wafers that were tested to determine the activation energy of the barrier, the height was almost the height of the Schottky barrier, which is an indication that the edge current generation was only a small fraction of the total [65].

Another interesting and relevant technique for reducing the edge effect was to passivate the p-n junction with hydrogenated amorphous silicon and perform a low temperature anneal [80]. This system performed better than a thermal oxide passivation system for a number of reasons. One is that hydrogen located at the interface occupies surface states consequently reducing the possibility of tunneling. Also, this suggests that

the excess hydrogen in the amorphous silicon can diffuse to hydrogen deficient regions, thereby reducing the available surface states preventing the onset of an inversion channel and edge breakdown. Furthermore, hydrogen can diffuse into silicon and passivate impurities.

In addition to guard rings and hydrogenated amorphous silicon passivation, Wall compared the forward bias characteristics of Schottky diodes fabricated on a planar wafer and on the top of mesas [76]. The saturation current increased significantly as the radius of the diode was reduced. However, the saturation current was almost constant for the mesa diode. He surmised that the increase was due to current injection around the edge of the diode, which becomes a more dominant effect as the radius shrinks.

2.5 Design Considerations for Solar Cell Mesa Diodes

Based on decades of research, it is apparent that how the edge effects are handled in a small area diode can be the determining factor as to whether or not reliable devices can be made. The primary difference between the mesa diode arrays that were modeled and discussed in this dissertation and the work discussed in the previous section is that the mesa diode will be subjected to dark as well as illuminated conditions since we are trying to obtain information regarding its solar cell performance. Four important points are part of the fabrication process of the mesa diode arrays. One is that low resistivity substrates are used. This is necessary because most solar cells are made using substrates in the 1-10 Ω-cm range. According to Tove et al. guard rings are unnecessary for devices fabricated on this type of material [65]. Two, mesa diodes were fabricated instead of planar diodes. This significantly reduces edge current injection and keeps the ideality factor of the diode

relatively constant [76]. Three, the chemical etch, the Sopori etch, used to delineate the diodes and form mesas, produces an oxide that reduces the edge effect in a similar way the hydrogenated amorphous silicon passivates the p-n junction described by Tarng et al. [80]. Four, the mesa diode diameter is 2.54 mm. According to the study made by Tove, et al., they analyzed planar diodes that were 2 mm or 3 mm, and indicated the edge effect became negligible at diameters ~10 mm. The choice of this diameter balances the need to make measurements under illumination, minimizes the edge effect, and maximizes the resolution for mapping an entire solar cell [81]. Consequently, the geometric design of the mesa diode, as well as the physical properties of the edge effects, will be incorporated into the model in this dissertation, which will be discussed in the following chapter.

CHAPTER 3

DISCUSSION OF THE MODEL OF A SILICON MESA DIODE

3.1 Introduction

In order to determine the influence of the edge conditions of a mesa diode on its overall electronic performance, a suitable model that describes the carrier dynamics as well as the electronic properties needs to be chosen. In Chapter 1, it was discussed that the continuity equations for electrons and holes, which use the drift – diffusion model to define the electron and hole currents, coupled with Poisson's equation for electric potential would adequately describe the operation of the mesa diode. The drift – diffusion model for electron and hole currents has assumptions that need to be discussed in context of how they relate the operation of the mesa diode. This chapter will start with how the drift – diffusion equations for electron and hole currents can be derived from a more general description of charge flow in a material, and how the assumptions used are valid for the operation of a mesa diode. This will be followed by a discussion of the model used to describe bulk and surface recombination as well as the incorporation of the bulk generation rate to model the mesa diode under illumination. In the next section, a discussion of the application of the finite element method to the system of equations, taking into account the bulk and surface conditions as well as geometric features, will be presented. Then, a detailed description of the implementation of this system into a commercial software package, COMSOL Multiphysics, will be discussed. Lastly, an explanation of the generalized solution method that is used to solve the system of equations, and how the current vs. voltage curve is obtained from the self – consistent solution will be provided.

3.2 Boltzmann Transport Equation

The classical approach to the description of particle flow through space has been defined by the Boltzmann transport equation, which is formulated from the classical mechanic's Liouville theorem [82]. It states that following a volume element along flowline, the distribution of the particles in that element is conserved unless there are collisions or recombination and generation processes [38, 82]. The Boltzmann transport equation can be viewed as a continuity equation where the distribution of particles changes their position and velocity over time. Alternatively, it can be interpreted as the particle distribution changes position and momentum due to a force over time. By changing classical momentum to crystal momentum used in quantum mechanics, the Boltzmann transport equation can be considered semiclassical [38]. It should be noted that the Boltzmann transport equation makes assumptions regarding the system it is describing. Notably, it is a classical description of the particles it models, namely electrons. This means that there are a large number of particles and they have a continuous spectrum of available energy levels. For the mesa diode that is the subject of this dissertation, a classical description of the electrons and holes in the device is adequate because the size of the device is large, which means there are many electrons and holes in the system and the availability of energy levels in the conduction and valence bands can be considered so numerous that they represent a continuum.

Since it is reasonable to use the classically defined Boltzmann transport equation to define the motion of electrons and holes in the mesa diode, it would be important to show the derivation of the drift – diffusion equations from the Boltzmann transport equation. The assumptions used to make this derivation can be explained in the context

of the mesa diode. The classically defined Boltzmann transport equation is shown in Equation (3.1).

$$\frac{\partial f}{\partial t} + \vec{v} \cdot grad_r f + \vec{\alpha} \cdot grad_v f = \left(\frac{\partial f}{\partial t}\right)_{coll} \tag{3.1}$$

The first assumption to get from the classical Boltzmann transport equation to the drift – diffusion equation is to use the relaxation time approximation, which describes what happens to the system of particles when they undergo a scattering process [82]. Specifically, for an electron or hole that experiences a collision in a lattice, it is assumed to be elastic or isotropic. This means the relaxation time is the average time it would take the system to come back to equilibrium after an elastic collision, or the average time between collisions. The main assumption that is made when using the relaxation time approximation is that the electric field has to be low enough that there is a linear relationship between the drift velocity of electron and holes and the electric field. For the operation of a mesa diode, this holds true for almost the entire device except the limit is probably exceeded in the space charge region, yet only slightly. This slight nonlinearity can be corrected using empirical data and will be discussed later in this chapter [83]. Equation (3.1) can be rewritten using the relaxation time approximation and is shown in Equation (3.2).

$$\frac{\partial f}{\partial t} + \vec{v} \cdot grad_r f + \vec{\alpha} \cdot grad_v f = -\frac{f - f_0}{\tau_c} \tag{3.2}$$

Since the mesa diode operates as a solar cell, it is a time independent problem, therefore the first term in Equation (3.2) can be removed since the distribution function is constant in time. The acceleration term, α, can be rewritten using Newton's second Law

and using the Lorentz force equation for a charged particle moving in electric and magnetic fields [82], which can be considered negligible in a mesa diode. Equation (3.3) incorporates the electric field and steady – state conditions of the mesa diode into Equation (3.2) [38].

$$\vec{v} \cdot grad_r f + \frac{q\vec{E}}{m^*} \cdot grad_v f = -\frac{f - f_0}{\tau_c} \tag{3.3}$$

An expression for the current density for electrons and holes can be obtained by choosing an appropriate distribution function and using the definition of particle flux density as shown in Equation (3.4) [38]. Alternatively, by noting that the right hand side

$$J(\vec{r}) = q \int \vec{v}\, f(\vec{v}, \vec{r})\, d\vec{v} \tag{3.4}$$

of Equation (3.3) is the local difference of the distribution function of electrons or holes from equilibrium, an expression for current density can be realized by taking the first moment of velocity of both sides of Equation (3.3) and multiplying by the electric charge constant of appropriate sign for electrons or holes. This is shown in one dimensional space in Equation (3.5) [38]. The right hand side of Equation (3.5) has two integrals that

$$\tau_c\, q \int v_x\, v_x \frac{\partial f}{\partial x} dv + \frac{q\,\tau_c\,\vec{E}}{m^*} q \int v_x \frac{\partial f}{\partial v} dv = q \int v_x\, f_0\, dv - q \int v_x\, f\, dv \tag{3.5}$$

need to be evaluated. The first integral on the right hand side of Equation (3.5) is zero because the equilibrium distribution function, f_0, is an even function and velocity function is an odd function. When they are integrated over all velocities, the result is zero. Physically, this term represents the current density of the system at equilibrium. Since there is no current flow at equilibrium, this term should be zero. The second term on the

right hand side of Equation (3.5) is the definition of current density of either electrons or holes as shown in Equation (3.4). In order to solve the left hand side of Equation (3.5), the two integrals can be evaluated using two known transformations and are shown as Equation (3.6) and Equation (3.7) [84].

$$\int \psi\, v_x \frac{\partial f}{\partial x} dv = \frac{\partial}{\partial x}\left(\rho \overline{\psi\, v_x}\right) - \rho\, \overline{v_x \frac{\partial \psi}{\partial x}} \tag{3.6}$$

$$\int \psi \frac{\partial f}{\partial v} dv = -\rho\, \overline{\frac{\partial \psi}{\partial v}} \tag{3.7}$$

If the dummy variable, ψ, is replaced the velocity function, v_x, the integrals in Equation (3.6) and (3.7) have the same form as the integrals on the left hand side of Equation (3.5). In Equation (3.6), the result of the integration has two parts. In a semiconductor device such as a mesa diode, it is assumed that the average velocity of electrons and holes is constant throughout the entire device. Therefore, the velocity factors in the first term can be taken out of the differential, and the second term is zero since it is assumed that the average velocity is constant. After evaluating the integrals in Equation (3.5), the result is shown in Equation (3.8). Further simplification can be made

$$\tau_c\, q < v_x^{\,2} > \frac{\partial n(x)}{\partial x} - \frac{q\,\tau_c \vec{E}}{m^*} q\; n(x) = -J(x) \tag{3.8}$$

using lumped parameters, such as mobility and diffusion coefficient, and the definition of the average velocity squared. In addition, for low electric fields, the Einstein relation also holds. Therefore, only the mobility or diffusion coefficient needs to be specified. The following simplifications are shown in Equation (3.9), (3.10), and (3.11), and when

Mobility $$\mu = \frac{q\tau_c}{m^*} \tag{3.9}$$

average velocity squared

$$< v_x^{\,2} >= \frac{k_B T}{m^*} \text{ (1D)}$$

$$< v_x^{\,2} >= \frac{3k_B T}{m^*} \text{ (3D)} \tag{3.10}$$

Einstein Relation $$D = \frac{k_B T}{q}\mu \tag{3.11}$$

they are incorporated into Equation 3.8 the resulting equations are the drift – diffusion current density equations for electrons and holes. They are exactly the same as shown in Equations (3.12) and (3.13).

Electron Current Density $$J_n = q\,n\,\mu_n\,\vec{E} + q\,D_n\,\nabla_r n \tag{3.12}$$

Hole Current Density $$J_p = q\,p\,\mu_p\,\vec{E} - q\,D_p\,\nabla_r p \tag{3.13}$$

As stated earlier, the relaxation time approximation assumes that the electric field is low enough that it is proportional to the velocity of the mobile electronic carriers. The constant of proportionality is the mobility, μ. At the junction, the electric field probably becomes nonlinear, although to a small extent. The drift-diffusion model can be extended by using a field dependent expression for mobility μ(E) if it is deemed necessary [83]. Therefore, the drift-diffusion model can adequately describe the electronic carrier dynamics of holes and electrons in a mesa diode.

In this section, it was shown that classically defined Boltzmann transport equation can be used to derive the standard drift-diffusion equations. This was done by using the

relaxation time approximation. The only other assumption made in the derivation was that the band diagram of silicon could be approximated by parabolic bands [38]. Physically, parabolic bands assume the carriers in the conduction and valence bands occupy a continuum of energy and momentum values where the classical description of a carrier's momentum is the same as its quantum mechanical crystal momentum. It was shown that the assumptions made in the derivation of the drift-diffusion model from the more general Boltzmann transport equation are applicable to modeling electronic transport in the mesa diode. In order to determine the carrier distributions and electric field, the equations for electron and hole current density need to be substituted into the continuity equations for electrons and holes, and solved self-consistently with Poisson's equation for electric potential. They are shown in Equations (3.14), (3.15), and (3.16) [21].

$$-\nabla \cdot J_n = q(G-U) \tag{3.14}$$

$$\nabla \cdot J_p = q(G-U) \tag{3.15}$$

$$-\nabla \cdot \varepsilon_0 \varepsilon_r \nabla V = \rho \tag{3.16}$$

The following section describes how the bulk and surface recombination rate were modeled as well as the process for determining and implementing the bulk generation rate. This makes it possible to completely describe the continuity equations for electrons and holes for modeling the mesa diode.

3.3 Recombination and Generation

Recombination and generation of electron hole pairs were discussed in general in Chapter 1. In this section, the specific mechanisms used to model a mesa diode will be discussed.

3.3.1 Bulk Recombination

The dominant mechanism of bulk recombination in silicon based semiconductor devices is due to recombination centers [85]. This mechanism occurs because energy levels inside the bandgap are a produced when impurities or defects alter the periodicity of the bulk lattice structure. Understanding how the expression for recombination via trapping is developed is important for determining a physical model representing it. With a single energy level introduced into the silicon bandgap, four possible energy level transitions are possible. They are electron capture and emission, and hole capture and emission [26, 27]. The rate of electron capture is proportional to the number of recombination centers that are not occupied, and the rate of electron emission is proportional to the number of recombination centers that are occupied [86]. The converse is the case for hole capture and emission. The rates of these four processes are shown in Equations (3.17), (3.18), (3.19), and (3.20).

Electron capture $$r_{ec} = v_{th}\,\sigma_n\, n\, N_t(1-f) \tag{3.17}$$

Electron emission $$r_{ee} = v_{th}\,\sigma_n\, n_i\, e^{(E_t-E_i)/kT}\, N_t f \tag{3.18}$$

Hole capture $$r_{hc} = v_{th}\,\sigma_p\, p\, N_t f \tag{3.19}$$

Hole emission $$r_{he} = v_{th}\,\sigma_p\, n_i\, e^{(E_i-E_t)/kT}\, N_t(1-f) \tag{3.20}$$

At equilibrium the rate of electron capture is the same as the electron emission rate. During steady-state operation, these rates are not equivalent, but the difference of rate of capture and emission of electrons has to be the same as that for holes [86].

Physically, this means the rate at which electrons move into and out of the energy level located within the bandgap has to be the same as the rate holes move into and out of the same energy level. Therefore, the steady-state non-equilibrium condition is shown in

$$r_{ec} - r_{ee} = r_{hc} - r_{he} \tag{3.21}$$

Equation (3.21). Using this condition, and the rate Equations (3.17)-(3.20), the probability that the energy level in the bandgap is occupied by an electron, *f*, can be determined and is shown in Equation (3.22). The rate difference of capture and emission

$$f = \frac{\sigma_n n + \sigma_p n_i e^{(E_i - E_t)/kT}}{\sigma_n [n + n_i e^{(E_t - E_i)/kT}] + \sigma_p [p + n_i e^{(E_i - E_t)/kT}]} \tag{3.22}$$

of electrons or holes shown in Equation (3.21) [86] is the definition of the recombination rate. Using the non-equilibrium expression for electron occupancy in Equation (3.22) [86], and the steady-state non-equilibrium condition in Equation (3.21), the recombination rate is defined in Equation (3.23) [86].

$$U = (r_{ec} - r_{ee}) = (r_{hc} - r_{he}) = \frac{\sigma_n \sigma_p v_{th} N_t [pn - n_i^2]}{\sigma_n [n + n_i e^{(E_t - E_i)/kT}] + \sigma_p [p + n_i e^{(E_i - E_t)/kT}]} \tag{3.23}$$

By explaining how the rate for recombination through an energy level located within the bandgap is derived, the assumptions used can be discussed and any additional simplifications used for modeling the mesa diode can be addressed. The bulk recombination rate in this section was originally developed by Hall, and Shockley and Reed. It is sometimes referred to as the simplified SRH Recombination model, because it makes two important assumptions [87]. They are that the number of recombination centers is assumed to be small so they do not behave as traps and there are an equal

number of excess holes and electrons that are not trapped. A more detailed derivation of the recombination of electrons and holes via energy levels located in the bandgap can be made by developing the steady-state solution to the coupled continuity equations with excess electronic carriers generated via illumination [87]. Using the previous two assumptions, the more general form for recombination via an energy level in the bandgap can be simplified into the SRH model.

The assumption that the excess hole and electron concentrations are equal is the condition used to simplify the equation for lifetime based on the SRH recombination rate. This is done by solving the continuity equations for electrons and holes by eliminating the value of recombination center concentration, N_T. However, in order to determine lifetime, and by extension the recombination rate, the number of recombination centers needs to be known. From the steady-state continuity equations, the ratio of excess holes to excess electrons can be set to unity, which is the SRH condition, and the critical value for the number of recombination centers can be determined. By choosing a value of N_T less than or equal to the critical value for modeling the mesa diode, the expression for recombination in Equation (3.23) will be valid as long as only one energy level is chosen. Equation (3.24) [87] was used to determine the maximum value for the number of recombination centers in the p-type material for modeling the mesa diode. N_A is the doping level and the ratio of capture time constants of electrons to holes is a

$$N_{T_{critical}} = N_A \frac{\tau_{n0}}{\tau_{p0}} \tag{3.24}$$

measure of how long a carrier remains free. The capture time constants, τ_{n0} and τ_{p0}, are defined in Equation (3.25) and (3.26) [24]. By using the more generalized model of

$$\tau_{n0} = \frac{1}{\sigma_n v_{th} N_t} \tag{3.25}$$

$$\tau_{p0} = \frac{1}{\sigma_p v_{th} N_t} \tag{3.26}$$

recombination via an energy level in the bandgap, it was shown that the critical value defined in Equation (3.24) has a broad minimum for recombination energy levels located towards the middle of the bandgap. The ratio of the capture cross-section for electrons to holes shifts the minimum critical value up for large ratios and down for ratios that approach zero. Also, as the doping level is increased, the minimum critical value broadens, thereby making shallow levels act like deep levels.

With respect to modeling the bulk recombination processing in the mesa diode, the following outlines the assumptions that were made and their rationale. First, the bulk recombination was modeled as recombination via an energy level in the bandgap. Other recombination processes, such as Auger, radiative, and impact ionization, were assumed to be negligible since the mesa diode is made from crystalline silicon, operates under steady-state, and does not have very high electric fields or doping levels. Second, the number of recombination centers was chosen not to exceed the critical value defined in Equation (3.24). This was done so the simplified SRH model would be valid for modeling the mesa diode. Third, a single energy level located at the middle of the bandgap was chosen for the energy level of the recombination centers. This is a common assumption made in modeling the recombination via an energy level in the bandgap for silicon based semiconductor devices [38]. It is done because recombination centers in the middle of the bandgap are more effective than levels near the band edges [86]. Physically, there is an equal probability that an electron and hole will emit when the

recombination center is located near the middle of the bandgap since the energy required for electron and hole emission from the band edge will be the same. Recombination centers with energy levels located near the band edges act more like dopant levels and tend to re-emit carriers back to the band from where they originated [86]. Consequently, they are poor recombination centers. Making the assumption that the energy level of all of the defects that act as recombination centers is located in the middle of the bandgap is a way of lumping them together to create the best probability that they will act as recombination centers rather than traps. The recombination equation used in the model of the mesa diode is shown as Equation (3.27) [24]. In addition to the aforementioned

$$U = \frac{pn - n_i^2}{\tau_{p0}[n + n_i] + \tau_{n0}[p + n_i]} \tag{3.27}$$

assumptions, the values for electron and hole capture cross-sections, σ_n and σ_p, have been obtained from other researchers' experimental data. The values for these parameters change as a function of recombination energy level in the bandgap. More importantly is that samples of the crystalline silicon can be grown in different ways and have different impurity concentrations and defects. These factors can change the values for capture cross-section of holes and electrons. In addition, doping levels and electric field also have an effect. This is because capture cross-section itself is a lumped parameter, which is essentially a measure of the distance around an atom that will have a great probability of capturing a mobile electronic charge [86]. This will be affected by a wide range of parameters such as the crystalline structure and orientation, the potential distribution between the atoms, impurities and defects, dopants, available energy levels, and the strength and direction of the electric field. Although many parameters determine the

magnitude of the capture cross-sections, its value is typically on the order of the atomic spacing of the crystal [86]. Values for capture cross-section were chosen at an energy level in the middle of the crystalline silicon bandgap from available published data for single crystal Czochralski silicon. Other researchers have also discussed that the ratio of the two values for capture cross-section with respect to the energy level for the recombination center can be a significant factor [88].

In this section assumptions were explained that showed the bulk recombination for the mesa diode could be modeled using the simplified SRH model for recombination via an energy level in the bandgap. Further assumptions and simplifications were explained. In particular, the maximum allowable recombination centers that could be used and have a valid SRH recombination model was discussed. Simplifications including using a recombination energy level at the middle of the bandgap and the associated capture cross-sections for electrons and holes were also explained.

3.3.2 Surface Recombination

Recombination of electrons and holes also occurs at the surfaces of the mesa diode. More appropriately, it occurs at the interface of the semiconductor silicon and an adjacent terminating surface. In the mesa diode, there are two different types of surfaces that are adjacent to the base semiconductor silicon. The backside aluminum metal contact and front metal contact are both considered metal contacts. The area on the top of the mesa diode that does not have metal, as well as the mesa diode's sidewall, and the area between adjacent diodes, are terminated with a chemically grown oxide or a deposited silicon nitride coating. The mesa diode requires a mathematical representation of these two boundary conditions.

The metal contact is assumed to have an infinite effective surface recombination velocity, which is defined in Equation (3.28) [24]. This means that the excess surface

$$s_r = \frac{U_s}{\Delta n_s, \Delta p_s} \tag{3.28}$$

concentration of the minority carrier will approach zero at the metal contacts [90]. Physically, minority carriers that come into contact with the metal will instantaneously recombine with the majority carrier. Consequently, the equilibrium condition for electrons and holes is valid at the metal contact and is shown in Equation (3.29) [89].

$$n\,p = n_i^2 \tag{3.29}$$

The assumption that the effective surface recombination velocity is infinite at the metal contacts is the simplest model for electronic behavior of electrons and holes at this surface [90]. More advanced models exist, but this assumption is good provided the contacts are ohmic. This is primarily a result of processing, and it is assumed that the mesa diodes are made properly. Therefore, the effective surface recombination velocity at a metal contact is very high, especially in comparison to a properly grown oxide or nitride, and then assuming an infinite value is valid. Furthermore, the metal contact on the top of the mesa diode covers less than one percent of the total area, and the goal of the model was to describe the effect the edge conditions have on the overall performance of the diode. Therefore, using the assumption of infinite effective surface recombination velocity at the metal contacts is valid and its implementation is straightforward.

Unlike the metal contacts, the effective surface recombination velocity at a passivating oxide or nitride surface occurs at a finite rate. The mechanism for recombination at the interface between the bulk silicon material and the adjacent oxide or

nitride layer is similar to bulk recombination via recombination centers described in the previous section [24]. The main difference is that the number of recombination centers in the bulk material is a result of defects and impurities, while the number of surface recombination centers, known as interface states, are primarily a result of lattice mismatch between the semiconductor and the passivating surface. The number of interface states is influenced by a number of factors, such as the doping level of the adjacent semiconductor and how the oxide or nitride layer was grown or deposited and under what conditions [30, 31, 63, 70]. The number of interface states can be distributed throughout the bandgap or can be dominated at one or more particular energy levels. As in bulk recombination via energy levels in the bandgap, interface states with energy levels near the middle of the bandgap are also the most effective recombination centers. Another difference between bulk recombination via energy levels in the bandgap and surface recombination via interface states is that the bulk rate occurs over a volume element, while the surface rate occurs over an area element. Surface recombination that occurs via interface states is defined in Equation (3.30) [86]. This equation is similar to

$$U_s = \frac{\sigma_n \sigma_p v_{th} N_{it} [p_s n_s - n_i^2]}{\sigma_n [n_s + n_i e^{(E_t - E_i)/kT}] + \sigma_p [p_s + n_i e^{(E_i - E_t)/kT}]} \tag{3.30}$$

Equation (3.23) except that the concentration of electrons and holes is the surface concentration, and the number of recombination centers is replaced with the number of interface states. Typically, Equation (3.30) is rewritten using surface recombination velocity parameters, s_{n0} and s_{p0}, shown in Equation (3.31) and (3.32) [85]. Using these

$$s_{n0} = \sigma_n v_{th} N_{it} \tag{3.31}$$

$$s_{p0} = \sigma_p v_{th} N_{it} \tag{3.32}$$

expressions, the surface recombination rate can be rewritten and is shown in Equation

$$U_s = \frac{s_{n0}\, s_{p0}[p_s n_s - n_i^2]}{s_{n0}[n_s + n_i e^{(E_t - E_i)/kT}] + s_{p0}[p_s + n_i e^{(E_i - E_t)/kT}]} \tag{3.33}$$

(3.33). In this formulation of the surface recombination rate, it is assumed that the number of interface states, N_{it}, occurs at a single energy level, E_t. In many cases, there is a distribution of energy levels produced by interface states that are available for recombination in the bandgap. If this distribution is wide or has significant peaks, it is more accurate to replace the number of interface states, N_{it}, with the density of interface states, D_{it}, and integrate over the energy. The expression for surface recombination velocity parameters using the density of interface states is shown in Equations (3.34) and

$$s_{n0} = \int_{E_v}^{E_c} \sigma_n(E) < v_{th} >_n D_{it}(E) dE \tag{3.34}$$

$$s_{p0} = \int_{E_v}^{E_C} \sigma_p(E) < v_{th} >_p D_{it}(E) dE \tag{3.35}$$

(3.35) [85]. For modeling recombination at the interface of the silicon and chemical grown oxide of the mesa diode, it was assumed that all interface states were located at a single energy level in the middle of the silicon bandgap. The number of interface states was obtained from data of thermally grown oxides on phosphorus doped n-type material and boron doped p-type material. These assumptions were incorporated into Equation (3.33), and the revised surface recombination rate used the model as defined in Equation

$$U_s = \frac{s_{n0}\, s_{p0}[p_s n_s - n_i^2]}{s_{n0}[n_s + n_i] + s_{p0}[p_s + n_i]} \tag{3.36}$$

(3.36) [85]. Assuming that all of the interface states are located at the middle of the silicon bandgap is reasonable because energy levels near the middle of the bandgap are

the most effective for recombination [86]. Using values for the number of interface states from oxides that were thermally grown is reasonable since these oxides are known to provide very good surface passivation. The chemically grown oxide used to passivate the edge of the mesa diode also provides good passivation, because if it did not, it would not be possible to use these devices for characterizing crystalline silicon solar cells.

The model for bulk recombination via defects and surface recombination at metal contacts and a passivating oxide surface has been discussed. The assumptions made for implementing these recombination processes into the model of the mesa diode have also been outlined. Using the expressions for bulk and surface recombination in the steady-state continuity equations and obtaining the electric potential from Poisson's equation provides a complete system that can be used to model the operation of a mesa diode under dark conditions. In order to determine how the diode operates under illumination, the generation rate needs to be incorporated into the continuity equations. This is the subject of the next section.

3.3.3 Bulk Generation

As discussed in Chapter 1, generation is the process where an incoming photon excites a valence band electron to the conduction band, which leaves a hole behind in the valence band [16]. To determine the generation rate, both the incident photon flux and the absorption coefficient of the crystalline silicon mesa diode as a function of wavelength of light is required. In addition, the absorption coefficient is made of two parts, the electron-hole pair and free carrier absorption. The leads to a summation of exponential decay terms, one for each wavelength, which determines the generation rate profile of electron-hole pairs through the device [91].

Using this methodology, one can obtain an estimate of the generation rate profile, however many effects that occur in an actual solar cell would be neglected. In particular, the use of antireflective coatings, texturing for light trapping, and absorption of light by the back metal contacts are not considered and can significantly alter the generation rate profile through the device. In order to get a realistic generation rate profile, PV Optics modeling software was used. PV Optics is an optical modeling software package developed at the National Renewable Energy Laboratory under the direction of Dr. Bhushan Sopori [92, 93].

PV Optics realistically determines many of the optical properties of an entire solar cell. In this section, the discussion will be limited to how PV Optics was used to model the mesa diode. The material used for the mesa diode was crystalline silicon and it was 199.5 μm thick. The back metal contact was 1 μm, and a 750 Å thick silicon-nitride antireflective coating was put on top of the crystalline silicon device. The top was planar, or flat, and the interface between the crystalline silicon and back metal contact was textured with a height of 1 μm.

For the modeling purposes of this dissertation, the two most important results of the optical simulation performed by PV Optics are the photon flux profile as a function of depth below the top of the device and the calculation of the maximum achievable current density. The photon flux profile is the end result of the simulation. It is a plot of the number of photons absorbed per unit area at different depths below the top of the device. Normally, this would be enough to determine the generation rate profile. PV Optics generates only a specific number of points on the photon flux profile, and this number cannot be changed. Specifically, it uses twenty points, and they are interpolated with

straight lines. Also, the first calculation point does not start at the surface of the device, but rather at some distance below it, which will depend on the thickness of the device and number of points, 20. In the case of a mesa diode with a thickness of 199.5 μm and 20 calculations points, the first point on the photon flux profile curve is 10 μm below the surface of the device.

Typically this is not a problem for PV Optics since it was primarily designed for thin-film photovoltaic applications, but is a problem here because a crystalline silicon semiconductor device such as the mesa diode is designed to absorb a significant amount of the spectrum near the top of the device and is much thicker than a thin film device. However, this problem can be solved using the calculated value of maximum achievable current density (MACD) to estimate the photon flux profile near the top of the device. The MACD is determined by assuming that each photon that is absorbed by the device generates an electron-hole pair that can be collected at the external contacts. Physically, this assumes no recombination of optically generated carriers. Therefore, if the photon flux profile is integrated over the region of thickness that is actually determined by PV Optics, the photon flux at the top of the device can be estimated by a step function so the total integral is equivalent to the MACD. This provides a first estimate, which was subsequently modified after the self-consistent simulation, described in the next section, was run with a mesa diode that had very low bulk and surface recombination. When the resultant electrical properties of the simulated mesa diode with a low recombination rate were in agreement with values previously obtained from experimental devices made on high quality single crystal silicon material and close to the predicted MACD value by PV Optics, it was assumed that generation rate profile was reliable for simulating the

operation of the mesa diode under illumination. The calculated photon flux from PV Optics' simulation and the corresponding nonlinear curve-fit are shown in Figure 3.1 [94].

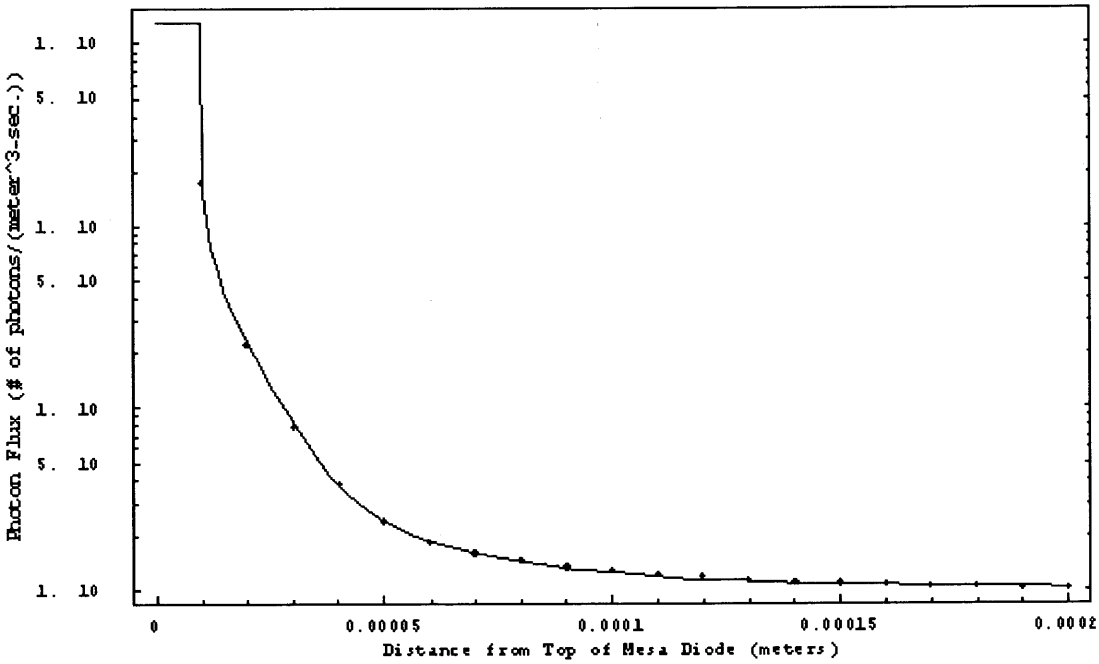

Figure 3.1 Nonlinear curve-fit to data from PV Optics simulation of a mesa diode.

By using PV Optics optical modeling software, a realistic generation rate profile as a function of depth below the top of the mesa diode can be simulated. In addition, supplemental experimental data and the calculated MACD value was used to estimate the generation rate profile for the top 10 μm of a mesa diode. These assumptions are valid since they were made using a well developed optical simulation software package and experimental data [61]. By using generation rate profiles calculated by PV Optics, the illuminated characteristics of the mesa diode can be modeled. The physical model for both dark and illuminated steady-state operation of the mesa diode has been detailed, including recombination and generation processes. The next section discusses how this physical system can be solved.

3.4 Numerical Modeling Using a Commercial Finite Element Solver

The steady-state continuity equations for electrons and holes along with Poisson's equation are coupled via the electric potential and the expressions for recombination and generation. This set is coupled in way that can be considered highly nonlinear. Analytic solutions are available for highly idealized devices, such as a one dimensional system with no recombination in the space charge region. Therefore, numerical methods are the only reasonable way to obtain a self-consistent solution. In order to solve this set of coupled nonlinear partial differential equations, a commercial finite element solver, COMSOL Multiphysics, was used. The following discusses an overview of the finite element method, how the physical model outlined in Sections 3.2 and 3.3 is implemented into the COMSOL Multiphysics software package, and an overview of the solution method used to obtain a self-consistent solution.

3.4.1 Overview of the Finite Element Method

The finite element method is a robust numerical method for solving partial differential equations. It involves discretizing a geometric space into a set of smaller pieces, or elements [95]. The elements are described by the number of nodes (points) and the interpolation function that goes through the nodes. The discretization of the geometric space that is subjected to the conditions of the partial differential equations and boundary conditions leads to a system of linear equations. The finite element method reduces a partial differential equation to a system of linear equations that can be solved by a wide range of techniques, including direct methods such Gaussian elimination, or iterative techniques such as Gauss-Seidel [96].

The finite element method has only become a useful tool for the solution of the electronic problems in semiconductor devices in the past two decades, while other techniques, the finite difference method in particular, have dominated this field for a longer time. This is because the main advantage of the finite element was also its main drawback. Since the interpolation function is incorporated into the definition of each element, the finite element method is typically more accurate than the finite difference method, but comes at the cost of significantly more computational and memory resources. Currently, these sophisticated calculations can be performed on a desktop personal computer.

Another important aspect of the finite element method is the choice of element shape, including how it is constructed. For a one-dimensional model, the choice of the element shape is limited to lines, but for a two-dimensional model, typically triangles or quadrilaterals are used. Since the mesa diode's cross-section is rectangular, a structured mesh can be used to discretize the mesa diode. As applied to the mesa diode, a structured mesh is also known as a mapped mesh, and it has a number of advantages over an unstructured, or free mesh. In particular, a mapped mesh uses less computer memory than a free mesh because the nodes can be calculated from a function rather than have all of the positions stored in memory. Also, the shape of the finite elements produced by mapped meshes can be more carefully controlled than those produced by a free mesh. This is particularly important when generating the elements that discretize the area near the n-p junction and the edge of the mesa. Less mapped mesh elements were needed to obtain a self-consistent solution that was smooth, especially in the space charge region and neighboring edge region, when compared to a self-consistent solution obtained using

triangular elements from a free mesh. Furthermore, using a mapped mesh made it possible to model the actual size of the mesa diode that was made in the laboratory. Using a free mesh to discretize the same geometry was not possible because the memory requirements exceeded what was available on the computer used to perform them. Also, the calculation time became excruciatingly slow when the free mesh was used.

In addition to choosing the finite element shape and how it is constructed, the type of interpolation function can also be specified. A common interpolation scheme is to use a polynomial function, and choosing a polynomial interpolation function based on Lagrange elements is one of the most widely used methods. Typically, the order of the interpolation function of the Lagrange element is chosen to be at least the order of the governing partial differential equations [97]. Choosing an element based on the order of the partial differential equation is reasonable for two reasons. One is that the function that defines the element that expresses the solution of the partial differential equation needs to be differentiable at least as many times as the order of the system. The one exception is linear elements can be used to discretize a quadratic partial differential equation if the integral of that equation is reduced by integrating by parts in a one dimensional problem or by using Green's theorem for a two dimensional problem. This is the standard procedure for using the Galerkin method, or weighted – residual method, where the interpolation functions are also the weight functions [97]. Two, the interpolation function should accurately reflect the solution over the entire element, not only at the nodes. Using a higher order interpolation function typically results in a better estimate to the solution over the entire element, but it comes at the expense of more calculations and memory usage [98].

Lastly, using the Galerkin method results in an equation that minimizes the residual of the governing partial differential equation. This is mathematically known as the Weak Form. This name can be misleading, because the Weak Form is a more generalized formulation of the problem, and the flux of the solution variable for the partial differential equation is part of the Weak Form formulation [99]. This is particularly useful for determining the flux of electrons and holes at the metal contacts [90]. Furthermore, the weak formulation made it possible to obtain very precise calculations of the overall current through the device. Precise current vs. voltage plots were made using the Weak Form contributions for electrons and holes obtained from the self-consistent solution to the continuity equations coupled with Poisson's equation [90].

3.4.2 Implementing the Physics Model using COMSOL Multiphysics

The commercial finite element solver, COMSOL Multiphysics, was used to the find the self – consistent solution to the continuity equations for electrons and holes coupled with Poisson's equation as shown in Equations (3.14), (3.15), and (3.16). Bulk recombination and generation rates were modeled using Equation (3.27) for recombination centers located at the middle of the bandgap, and Figure 3.1 for a curve fit to the generation rate data calculated by PV Optics. The surface recombination rate at the oxide passivated surfaces was modeled using Equation (3.36) for interface states located at the center of silicon's bandgap. The recombination rate at the metal contacts, both front and back, were modeled by assuming the equilibrium condition in Equation (3.29) holds at these locations. Also, the value of the electric potential at the contacts was fixed to the level determined by Fermi statistics [19]. This results in no potential loss between the metal

contact and the semiconductor. The following explains how these conditions were implemented into COMSOL Multiphysics.

In order solve this system of equations for the mesa diode geometry, four modules were used in COMSOL Multiphysics. Two electrostatics modules and two convection and diffusion modules were used. The additional electrostatic module was used to obtain the initial electric potential distribution for zero external bias across the diode, and estimate the electron and hole distributions using a single exponential function based on Fermi statistics [90]. From this electrostatics module, the calculated electric potential, electron, and hole distributions were used as the initial guess for coupled electron and hole continuity equations with charge distribution from Poisson's equation. All four modules were implemented in axially symmetric two-dimensional space, thereby reducing the three-dimensional problem to a two-dimensional one. In addition, since it is axially symmetric, only half of the cross-section through the mesa diode is required, which further reduces the number of finite elements that would be needed. Using axially symmetric space assumes the solution is invariant in the angular direction. This assumption is reasonable for mesa diodes fabricated on a single crystal silicon wafer or ones that are completely contained on a single grain of a multicrystalline silicon wafer. However, this assumption is probably not good for a mesa diode fabricated on top of an area of a multicrystalline silicon wafer that contains more than one grain. Since the main objective of this dissertation was to explain how the edge conditions affect the overall performance of the device, assuming an axially symmetric system is all that is essential. A three-dimensional model including grain boundary recombination and other bulk phenomena would be interesting, but would not reveal much new information regarding

the effects of edge conditions. Using the axially symmetric conditions converts the space from a Cartesian system to a cylindrical one and then sets all of the derivatives with respect to the angle to zero. This leaves a system where only the radial and height components are variable. The conversion of coordinate systems is performed automatically by COMSOL Multiphysics as long as the user specifies axially symmetric space for each module [100].

The convection and diffusion module was used instead of a generalized PDE (Partial Differential Equation) module because it is equivalent to the continuity equation for electrons and holes and is easier to use since the bulk, also known as subdomain, and boundary conditions have useful predefined options. The following derivation shows the equivalence of the COMSOL convection and diffusion partial differential equation and the continuity equations for electrons and holes.

Equation (3.37) is the COMSOL convection and diffusion equation [90]. c is the

$$\nabla \cdot (-D \nabla c + c \cdot \vec{u}) = R \tag{3.37}$$

concentration, D is the diffusion coefficient, $\bar{u}$ is the velocity, and R is the reaction rate. By substituting the electron current density given by Equation (3.12) into the continuity equation for electrons given by Equation (3.14), and then using the definition of the electric field as the negative of the gradient of the electric potential, the following expression is obtained and is shown in Equation (3.38). The last line in Equation (3.38)

$$\begin{aligned} J_n &= -q\, cn\, \mu_n \nabla V2 + q\, D_n \nabla cn \\ J_n &= q\, (-cn\, \mu_n \nabla V2 + D_n \nabla cn) \\ -\nabla \cdot J_n &= q\, \nabla(cn\, \mu_n \nabla V2 - D_n \nabla cn) = q\,(G_{PV\ Optics} - U_{SRH}) \\ \nabla(-D_n \nabla cn + cn\, \mu_n \nabla V2) &= (G_{PV\ Optics} - U_{SRH}) \end{aligned} \tag{3.38}$$

has the same form as the COMSOL convection and diffusion equation, Equation (3.37). Note the following parameter correlations shown in Equation (3.39). By substituting the

$$\begin{aligned} c &= cn \\ D &= D_n \\ \vec{u} &= \mu_n \nabla \overrightarrow{V2} \\ R &= G_{PV\ Optics} - U_{SRH} \end{aligned} \tag{3.39}$$

hole current density into the continuity equation for holes, the result is Equation (3.40). Compare the last line of Equation (3.40) with Equation (3.37). They are equivalent,

$$\begin{aligned} J_p &= -q\ cp\ \mu_p \nabla V2 - q\, D_p \nabla cp \\ J_p &= q\ (-cp\ \mu_p \nabla V2 - D_p \nabla cp) \\ \nabla \cdot J_p &= q\ \nabla(-cp\ \mu_p \nabla V2 - D_p \nabla cp) = q(G_{PV\ Optics} - U_{SRH}) \\ \nabla(-D_p \nabla cp - cp\ \mu_p \nabla V2) &= (G_{PV\ Optics} - U_{SRH}) \end{aligned} \tag{3.40}$$

noting the following parameter correlations in Equation (3.41).

$$\begin{aligned} c &= cp \\ D &= D_p \\ \vec{u} &= -\mu_p \nabla \overrightarrow{V2} \\ R &= G_{PV\ Optics} - U_{SRH} \end{aligned} \tag{3.41}$$

The initial conditions are determined by the solution of Poisson's equation under no external bias applied across the mesa diode. The charge distribution for Poisson's equation, shown in Equation (3.16), is defined in Equation (3.42). p and n in Equation

$$\rho = q(p - n + N) \tag{3.42}$$

(3.42) are the hole and electron distributions based on a continuous Fermi level at zero applied voltage, and are shown in Equations (3.43) and (3.44). The doping profile was

$$n = n_i e^{\frac{q}{kT}V} \tag{3.43}$$

$$p = n_i e^{-\frac{q}{kT}V} \tag{3.44}$$

modeled as an abrupt junction with the number of donors (n-type) significantly greater than the base acceptor concentration. The expression for N is shown in Equation (3.45).

$$N = N_D(z > junction) - N_A \tag{3.45}$$

Figure 3.2 indicates the subdomain and boundary conditions used to solve Poisson's equation for the electrostatics module (es).

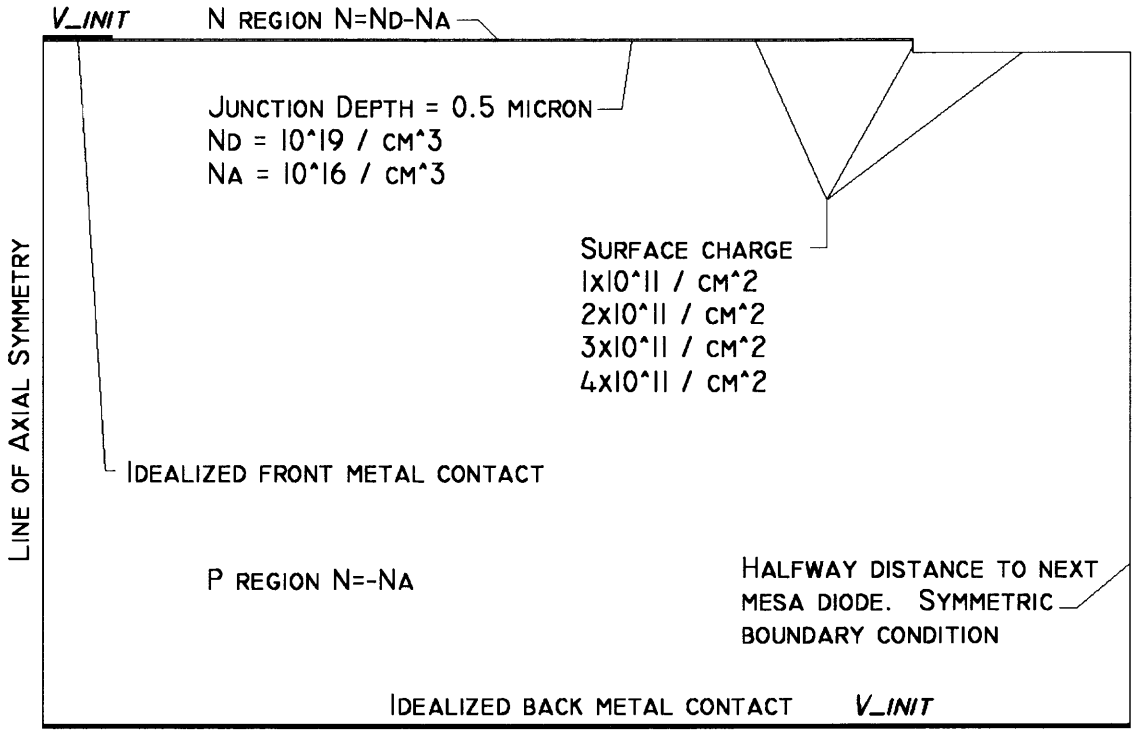

Figure 3.2 Electrostatics bulk and boundary conditions.

The *V_init* parameter determines the equilibrium Fermi level at the metal contacts on the n and p sides away from the junction and is defined in Equation (3.46) [90]. The

$$V\_init = \frac{kT}{q}\left(-\ln\frac{|N|}{n_i}\right) \qquad for \quad N < 0$$
$$V\_init = \frac{kT}{q}\left(\ln\frac{|N|}{n_i}\right) \qquad for \quad N \geq 0 \tag{3.46}$$

electrostatics module has a boundary condition option for a fixed charge, and this was utilized to model the fixed charge due to an oxide layer on top, edge, and step of the mesa diode as shown in Figure 3.2.

After the initial electrostatics module is solved, its solution is used as the initial conditions for the next set of calculations. A second electrostatics module (es2) is used to determine the electric potential and is coupled to the convection and diffusion module for electrons (cd) and holes (cd2). Poisson's equation is solved again, but this time for the variable *V2*. There are three differences between module (es) and module (es2). First is that the hole and electron distributions in the expression for charge density are given by *cp* and *cn*, and are determined making convection and diffusion modules (cd) and (cd2) self-consistent with the electrostatics module (es2). Second is that the initial value electric potential for the nonlinear solver is the distribution determined by the initial electrostatics module (es). Third is that the V_f parameter is applied to the metal contact at the base of the p subdomain. The self-consistent solution is performed at each value of V_f in order to obtain a current density vs. voltage curve. The calculated current is determined by using the Weak Form of the convection and diffusion modules for electrons and holes. The Weak Form is explained in the COMSOL Model library. Simply, it is a result of the finite element method formulation of the Weak Form and the use of Lagrange multipliers. Using Lagrange multipliers to determine the flux of holes and electrons at each finite element along a boundary is a more accurate method of

solving for the current density. An overview of the Galerkin finite element method was also presented in the previous section.

The last part of implementing the physical model into COMSOL Multiphysics is to define the boundary conditions. The second electrostatics module (es2) has the same boundary conditions as the initial electrostatics module (es). Additionally, there are four types of boundary conditions that need to be defined for the continuity equations for electrons and holes. At the metal contacts, the boundary condition is a fixed concentration of electrons for the convection and diffusion module (cd) and a fixed concentration of holes for the convection and diffusion module (cd2). The values are determined by using the equilibrium condition from Equation (3.29), and the equations for electron and hole concentrations are shown in Equations (3.47) and (3.48) [90],

$$\begin{aligned} n\_init &= \frac{|N|}{2} + \sqrt{\frac{N^2}{4} + n_i^2} \quad for \quad N \geq 0 \\ n\_init &= \frac{n_i^2}{\frac{|N|}{2} + \sqrt{\frac{N^2}{4} + n_i^2}} \quad for \quad N < 0 \end{aligned} \tag{3.47}$$

$$\begin{aligned} p\_init &= \frac{|N|}{2} + \sqrt{\frac{N^2}{4} + n_i^2} \quad for \quad N < 0 \\ p\_init &= \frac{n_i^2}{\frac{|N|}{2} + \sqrt{\frac{N^2}{4} + n_i^2}} \quad for \quad N \geq 0 \end{aligned} \tag{3.48}$$

respectively. The boundary condition for surface recombination rate at the silicon and oxide interface is defined by using the boundary flux condition, and setting it equal to the expression developed for surface recombination rate as shown in Equation (3.36). It should be noted that the surface concentrations of electrons and holes in Equation (3.36)

are the calculated values of *cn* and *cp* at these locations. The flux condition is shown in Equation (3.49), where *n* is the normal unit vector, *N* is the electron or hole current,

$$-\hat{n}\cdot\vec{N} = N_0 \tag{3.49}$$

depending on the module, and N_0 is the recombination rate. *N* and N_0 are defined in Equations (3.50) and (3.51), respectively. In Equation (3.50), the proper substitutions for electrons or holes can be made using Equation (3.39) or Equation (3.41). The negative

$$\vec{N} = -D\,\nabla c + c\,\vec{u} \tag{3.50}$$

$$N_0 = -U_{SRH} \tag{3.51}$$

sign in Equation (3.51) changes the definition from an inward flux to an outward flux. This is needed because when electrons and holes recombine at the silicon oxide interface, they need to be removed from the system. COMSOL Multiphysics also allows for the transport processes defined for electrons and holes to be conservative. This option was utilized and it helped ensure charge neutrality of the mesa diode model.

The other two boundary conditions are not physical, but are a result of the mathematical formulation of the problem and setting a practical limit on the size of the mesa diode that was modeled. First, the axially symmetric boundary condition is used for all four modules and defines the r=0 line. Its use states that the electric potential, electron current, and hole current are symmetric about this line. In other words, there are no losses across this line, and the gradient of all of these parameters is zero. Since the mesa diode is fabricated as an array on top of a solar cell, a cut-off distance between one mesa diode and an adjacent one needs to be chosen. A distance of 317.5 μm was chosen since it is halfway between adjacent diodes. Furthermore, this distance is more than 1.5 times

the thickness of the mesa diode. Therefore, there is enough distance for an excess carriers to diffuse before it would affected by the adjacent mesa diode. This boundary was modeled as a symmetric boundary for all four modules. Therefore, no electron or hole current was lost at this boundary, and the electric potential was constant across it as well. The locations of these boundary conditions are shown in Figure 3.3.

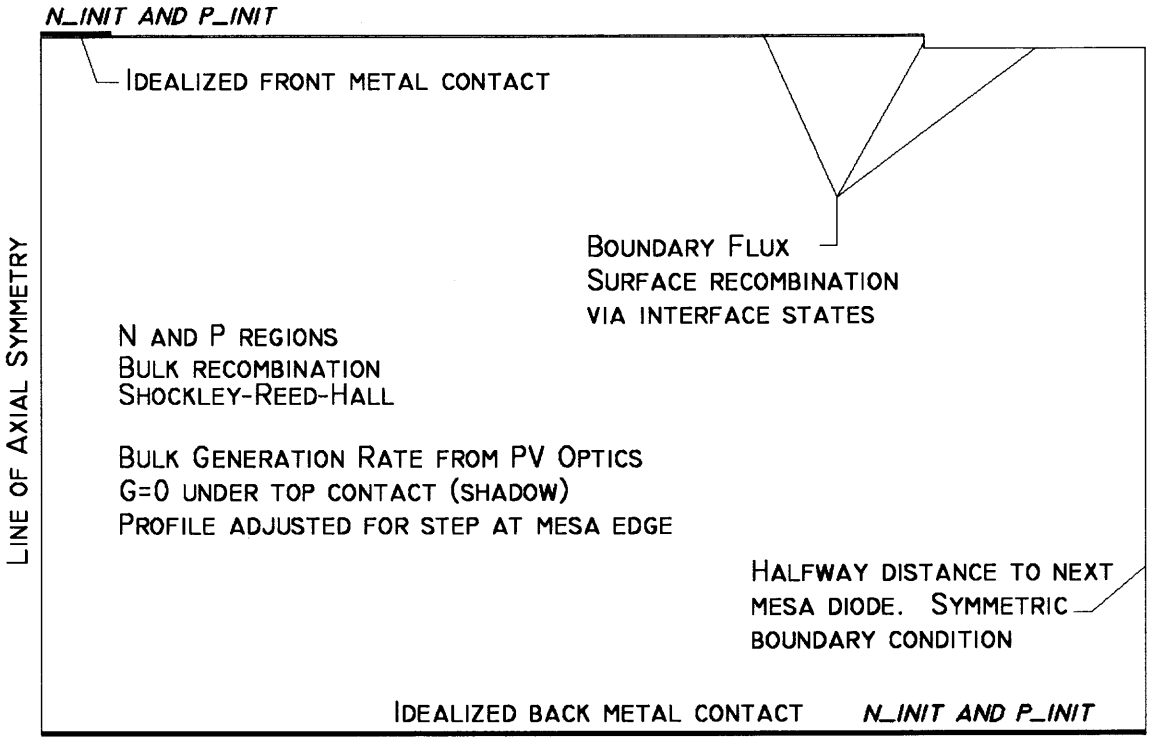

Figure 3.3 Bulk and boundary conditions for continuity equations.

3.4.3 COMSOL Multiphysics' Solution Method

This section describes an overview of the solution method that COMSOL Multiphysics uses. It is important to understand the solution method, because it affects how to formulate the problem mathematically. COMSOL Multiphysics uses a stationary non-linear solver that utilizes a version of the damped Newton's method [101]. It can be considered an extension of Newton's method for finding a root of an equation, which is shown in Equation (3.52) [102]. As stated in section 3.4.1, the finite element method

$$x_{n+1} = x_n - \frac{f(x_n)}{f'(x_n)} \tag{3.52}$$

used for the mesa diode is the weighted – residual method. The residual is the difference between the right-hand side and left-hand side of an equation, and should theoretically equal zero [97]. Therefore, the model for the mesa diode has three coupled equations that are set equal to zero. The one variable expression in Equation (3.52) becomes a matrix equation and is shown in Equation (3.53) [102], where the derivative in Equation 3.52

$$x^{(n+1)} = x^{(n)} - A_f^{-1}(x^{(n)}) f(x^{(n)}) \tag{3.53}$$

has been replaced by the inverse of the matrix of first order derivatives, which is also known as the Jacobian [102, 103]. For the mesa diode model A_f is shown in Equation (3.54). In many cases, the derivatives in the Jacobian matrix can be very complicated and

$$A_f(V,n,p) = \begin{bmatrix} \frac{\partial r_V}{\partial V}^{(n)} & \frac{\partial r_V}{\partial n}^{(n)} & \frac{\partial r_V}{\partial p}^{(n)} \\ \frac{\partial r_n}{\partial V}^{(n)} & \frac{\partial r_n}{\partial n}^{(n)} & \frac{\partial r_n}{\partial p}^{(n)} \\ \frac{\partial r_p}{\partial V}^{(n)} & \frac{\partial r_p}{\partial n}^{(n)} & \frac{\partial r_p}{\partial p}^{(n)} \end{bmatrix} \tag{3.54}$$

almost impossible to solve analytically. Therefore, they are typically calculated numerically [104]. This is important because calculating numeric derivatives can be lead to instabilities when trying to get a solution. These instabilities can lead to large oscillations, particularly at the beginning of the iteration process, which eventually leads the system to diverge. In addition, A_f needs to be inverted after it has been solved. This can also lead to more numeric instabilities especially when numerical derivatives are used. In order to minimize these potential problems two measures can be implemented.

First, the initial guess for electric potential, electron concentration, and hole concentration needs to be very close to the solution. This is the purpose of the initial electrostatics module and corresponding distribution functions for electron and hole distributions. The other measure is to use a damping factor, λ, which is implemented by COMSOL Multiphysics, and modifies Equation (3.53) into Equation (3.55) [102]. The damping

$$x^{(n+1)} = x^{(n)} - \lambda A_f^{-1}(x^{(n)}) f(x^{(n)}) \tag{3.55}$$

factor is a value greater than zero and can be at most one. COMSOL Multiphysics uses an algorithm to choose a value of λ based on the previous iteration, thereby minimizing oscillations. The minimum value of the damping factor is user defined. The damping factor is adjusted so that eventually it can obtain a value of one, which is required for Newton's method to be valid [101]. Convergence occurs when the residuals, also known as the error estimate, of the entire system is less than a tolerance value that is user defined, and when the damping factor equals one. In almost all of the calculations performed on the mesa diode the default tolerance of 10^{-6} was used. Although Newton's method can be prone to oscillating behavior, using an accurate initial guess and a damping factor makes it an excellent method for solving nonlinear equations. It is particularly useful to use Newton's method because it has a high rate of convergence [102]. Therefore, the solution can be obtained with relatively few iterations as long as the initial guess is very close.

3.5 Summary

In this chapter it was shown how the drift – diffusion equations for electrons and holes were developed from the more general Boltzmann Transport Equation. The assumptions that were made were discussed in reference to modeling the operation of the mesa diode. The process of bulk and surface recombination via energy levels in the silicon bandgap were presented and the assumptions made to develop this model were applied to the operation of the mesa diode. An overview of how the optical generation rate profile using PV Optics simulation software was discussed. Lastly, an overview of the finite element method was discussed as well as how the physical model was implemented in the commercial finite element software package, COMSOL Multiphysics, and a brief discussion of the solution method was also included. The following chapter discusses the results of the simulations of the physical model presented in the chapter using COMSOL Multiphysics.

CHAPTER 4

RESULTS OF NUMERIC SIMULATIONS

4.1 Introduction

The primary goal of this dissertation is to use an appropriate physical model of the operation of a mesa diode to determine what happens to its overall performance when the edge conditions are altered. In Chapter 2, the influence of edge conditions on the operation of semiconductor diode were discussed. In Chapter 3 a model of the entire operation of a semiconductor diode was presented including the edge conditions of surface charge and surface recombination. These were considered to be highly significant from the discussion of previous work in Chapter 2. In this chapter a series of calculations based on the model discussed in Chapter 3 will be presented. The calculations were performed by utilizing COMSOL Multiphysics finite element software [95]. First, the analysis of a small rectangular diode will be presented. In numerical simulations, a small simple device is typically easier to model and provides a baseline for a larger, more complex geometry. Simulations of edge conditions next to junction devices have been performed on a small scale by other research groups [105-108]. Therefore, quantitative and qualitative comparisons of the results can be made. Next, simulations using the actual size of the mesa diode will be presented, in which the edge conditions are changed. Lastly, the important results of simulations of the mesa diode will be discussed with respect to the actual measurements of a mesa diode.

4.2 Simulation of a Small Area Diode

As an initial test of the physical model discussed in Chapter 3, simulations were performed on a small area diode. The small diode was modeled in axially symmetric two – dimensional space. It had a radius of 2 μm and a height of 5 μm. For comparison, the main area of the mesa diode had a radius of 1270 μm and a height of 199.5 μm. The top and bottom surfaces were modeled as metallic contacts. The right side of the rectangle was modeled with a fixed positive surface charge and a flux condition was set to be equal to the surface recombination rate given by Equation (3.36). Figure 4.1 is a sketch of the small area diode with the aforementioned boundary conditions.

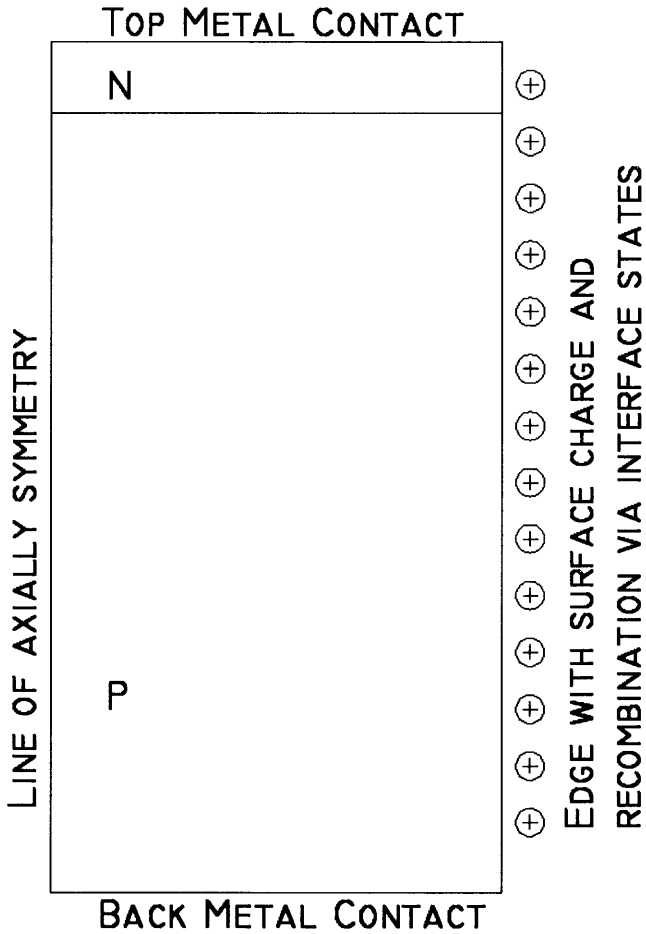

Figure 4.1 Sketch of a small sample diode with boundary conditions (radius = 2 μm and height = 5 μm).

The first test was to change the surface charge around the edge of the device and compare the results to those calculated by another research group. Figure 4.2 shows the dark current density versus voltage plots when the surface charge along the right-hand segment was changed from $5x10^{10}$ cm^{-2} to $5x10^{11}$ cm^{-2}. Also, the surface recombination velocity parameters, s_{n0} and s_{p0}, were set to 1000 cm/s, so that they would be the same as the values used by the study performed by Kuhn et al. [105]. The dark current density increases with increasing charge along the edge of the device. For a surface charge of $1.5x10^{11}$ cm^{-2}, small bumps appear at about 0.3 volts forward bias and they move toward lower voltages as the surface charge increases until $2x10^{11}$ cm^{-2}. These bumps in the current density versus voltage curve correspond to the applied forward bias that results in the maximum surface and bulk recombination rates. This maximum occurs because the hole and electron concentration are nearly equivalent. However, as the surface charge is further increased, the dark current also increases. This is the opposite of what would be expected. As the surface charge is increased from $3x10^{11}$ to $5x10^{11}$ cm^{-2}, the current density versus voltage curves move upward, with the greatest increases at lower applied forward biases. This is typically the behavior of an electric shunt. A detailed analysis of the dark and illuminated operation of the small sample diode is included in the Appendix.

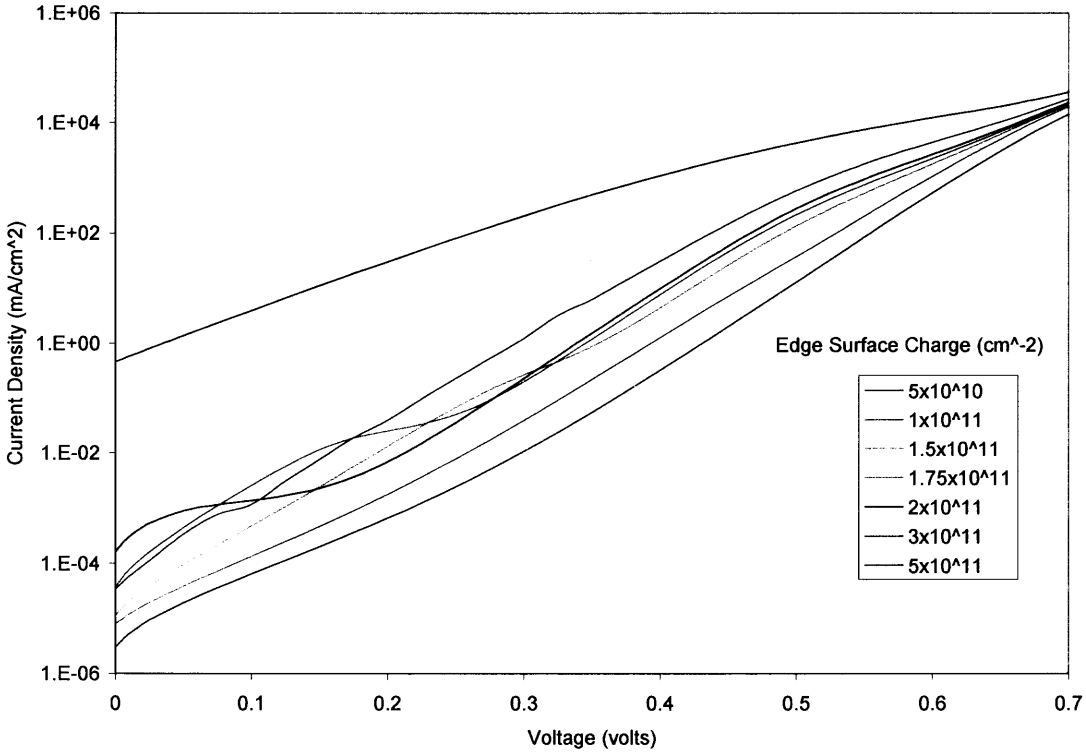

Figure 4.2 Dark current density vs. voltage for small sample diode for different vertical edge charges.

The following explains how the shunting mechanism occurs for this simulated device. The space charge region becomes extended from the junction to the back contact as the positive charge increases. Figure 4.3 shows this development by comparing the bulk recombination rate at 0.1 volts forward bias for vertical edge surface charges of $5x10^{10}$ cm^{-2} and $5x10^{11}$ cm^{-2}. The shunt occurs because as the edge charge increases, the region adjacent to it on the p-side changes from a slightly depleted to a completely inverted state. As the edge charge becomes more positive, the adjacent region becomes more strongly inverted. Since this region now is a majority n region, the space charge region bends ninety degrees and extends towards the back contact.

Typically a strongly inverted region adjacent to a passivating surface such as an oxide or nitride is desirable since it significantly reduces surface

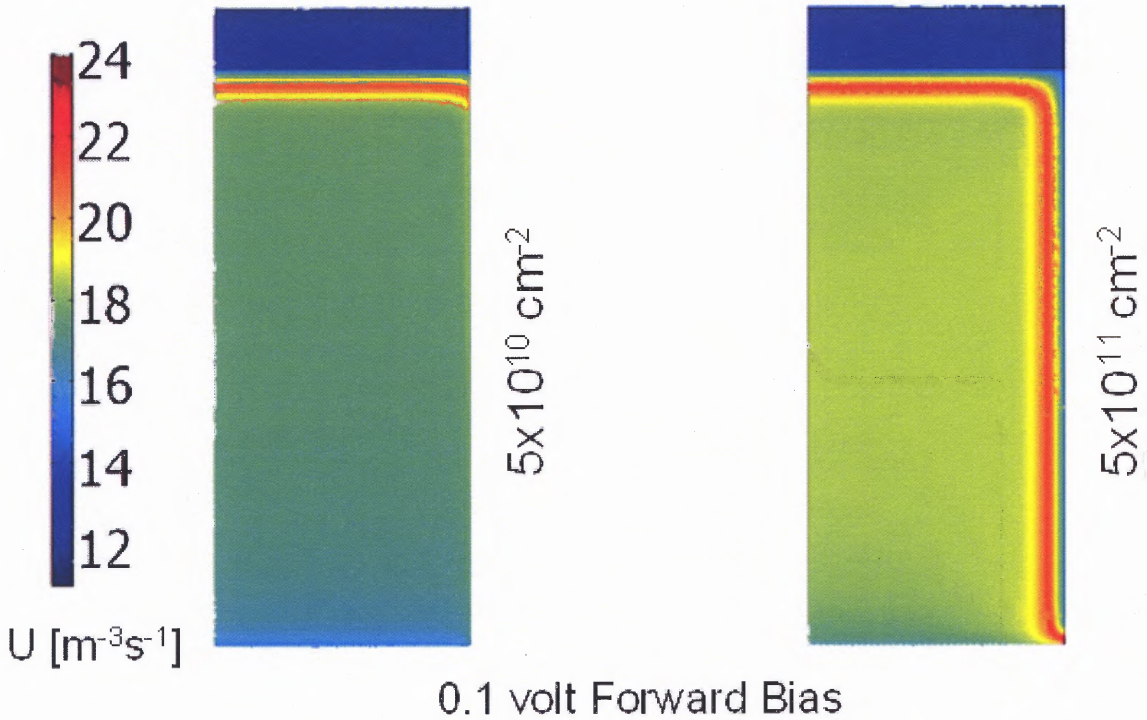

Figure 4.3 Bulk recombination rate at 0.1 volts forward bias for surface charges of $5x10^{10}$ cm^{-2} and $5x10^{11}$ cm^{-2}.

recombination. However, if this inverted region extends to the back contact, bulk and surface recombination can significantly increase as shown in Figure 4.3.

The primary mechanism occurs because the concentration of holes at the back contact is a maximum and the minority carrier electrons in the inverted region are at its greatest concentration on the p-side of the junction as well. Therefore, the concentration of holes and electrons are closer to one another than at any other point in the device and they are both close to their maximum values. When viewed in the context of recombination via a single energy level recombination center, this is the worst possible scenario. The recombation rate is at a maximum when the concentrations of electrons and holes are equal. Also, upon review of Equation (3.27), the recombination rate is

proportional to (pn-n_i^2). Since the concentrations of electrons and holes are near their maximum values, this further increases the recombination rate in this area.

Although the explanation of the increase in dark current as a result of the increase of bulk and surface recombination rates due to the connection of the space charge region to the back contact is satisfactory, there are two additional mechanisms that further exacerbate this problem. One is that increasing the positive edge charge increases the width of the space region. More importantly, the increase of the edge charge increases the space charge region next to back contact, increasing the area in which the maximum recombination rate can occur. It is known that the saturation current density associated with recombination in the space charge region is proportional to the width of the space charge region in one dimensional space. Although a two dimensional analytic solution for the specific diode that was modeled is not known, it is reasonable to expect that increasing the region, in which recombination occurs will increase the dark current. Figure 4.4 is a cross-section of the electron concentrations and bulk recombination rates for two microns above the back contact on the p-side of the small sample diode for surface charges of $5\text{x}10^{10}$ cm^{-2} and $5\text{x}10^{11}$ cm^{-2}. It shows that the space charge region for the larger surface charge is significantly greater than that of the smaller surface charge. This increase in space charge region is coupled with a corresponding increase in bulk recombination rate. The other mechanism that also contributes to the

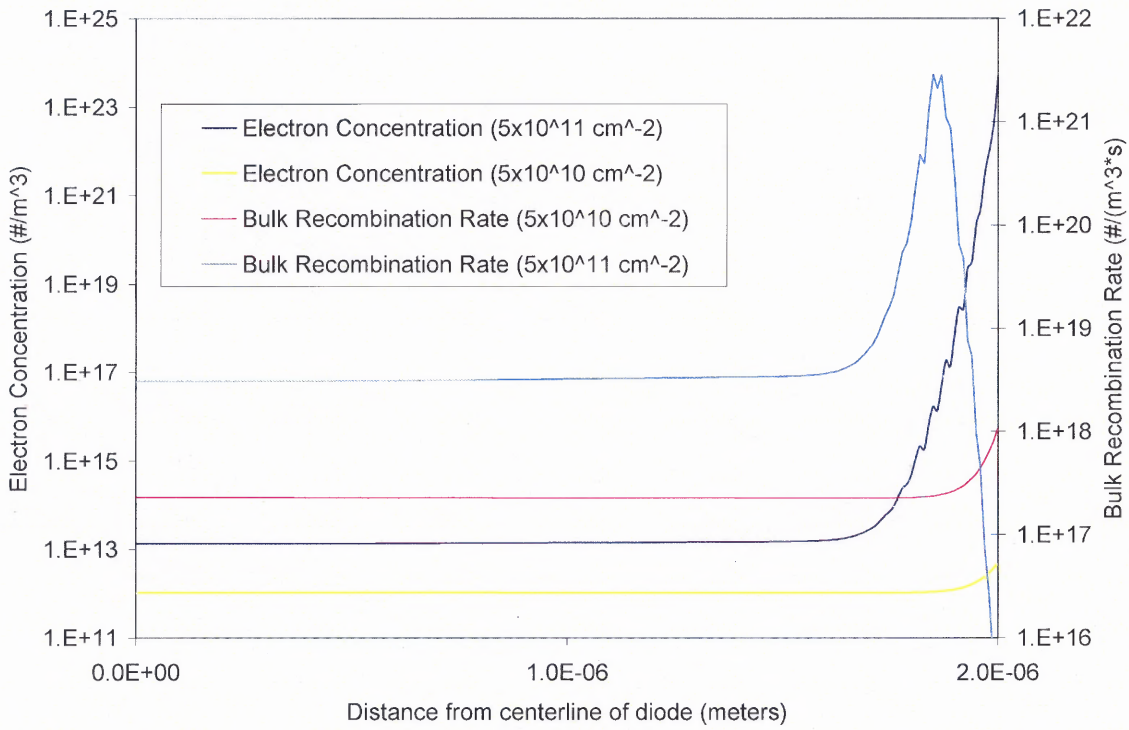

Figure 4.4 Cross-section plot of electron concentration and bulk recombination rate at 2 microns above the back metal contact for two edge charges at 0.1 volts forward bias.

increase in dark current density is that the electric field becomes increasingly distorted at the corner between the back metal contact and the edge surface charge. This causes the space charge region to extend horizontally near the back metal contact adjacent to the edge surface charge. This results in two problems that further contribute to a greater recombination rate. The first is that as the space charge region becomes longer, more space charge recombination will take place. The second is that the extension of the electric field from the lower right-hand corner along the back contact will extend the width of the space charge region is this area. This is a result of the boundary condition at the back contact, which keeps the concentration at a constant value based on the doping so that there is no loss of electric potential from the metal contact boundary to the bulk semiconductor. The change in electric potential and distortion of the electric field at the

lower right-hand corner of the diode are shown in Figure 4.5 for the two edge surface charges of $5x10^{10}$ cm^{-2} and $5x10^{11}$ cm^{-2}.

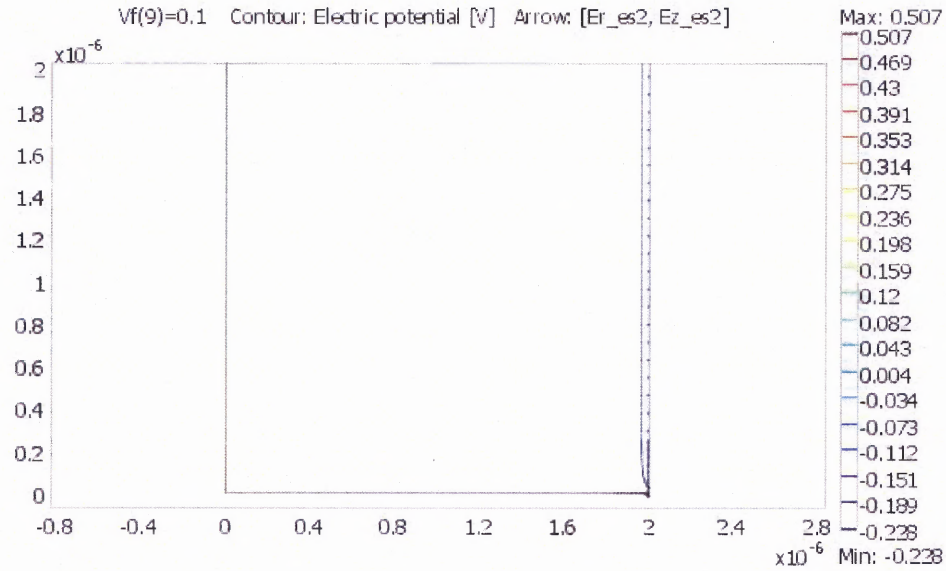

Surface Charge = $5x10^{10}$ cm^{-2}, Forward Bias = 0.1 volts

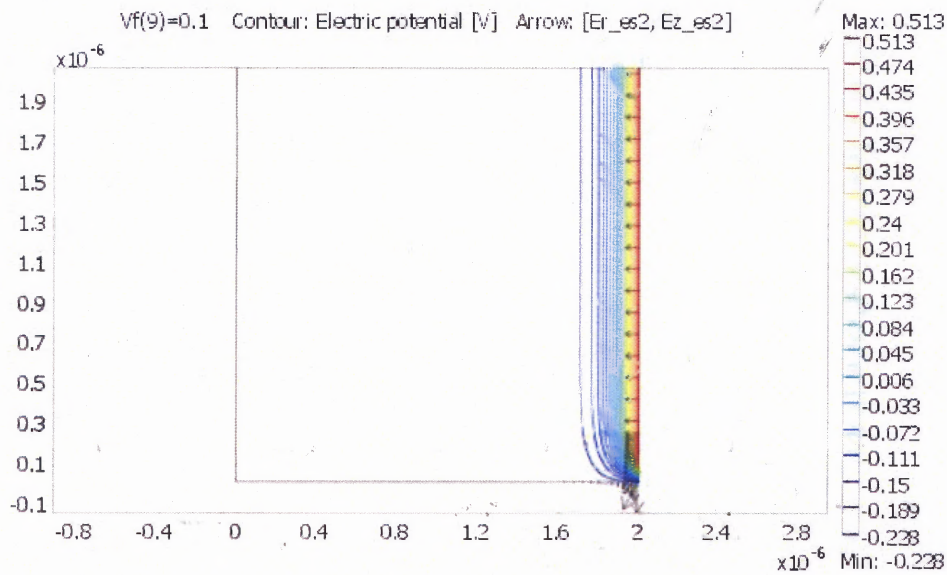

Surface Charge = $5x10^{11}$ cm^{-2}, Forward Bias = 0.1 volts

Figure 4.5 Contour plots of the electric potential and boundary arrow plots of the electric field for edge surface charges of $5x10^{10}$ cm^{-2} and $5x10^{11}$ cm^{-2}.

In a similar study, Kuhn et al. [105] state that if the depletion or inversion region next to the fixed edge charge is continuous from the junction to the back contact, then shunting will occur. Furthermore, they state that this type of shunting has been observed experimentally in nonstandard solar cells, such as POWER and EWT that have interdigitated n and p regions adjacent to a highly charged silicon nitride passivation surface [105, 106]. In their study, they did not have a shunting problem in the device that they modeled because a back-surface field was included for this dissertation. The simulations that led to the results shown in Figure 4.2 were run again, but with a back-surface field that extended 0.25 microns above the bottom of the device. The results of these simulations for the small diode including the back-surface field are shown in Figure 4.6. They are in very good agreement with the results of simulations performed by Kuhn et al. [105], which are shown in Figure 4.7. The bumps in the current density versus voltage curve are more pronounced indicating that the surface recombination is a more important mechanism than shunting. Also, as the surface charge increases to its maximum value, the lowest dark current is achieved, and this is expected. Therefore, adding the back surface field significantly reduces resistive shunting in the

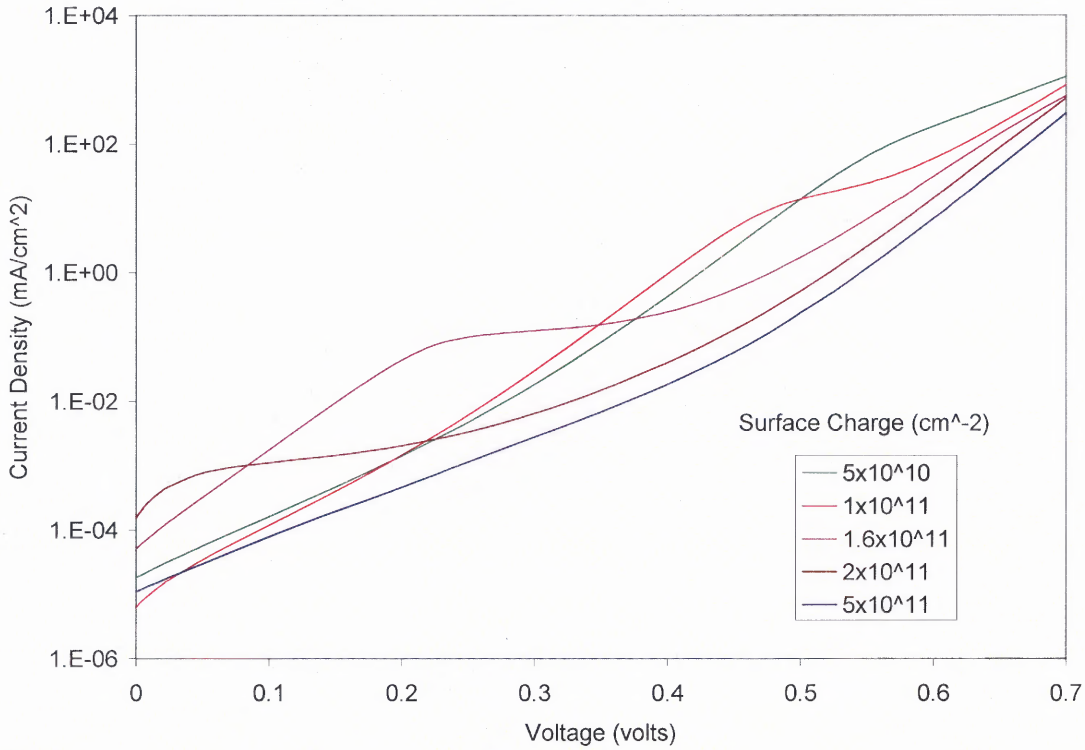

Figure 4.6 Dark current density vs. voltage for small sample diode with a back surface field at different vertical edge charges.

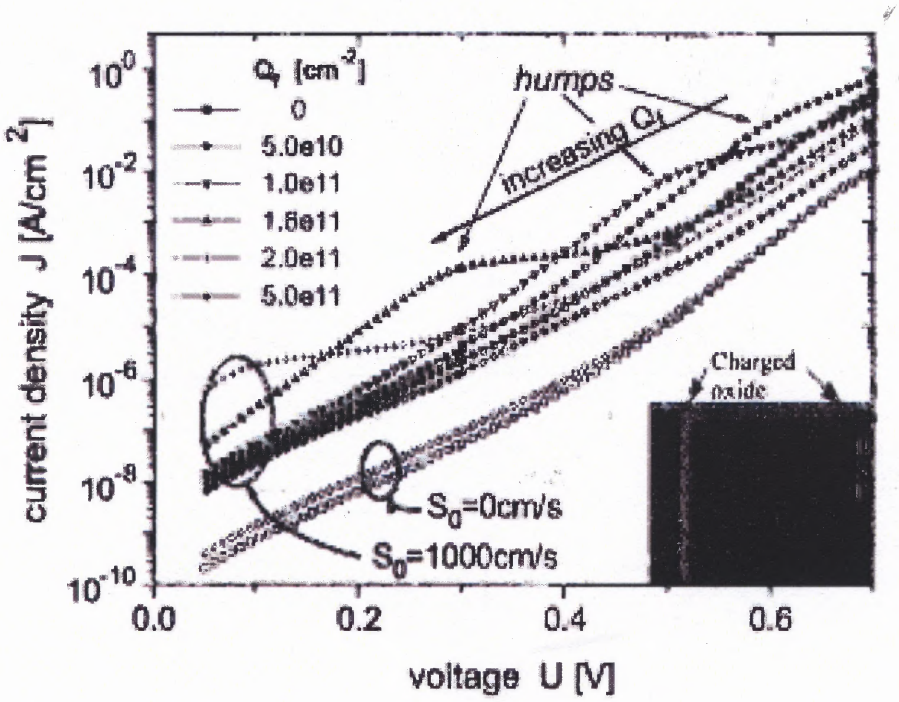

Figure 4.7 Dark current density vs. voltage for small sample diode with a back surface field at different vertical edge charges. Study performed by Kuhn et al. [105].

simulated small diode. In particular, the addition of the back surface prevented the region adjacent to the edge surface charge and the back metal contact from becoming inverted as shown in Figure 4.8. Consequently, the electric field and its associated space charge

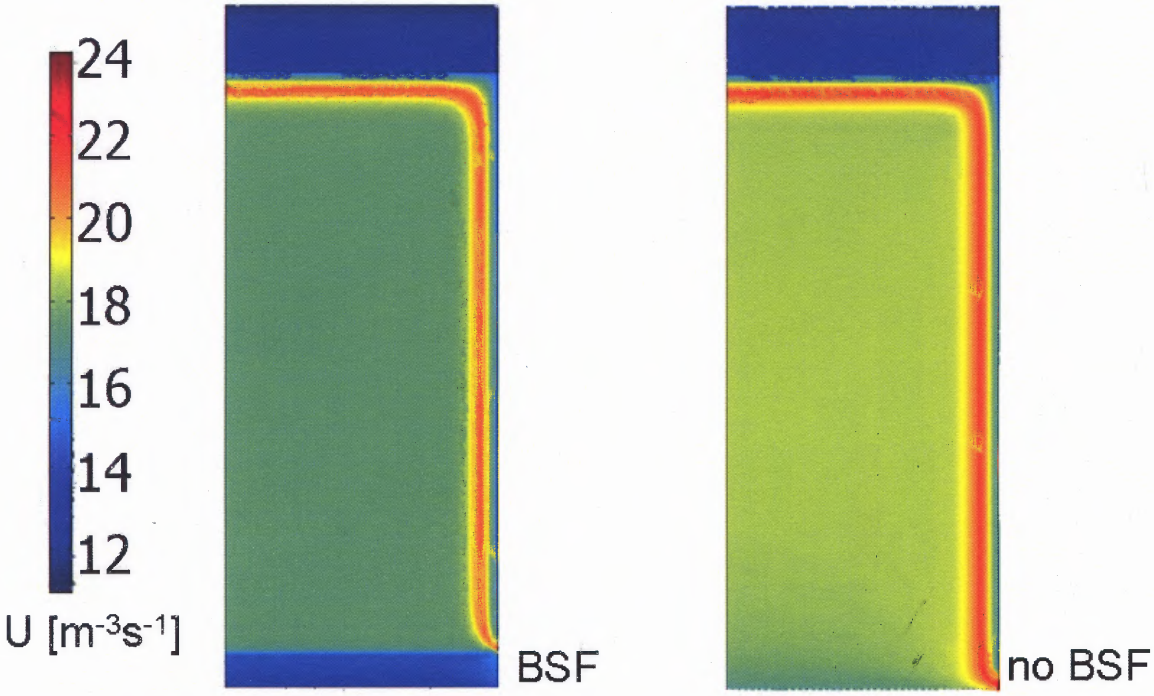

Figure 4.8 Bulk recombination rate for a small sample diode with and without a back surface at 0.1 volts forward bias and a vertical edge charge of $5x10^{11}$ cm^{-2} (dark condition).

region extend from the junction to the back surface field and do not reach the back metal contact. Therefore, the mechanisms that increase the bulk and surface recombination rates in the diode without a back surface field are suppressed and the benefit of a greater positive edge surface charge significantly reduces the surface recombination rate. More detailed analyses are shown in the Appendix.

As further confirmation, the diode was simulated under illuminated conditions. The generation curve was obtained by using PVOPTICS [93], an optical simulation software package developed at the National Renewable Energy Laboratory, which was

briefly reviewed in Chapter 3. It was used to determine the number of electron-hole pairs that were generated as a function of distance below the top of the device. The illuminated current density versus voltage curves for the diode without and with a back-surface field are shown in Figures 4.9 and 4.10, respectively. In the case with no back-surface field, the open-circuit voltage (V_{oc}) and fill factor (FF) decrease as the surface charge is increased. With a back-surface field, the V_{oc} and FF initially decrease with increasing surface charge, and then increase as the charge is further increased, reaching the best values for short-circuit current density (J_{sc}), V_{oc}, and FF. This is because shunting has been minimized and the additional positive charge pins electrons near the edge, thereby reducing the recombination rate in this area. Furthermore, the simulations

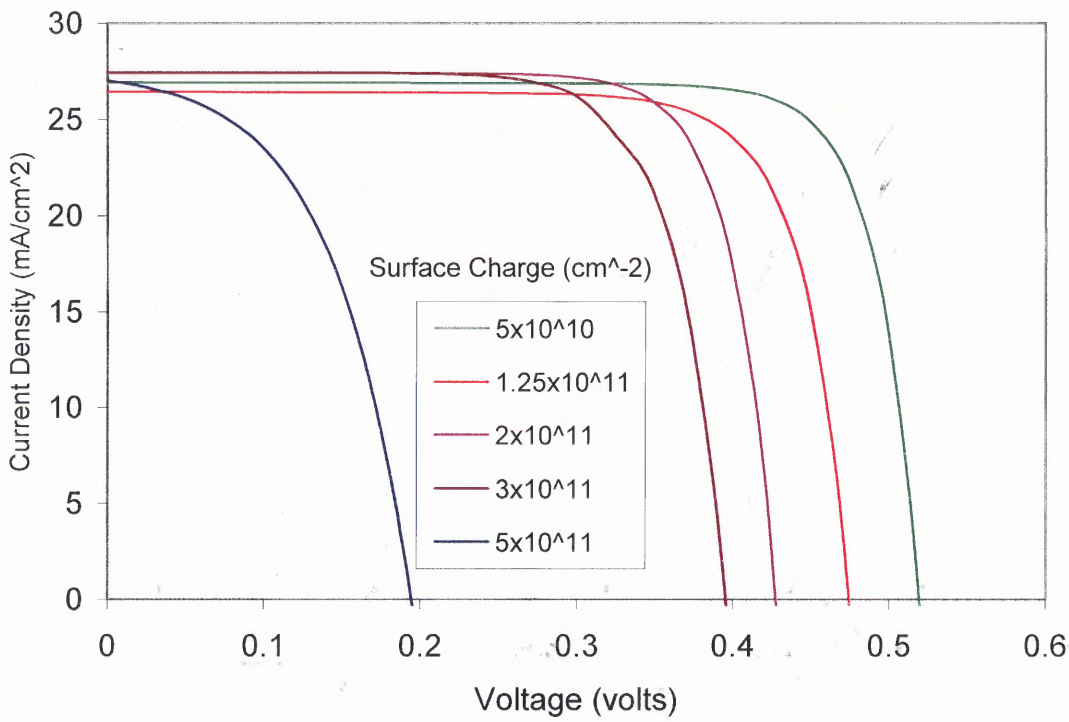

Figure 4.9 Illuminated current density vs. voltage for small sample diode at different vertical edge charges.

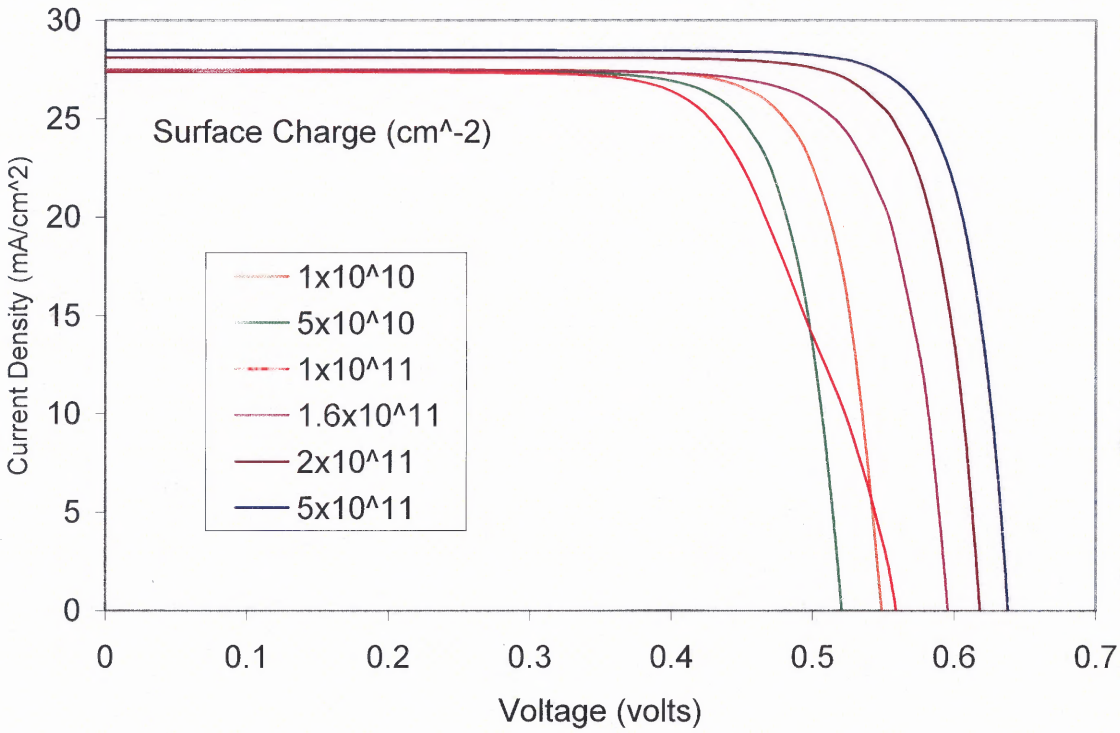

Figure 4.10 Illuminated current density vs. voltage for small sample diode with a back surface field at different vertical edge charges.

with the back surface field are in good qualitative agreement with the simulations performed by Kuhn et al., and are shown in Figure 4.11. Both Figure 4.10 and Figure 4.11 show that the V_{oc} and FF decrease for surface charges less than $1x10^{11}$ cm^{-2}, then increase with increasing surface charge.

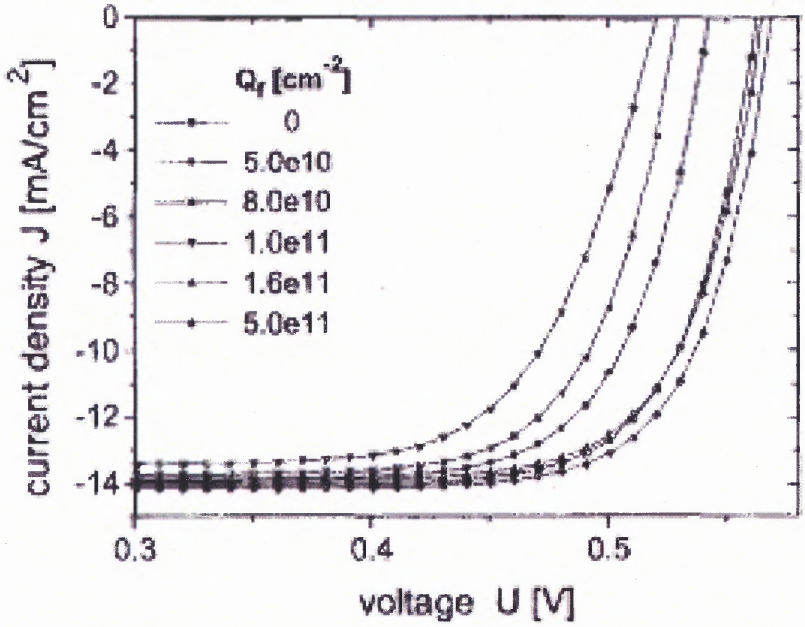

Figure 5: simulated, illuminated J(U)-characteristic for different surface charge densities Q_f. $Q_f < 10^{11} cm^{-2}$ reduces fill factor and V_{OC}.

Figure 4.11 Illuminated current density vs. voltage for small sample diode with a back surface field at different vertical edge charges. Study performed by Kuhn et al. [105].

The primary mechanisms that cause the V_{oc} and FF to decrease in the illuminated simulations for a small sample diode without a back surface field are the same as those that cause an increase in the recombination current density under dark simulations. In particular, connecting the space charge region from the junction to the back metal contact results in an increased recombination rate near the region adjacent to the back metal contact and edge surface charge. This is shown in Figure 4.12. Additional analyses of the illuminated conditions are also included in the Appendix.

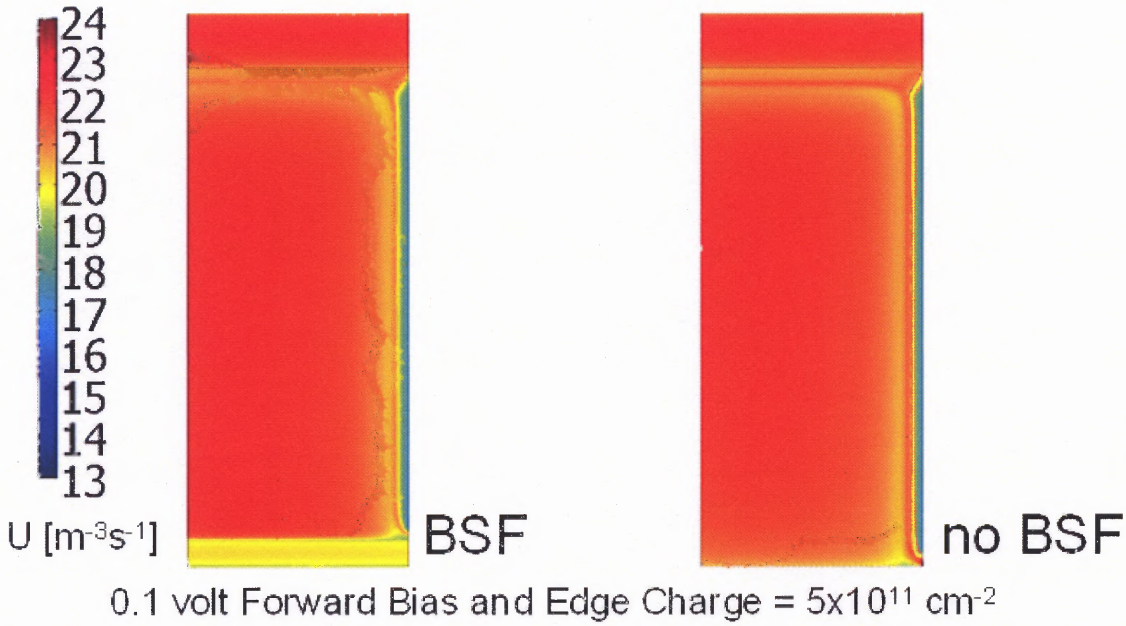

Figure 4.12 Bulk recombination rate for a small sample diode with and without a back surface at 0.1 volts forward bias and a vertical edge charge of $5x10^{11}$ cm^{-2} (illuminated condition).

4.3 Simulation of a Mesa Diode

After using the model to simulate a small sample diode and obtaining very good agreement with results from a similar study performed by another group [105], the mesa diode was simulated under dark and illuminated conditions. Figure 4.13 shows a cross section of the device. In this set of simulations, the top and step segments were modeled as passivating surfaces with a fixed charge of $1x10^{11}$ cm^{-2}, while the vertical edge of the mesa was modeled as a passivating surface whose surface charge was changed from

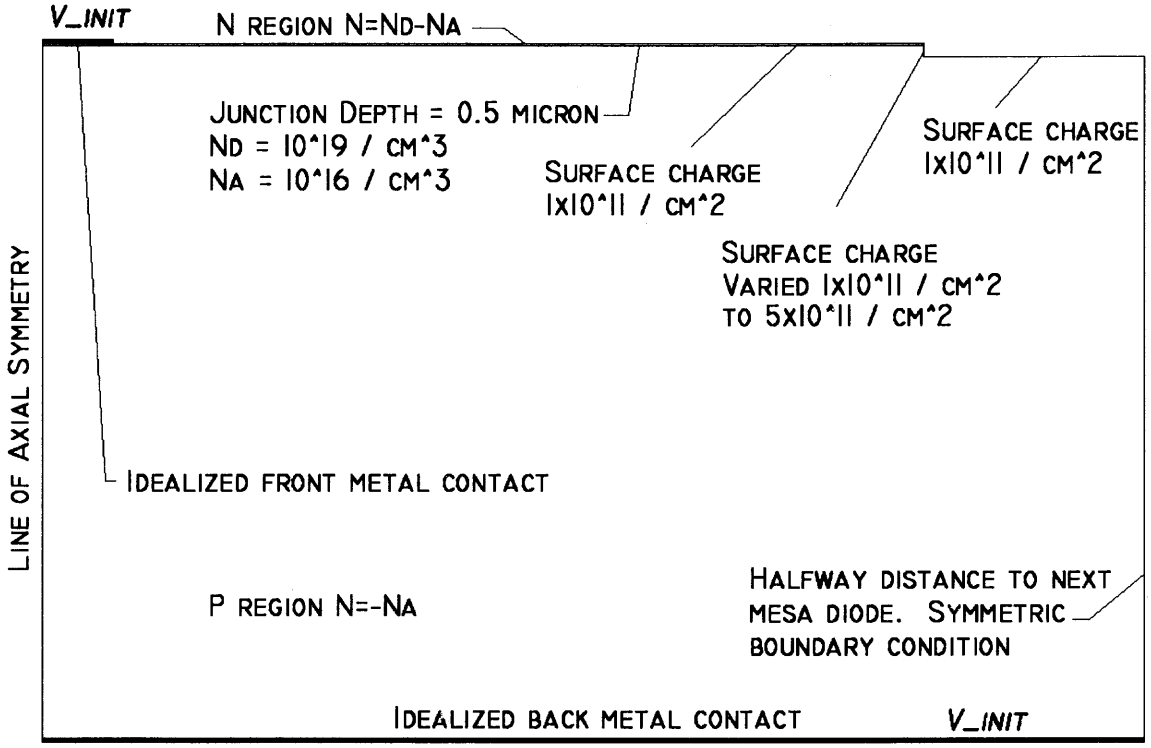

Figure 4.13 Cross-section of modeled mesa diode with bulk and surface conditions.

$1x10^{11}$ cm^{-2} to $5x10^{11}$ cm^{-2}. The dark current density vs. voltage plots of the simulations are shown in Figure 4.14. The current density increases with increasing surface charge. The initial increase in dark current density is predominantly due to additional recombination near the mesa's edge. This is similar to behavior of the current density vs. voltage curves of the small sample diode without a back surface field. The greatest increase occurs at low voltages and is due to resistive shunting, which is related to the distortion of the electric field at the edge of the mesa.

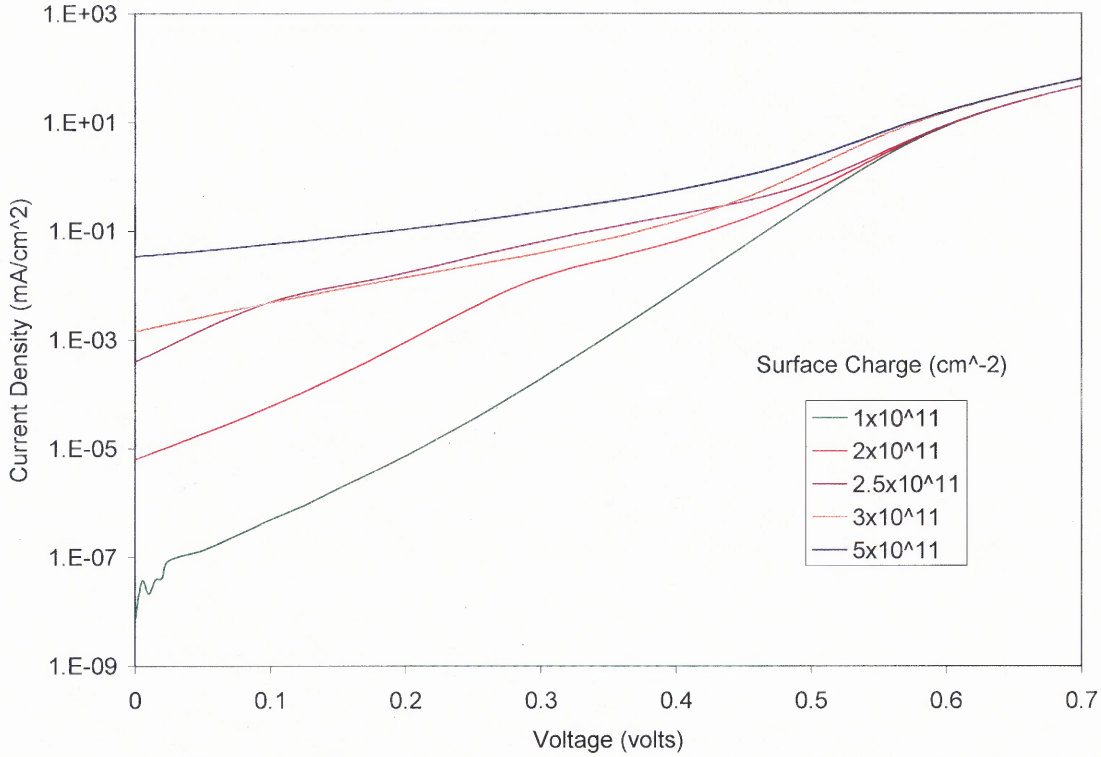

Figure 4.14 Dark current density vs. voltage for the mesa diode at different vertical edge charges.

One of the most important results of the simulations performed on the mesa diode was the calculation of a high point in the electric field at the corner of the vertical edge and the step. The resultant current density vs. voltage curves for the simulations performed in Figure 4.14 were performed with a corner that was a right angle with a sharp point. In order to determine if this feature of the mesa diode was responsible for the increase in dark current density, similar simulations were run with a curved transition rather than a sharp corner. A sketch of the sharp and curved transitions is shown in Figure 4.15.

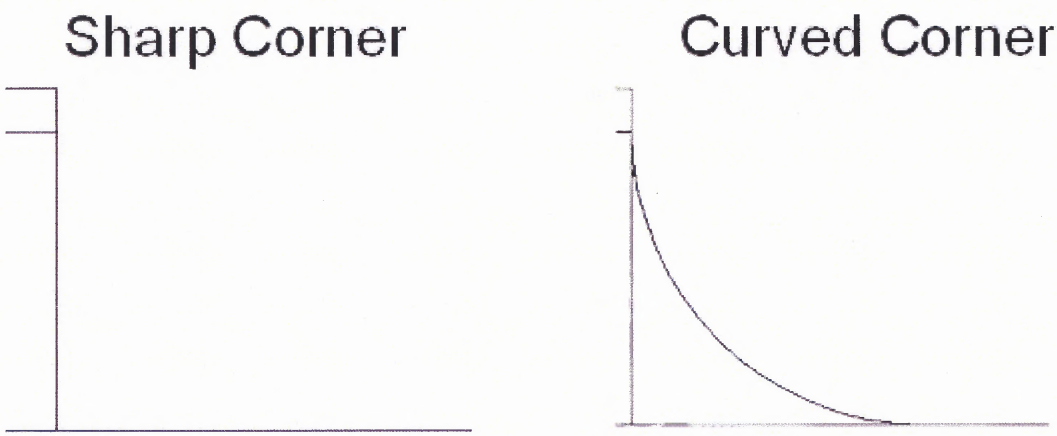

Figure 4.15 Sharp and curved transitions between the vertical edge and the step used in simulations of the mesa diode.

The bulk recombination rate and electric field are plotted in Figure 4.16 for three cases shown in Figure 4.14 at 0.1 volts forward bias.

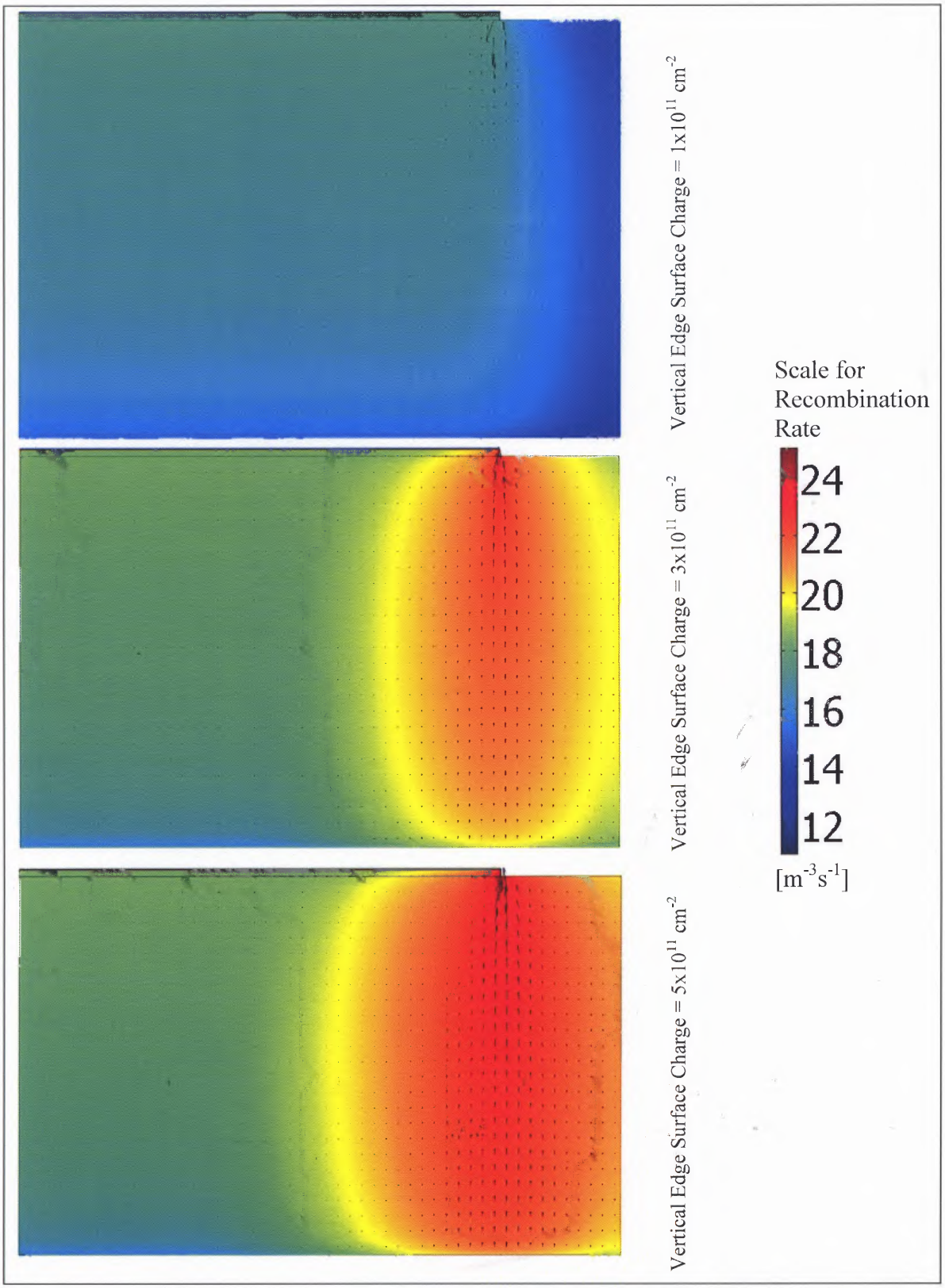

Figure 4.16 Bulk recombination rate and electric field at 0.1 volts forward bias for mesa diode simulations (dark).

It shows that the electric field becomes distorted and its strength is greatest near the mesa's edge. This can be explained by fundamental principles of electric fields [109]. In particular, the electric field is perpendicular to lines of equivalent electric potential. Therefore, at areas with a low radius of curvature, such as sharp corners, the electric field will be a maximum. It is interesting to see that such a short mesa, 4 μm in these simulations, can cause a great disturbance throughout the device. For the simulation of a vertical edge surface charge of $5x10^{11}$ cm^{-2}, the edge effect extends over 200 μm in all directions from the corner of the vertical edge of the mesa and the step. In addition to this sharp corner, there are two additional factors that contribute to the simulated edge effect. One is the interface on the junction next to the vertical edge surface charge. The electric field from the junction and electric field from the vertical edge surface charge intersect at a right angle. This produces another high point in the electric field because it has low radius of curvature. The other factor is the choice of surface charge on the boundary of step. When the surface charge on the step is different from that on the vertical edge, the calculated electric potential will be different, and this potential difference will also alter the electric field, specifically where they intersect, which happens to be the corner of the mesa's edge at the step.

In order to test if the edge effect of a mesa diode is a result of the distortion and increase of the electric field due to its geometric features, a small, curved piece of p-type semiconductor was added at the corner of the vertical edge of the mesa and the step as shown in Figure 4.15. It was defined as a second order Bezier curve with a height and length of 3.5 μm. This height was chosen because the junction is 3.5 μm above the step. Also, the surface charge of the step was kept the same as the curved piece. By adding the

curved piece of semiconductor and adjusting the charge on the step, three problems were addressed in the model. First, the curved piece significantly reduces the radius of curvature at the step and vertical edge. Second, the addition of the curved piece will also reduce the radius of curvature at the junction and the vertical edge. Third, making the surface charges of the curved piece and step equivalent should reduce the potential difference, and hence the electric field at the corner of the vertical edge and the step. To make the comparison of the effect of a sharp and curved transition as definitive as possible, the simulations with a sharp transition shown in Figure 4.16 were repeated; however, this time, the step and vertical edge charges were kept the same, thereby reducing any effect from a potential difference produced by two different surface charges. A sketch of these conditions used to compare a sharp corner and a curved transition are shown in Figure 4.17.

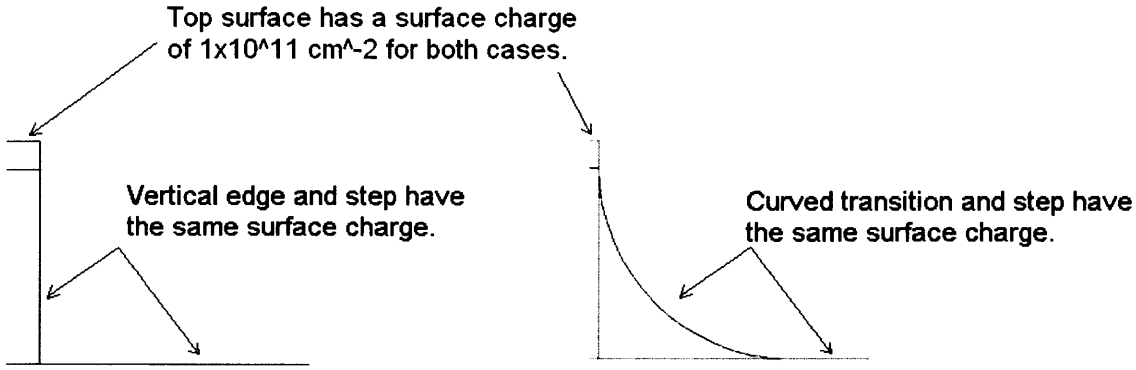

Figure 4.17 Surface charges and geometry for comparison of simulations performed with a sharp edge and a curved transition.

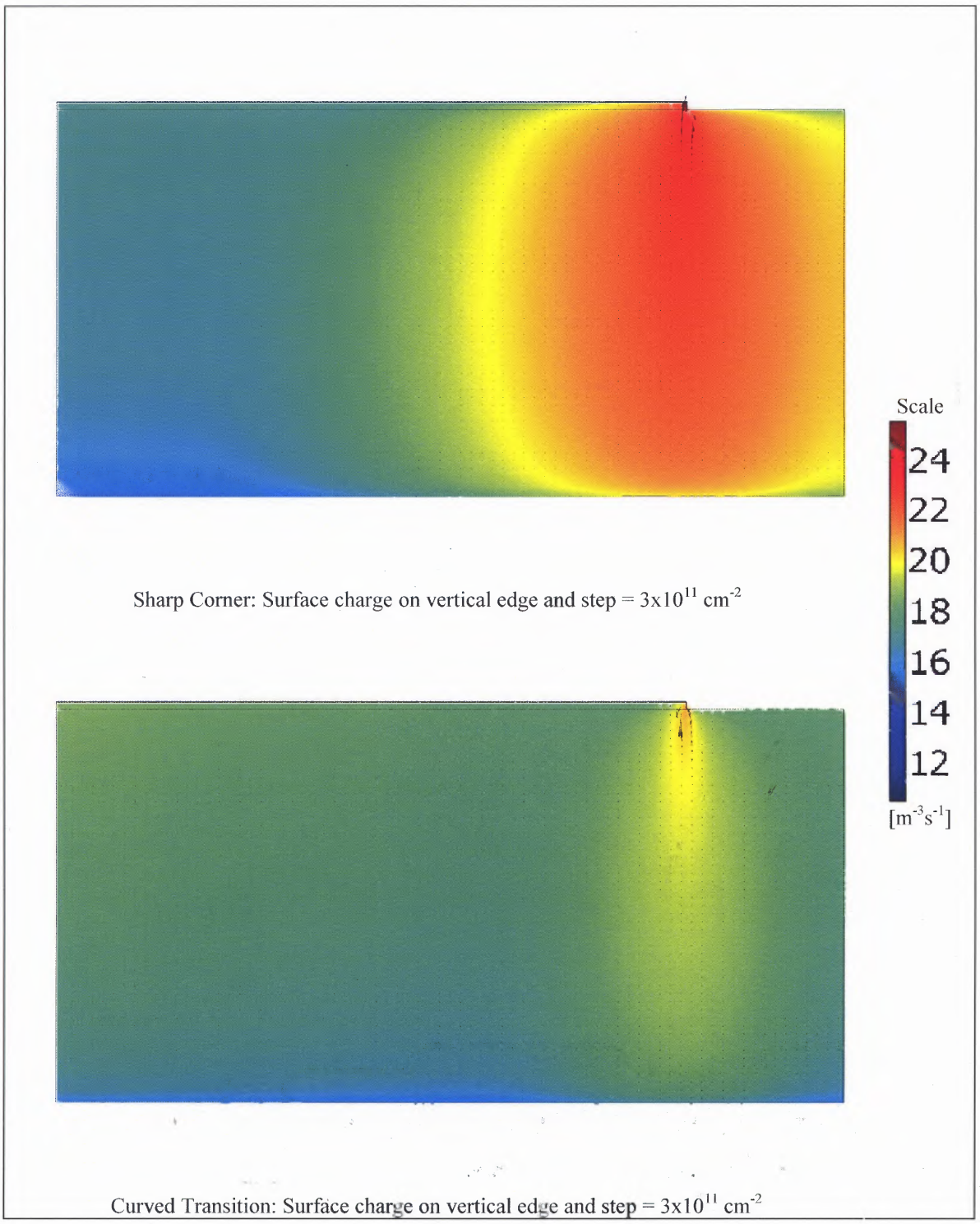

Figure 4.18 Comparison of bulk recombination rate and electric field at 0.1 volts forward bias for a mesa diode with sharp and curved corners with a surface charge of $3x10^{11}$ cm^{-2} under dark conditions.

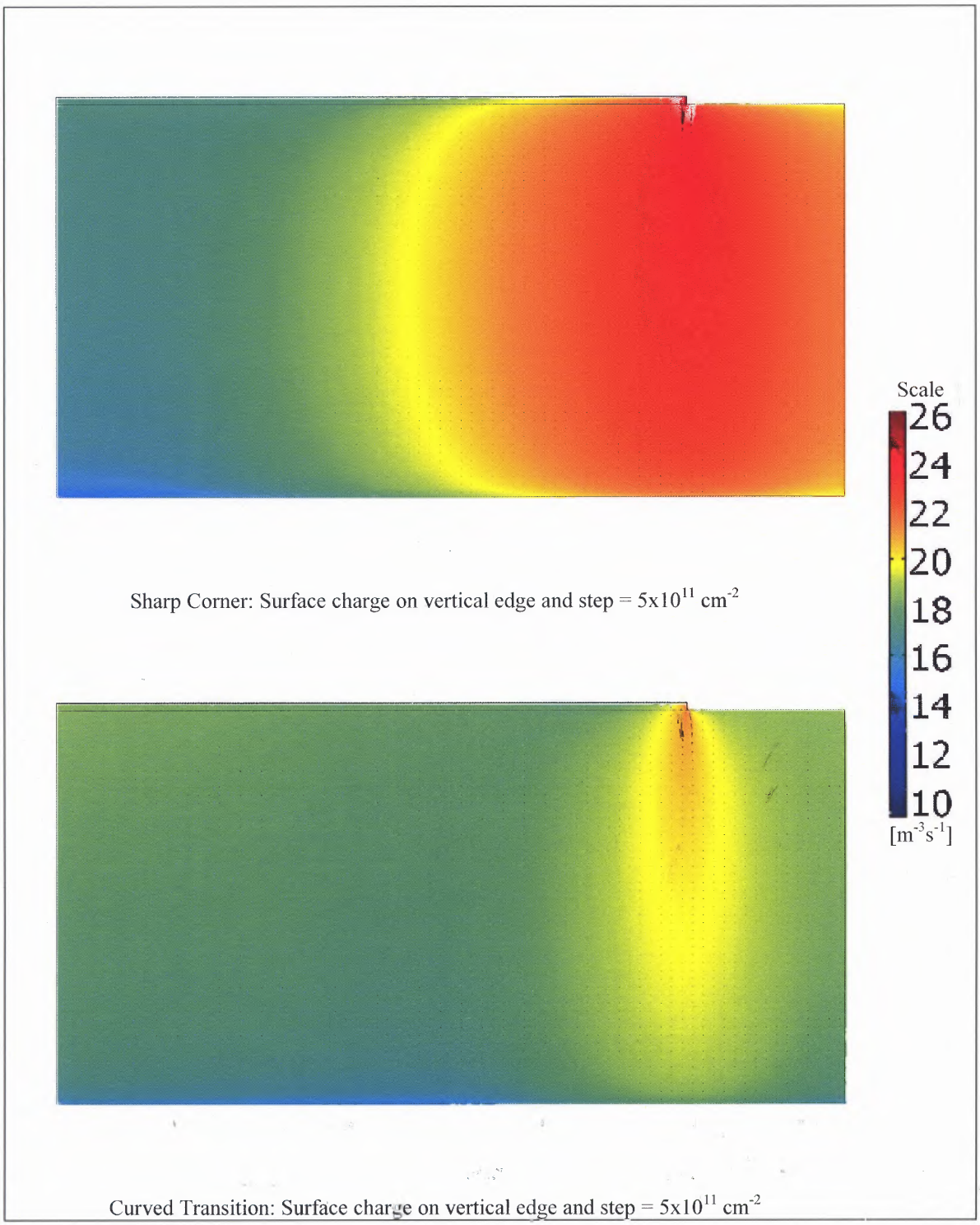

Figure 4.19 Comparison of bulk recombination rate and electric field at 0.1 volts forward bias for a mesa diode with sharp and curved corners with a surface charge of $5x10^{11}$ cm^{-2} under dark conditions.

The bulk recombination rate and electric field for simulations with the vertical edge and step surface charges of $3x10^{11}$ cm^{-2} and $5x10^{11}$ cm^{-2} are shown for sharp and curved corners in Figure 4.18 and Figure 4.19, respectively. For both cases, there is a significant reduction in bulk recombination rate at the mesa's edge. Figure 4.20 and Figure 4.21 are close-ups of the edge region of the simulations shown in Figure 4.18 and Figure 4.19.

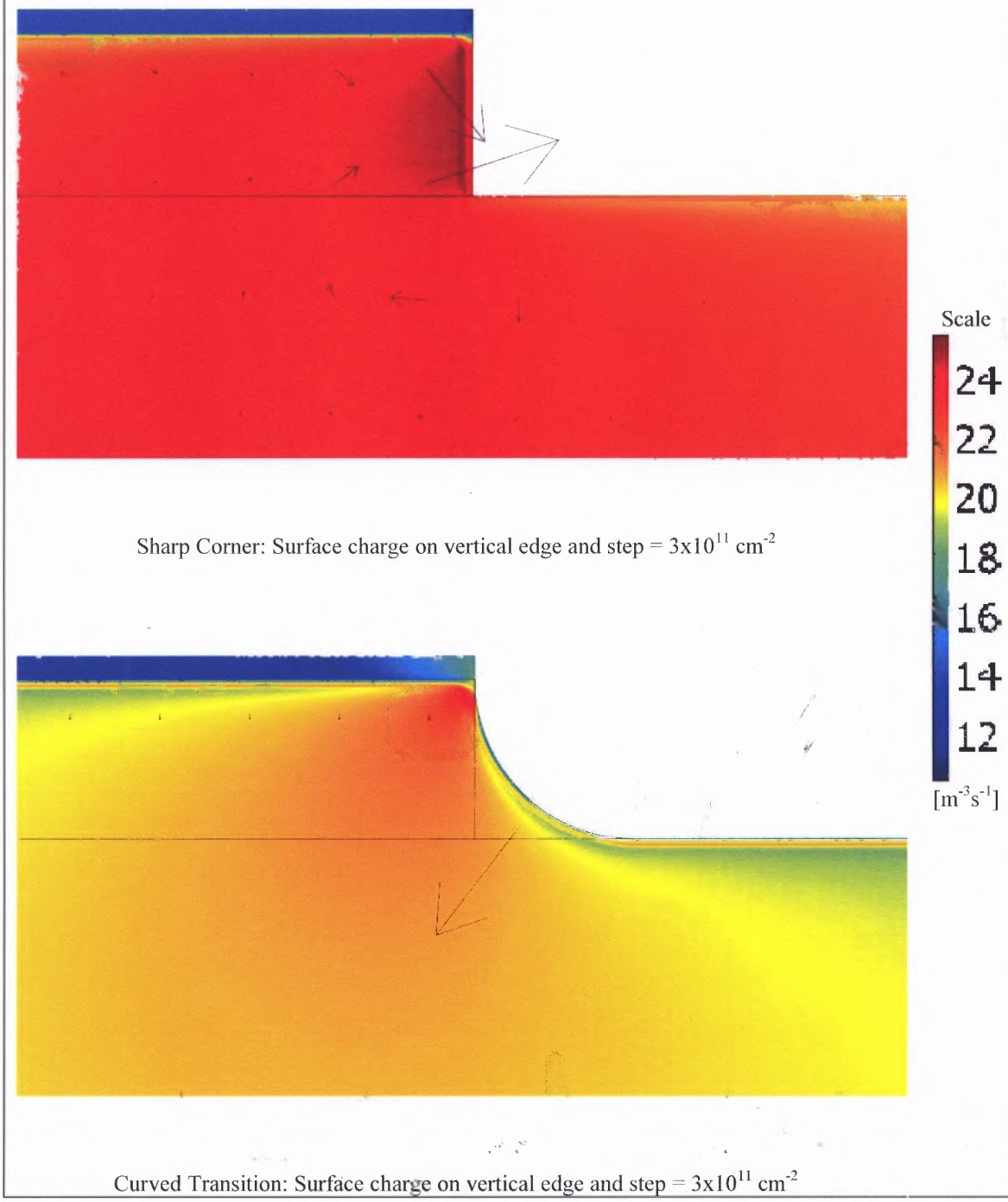

Figure 4.20 Close-up of bulk recombination rate and electric field at 0.1 volts forward bias for a mesa diode with sharp and curved corners with a surface charge of $3x10^{11}$ cm^{-2} under dark conditions (20 μm wide x 10 μm high).

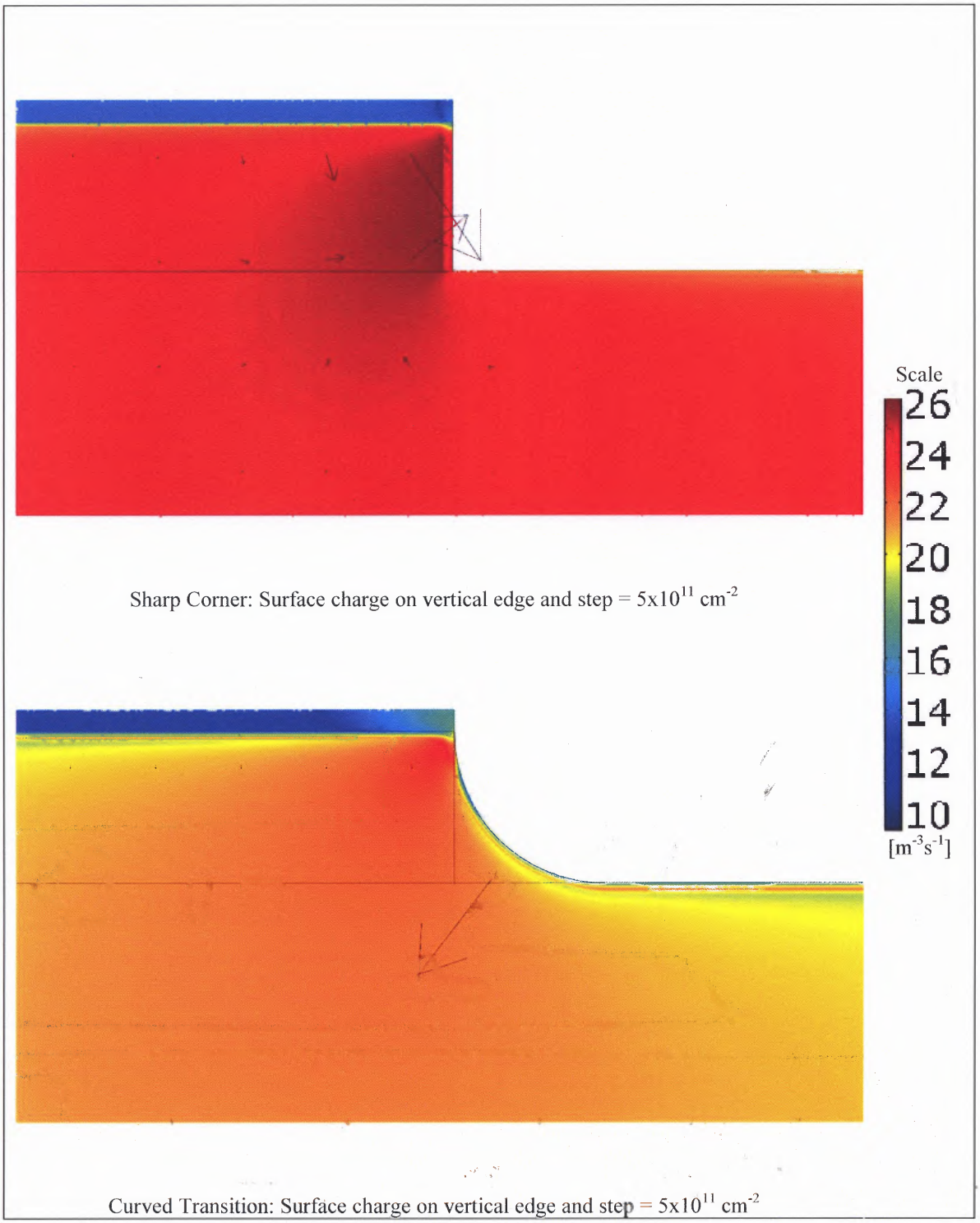

Figure 4.21 Close-up of bulk recombination rate and electric field at 0.1 volts forward bias for a mesa diode with sharp and curved corners with a surface charge of $5x10^{11}$ cm^{-2} under dark conditions (20 μm wide x 10 μm high).

The addition of a curved piece at the mesa's edge clearly reduces the bulk recombination rate in this region. However, the curved piece has a smaller radius of curvature than the flat continuous sections away from it. Therefore, even with an additional curved piece, the bulk recombination rate and electric field in this region are greater than the rest of the device except for the junction where they are almost equal. Consequently, the results of the dark simulations of the mesa diode indicate that the distortion of the electric field at the corner of the junction and the vertical edge, and the step and the vertical edge in conjunction with the inversion layer on the p-side adjacent to the junction, results in an extension of the space charge region deep into the bulk of the device. This leads to an increase in the recombination rate and the dark current, particularly at low forward biases.

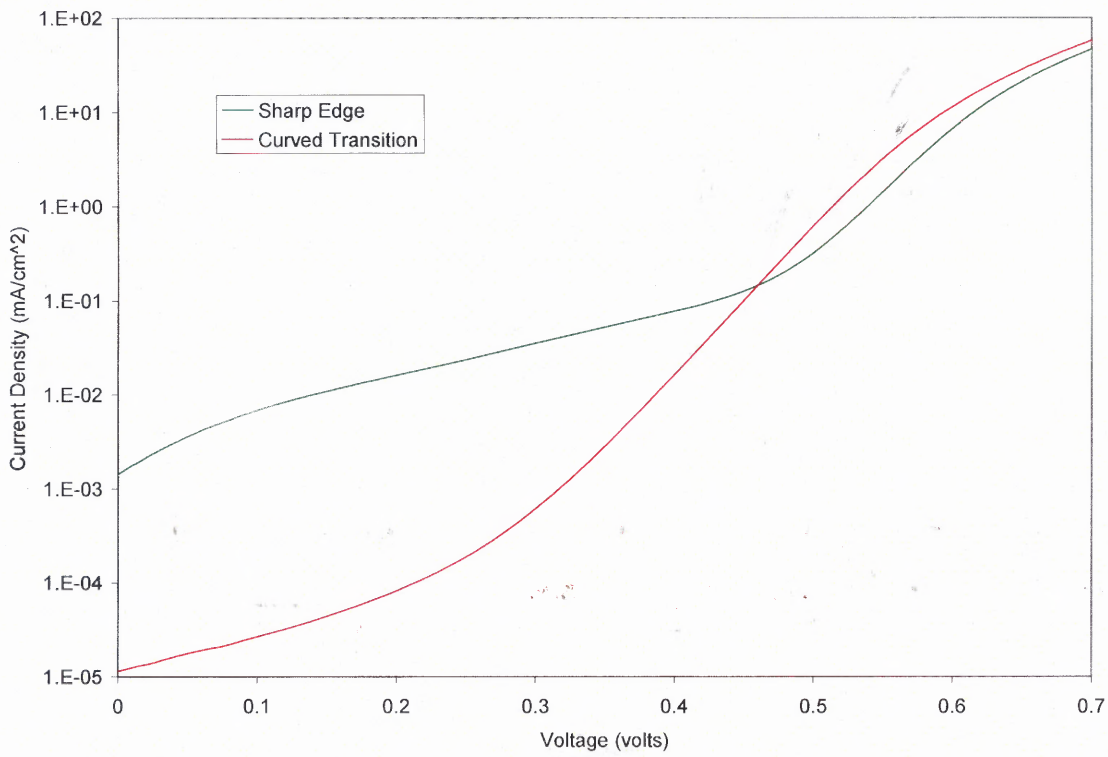

Figure 4.22 Current density vs. voltage plots of the comparison of sharp and curved corner between the step and the vertical lines with a surface charge of $3x10^{11}$ cm^{-2} under dark conditions.

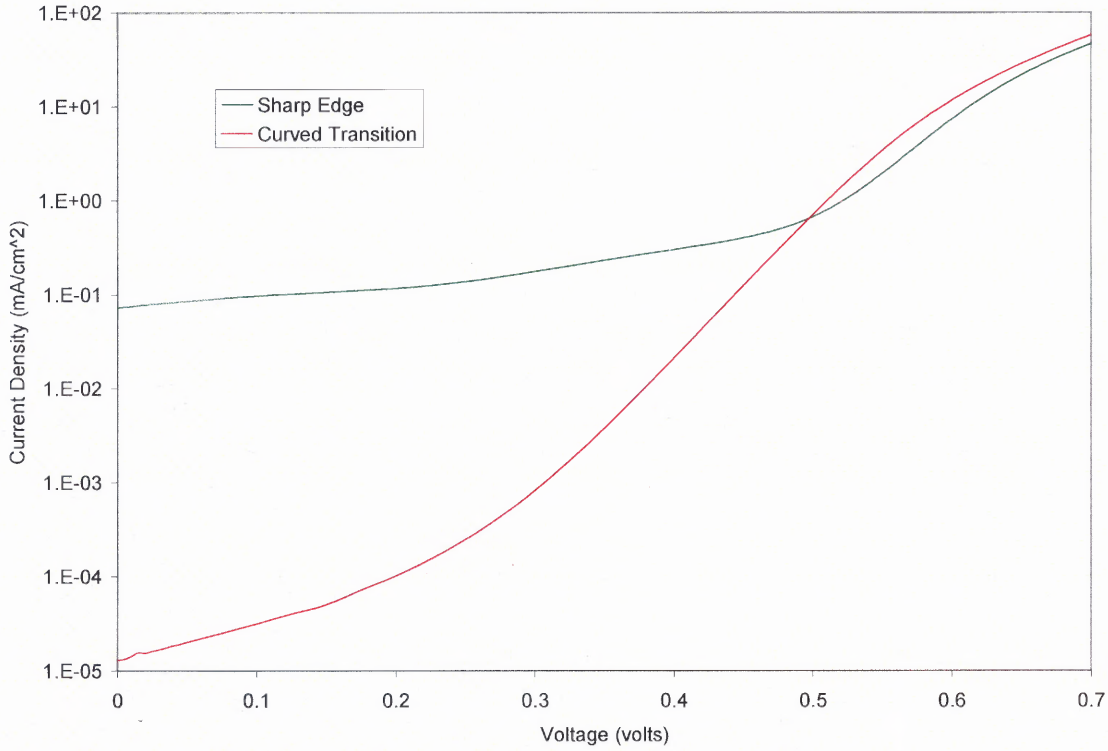

Figure 4.23 Current density vs. voltage plots of the comparison of sharp and curved corner between the step and the vertical lines with a surface charge of $5x10^{11}$ cm^{-2} under dark conditions.

A comparison of the dark current density vs. voltage for sharp and curved corners is shown in Figure 4.22 and Figure 4.23, for surface charges of $3x10^{11}$ cm^{-2} and $5x10^{11}$ cm^{-2}, respectively. By increasing the radius of curvature of corner at the step and vertical edge, the resistive shunting caused by excessive bulk recombination can be significantly reduced. For a surface charge of $3x10^{11}$ cm^{-2}, there is a reduction of dark current density by two orders of magnitude at low forward biases, and for a surface charge of $5x10^{11}$ cm^{-2}, there is a reduction of dark current density of almost four orders of magnitude at low forward biases. Figure 4.22 and Figure 4.23 also show that the dark current density is lower for a sharp corner at higher forward biases. Specifically, for a surface charge of

$3x10^{11}$ cm^{-2}, the dark current density is lower for the simulation with a sharp corner at forward biases greater than 0.45 volts and greater than 0.5 volts when the surface charge is $5x10^{11}$ cm^{-2}. This occurs because the simulations performed with a sharp corner are dominated by space charge recombination as shown in Figure 4.16. Since the space charge recombination dominates the operation of the device because of the increase in the electric field and the inversion layer on the p-side of the junction at the mesa's edge, additional electric potential is required to make the operation of the rest of mesa diode, away from the edge, have the same recombination rate and operating conditions as the edge. This moves the onset of the operation of the mesa diode that is dominated by diffusion current to a higher forward bias.

Simulations of the mesa diode were also performed on a model of the mesa diode under illuminated conditions, in which the vertical edge surface charge was changed from $1x10^{11}$ cm^{-2} to $5x10^{11}$ cm^{-2}. The resulting illuminated current density vs. voltage curves are shown in Figure 4.24. The behavior has a similar pattern to what was simulated for the mesa diode modeled under dark conditions.

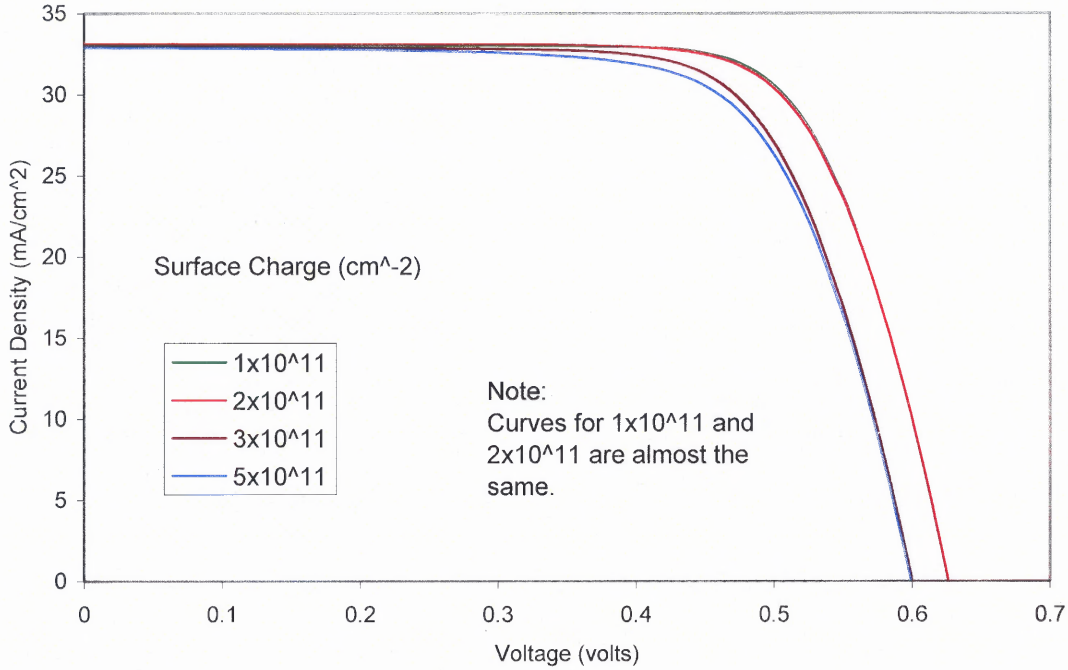

Figure 4.24 Illuminated current density vs. voltage for the mesa diode at different vertical edge charges.

The open circuit voltage and fill factor become reduced as the vertical edge surface charge is increased from $1x10^{11}$ cm^{-2} to $5x10^{11}$ cm^{-2}. The reduction in open circuit voltage and fill factor is not as dramatic as the increase in dark current density vs. voltage because of two factors. One is there are significantly more excess electrons and holes when the mesa diode is simulated under illuminated conditions. Therefore, any additional recombination effects from a sharp corner can be compensated by additional free carriers. The other is recombination current occurs typically for low forward biases, but the open circuit voltage is more dominated by diffusion currents and the fill factor value typically occurs near the transition region from recombination to diffusion current. Nevertheless the loss in V_{oc} and FF are significant and the mechanism that causes them as

the charge increases is a result of increased recombination due to the increased electric field caused by the sharp corner at the edge of the mesa.

In order to determine if the sharp corner at the edge of mesa was the cause of the reduction in open circuit voltage and fill factor, simulations under illumination were performed with a curved piece at the corner of the vertical edge and the step. It had exactly the same dimensions as the one used for the dark simulations. Also, the simulations using a sharp corner were repeated with the surface charge of the vertical edge and the step set to the same value, as shown in Figure 4.17. Plotting the bulk recombination and electric field of any of the simulations shown in Figure 4.24 over the entire mesa diode does not readily reveal the cause of the reduction in V_{oc} and FF, as it does for the increase in the dark current density as shown in Figure 4.16. However, a close-up of the bulk recombination rate and electric field at the mesa's edge shows a noticeable difference, which accounts for the reduced V_{oc} and FF. Figure 4.25 and Figure 4.26 show the bulk recombination rate and electric field at the mesa's edge under illumination with a forward bias of 0.45 volts for surface charges of $3x10^{11}$ cm^{-2} and $5x10^{11}$ cm^{-2} on the vertical edge and curved transition and the step, respectively. For both surface charges, the simulation with the curved transition has a recombination rate one order of magnitude less than the simulation with a sharp corner. Also, the electric field for the simulations performed with the curved transition is more uniform than the simulations with the sharp corner. Furthermore, the electric field for the simulations with the sharp corner is highly distorted and is strongest near the intersection between the vertical edge and the step. This distortion and increased level of the electric field at the sharp corner accounts for the reduction in the open circuit voltage and fill factor.

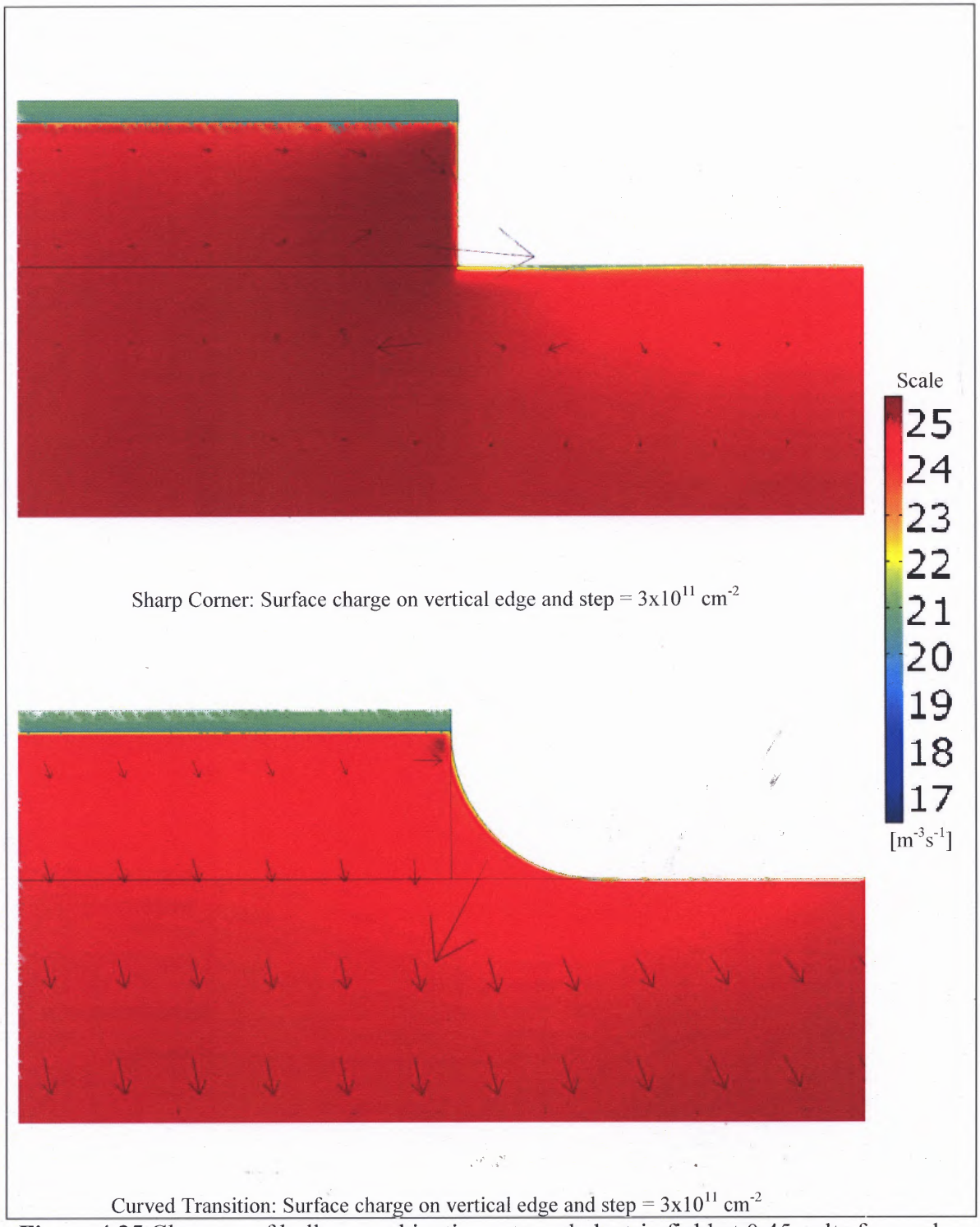

Figure 4.25 Close-up of bulk recombination rate and electric field at 0.45 volts forward bias for a mesa diode with sharp and curved corners with a surface charge of $3x10^{11}$ cm^{-2} under illuminated conditions (20 μm wide x 10 μm high).

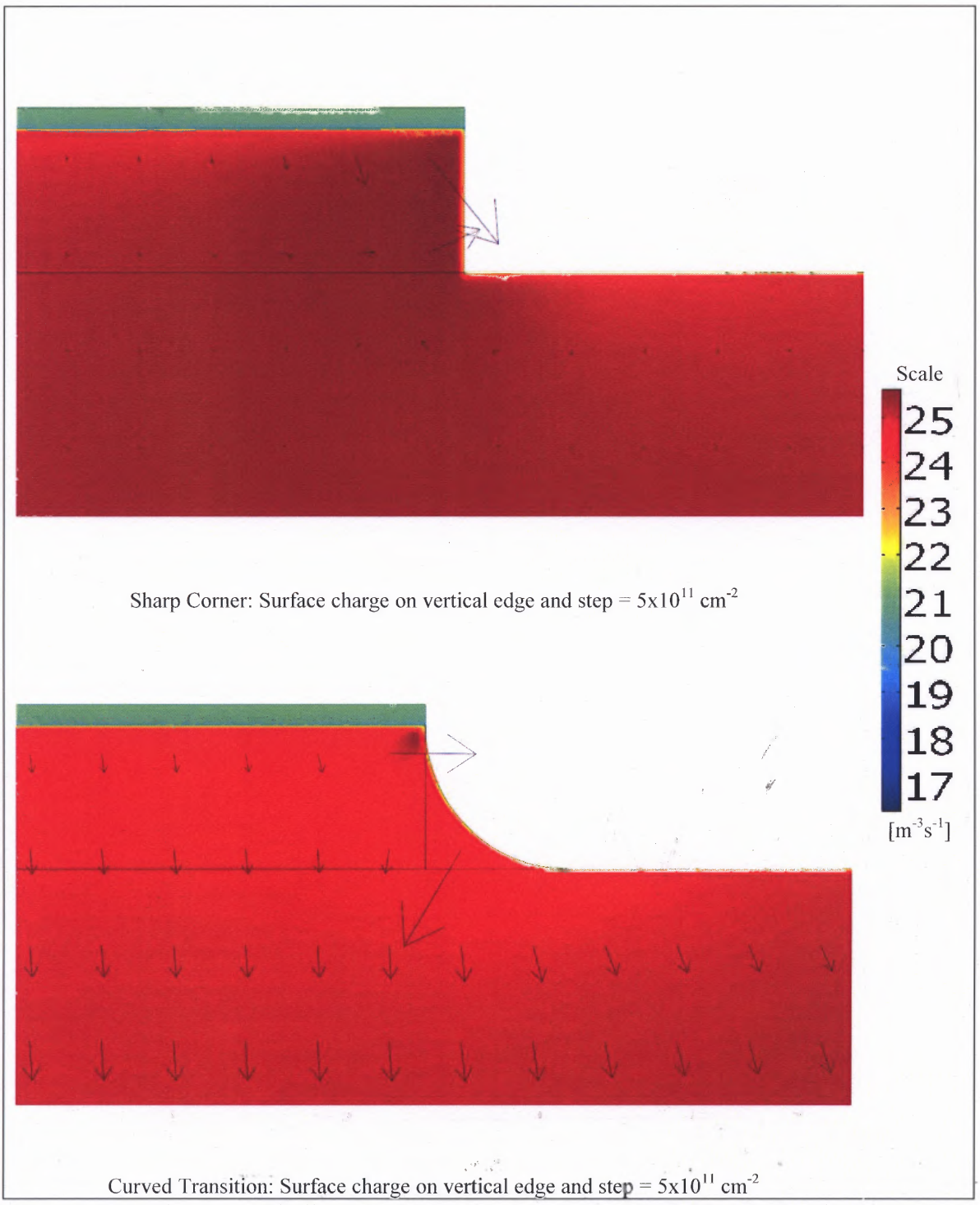

Figure 4.26 Close-up of bulk recombination rate and electric field at 0.45 volts forward bias for a mesa diode with sharp and curved corners with a surface charge of $5x10^{11}$ cm^{-2} under illuminated conditions (20 μm wide x 10 μm high).

The illuminated current density vs. voltage plots for simulations performed with a sharp corner and a curved transition with surface charges of $3x10^{11}$ cm^{-2} and $5x10^{11}$ cm^{-2} are shown in Figure 4.27 and Figure 4.28, respectively.

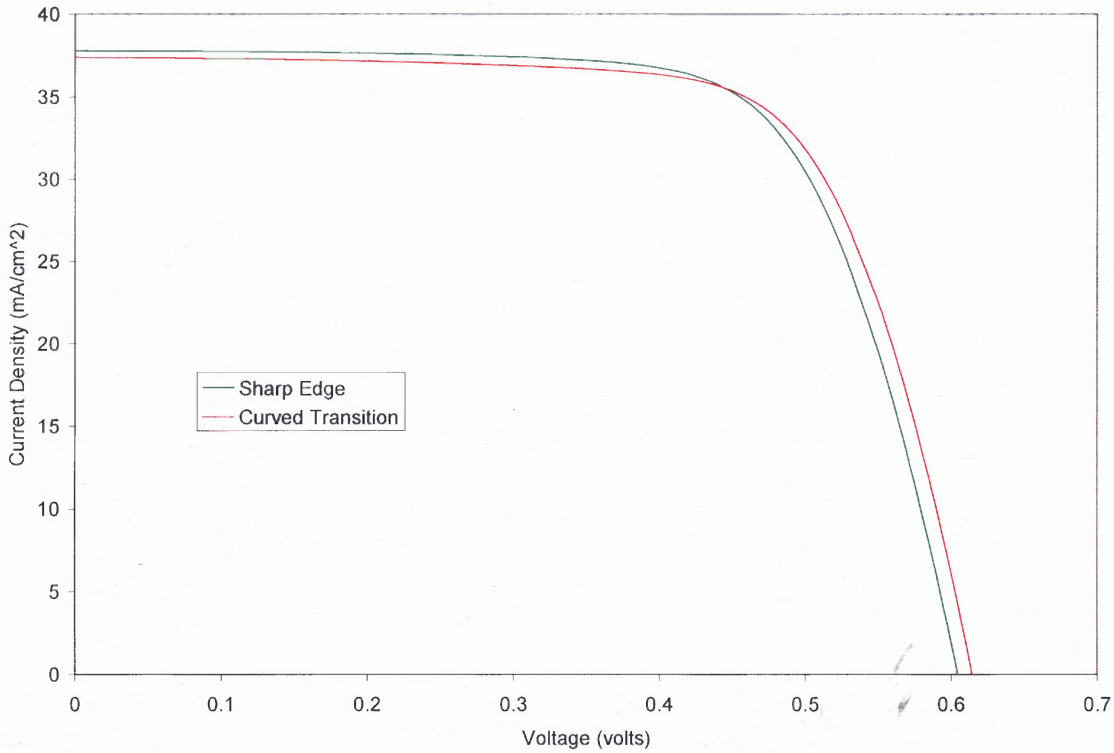

Figure 4.27 Current density vs. voltage plots of the comparison of sharp and curved corner between the step and the vertical lines with a surface charge of $3x10^{11}$ cm^{-2} under illuminated conditions.

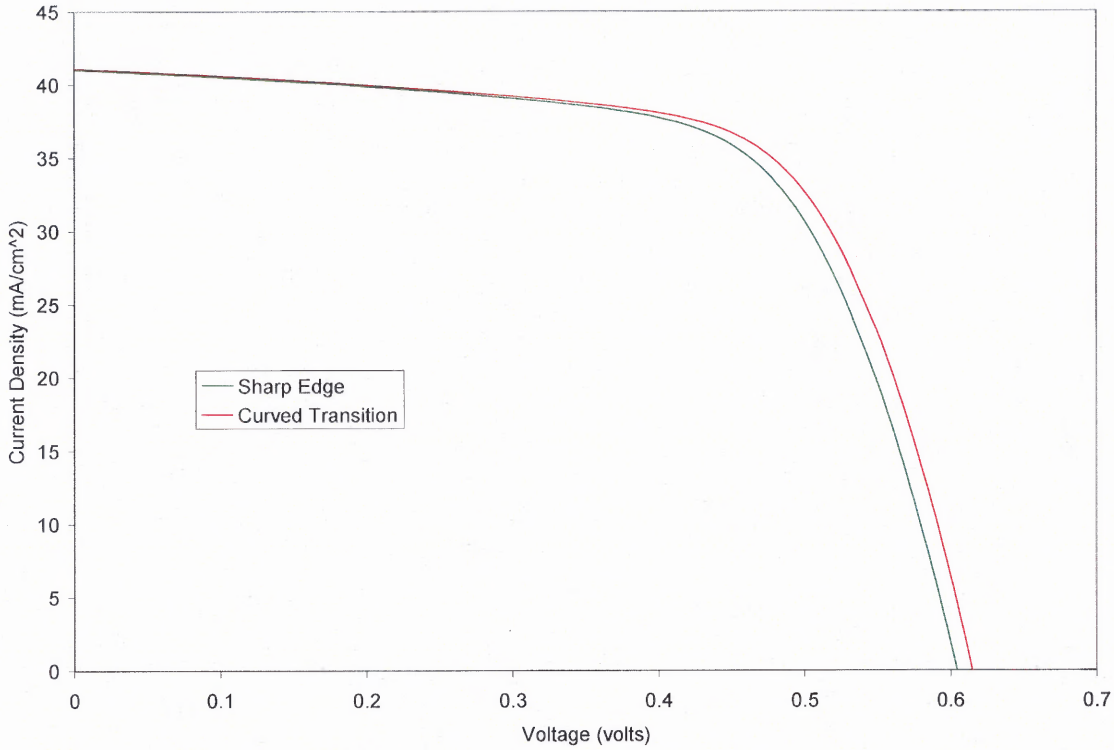

Figure 4.28 Current density vs. voltage plots of the comparison of sharp and curved corner between the step and the vertical lines with a surface charge of $5x10^{11}$ cm^{-2} under illuminated conditions.

For both surface charges, the simulations with a curved transition show that the open circuit voltage and fill factor improve. This occurs because there is a lower recombination rate in the mesa diodes modeled with a curved transition as shown in Figure 4.25 and Figure 4.26. It should be noted that the short – circuit current (J_{sc}) values for the simulations shown in Figure 4.27 and Figure 4.28 are significantly greater than the J_{sc} values shown in Figure 4.24 because the surface charge was increased on the step adjacent to the mesa's edge. This results in an inverted surface, which significantly reduces the recombination rate in this region, and consequently leads to an improved J_{sc} value.

4.4 Confirmation of a Tapered Edge of a Mesa Diode

Based on the simulations of the mesa diode presented in the previous section, if the edge of the diode forms a sharp corner during the etching process, the resulting diode will have severe resistive shunting primarily due to a high point in the electric field at the corner, which propagates the space charge region into a large portion of the bulk device. It was also shown in the previous section that modeling the mesa diode with a curved transition from the vertical edge to the step significantly improves the performance of the device under dark and illuminated conditions. Therefore, it would be useful to confirm that this transition is tapered. Figure 4.29 is a current density vs. voltage measurement of mesa diode made on single crystal silicon wafer with a shallow junction, a front contact dot, a continuous back contact, and no antireflective coating. In comparison to the dark plots

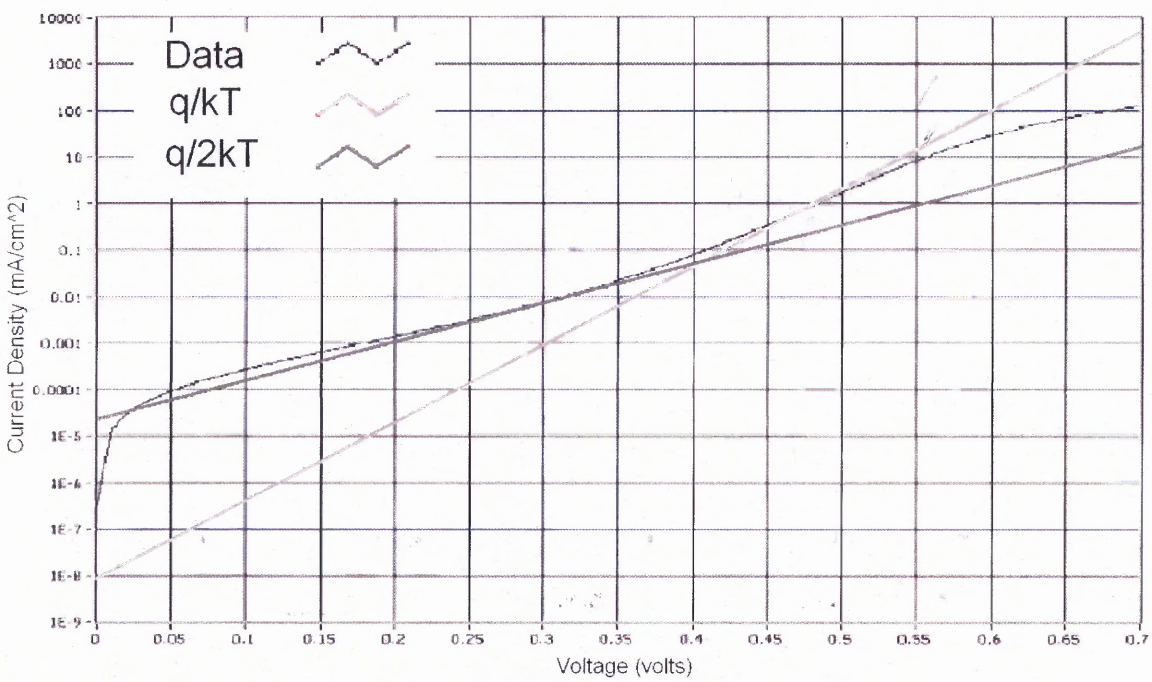

Figure 4.29 Dark J-V measurements of a mesa diode (single crystal silicon material).

for simulations made with a curved transition in Figure 4.22 and Figure 4.23, the measured data in Figure 4.29 is in very good agreement except at voltages greater than

0.65 volts, which is probably a result of additional resistance in the wires of the measurement setup. Although there is good agreement between the measured data of a single mesa diode, a more direct measurement would be more convincing. In Figure 4.30, PVSCAN [110] was used to make LBIC (Light Beam Induced Current) maps of a mesa diode using the 630 nm and 980 nm lasers. The 630 nm laser is used to scan the

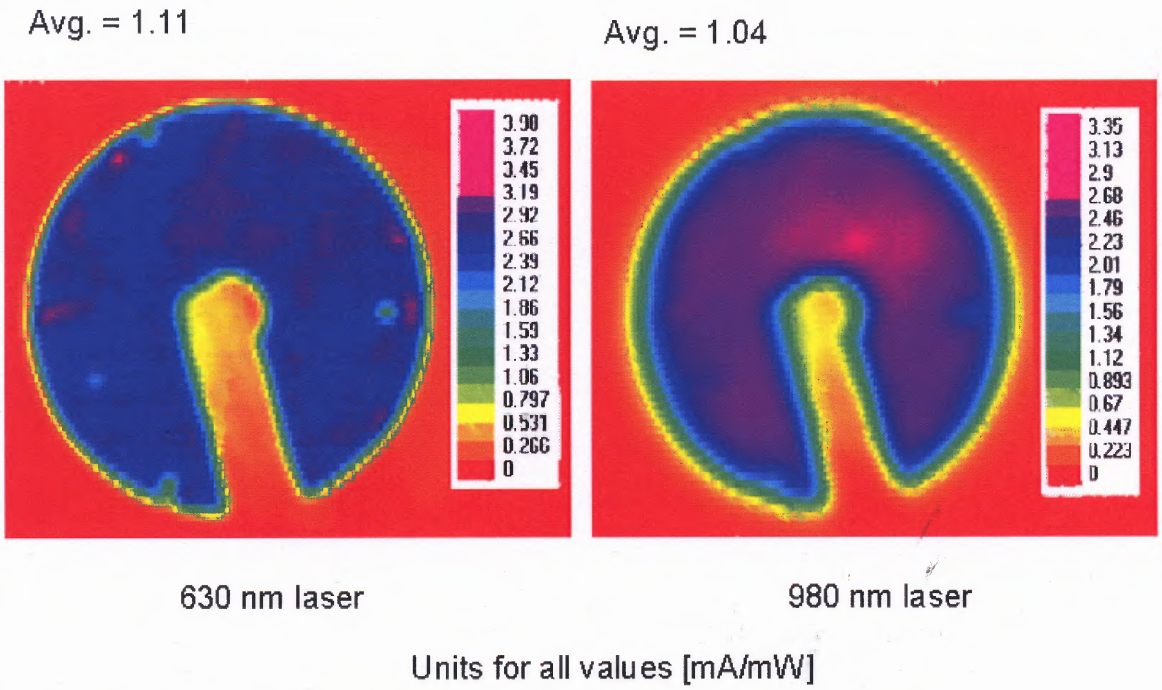

Figure 4.30 LBIC Maps of a mesa diode (single crystal silicon material).

surface, while the 980 nm laser is used to obtain measurements of the bulk. The LBIC scan resolution is approximately 10 μm. In both scans there is less current generated around the perimeter of the device, but it significantly greater than the surrounding area. In the 980 nm laser bulk scan, the perimeter region goes through a wide range of current generation over a distance of at least 10 μm. This strongly suggests that the vertical edge of mesa diodes is tapered. In addition, it is known that wet chemical etching such as the type used to delineate the mesa diode arrays does not form vertically abrupt perpendicular interfaces, but sloping ones that are dependent on the type of etch and the

crystallographic orientation of the silicon that is being etched [111]. Based on the experimental data in this section and literature regarding wet chemical etching of silicon, the vertical edge is most likely tapered. Furthermore, previous studies using these devices [45, 61] could not have been performed if the vertical edge was formed perpendicular to the step unless the surface charge was kept extremely low.

4.5 Summary

In this chapter, the physical model described in Chapter 3 was used to describe a small sample diode and the mesa diode used for characterization. The results of simulations, under dark and illumination, using the commercial finite element software package, COMSOL Multiphysics, were presented [95]. The performance of the model of the small sample diode and mesa diode can be significantly degraded because of detrimental edge effects resulting in additional space charge recombination. Simulations were also presented to reduce the additional recombination caused by edge effects in both the small sample diode and the mesa diode. Lastly, experimental measurements of real mesa diodes were presented to support the design of a tapered edge of a mesa diode. The following chapter will present the conclusions and recommendations for future work.

CHAPTER 5

CONCLUSIONS AND FUTURE WORK

5.1 Conclusions

The edge effects that occur in the simulation of the forward bias operation of a mesa diode are a unique combination of three established phenomena that can occur in the operation of a silicon based semiconductor device. First, the recombination of electrons and holes via bulk recombination centers and interface states at passivating surfaces has been thoroughly described in the literature and has been used in modeling recombination in silicon semiconductors for decades. The initial theoretical work of describing this mechanism was done by Shockley, Reed, and Hall [26, 27]. Second, surface depletion and inversion of the p type region adjacent to passivating layer such as an oxide has been known for decades and much of the initial work was done by Grove et al. at a time when MOS transistors were being developed [30, 31, 63]. Third, the electric field becomes very strong at sharp corners or regions that have a very small radius of curvature [109]. This work is fundamental to the understanding of electric fields and was initially developed by Charles Coulomb and Carl Friedrich Gauss well over a hundred years ago [112]. What is unique regarding the simulation of the operation of the mesa diode performed for this dissertation is how they come together to account for the edge effects during its operation.

According to the analyses of dark and illuminated simulations of the model of the mesa diode, the increase in the vertical edge surface charge results in an increase of the recombination rate, which increases the dark current density versus voltage and reduces the open circuit voltage and fill factor under illumination. In a silicon based

semiconductor device recombination via recombination centers is the dominant bulk mechanism and recombination via interface states is the dominant surface mechanism. An n-p junction that borders on a passivating surface with a fixed positive charge will cause the region adjacent to the p-side of the junction to become depleted or inverted depending on the interface charge and the base doping. Using a passivating material with a positive charge that is high enough to cause strong inversion can significantly reduce the bulk and surface recombination rates as long as the space charge region does not extend to a metallic contact. This was detailed in the analyses of the simulations of a small sample diode in Chapter 4. It was shown that using a more highly doped region next to the back metal contact prevents the extension of the space charge region through the inversion layer from reaching the back metal contact. The results of the simulations performed with a back surface field matched those performed by Kuhn et al. [105].

Unlike the mechanism in the small sample diode without a back surface field, in which the connection of the space charge region to the back metal contact results in resistive shunting, the geometric features of the edge of the mesa diode can significantly distort the electric field throughout a large portion of the bulk device. Specifically, there are two significant changes in geometry that cause the electric field to become distorted. One location is at the intersection between the junction and vertical edge of the mesa. This results in a concave concentration of the electric field in this region. The other location is the intersection of the vertical edge and the step. This is the most important geometric feature because "the electric field is large near points having a convex radius of curvature and reaches very high values at sharp points [109]." In certain cases, the distortion can expand the space charge region over hundreds of microns in all directions

emanating from the edge. It was shown that changing the interface from a sharp perpendicular step to a Bezier curve can greatly reduce the dark current density and increase the open circuit voltage and fill factor. Even with a curved interface at the vertical edge and step, the edge effect is a significant source of recombination in the mesa diode, in which the recombination rate can be more than two orders of magnitude greater than the rest of the bulk and this region can extend approximately 100 μm into the device from the curved interface. Therefore, the edge effect in a mesa diode is a result of the space charge region extending along the vertical edge because of the inverted region on the p-side of the junction, then expanding deep into the bulk device because of the strong electric field at the intersection of the vertical edge and the step. This results in a significant increase in recombination rate throughout the device, an increase in dark current density, and a reduction in open circuit voltage and fill factor under illumination. Experimental measurements show that the intersection of the vertical edge and step is a slope or curved interface rather than a sharp perpendicular interface. This greatly minimizes the edge effect and allows mesa diodes to be used for crystalline silicon solar cell characterization. It also means that any process used to make a mesa diode array should avoid producing sharp corners at the step.

5.2 Future Work

The following is a list of additional work that will help develop a better understanding of the edge effects in a silicon mesa diode:

- It was determined from the simulations of a small sample diode that using a higher doped p^+ region adjacent to a positively charged passivated layer prevents

that surface from becoming depleted or inverted. This led to a reduction in the recombination rate in the bulk and surface, and ultimately produced the best performance for the highest surface charges. It would be useful to model a mesa diode with either a sharp edge or curved transition with a thin p^+ adjacent to the vertical edge and step. If this prevents inversion of the surface in this region, a strong electric field may not develop, thereby minimizing the extension of the space charge region into the bulk.

- The curve used in the simulations was implemented because it was a reasonable estimate of a curved profile and its purpose was to show that the intersection between the vertical edge and the step produces a high point in the electric field when the surface is inverted, which ultimately leads to increased bulk recombination. However, during isotropic etching, the curved section actually removes part of the junction and the curve goes through the n-type layer. A more accurate curve would be shifted to the left and cut across the n-type layer. In addition to performing this calculation, various curve shapes at the edge of a mesa diode can be modeled to see if a further reduction in the edge effect could be achieved.
- There are a number of incremental improvements that could be made to the implementation of the model of the mesa diode in COMSOL Multiphysics. In particular, the following is a list of features that would improve the accuracy of the calculations:
    1. Use a graded junction with a Gaussian profile rather than a step junction.

2. Implement a graded back surface field with a Gaussian profile. Currently there is no back surface field in the model of the mesa diode.
3. Incorporate a function that defines mobility based on doping level. Currently mobility values for electrons and holes are based on a single value according to the doping of the n and p type regions.
4. Incorporate a function that defines mobility based on electric field.
5. Use a density of interface states rather a number of interface states when defining surface recombination rate.
6. Use a model of a metal contact that has a finite surface recombination velocity, rather than the idealized model that is currently used, which assumes infinite recombination at a metal contact.

APPENDIX

DETAILED ANALYSES OF A SMALL SAMPLE DIODE

This appendix contains the results of a series of simulations performed on the small sample diode described in Chapter 4. It contains four main simulations. They are the small sample diode operating under dark and illuminated conditions with and without a back surface field. Surface plots of bulk recombination rate, electron concentration, hole concentration, and electric potential were made for all four cases at forward biases of 0.1 and 0.4 volts. Also, the electric field is shown as an arrow plot on top of the electric potential surface plots. At the end of this appendix are graphs of the surface recombination rate, surface electron concentration, and surface hole concentration for the edge of the small sample diode that was modeled with a surface charge and recombination as shown in Figure 4.1. All of the cases were simulated under six different surface charges. They are $5x10^{10}$ cm^{-2}, $1.25x10^{11}$ cm^{-2}, $1.75x10^{11}$ cm^{-2}, $2x10^{11}$ cm^{-2}, $3x10^{11}$ cm^{-2}, and $5x10^{11}$ cm^{-2}.

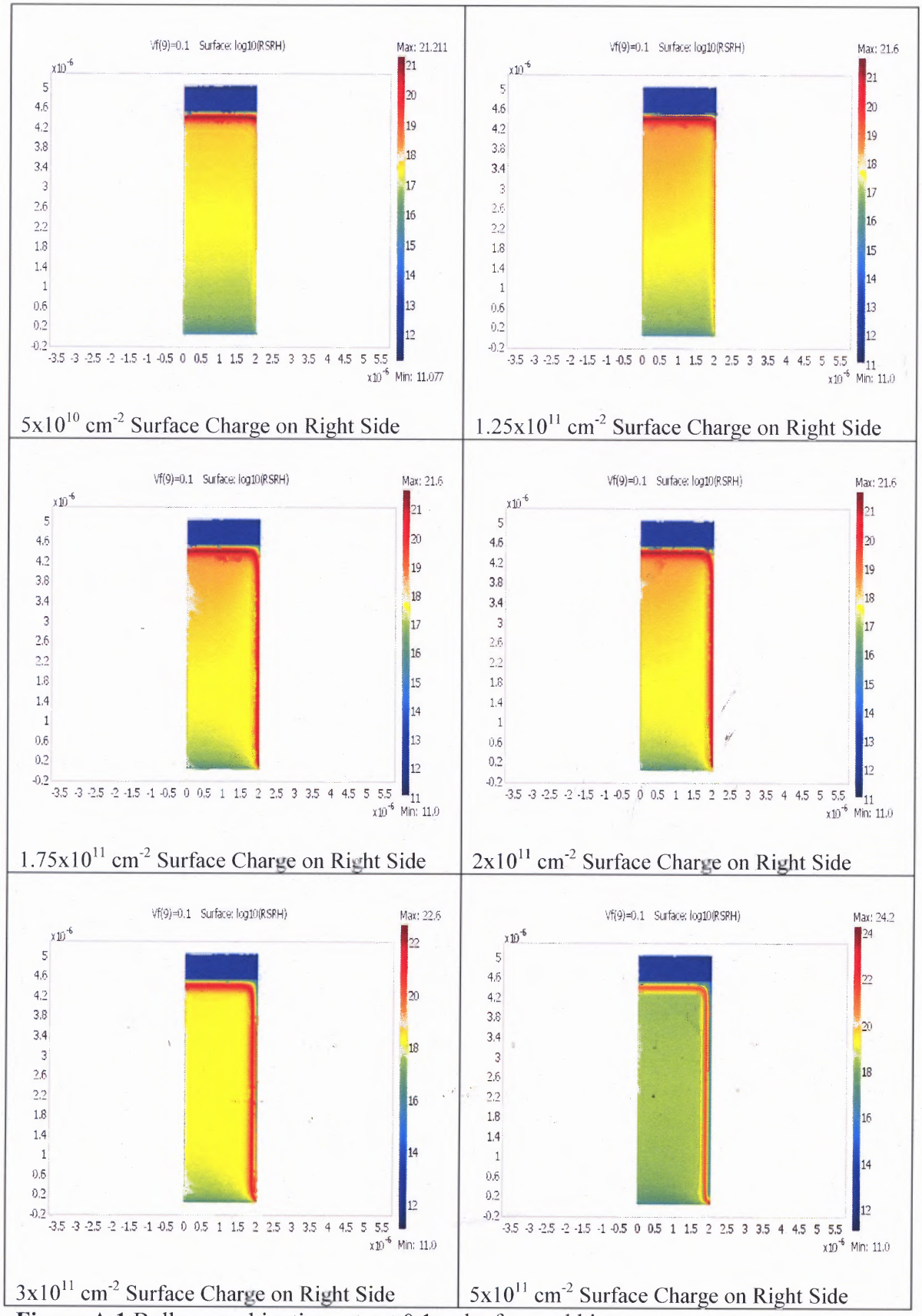

$5x10^{10}$ cm^{-2} Surface Charge on Right Side

$1.25x10^{11}$ cm^{-2} Surface Charge on Right Side

$1.75x10^{11}$ cm^{-2} Surface Charge on Right Side

$2x10^{11}$ cm^{-2} Surface Charge on Right Side

$3x10^{11}$ cm^{-2} Surface Charge on Right Side

$5x10^{11}$ cm^{-2} Surface Charge on Right Side

Figure A.1 Bulk recombination rate at 0.1 volts forward bias.

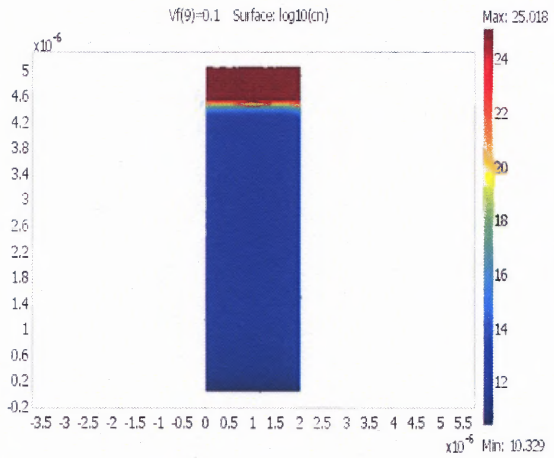

$5x10^{10}$ cm^{-2} Surface Charge on Right Side

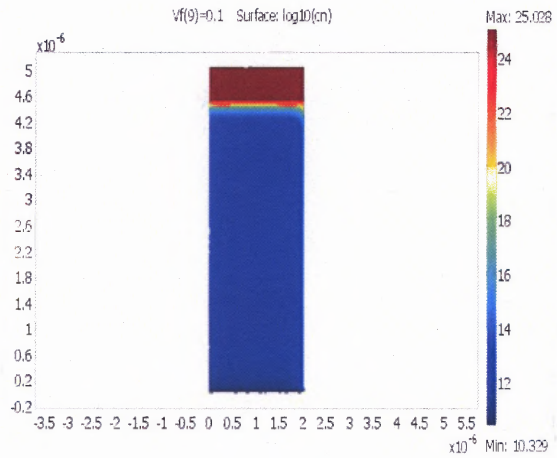

$1.25x10^{11}$ cm^{-2} Surface Charge on Right Side

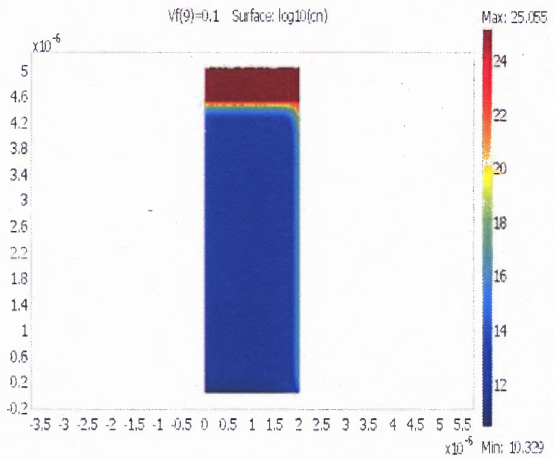

$1.75x10^{11}$ cm^{-2} Surface Charge on Right Side

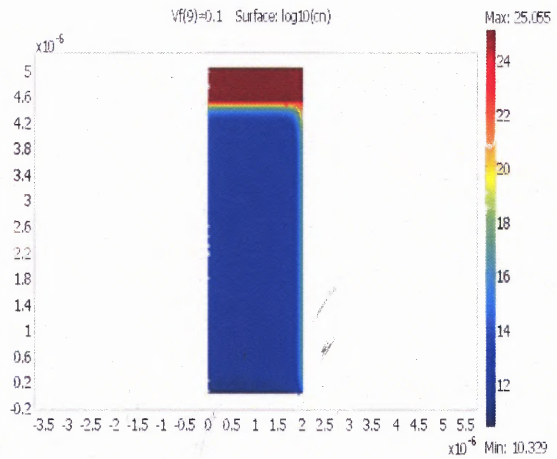

$2x10^{11}$ cm^{-2} Surface Charge on Right Side

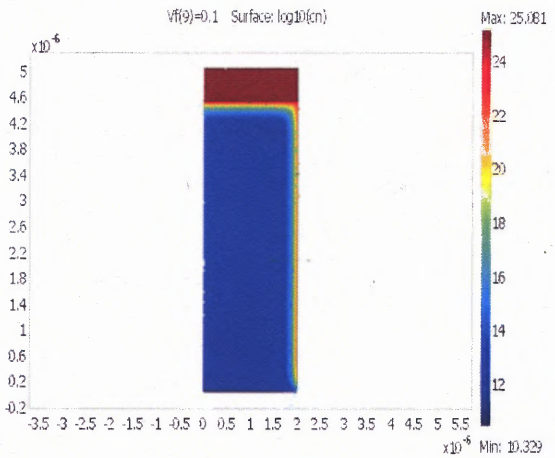

$3x10^{11}$ cm^{-2} Surface Charge on Right Side

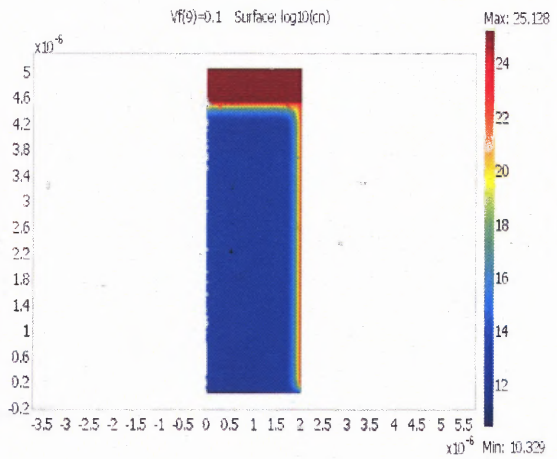

$5x10^{11}$ cm^{-2} Surface Charge on Right Side

Figure A.2 Electron concentration at 0.1 volts forward bias.

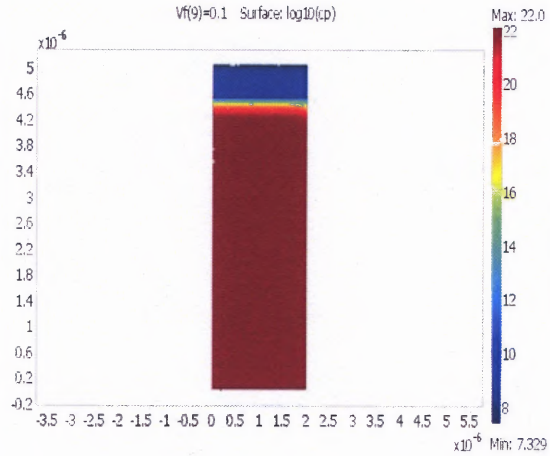

$5x10^{10}$ cm^{-2} Surface Charge on Right Side

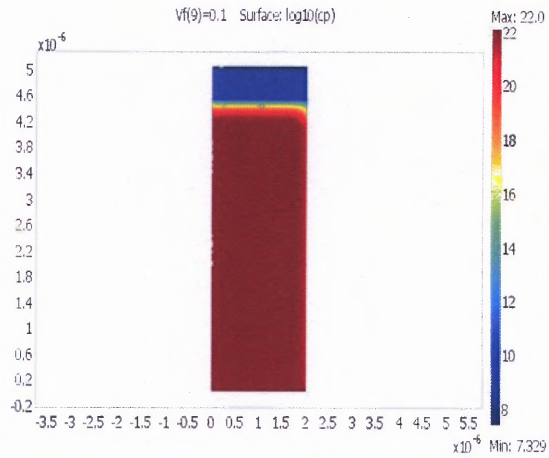

$1.25x10^{11}$ cm^{-2} Surface Charge on Right Side

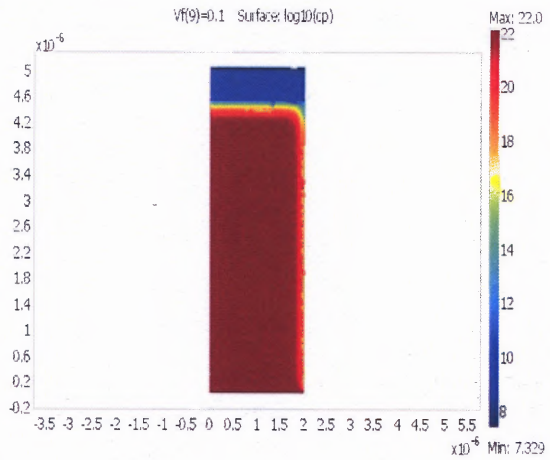

$1.75x10^{11}$ cm^{-2} Surface Charge on Right Side

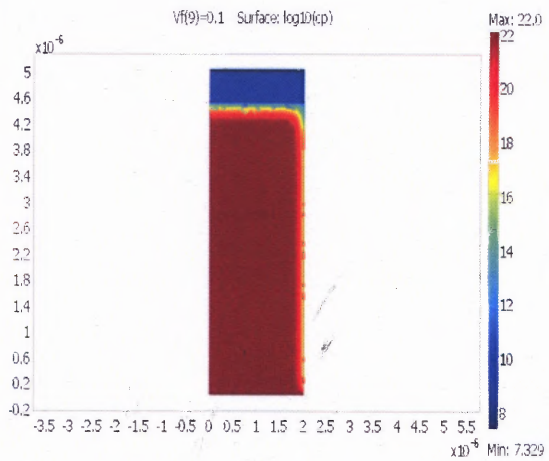

$2x10^{11}$ cm^{-2} Surface Charge on Right Side

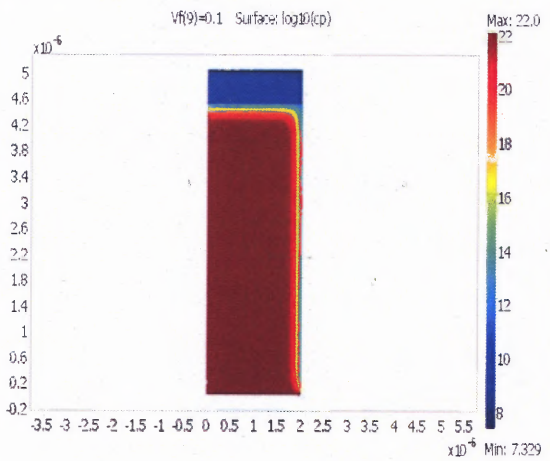

$3x10^{11}$ cm^{-2} Surface Charge on Right Side

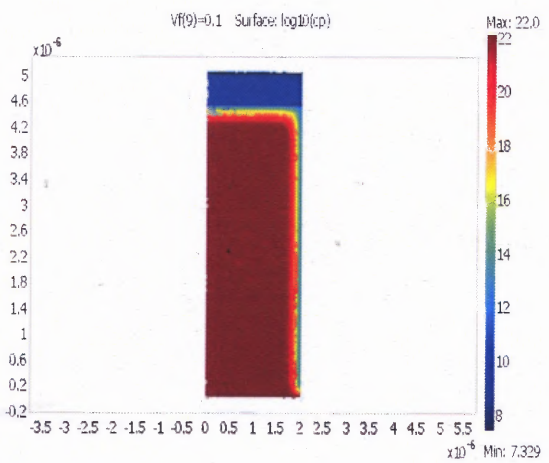

$5x10^{11}$ cm^{-2} Surface Charge on Right Side

Figure A.3 Hole concentration at 0.1 volts forward bias.

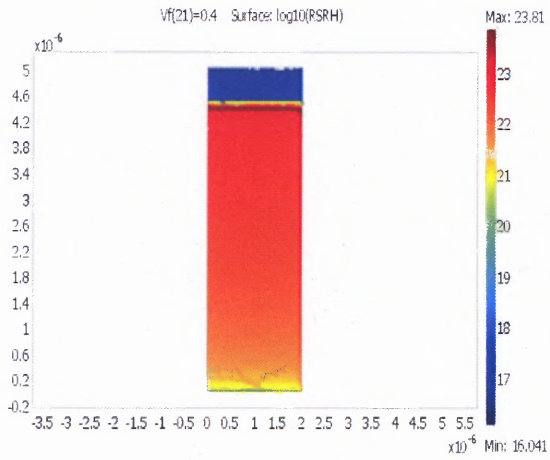

$5x10^{10}$ cm^{-2} Surface Charge on Right Side

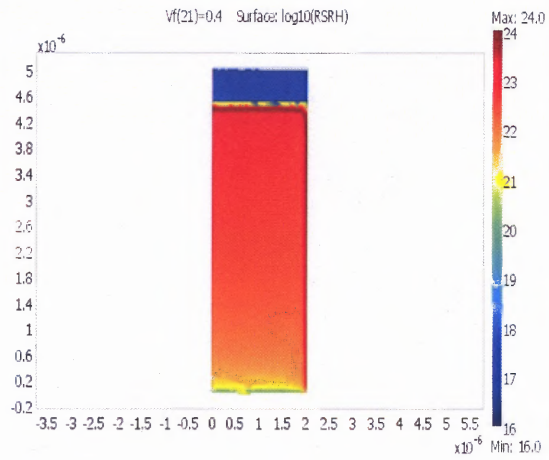

$1.25x10^{11}$ cm^{-2} Surface Charge on Right Side

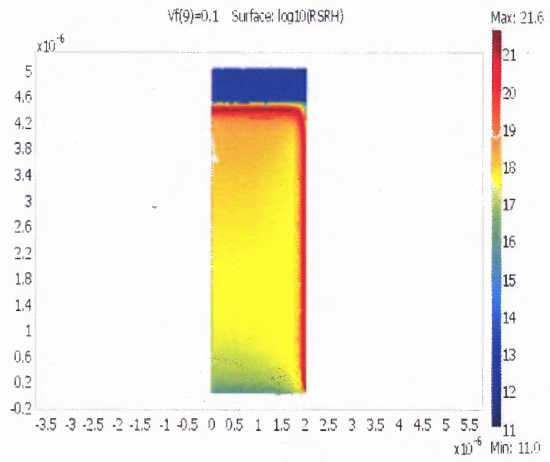

$1.75x10^{11}$ cm^{-2} Surface Charge on Right Side

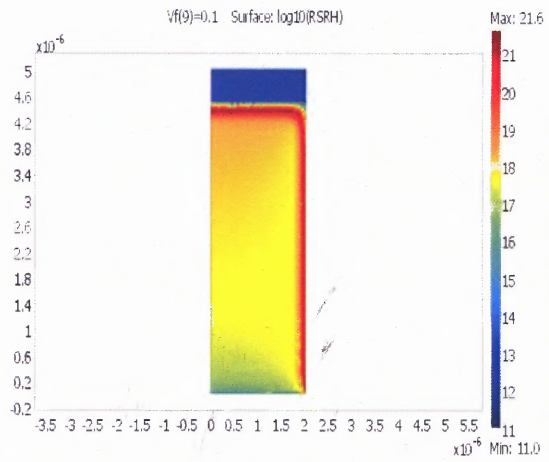

$2x10^{11}$ cm^{-2} Surface Charge on Right Side

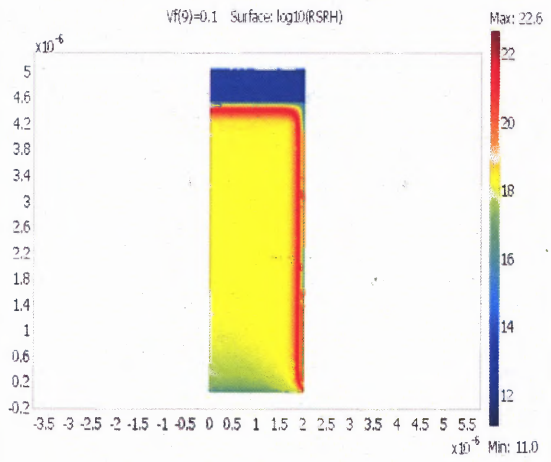

$3x10^{11}$ cm^{-2} Surface Charge on Right Side

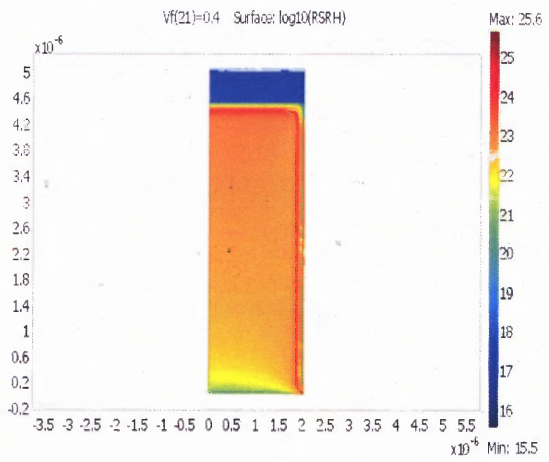

$5x10^{11}$ cm^{-2} Surface Charge on Right Side

Figure A.4 Bulk recombination rate at 0.4 volts forward bias.

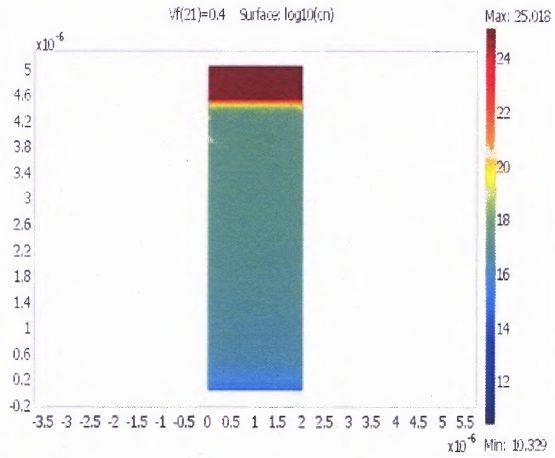

$5x10^{10}$ cm^{-2} Surface Charge on Right Side

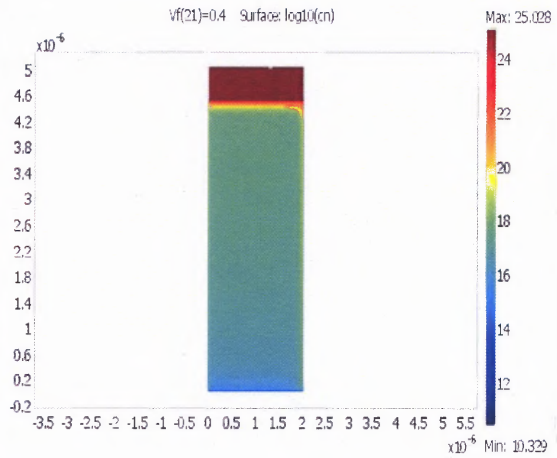

$1.25x10^{11}$ cm^{-2} Surface Charge on Right Side

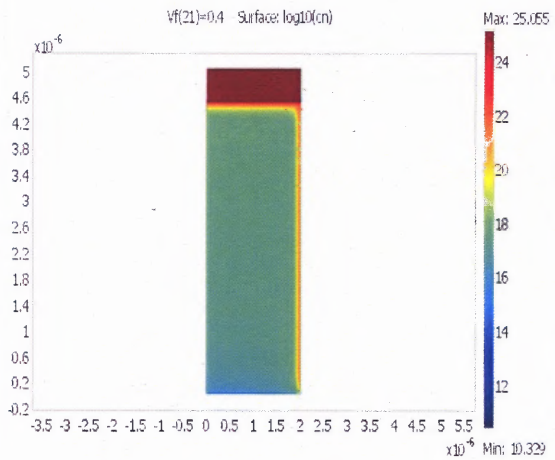

$1.75x10^{11}$ cm^{-2} Surface Charge on Right Side

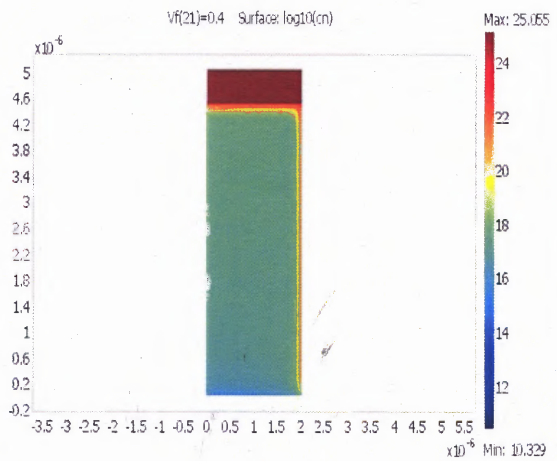

$2x10^{11}$ cm^{-2} Surface Charge on Right Side

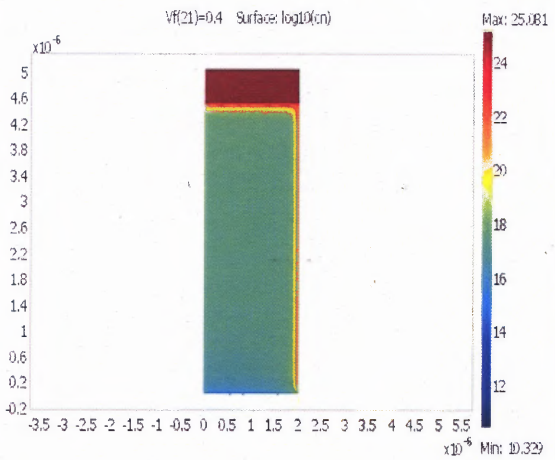

$3x10^{11}$ cm^{-2} Surface Charge on Right Side

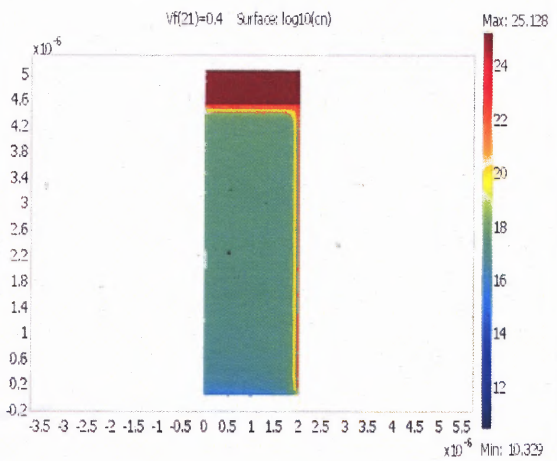

$5x10^{11}$ cm^{-2} Surface Charge on Right Side

Figure A.5 Electron concentration at 0.4 volts forward bias.

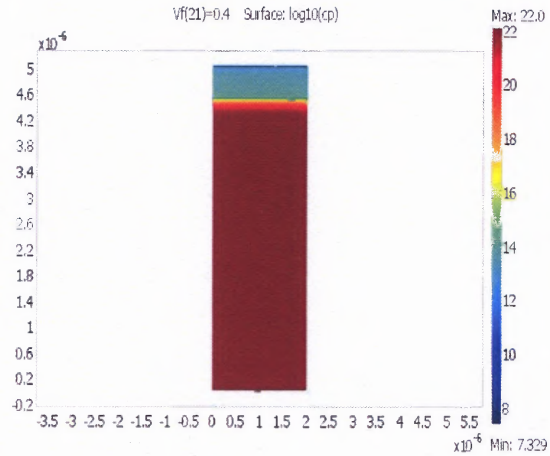

$5x10^{10}$ cm^{-2} Surface Charge on Right Side

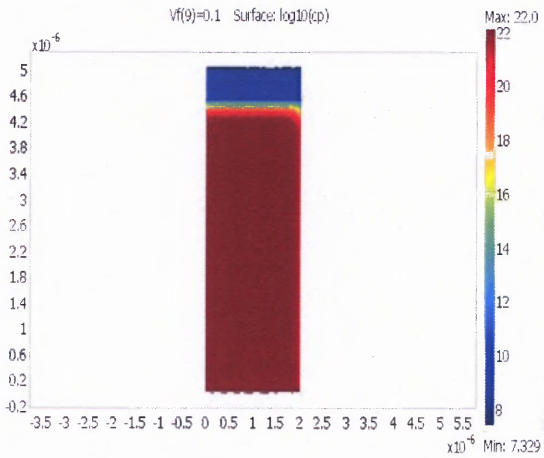

$1.25x10^{11}$ cm^{-2} Surface Charge on Right Side

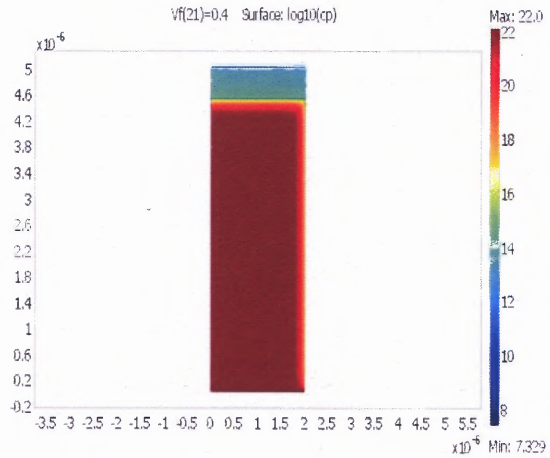

$1.75x10^{11}$ cm^{-2} Surface Charge on Right Side

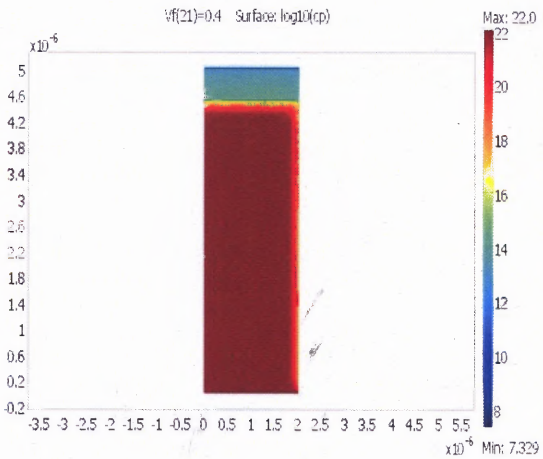

$2x10^{11}$ cm^{-2} Surface Charge on Right Side

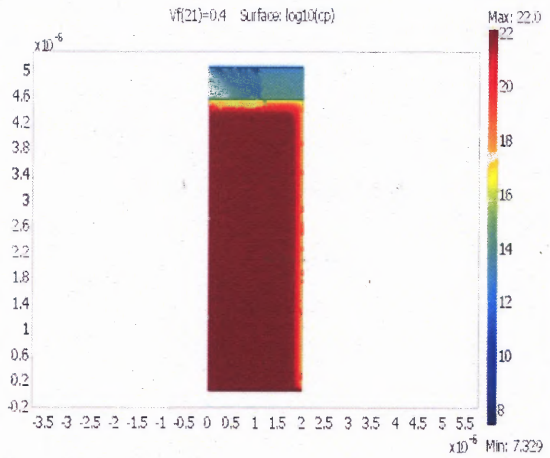

$3x10^{11}$ cm^{-2} Surface Charge on Right Side

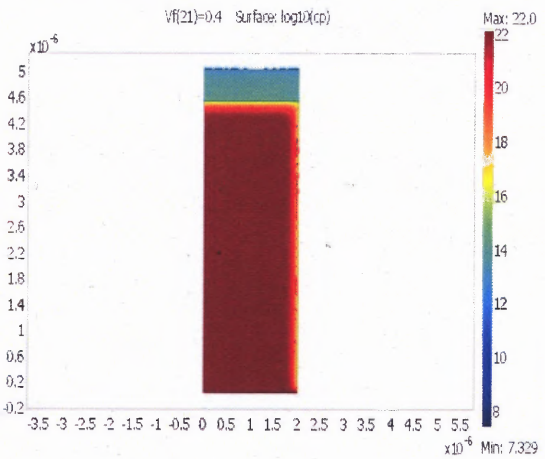

$5x10^{11}$ cm^{-2} Surface Charge on Right Side

Figure A.6 Hole concentration at 0.4 volts forward bias.

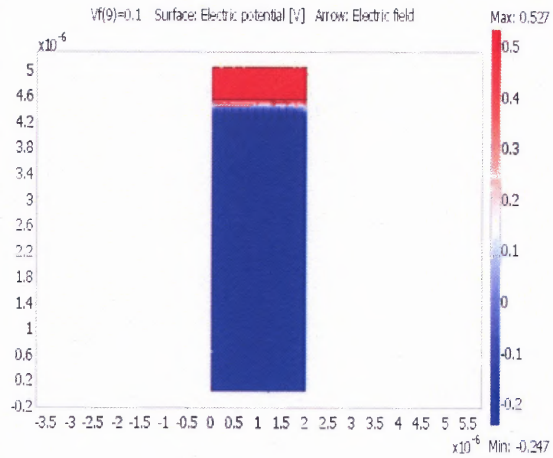

$5x10^{10}$ cm^{-2} Surface Charge on Right Side

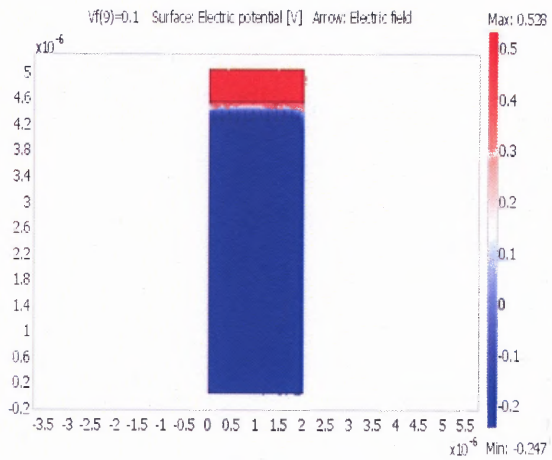

$1.25x10^{11}$ cm^{-2} Surface Charge on Right Side

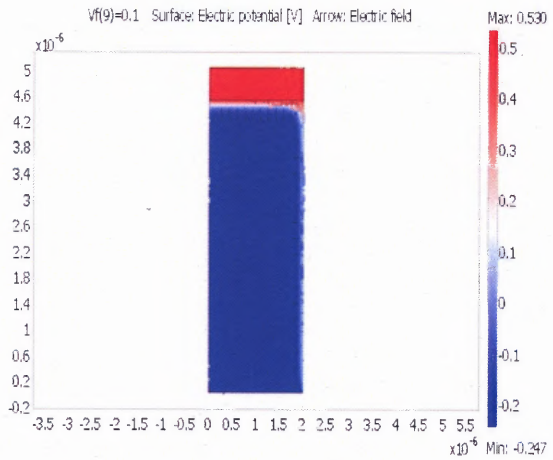

$1.75x10^{11}$ cm^{-2} Surface Charge on Right Side

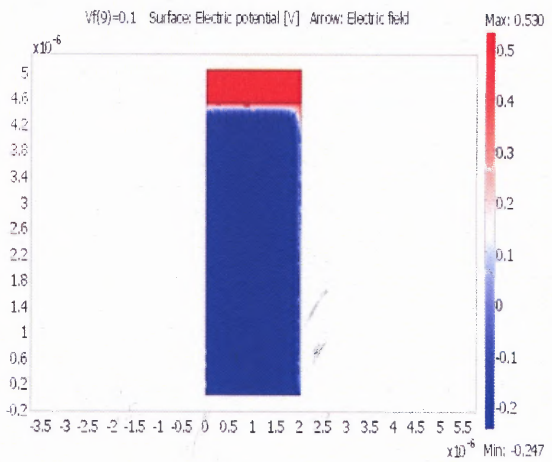

$2x10^{11}$ cm^{-2} Surface Charge on Right Side

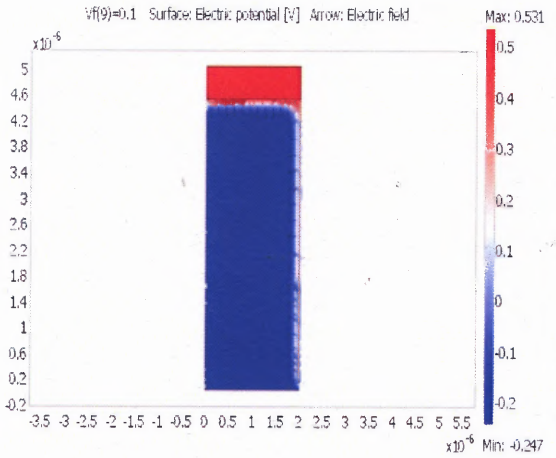

$3x10^{11}$ cm^{-2} Surface Charge on Right Side

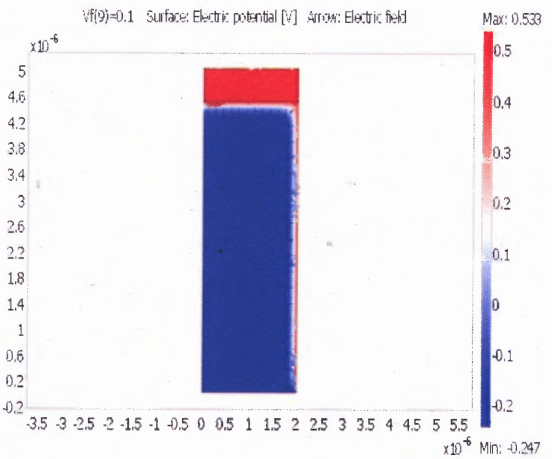

$5x10^{11}$ cm^{-2} Surface Charge on Right Side

Figure A.7 Electric potential and electric field (arrow) at 0.1 volts forward bias.

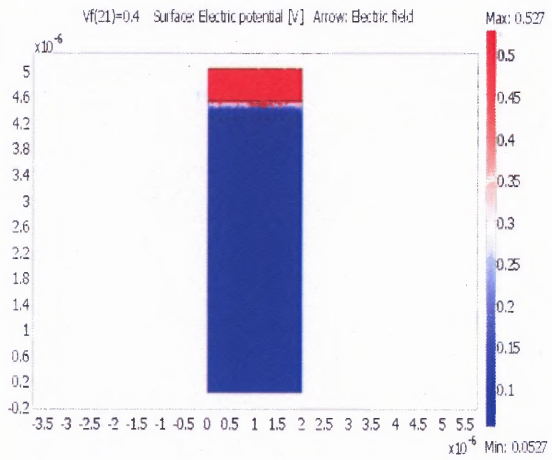

$5x10^{10}$ cm^{-2} Surface Charge on Right Side

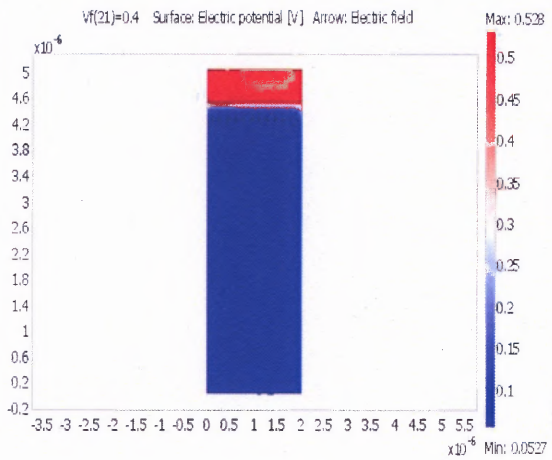

$1.25x10^{11}$ cm^{-2} Surface Charge on Right Side

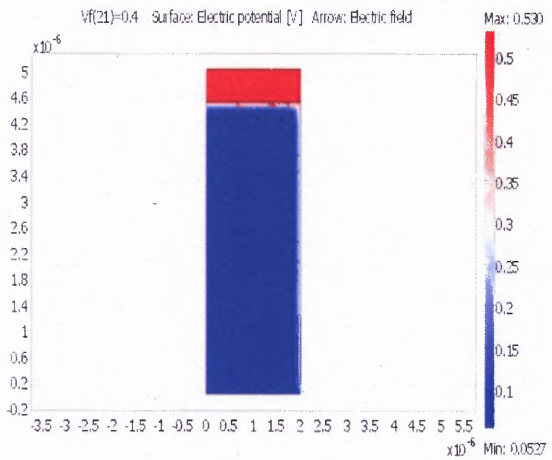

$1.75x10^{11}$ cm^{-2} Surface Charge on Right Side

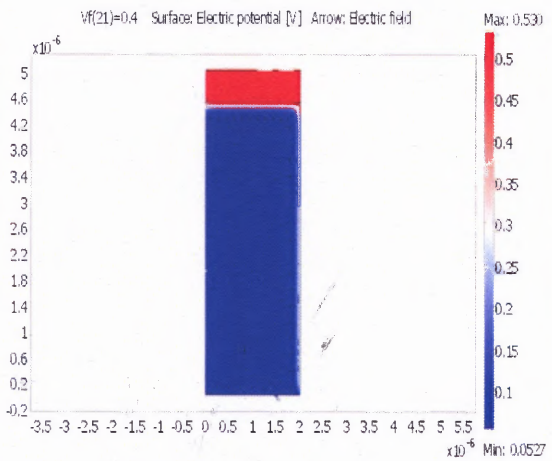

$2x10^{11}$ cm^{-2} Surface Charge on Right Side

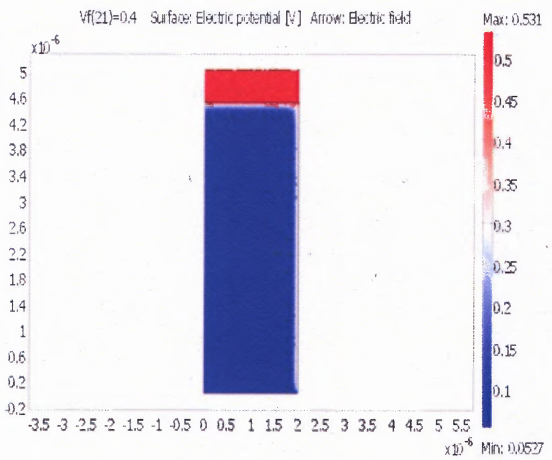

$3x10^{11}$ cm^{-2} Surface Charge on Right Side

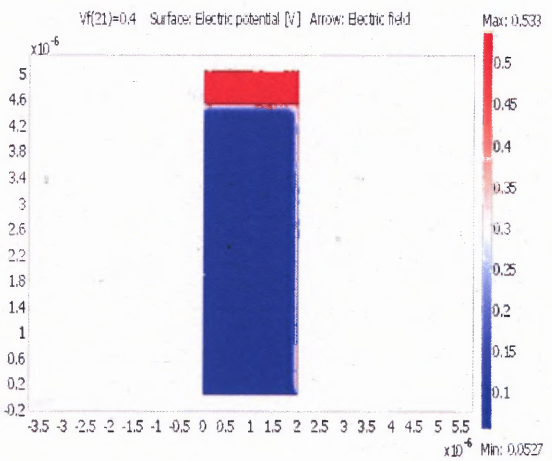

$5x10^{11}$ cm^{-2} Surface Charge on Right Side

Figure A.8 Electric potential and electric field (arrow) at 0.4 volts forward bias.

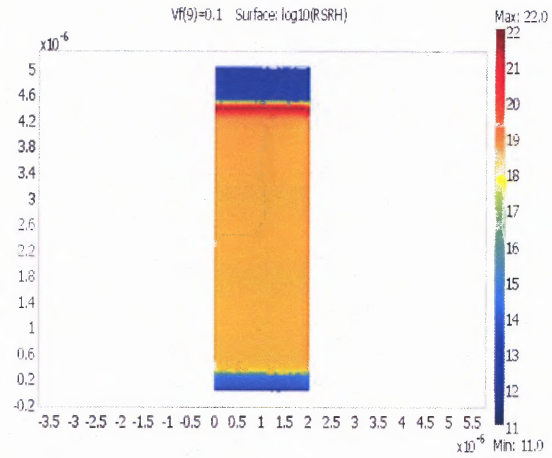

$5x10^{10}$ cm^{-2} Surface Charge on Right Side

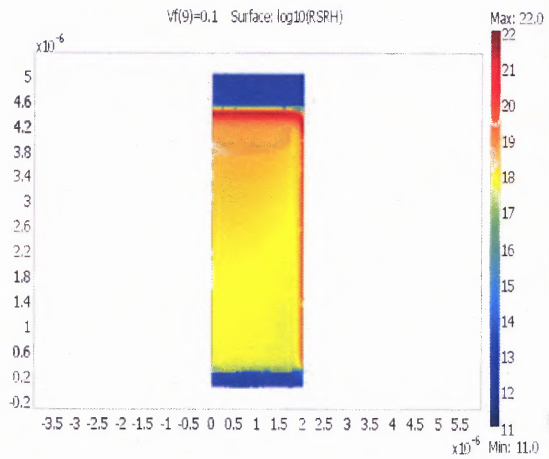

$1.25x10^{11}$ cm^{-2} Surface Charge on Right Side

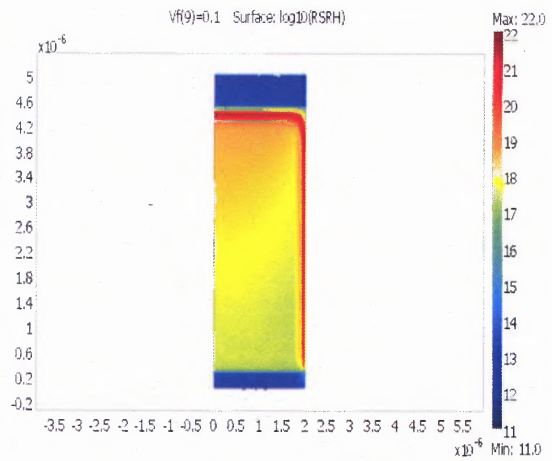

$1.75x10^{11}$ cm^{-2} Surface Charge on Right Side

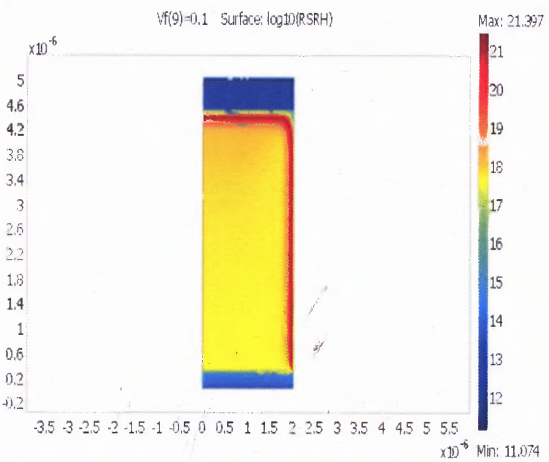

$2x10^{11}$ cm^{-2} Surface Charge on Right Side

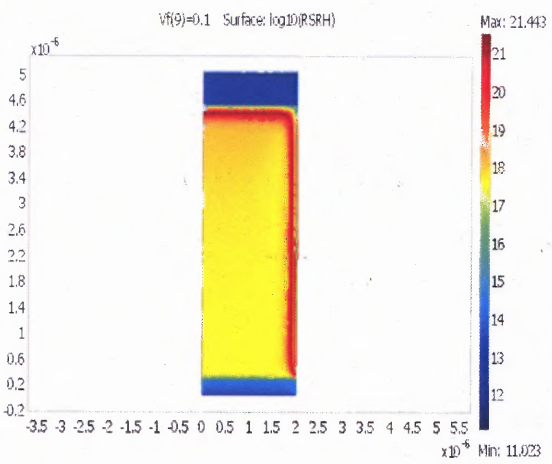

$3x10^{11}$ cm^{-2} Surface Charge on Right Side

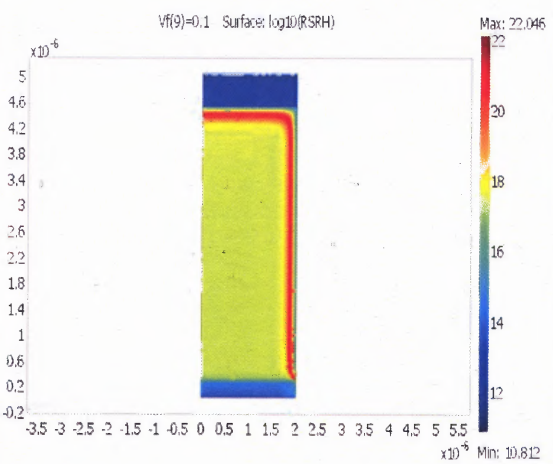

$5x10^{11}$ cm^{-2} Surface Charge on Right Side

Figure A.9 Bulk recombination rate at 0.1 volts forward bias with BSF.

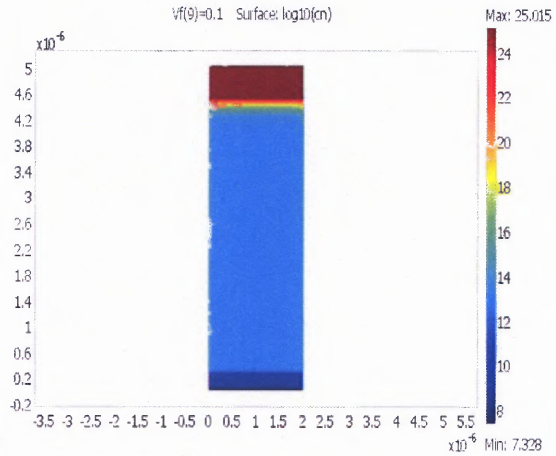

$5x10^{10}$ cm^{-2} Surface Charge on Right Side

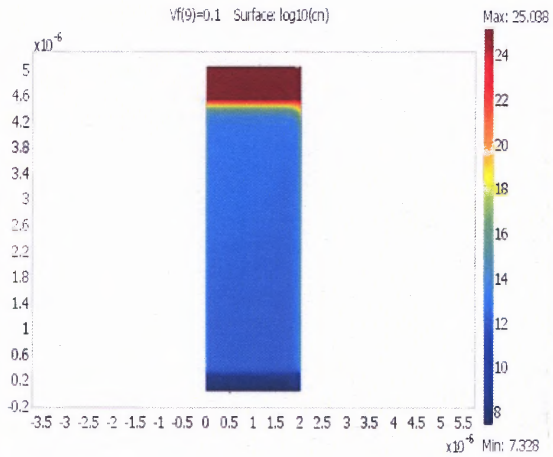

$1.25x10^{11}$ cm^{-2} Surface Charge on Right Side

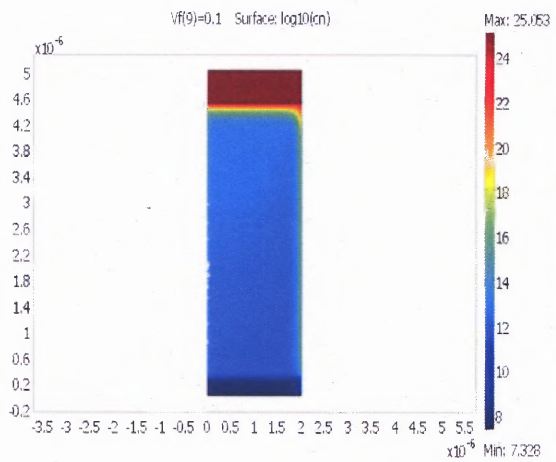

$1.75x10^{11}$ cm^{-2} Surface Charge on Right Side

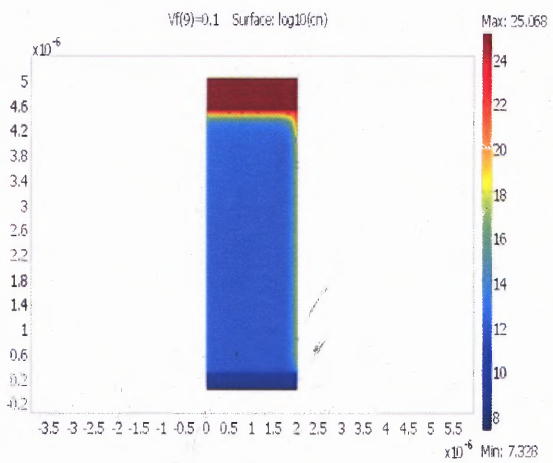

$2x10^{11}$ cm^{-2} Surface Charge on Right Side

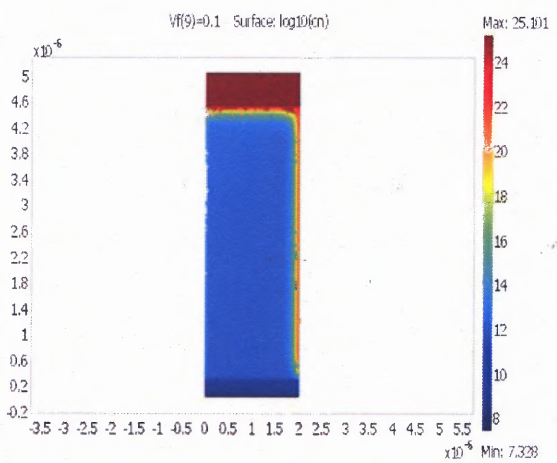

$3x10^{11}$ cm^{-2} Surface Charge on Right Side

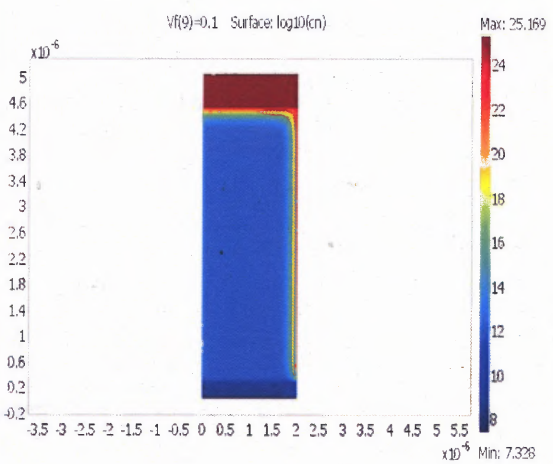

$5x10^{11}$ cm^{-2} Surface Charge on Right Side

Figure A.10 Electron concentration at 0.1 volts forward bias with BSF.

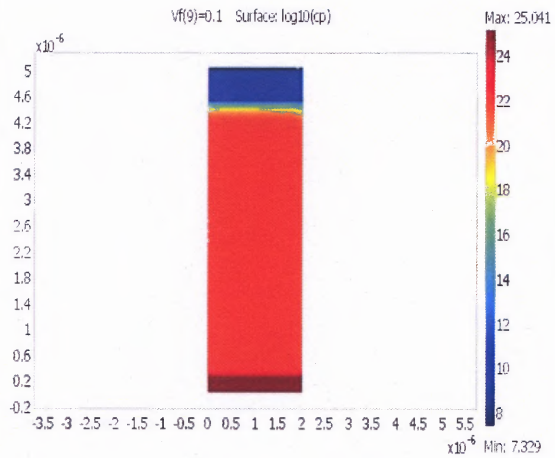

$5x10^{10}$ cm^{-2} Surface Charge on Right Side

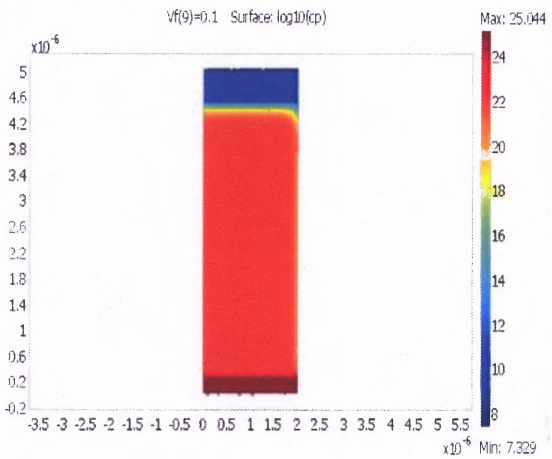

$1.25x10^{11}$ cm^{-2} Surface Charge on Right Side

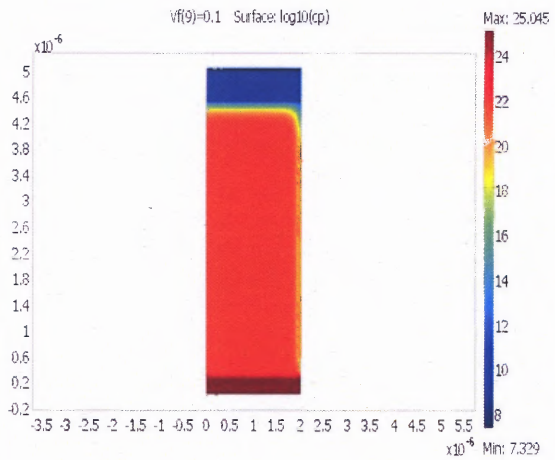

$1.75x10^{11}$ cm^{-2} Surface Charge on Right Side

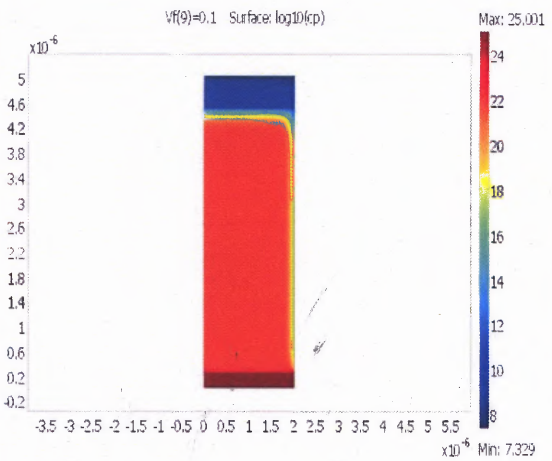

$2x10^{11}$ cm^{-2} Surface Charge on Right Side

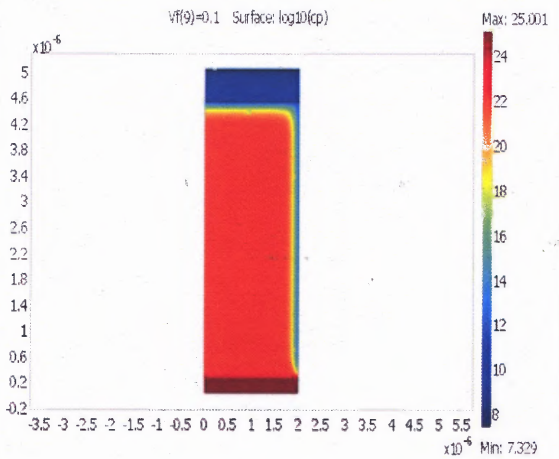

$3x10^{11}$ cm^{-2} Surface Charge on Right Side

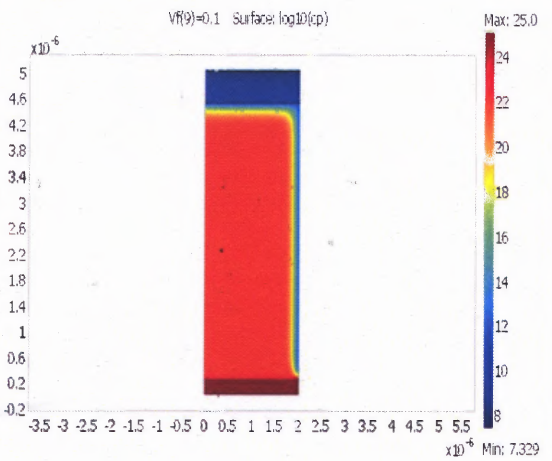

$5x10^{11}$ cm^{-2} Surface Charge on Right Side

Figure A.11 Hole concentration at 0.1 volts forward bias with BSF.

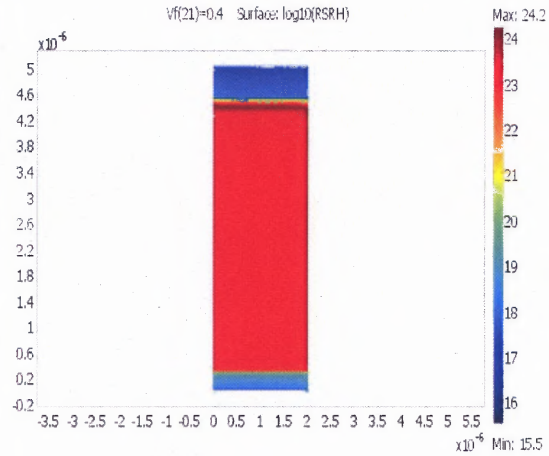

$5x10^{10}$ cm^{-2} Surface Charge on Right Side

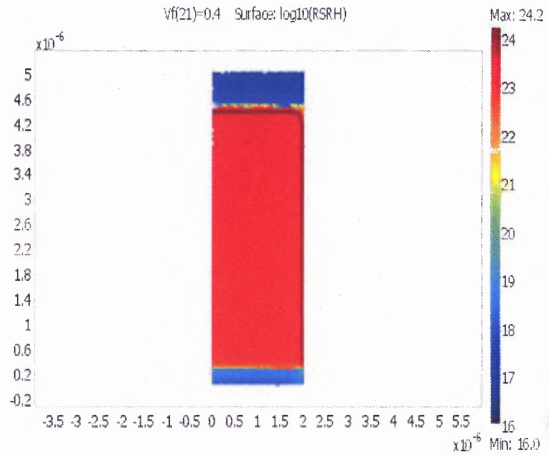

$1.25x10^{11}$ cm^{-2} Surface Charge on Right Side

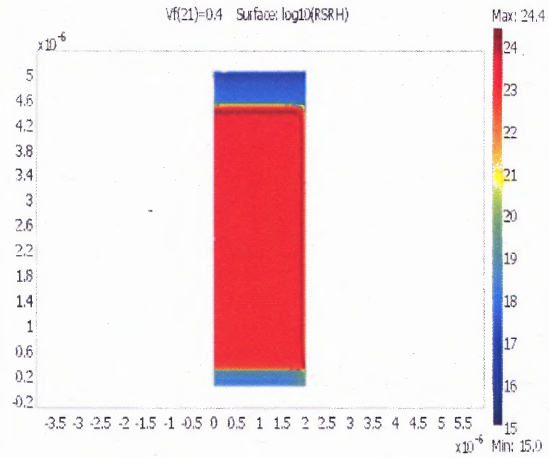

$1.75x10^{11}$ cm^{-2} Surface Charge on Right Side

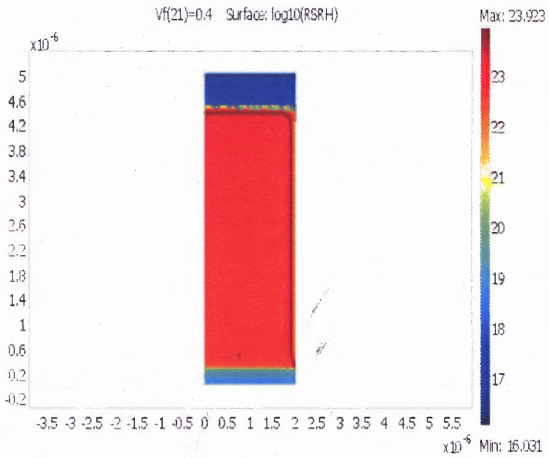

$2x10^{11}$ cm^{-2} Surface Charge on Right Side

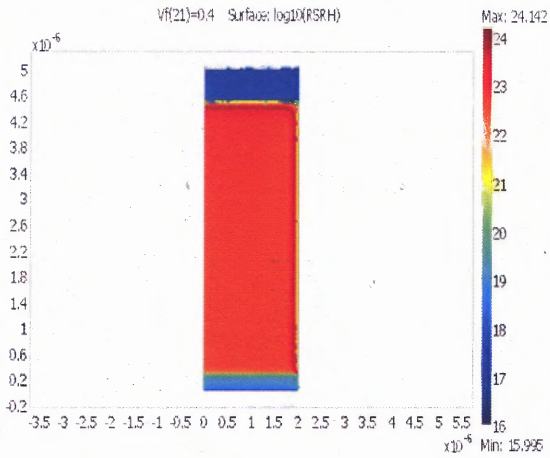

$3x10^{11}$ cm^{-2} Surface Charge on Right Side

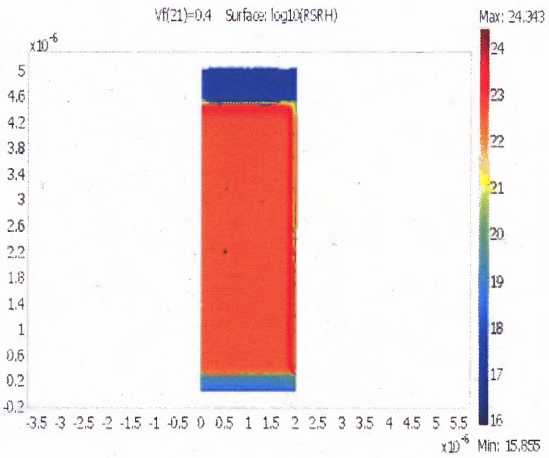

$5x10^{11}$ cm^{-2} Surface Charge on Right Side

Figure A.12 Bulk recombination rate at 0.4 volts forward bias with BSF.

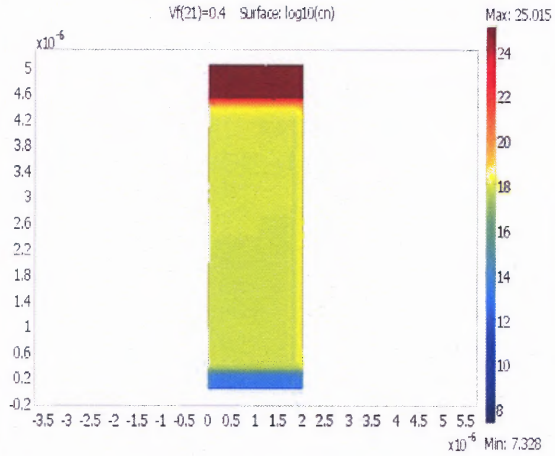

$5x10^{10}$ cm^{-2} Surface Charge on Right Side

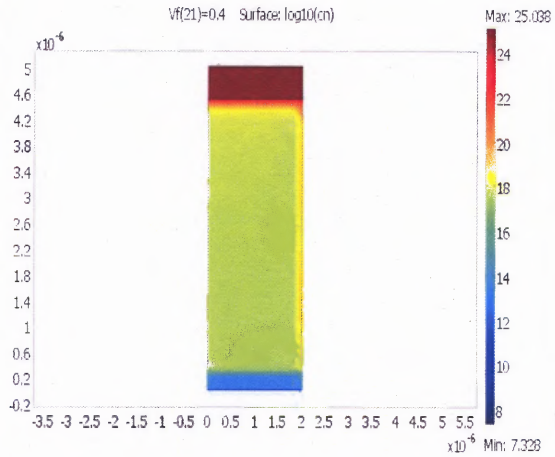

$1.25x10^{11}$ cm^{-2} Surface Charge on Right Side

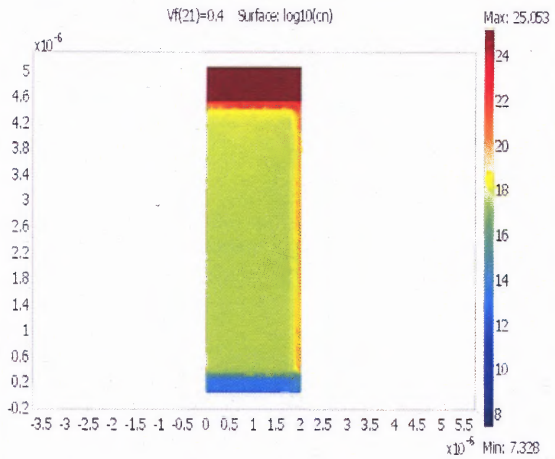

$1.75x10^{11}$ cm^{-2} Surface Charge on Right Side

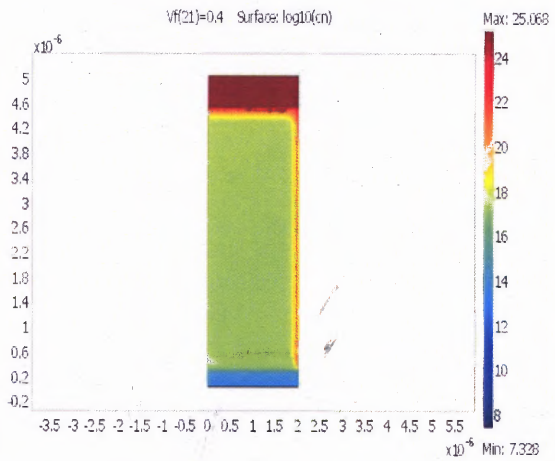

$2x10^{11}$ cm^{-2} Surface Charge on Right Side

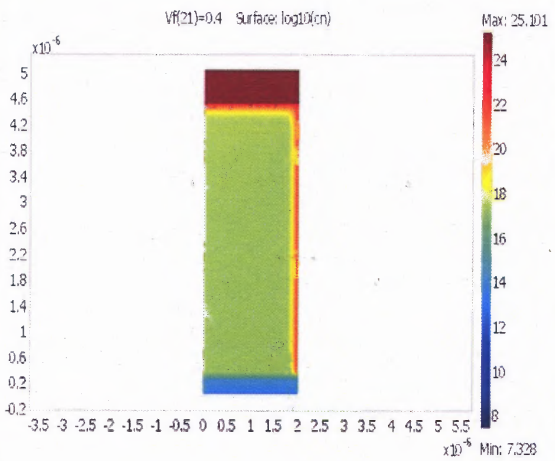

$3x10^{11}$ cm^{-2} Surface Charge on Right Side

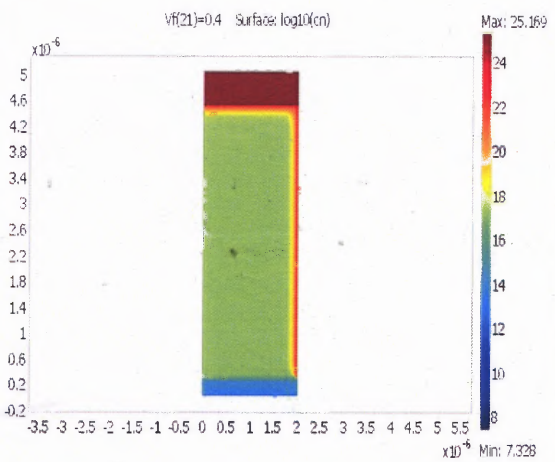

$5x10^{11}$ cm^{-2} Surface Charge on Right Side

Figure A.13 Electron concentration at 0.4 volts forward bias with BSF.

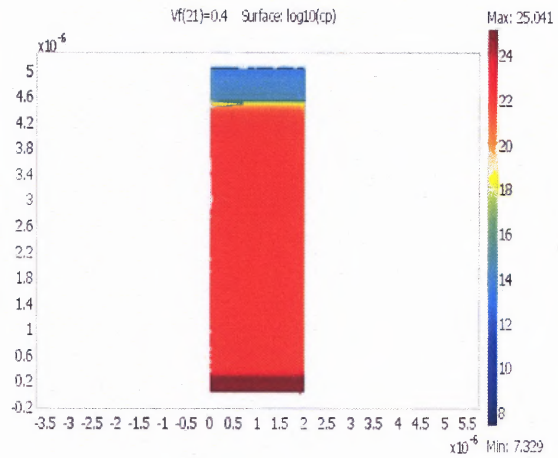

$5x10^{10}$ cm^{-2} Surface Charge on Right Side

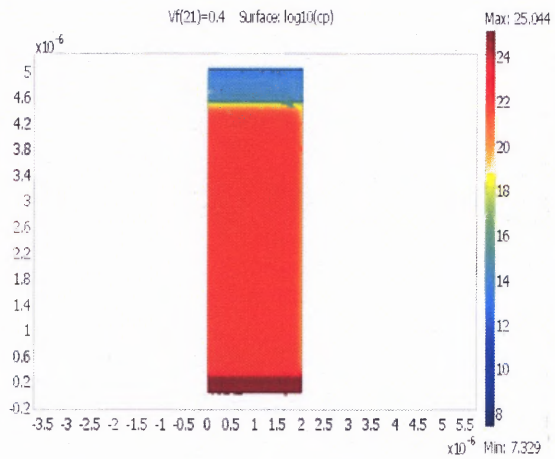

$1.25x10^{11}$ cm^{-2} Surface Charge on Right Side

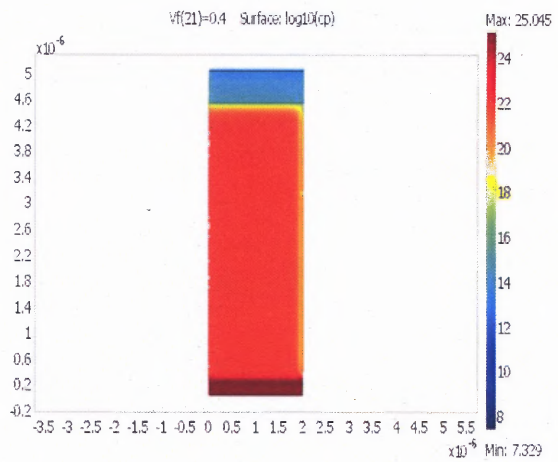

$1.75x10^{11}$ cm^{-2} Surface Charge on Right Side

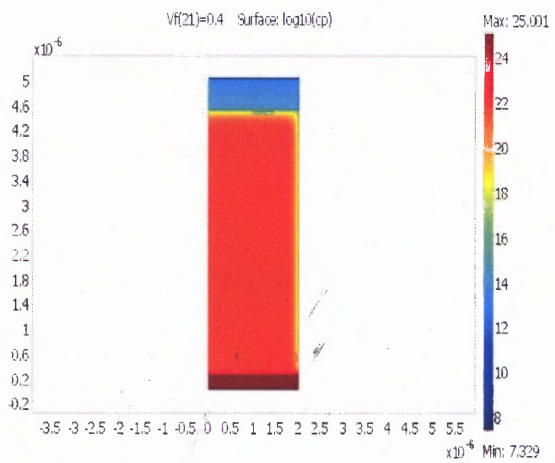

$2x10^{11}$ cm^{-2} Surface Charge on Right Side

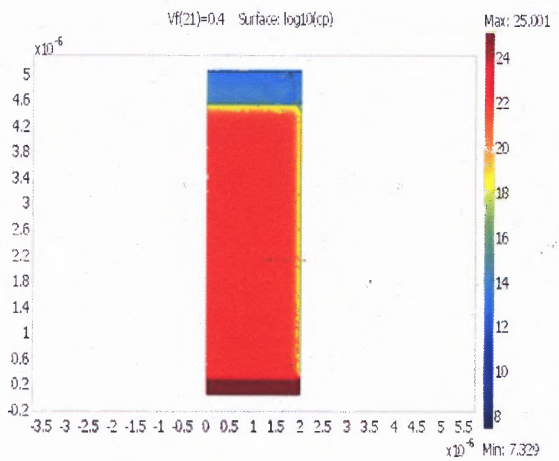

$3x10^{11}$ cm^{-2} Surface Charge on Right Side

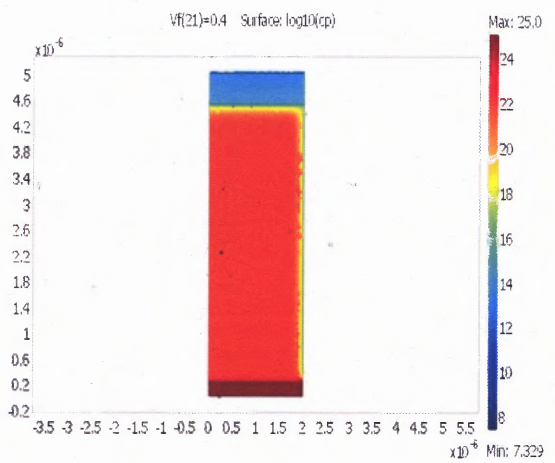

$5x10^{11}$ cm^{-2} Surface Charge on Right Side

Figure A.14 Hole concentration at 0.4 volts forward bias with BSF.

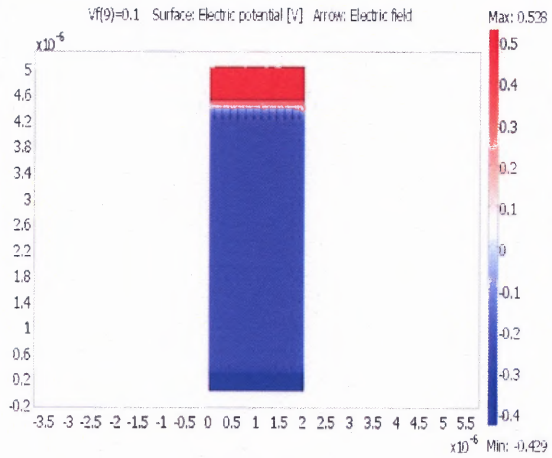

$5x10^{10}$ cm^{-2} Surface Charge on Right Side

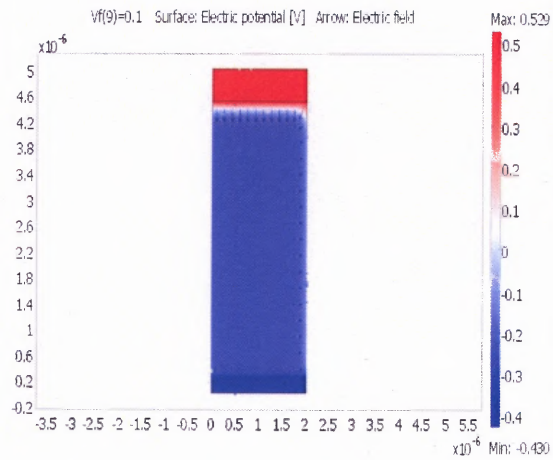

$1.25x10^{11}$ cm^{-2} Surface Charge on Right Side

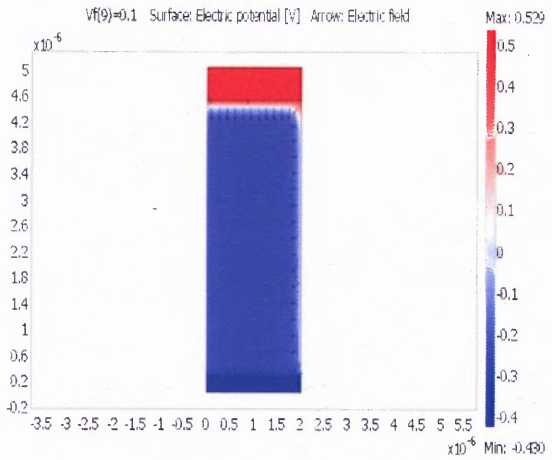

$1.75x10^{11}$ cm^{-2} Surface Charge on Right Side

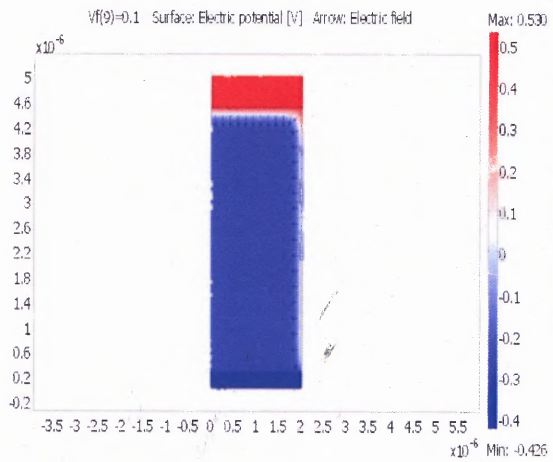

$2x10^{11}$ cm^{-2} Surface Charge on Right Side

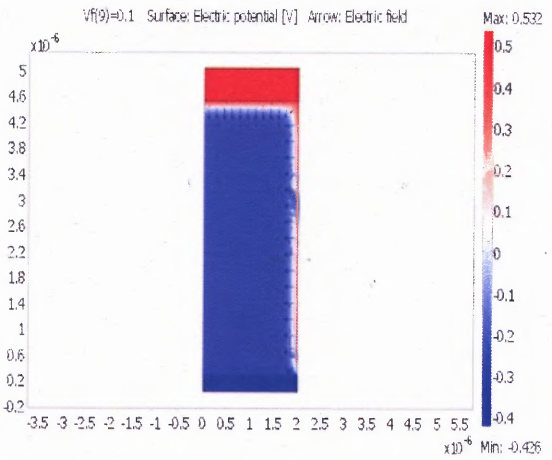

$3x10^{11}$ cm^{-2} Surface Charge on Right Side

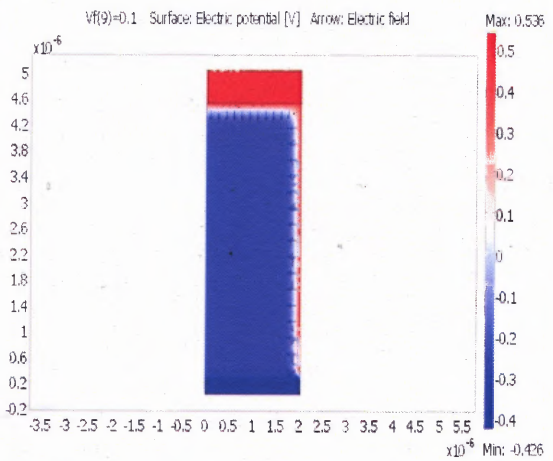

$5x10^{11}$ cm^{-2} Surface Charge on Right Side

Figure A.15 Electric potential and electric field (arrow) at 0.1 volts FB with BSF.

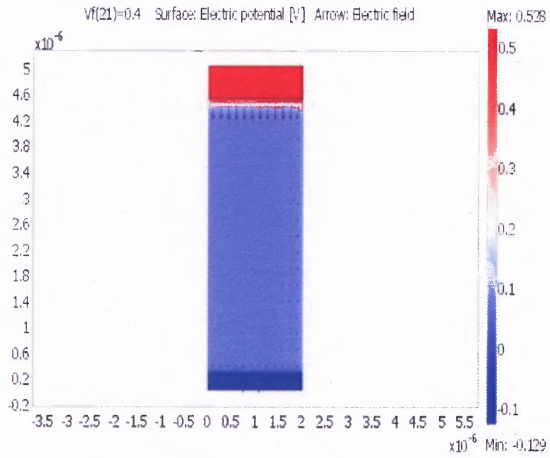

$5x10^{10}$ cm^{-2} Surface Charge on Right Side

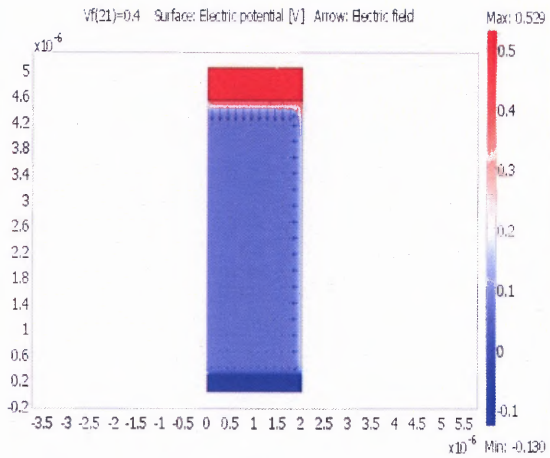

$1.25x10^{11}$ cm^{-2} Surface Charge on Right Side

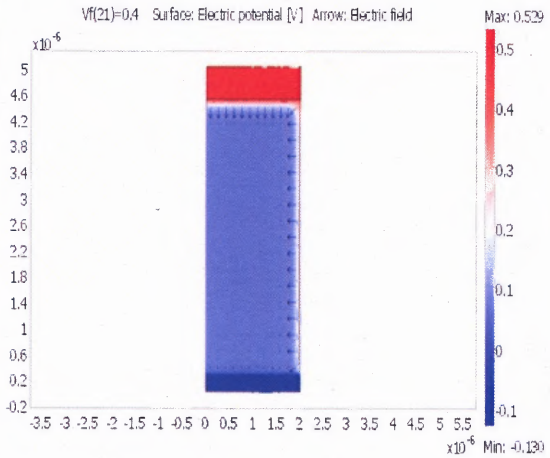

$1.75x10^{11}$ cm^{-2} Surface Charge on Right Side

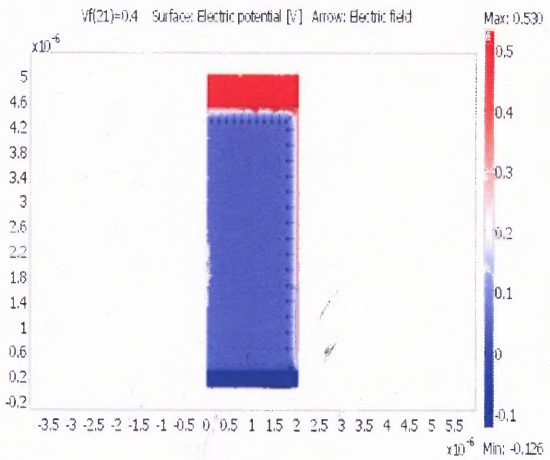

$2x10^{11}$ cm^{-2} Surface Charge on Right Side

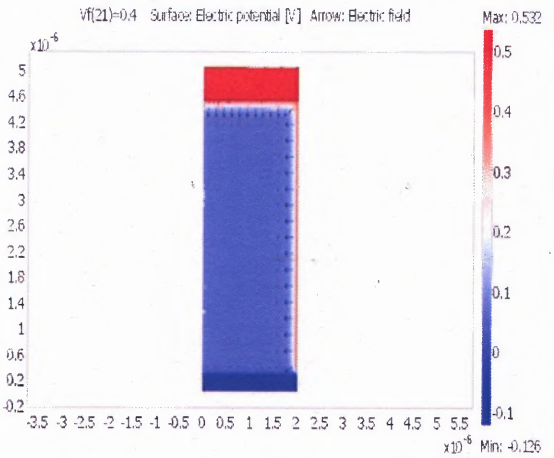

$3x10^{11}$ cm^{-2} Surface Charge on Right Side

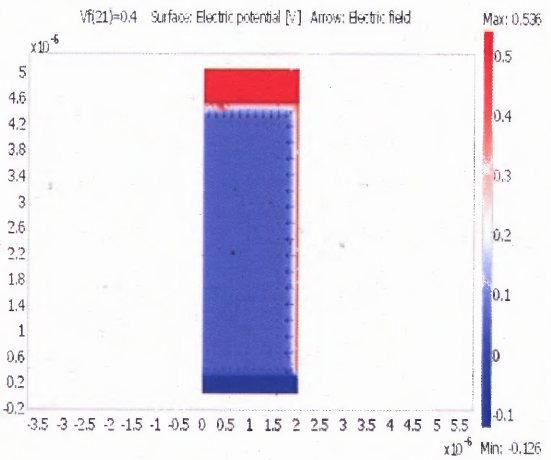

$5x10^{11}$ cm^{-2} Surface Charge on Right Side

Figure A.16 Electric potential and electric field (arrow) at 0.4 volts FB w/ BSF.

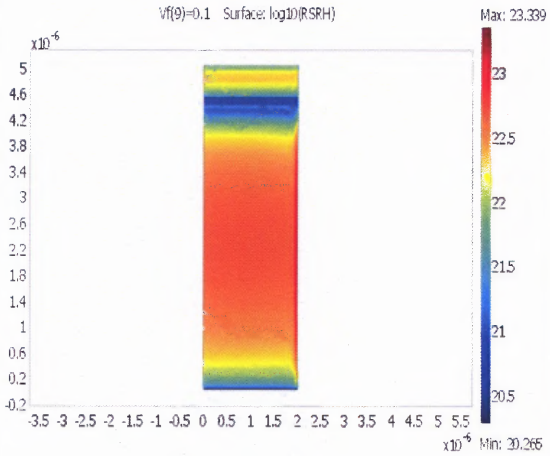

$5x10^{10}$ cm^{-2} Surface Charge on Right Side

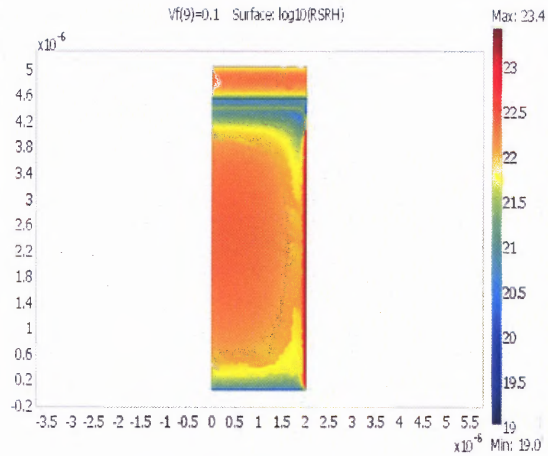

$1.25x10^{11}$ cm^{-2} Surface Charge on Right Side

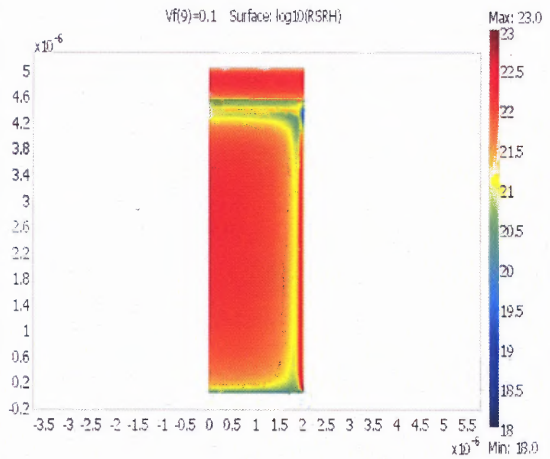

$1.75x10^{11}$ cm^{-2} Surface Charge on Right Side

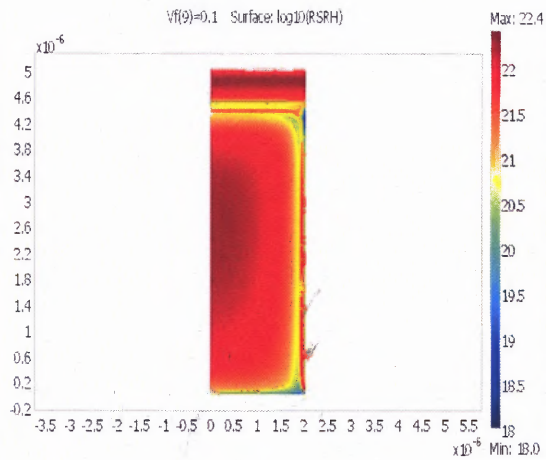

$2x10^{11}$ cm^{-2} Surface Charge on Right Side

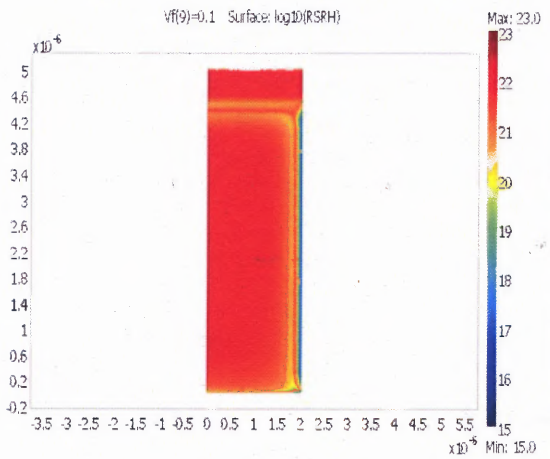

$3x10^{11}$ cm^{-2} Surface Charge on Right Side

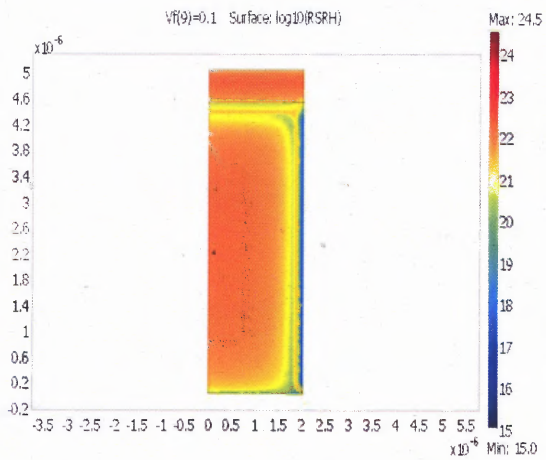

$5x10^{11}$ cm^{-2} Surface Charge on Right Side

Figure A.17 Bulk recombination rate at 0.1 volts forward bias (illuminated).

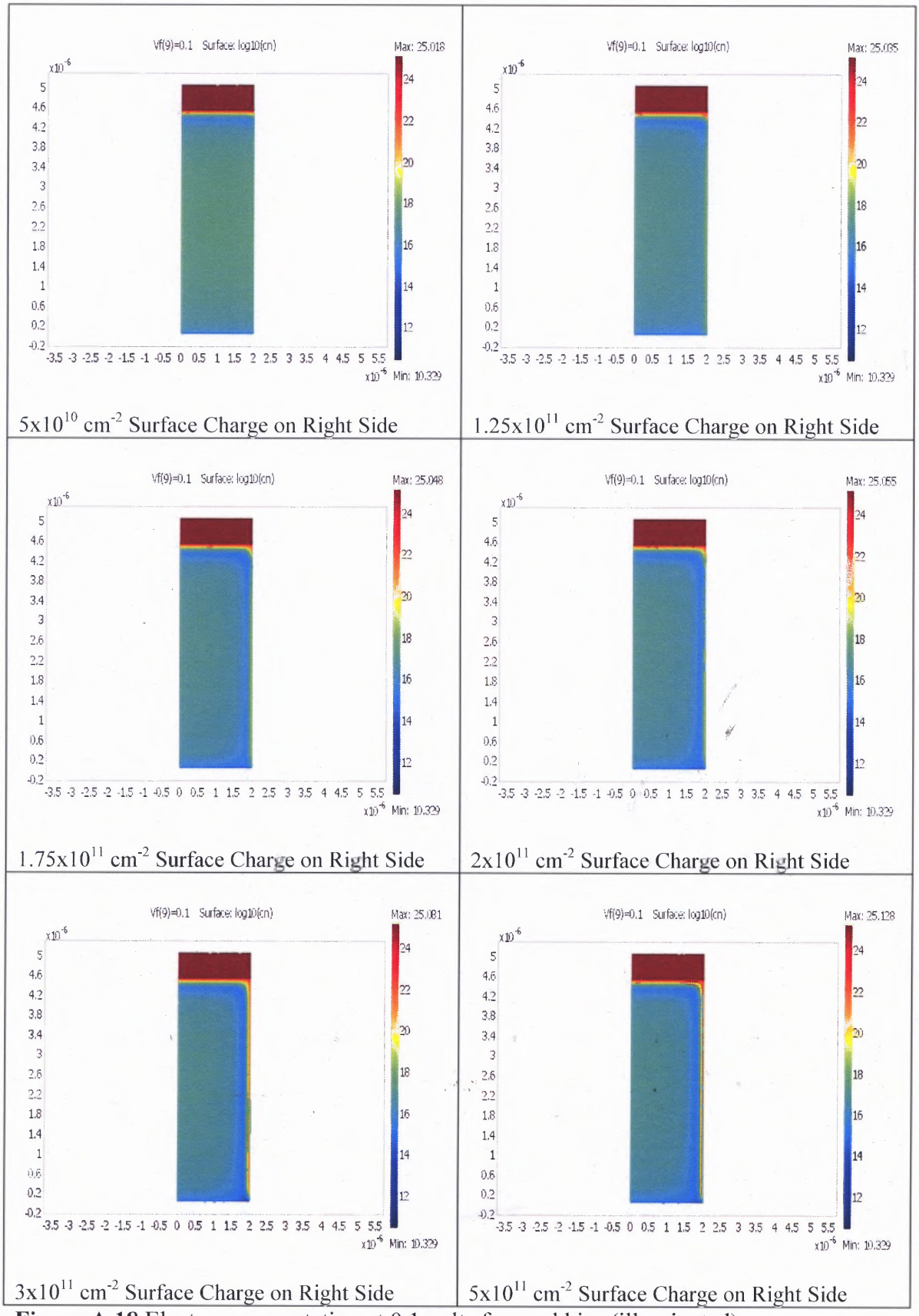

$5x10^{10}$ cm^{-2} Surface Charge on Right Side

$1.25x10^{11}$ cm^{-2} Surface Charge on Right Side

$1.75x10^{11}$ cm^{-2} Surface Charge on Right Side

$2x10^{11}$ cm^{-2} Surface Charge on Right Side

$3x10^{11}$ cm^{-2} Surface Charge on Right Side

$5x10^{11}$ cm^{-2} Surface Charge on Right Side

Figure A.18 Electron concentation at 0.1 volts forward bias (illuminated).

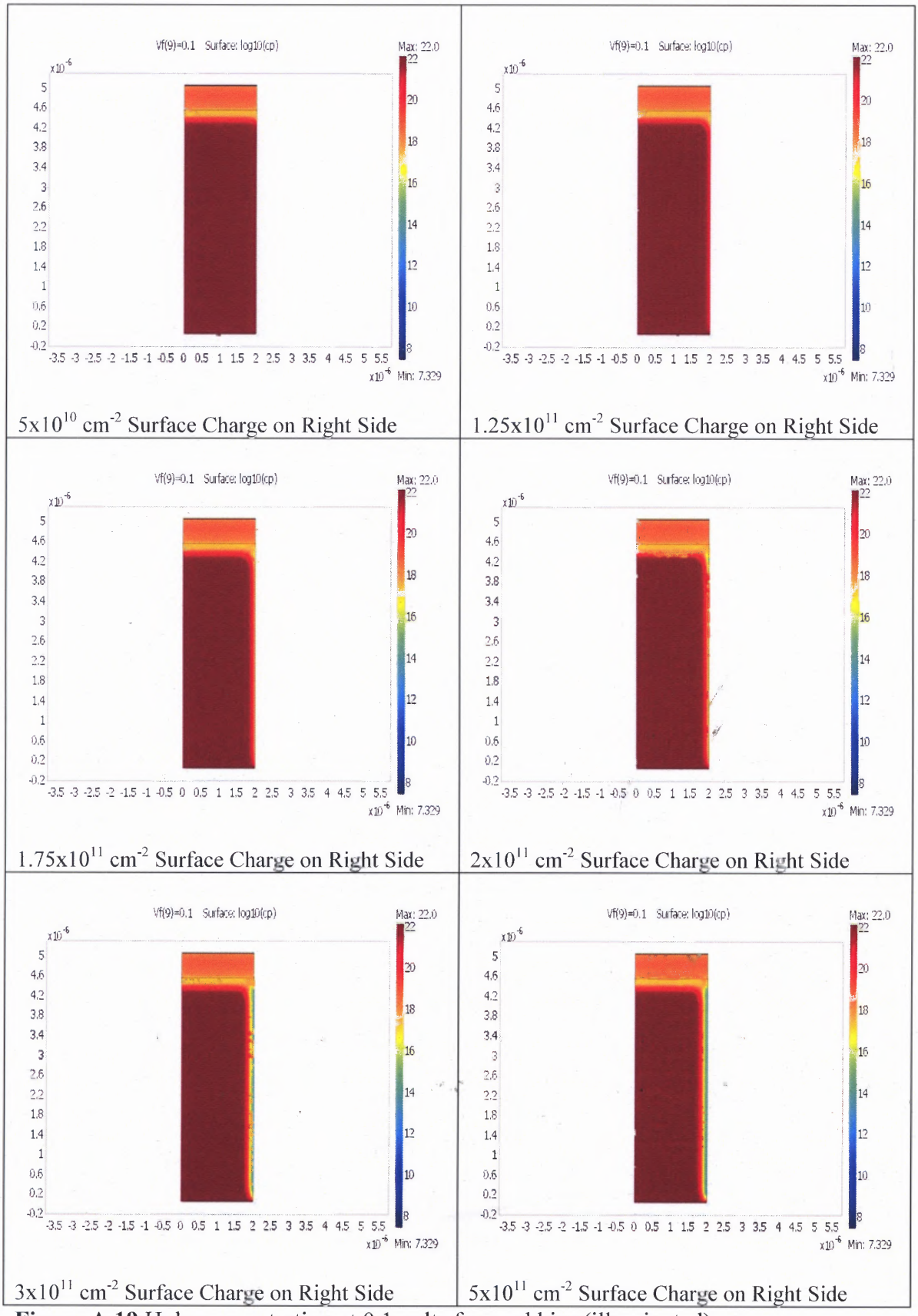

$5x10^{10}$ cm^{-2} Surface Charge on Right Side

$1.25x10^{11}$ cm^{-2} Surface Charge on Right Side

$1.75x10^{11}$ cm^{-2} Surface Charge on Right Side

$2x10^{11}$ cm^{-2} Surface Charge on Right Side

$3x10^{11}$ cm^{-2} Surface Charge on Right Side

$5x10^{11}$ cm^{-2} Surface Charge on Right Side

Figure A.19 Hole concentration at 0.1 volts forward bias (illuminated).

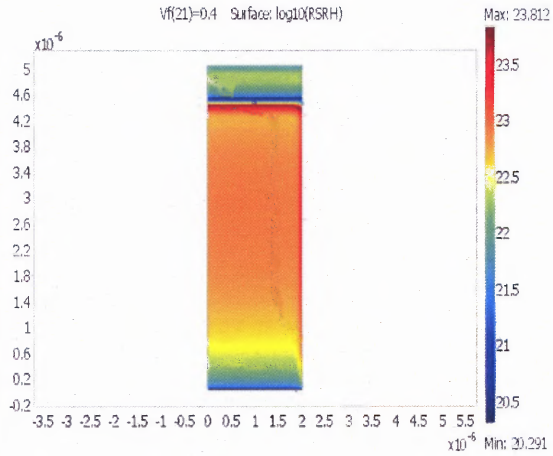

$5x10^{10}$ cm^{-2} Surface Charge on Right Side

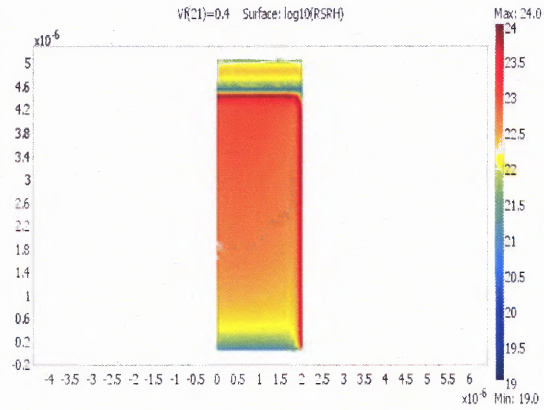

$1.25x10^{11}$ cm^{-2} Surface Charge on Right Side

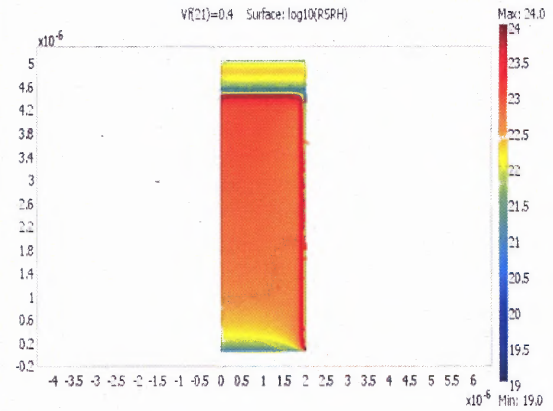

$1.75x10^{11}$ cm^{-2} Surface Charge on Right Side

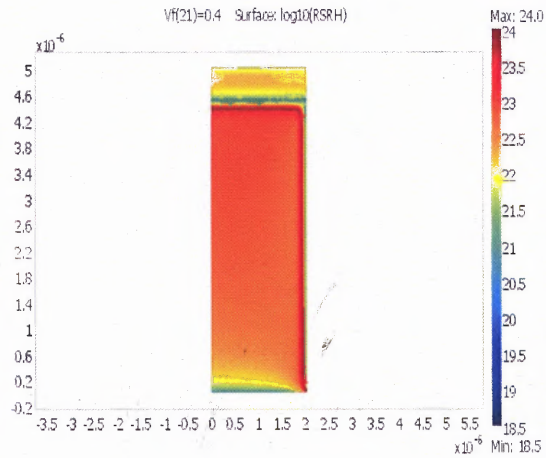

$2x10^{11}$ cm^{-2} Surface Charge on Right Side

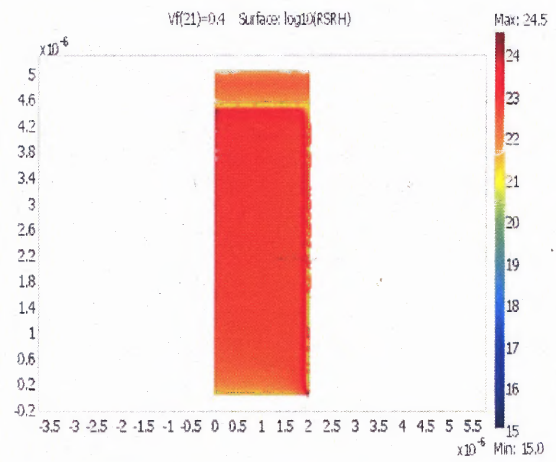

$3x10^{11}$ cm^{-2} Surface Charge on Right Side

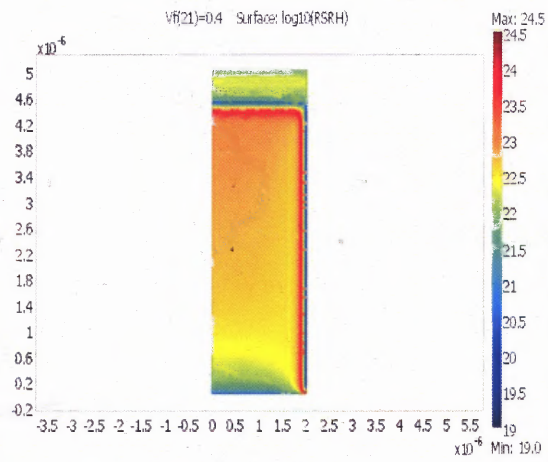

$5x10^{11}$ cm^{-2} Surface Charge on Right Side

Figure A.20 Bulk recombination rate at 0.4 volts forward bias (illuminated).

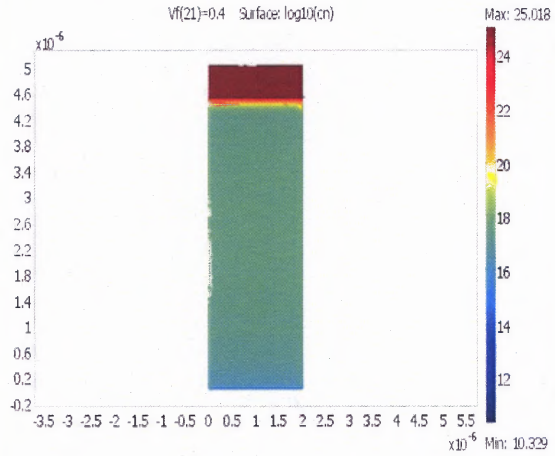

$5x10^{10}$ cm^{-2} Surface Charge on Right Side

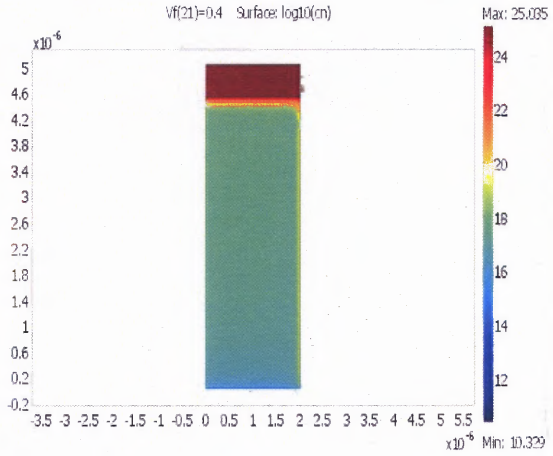

$1.25x10^{11}$ cm^{-2} Surface Charge on Right Side

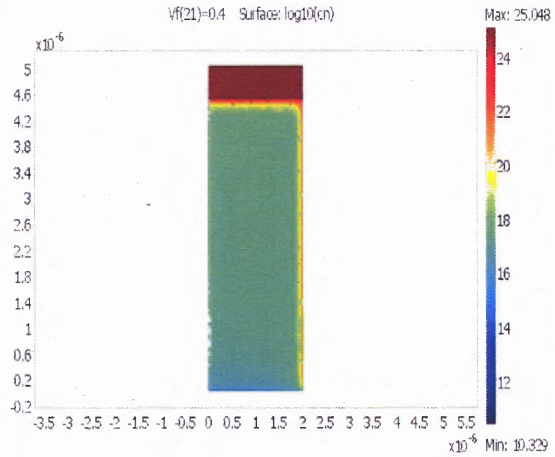

$1.75x10^{11}$ cm^{-2} Surface Charge on Right Side

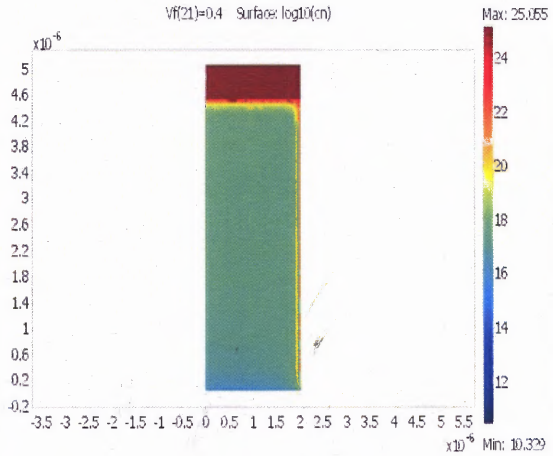

$2x10^{11}$ cm^{-2} Surface Charge on Right Side

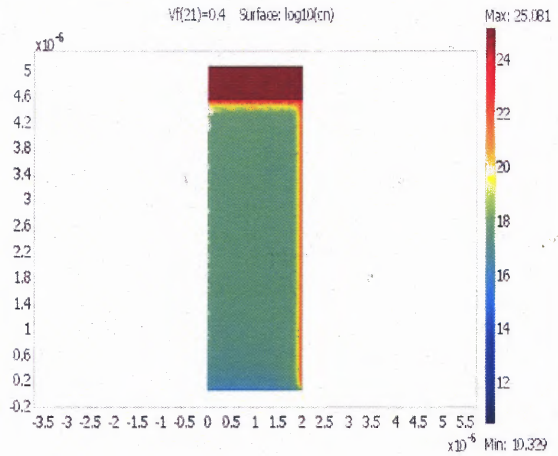

$3x10^{11}$ cm^{-2} Surface Charge on Right Side

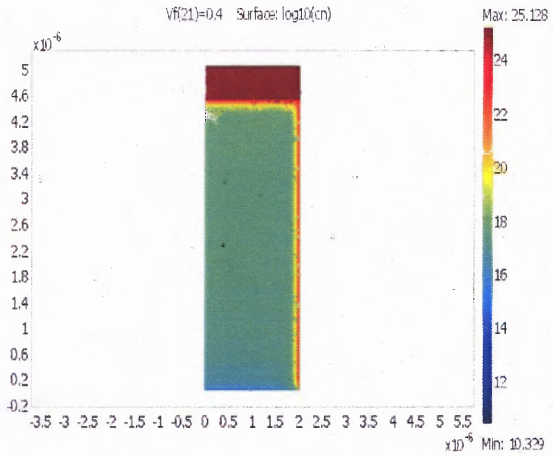

$5x10^{11}$ cm^{-2} Surface Charge on Right Side

Figure A.21 Electron concentration at 0.4 volts forward bias (illuminated).

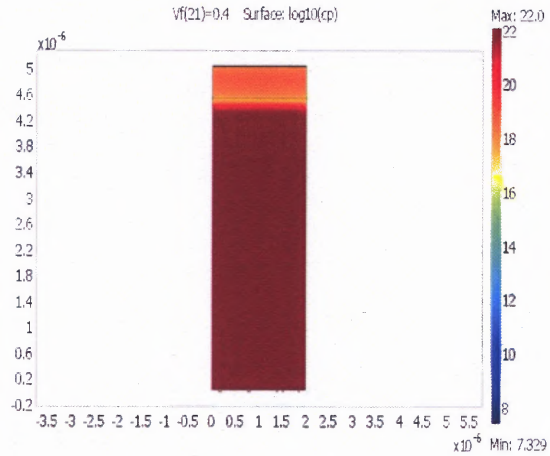

$5x10^{10}$ cm^{-2} Surface Charge on Right Side

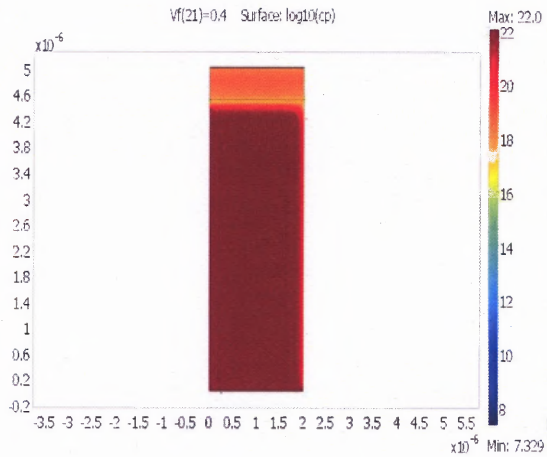

$1.25x10^{11}$ cm^{-2} Surface Charge on Right Side

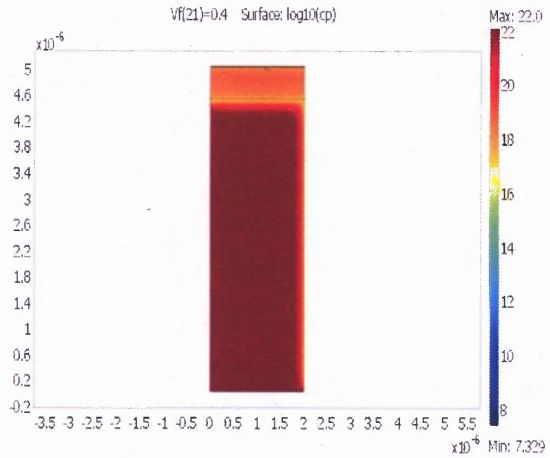

$1.75x10^{11}$ cm^{-2} Surface Charge on Right Side

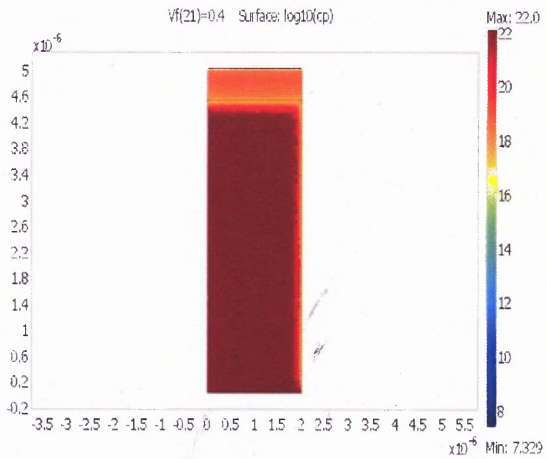

$2x10^{11}$ cm^{-2} Surface Charge on Right Side

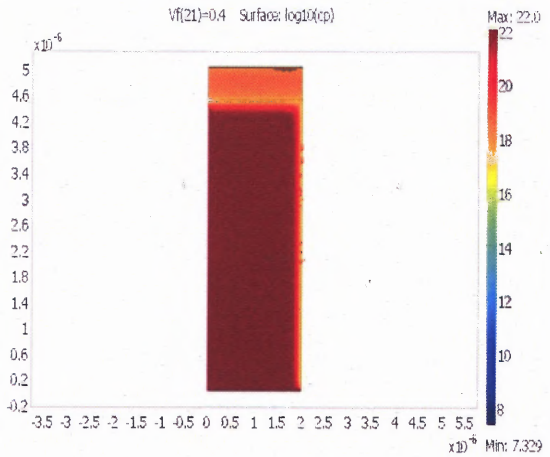

$3x10^{11}$ cm^{-2} Surface Charge on Right Side

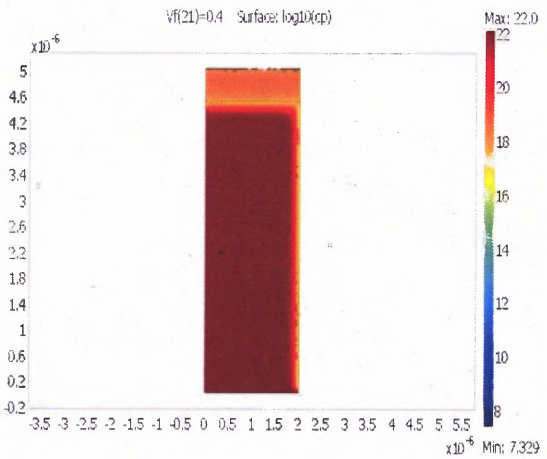

$5x10^{11}$ cm^{-2} Surface Charge on Right Side

Figure A.22 Hole concentration at 0.4 volts forward bias (illuminated).

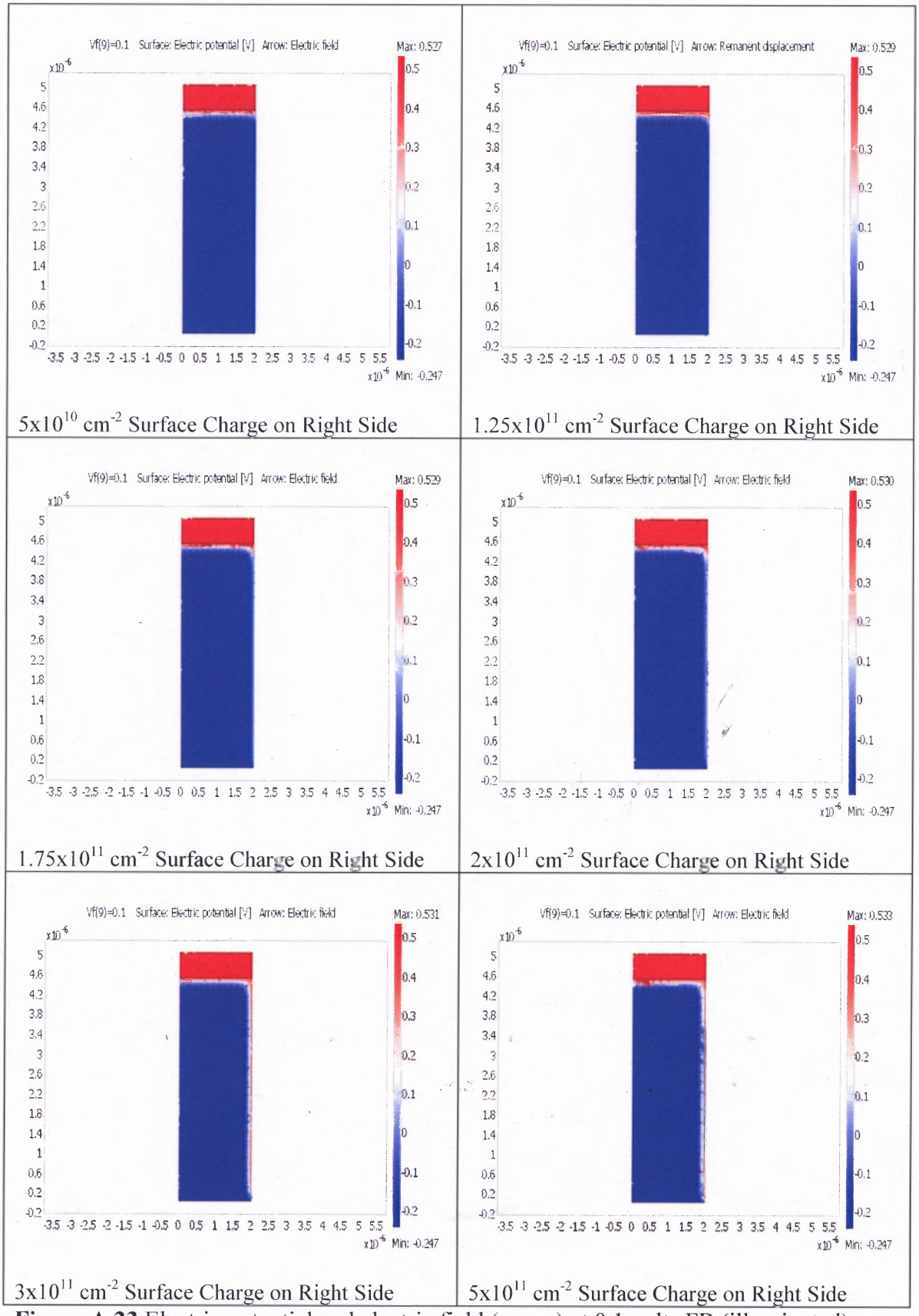

Figure A.23 Electric potential and electric field (arrow) at 0.1 volts FB (illuminated).

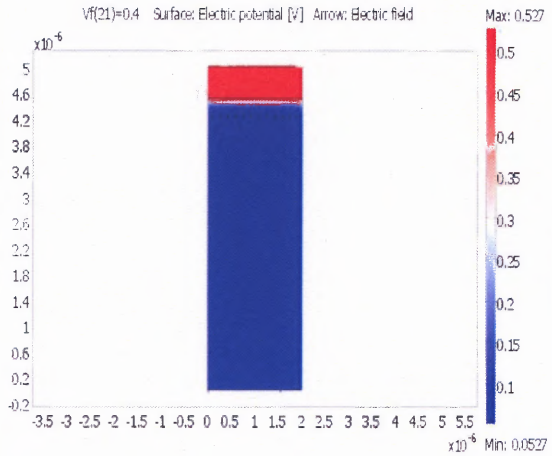

$5x10^{10}$ cm^{-2} Surface Charge on Right Side

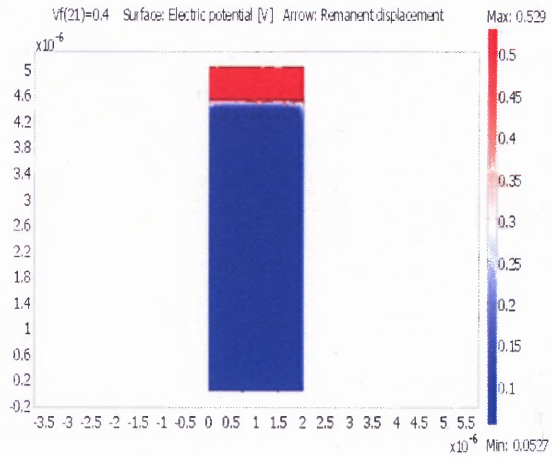

$1.25x10^{11}$ cm^{-2} Surface Charge on Right Side

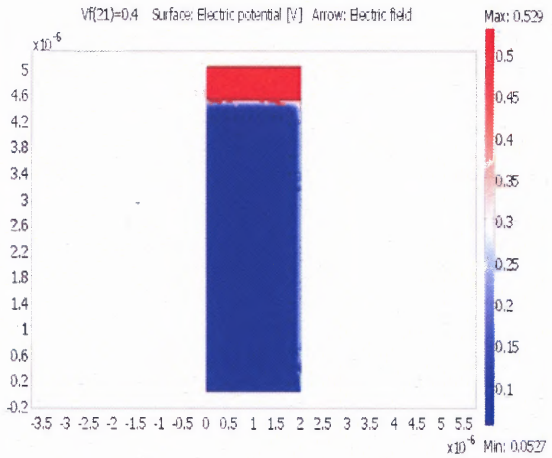

$1.75x10^{11}$ cm^{-2} Surface Charge on Right Side

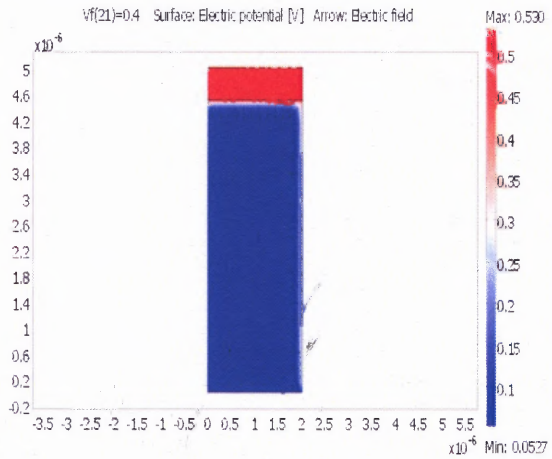

$2x10^{11}$ cm^{-2} Surface Charge on Right Side

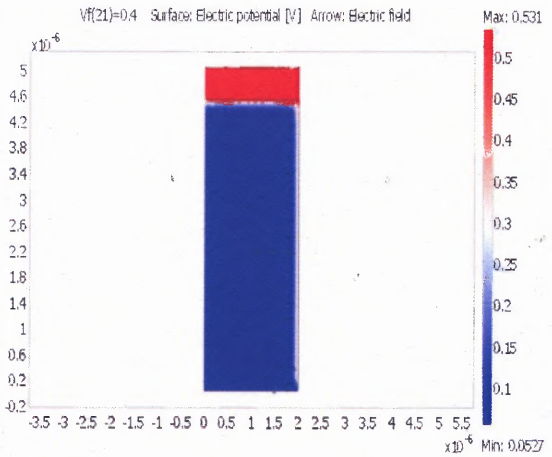

$3x10^{11}$ cm^{-2} Surface Charge on Right Side

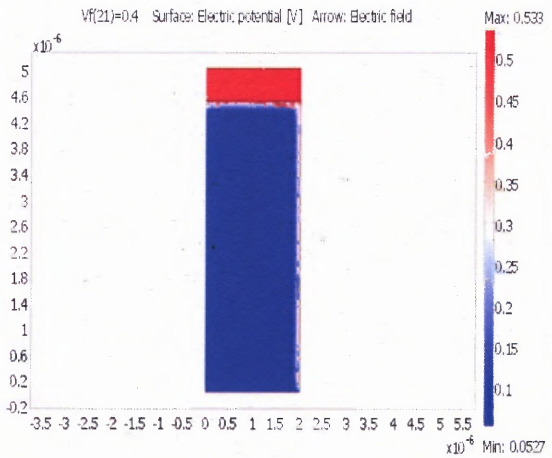

$5x10^{11}$ cm^{-2} Surface Charge on Right Side

Figure A.24 Electric potential and electric field (arrow) at 0.4 volts FB (illuminated).

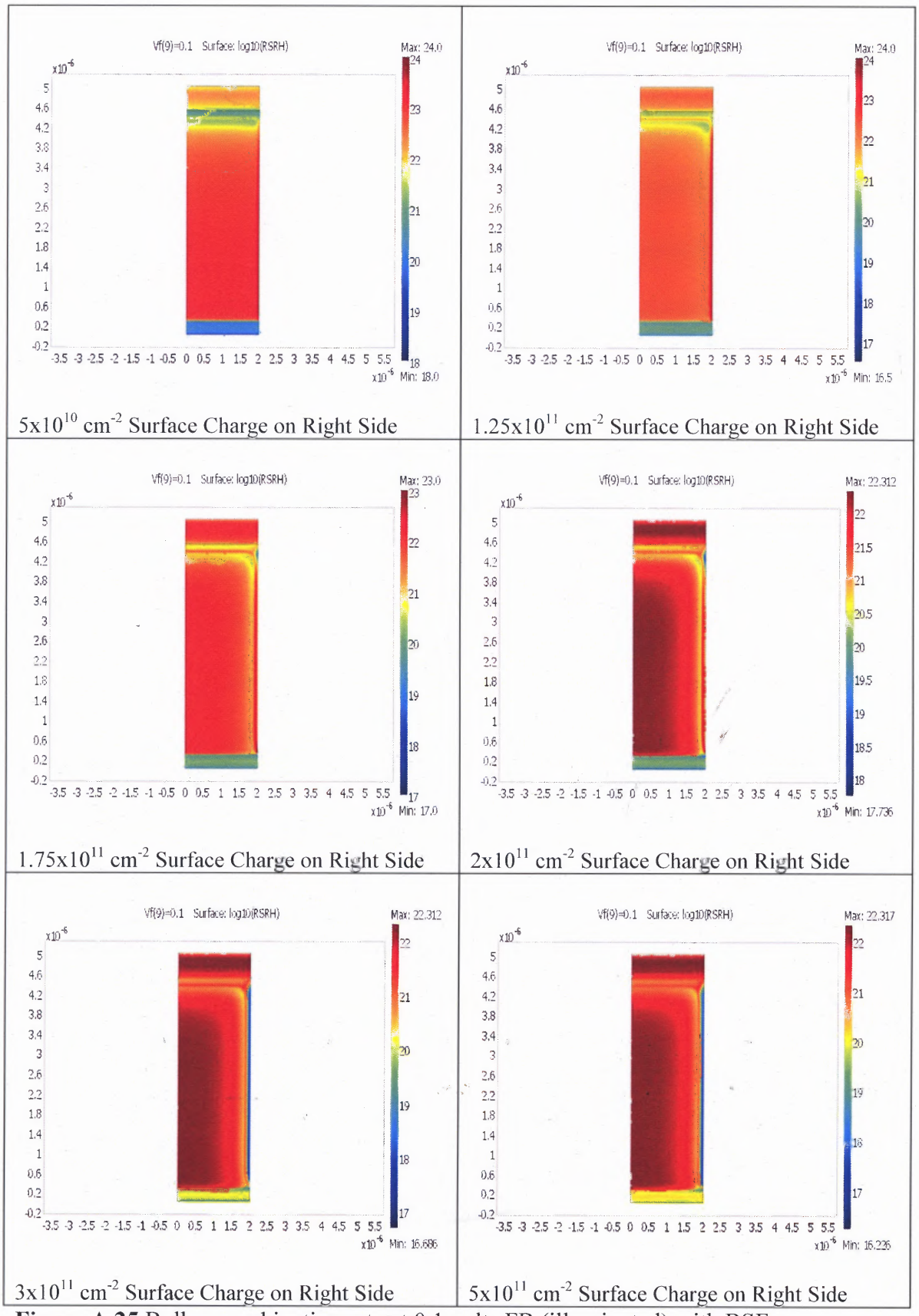

Figure A.25 Bulk recombination rate at 0.1 volts FB (illuminated) with BSF.

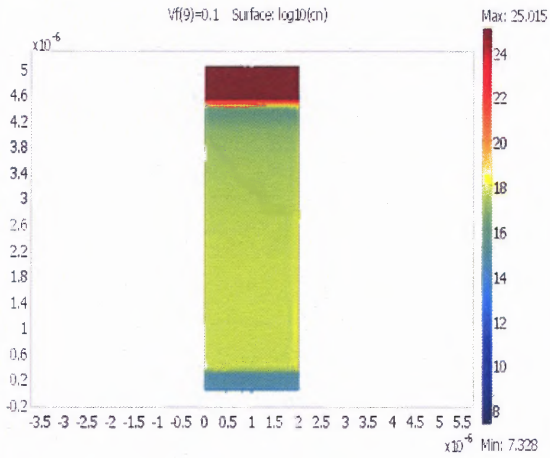

$5x10^{10}$ cm^{-2} Surface Charge on Right Side

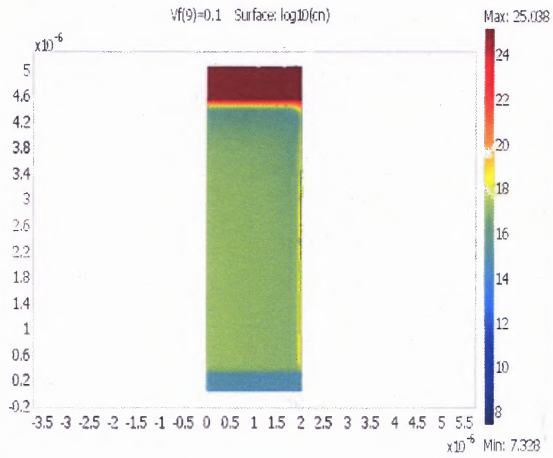

$1.25x10^{11}$ cm^{-2} Surface Charge on Right Side

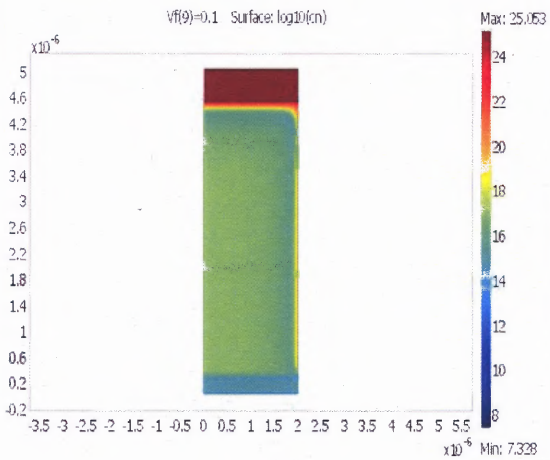

$1.75x10^{11}$ cm^{-2} Surface Charge on Right Side

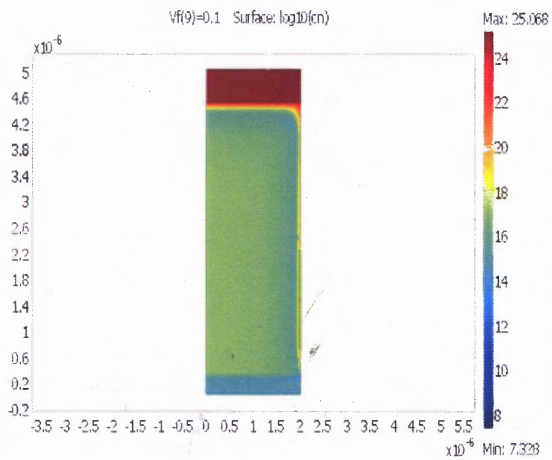

$2x10^{11}$ cm^{-2} Surface Charge on Right Side

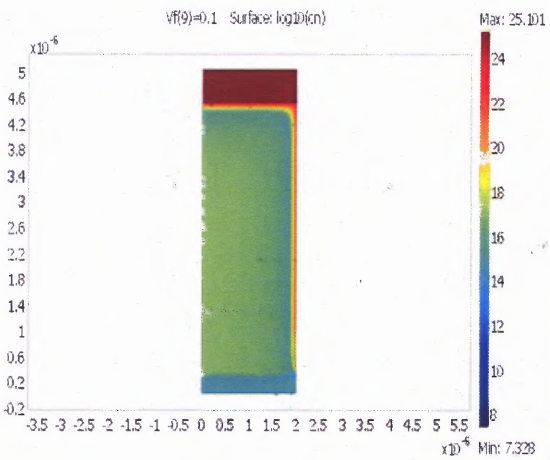

$3x10^{11}$ cm^{-2} Surface Charge on Right Side

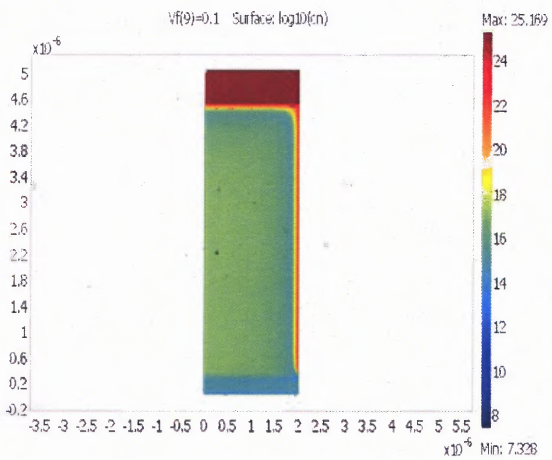

$5x10^{11}$ cm^{-2} Surface Charge on Right Side

Figure A.26 Electric concentration at 0.1 volts FB (illuminated) with BSF.

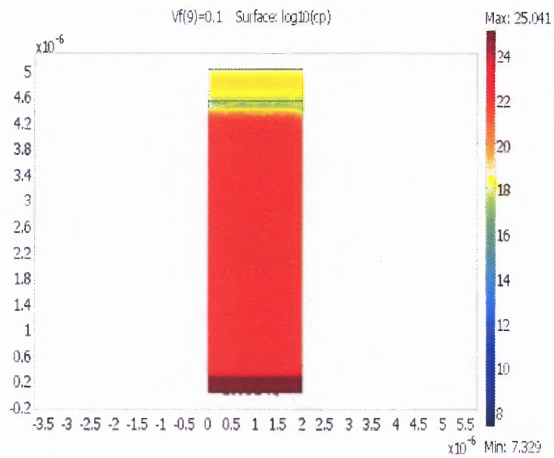

$5x10^{10}$ cm^{-2} Surface Charge on Right Side

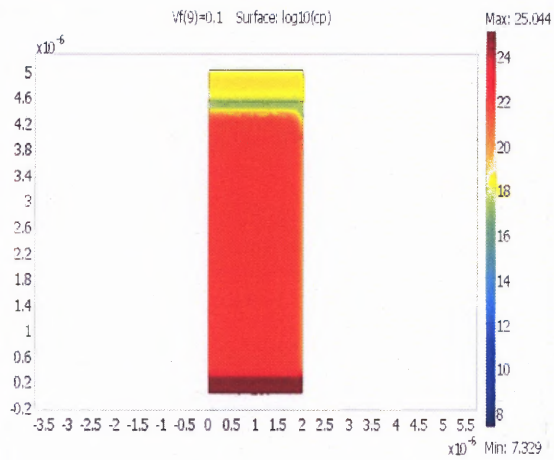

$1.25x10^{11}$ cm^{-2} Surface Charge on Right Side

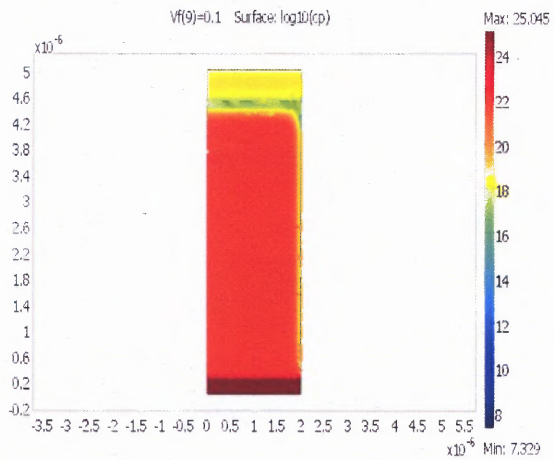

$1.75x10^{11}$ cm^{-2} Surface Charge on Right Side

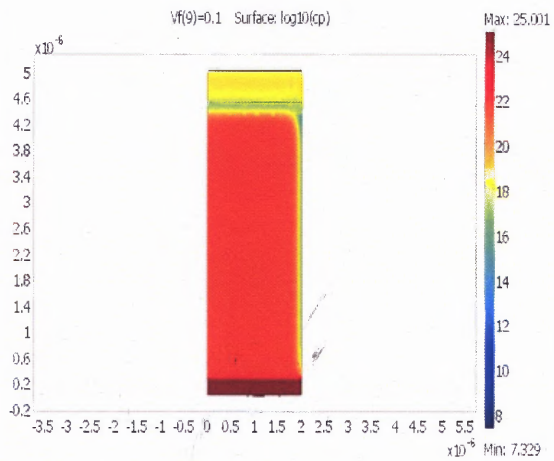

$2x10^{11}$ cm^{-2} Surface Charge on Right Side

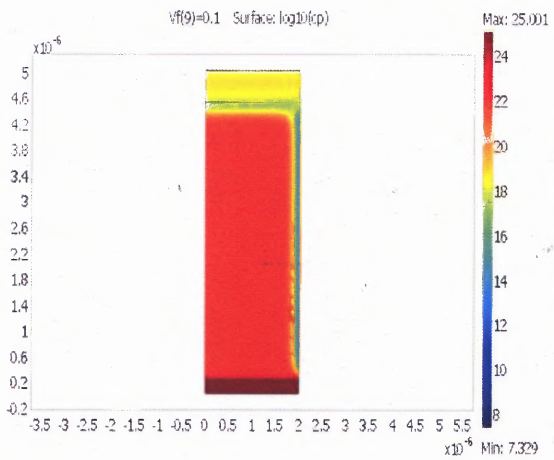

$3x10^{11}$ cm^{-2} Surface Charge on Right Side

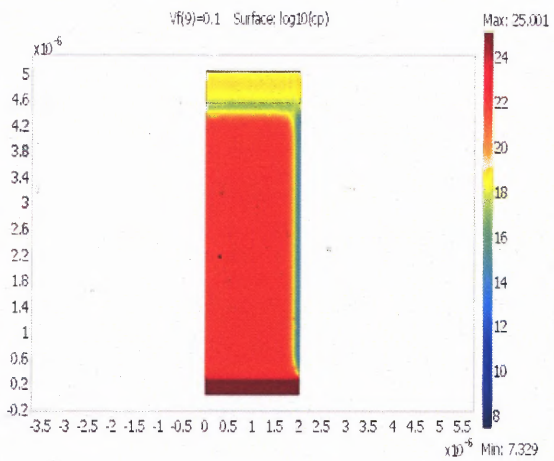

$5x10^{11}$ cm^{-2} Surface Charge on Right Side

Figure A.27 Hole concentration at 0.1 volts FB (illuminated) with BSF.

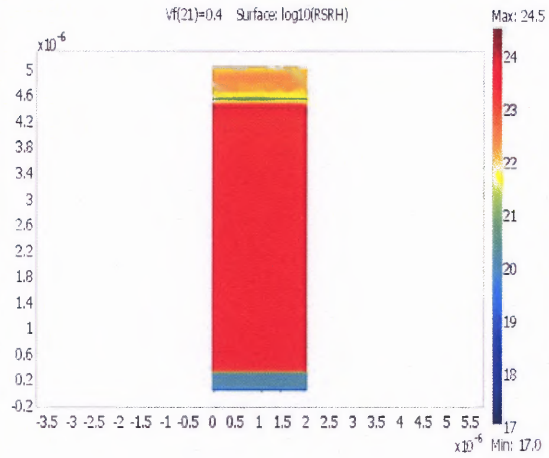

$5x10^{10}$ cm^{-2} Surface Charge on Right Side

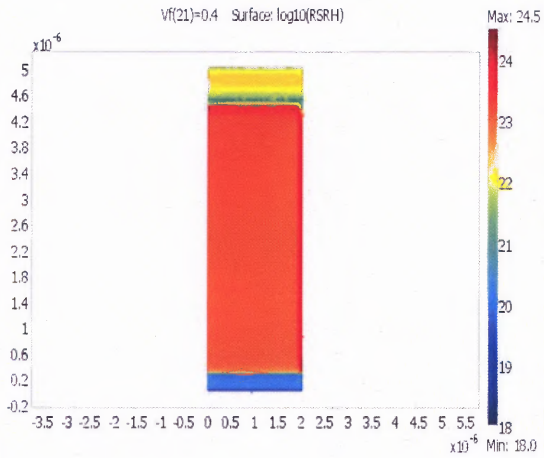

$1.25x10^{11}$ cm^{-2} Surface Charge on Right Side

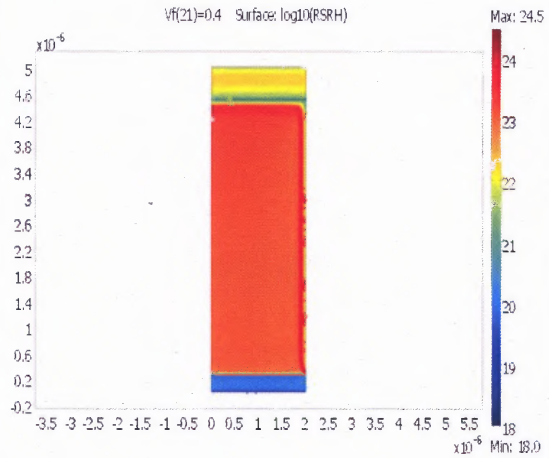

$1.75x10^{11}$ cm^{-2} Surface Charge on Right Side

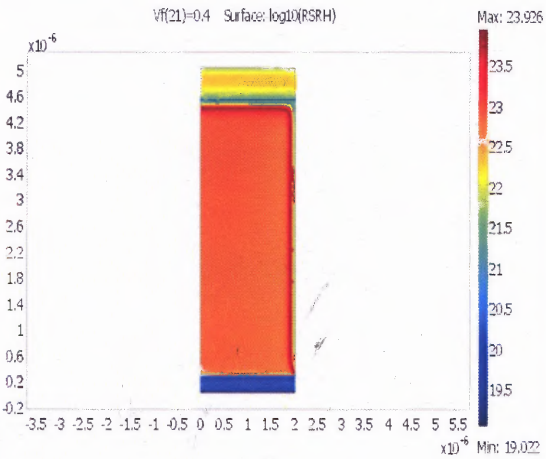

$2x10^{11}$ cm^{-2} Surface Charge on Right Side

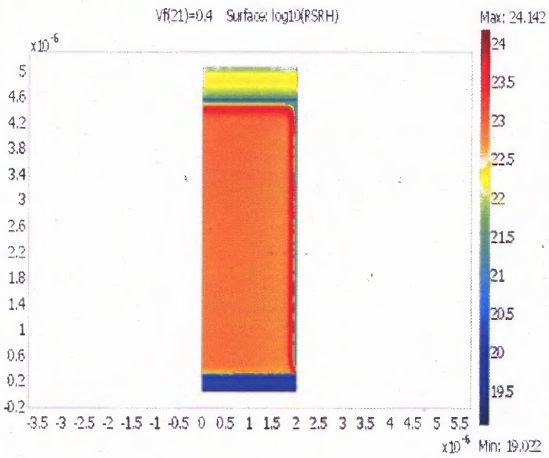

$3x10^{11}$ cm^{-2} Surface Charge on Right Side

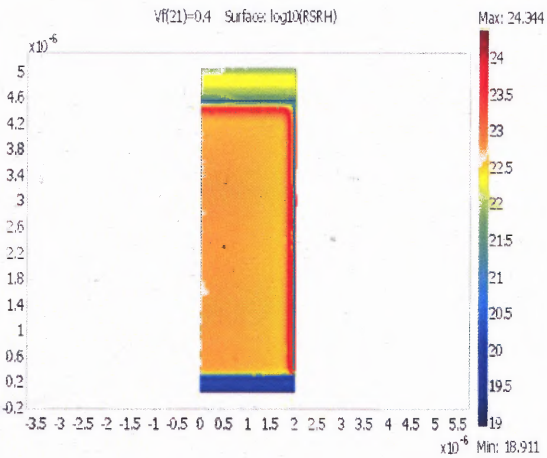

$5x10^{11}$ cm^{-2} Surface Charge on Right Side

Figure A.28 Bulk recombination rate at 0.4 volts FB (illuminated) with BSF.

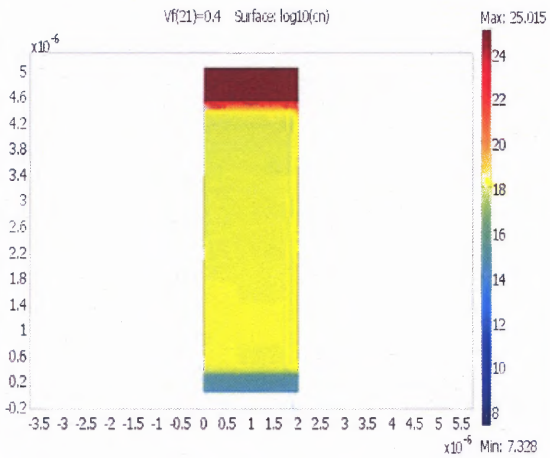

$5x10^{10}$ cm^{-2} Surface Charge on Right Side

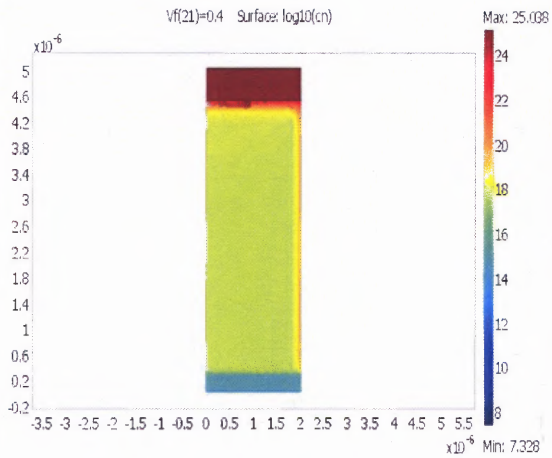

$1.25x10^{11}$ cm^{-2} Surface Charge on Right Side

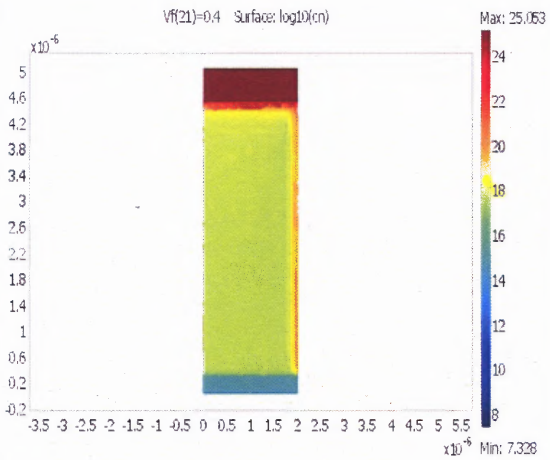

$1.75x10^{11}$ cm^{-2} Surface Charge on Right Side

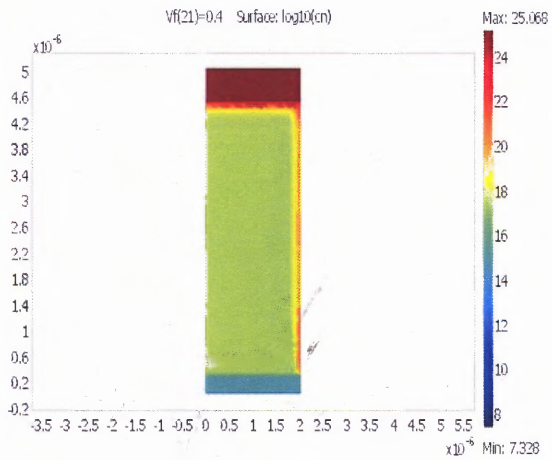

$2x10^{11}$ cm^{-2} Surface Charge on Right Side

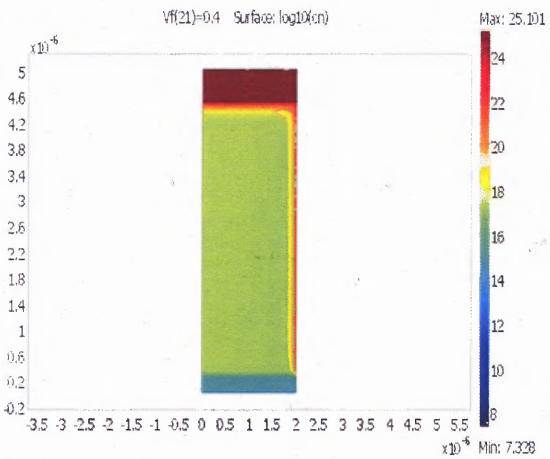

$3x10^{11}$ cm^{-2} Surface Charge on Right Side

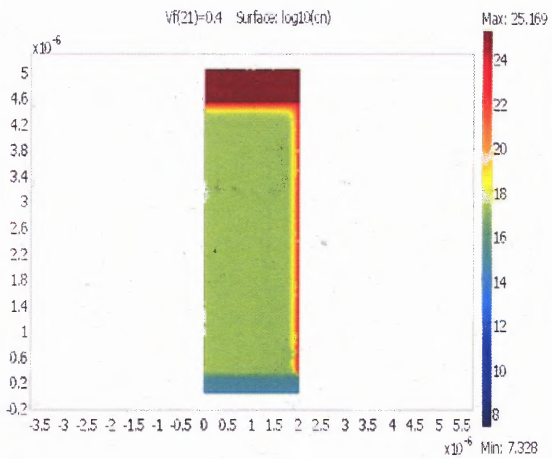

$5x10^{11}$ cm^{-2} Surface Charge on Right Side

Figure A.29 Electron concentration at 0.4 volts FB (illuminated) with BSF.

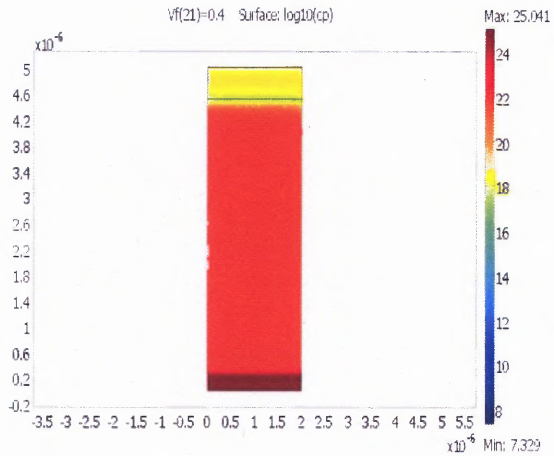

$5x10^{10}$ cm^{-2} Surface Charge on Right Side

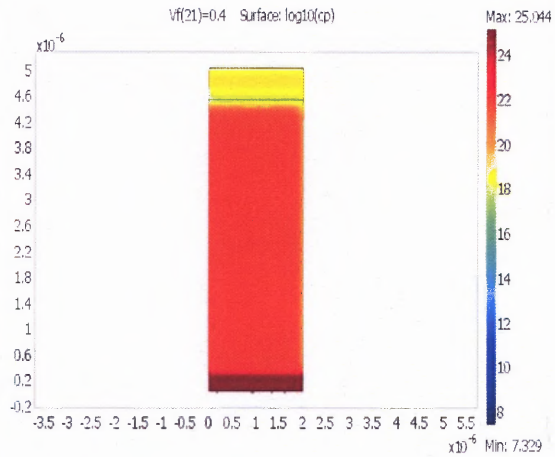

$1.25x10^{11}$ cm^{-2} Surface Charge on Right Side

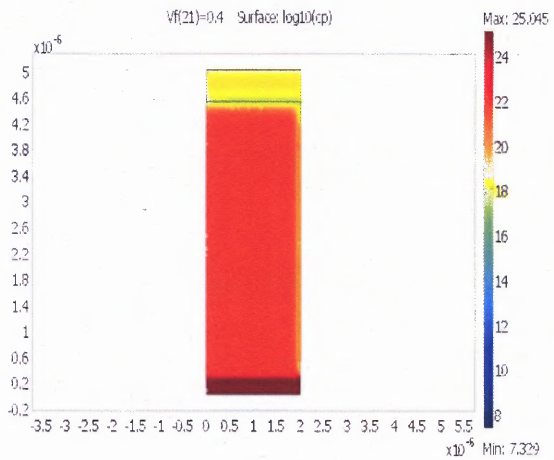

$1.75x10^{11}$ cm^{-2} Surface Charge on Right Side

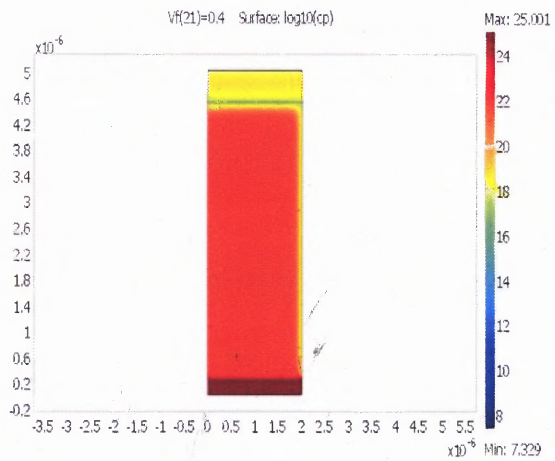

$2x10^{11}$ cm^{-2} Surface Charge on Right Side

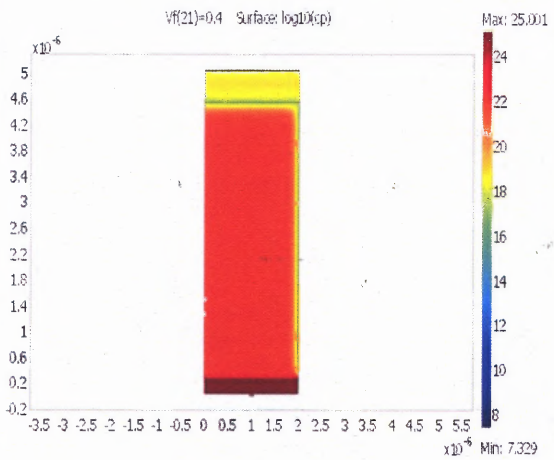

$3x10^{11}$ cm^{-2} Surface Charge on Right Side

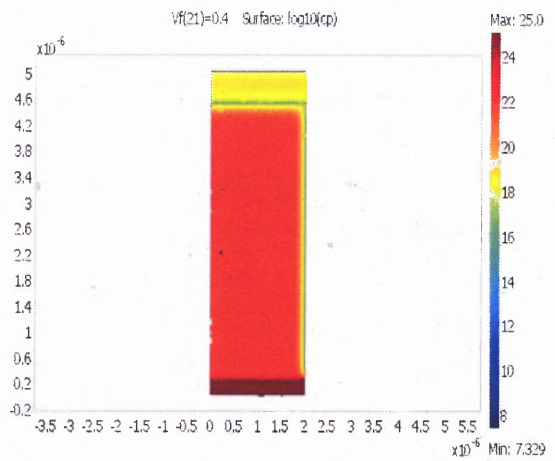

$5x10^{11}$ cm^{-2} Surface Charge on Right Side

Figure A.30 Hole concentration at 0.4 volts FB (illuminated) with BSF.

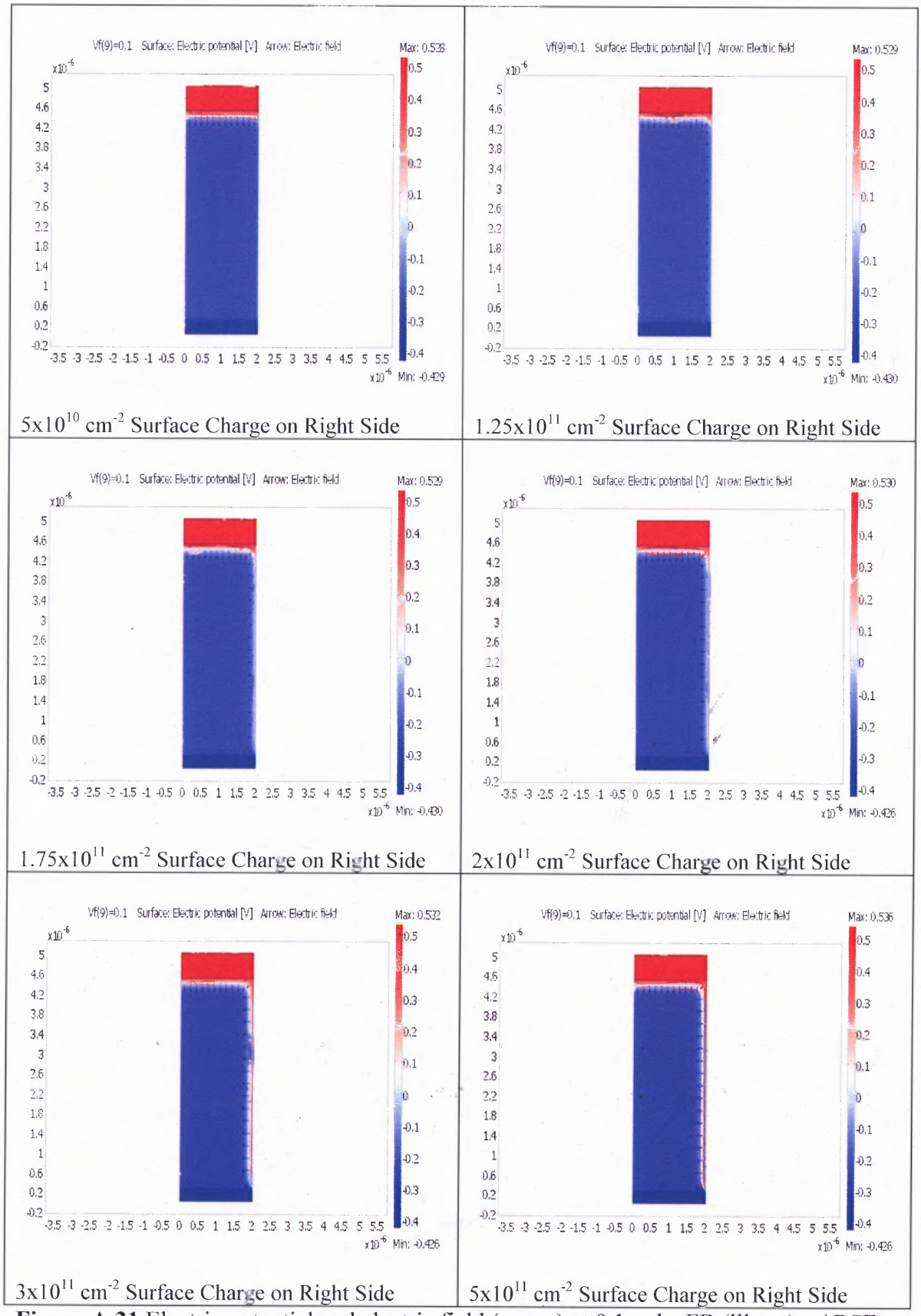

Figure A.31 Electric potential and electric field (arrow) at 0.1 volts FB (illum.) w/ BSF.

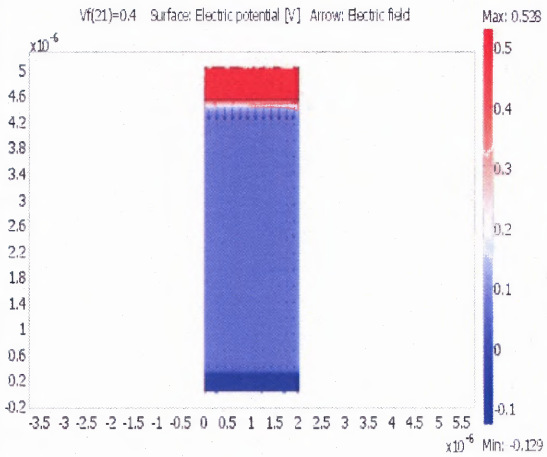

$5x10^{10}$ cm^{-2} Surface Charge on Right Side

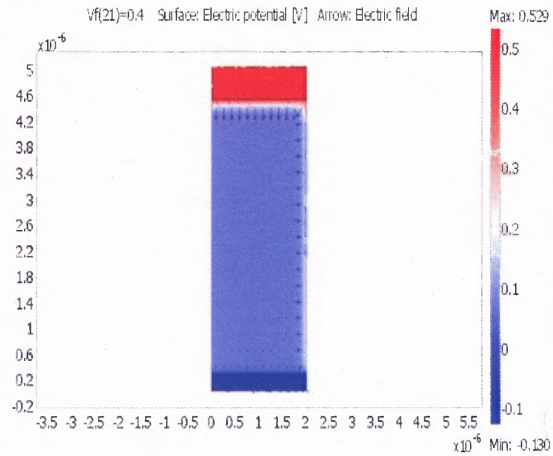

$1.25x10^{11}$ cm^{-2} Surface Charge on Right Side

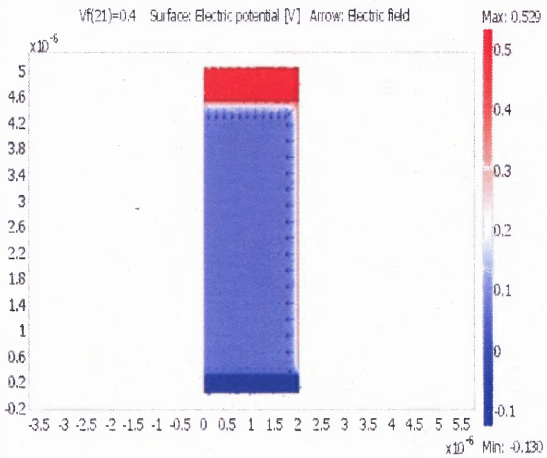

$1.75x10^{11}$ cm^{-2} Surface Charge on Right Side

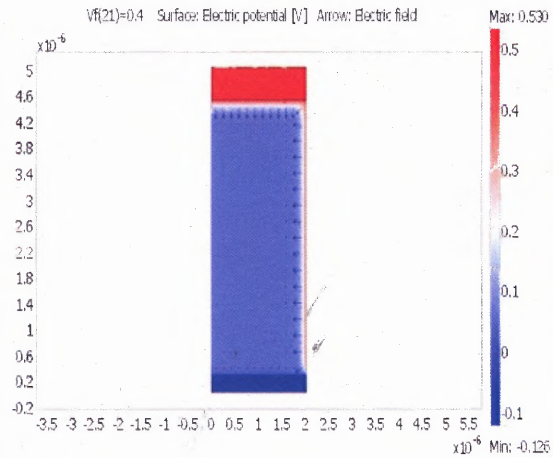

$2x10^{11}$ cm^{-2} Surface Charge on Right Side

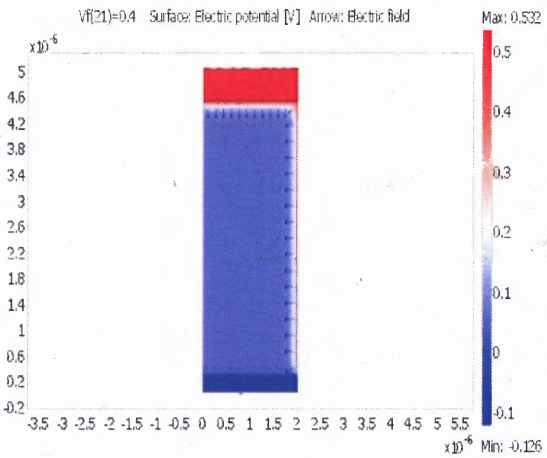

$3x10^{11}$ cm^{-2} Surface Charge on Right Side

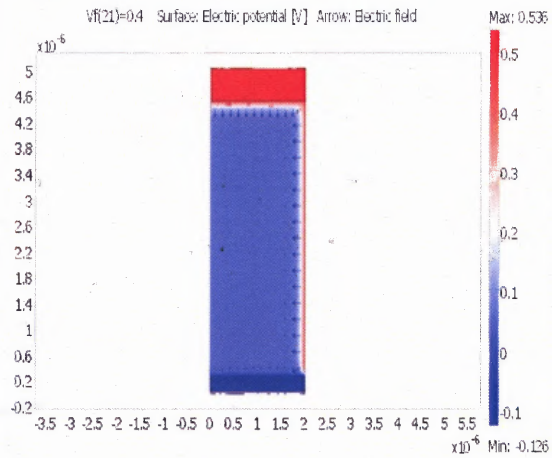

$5x10^{11}$ cm^{-2} Surface Charge on Right Side

Figure A.32 Electric potential and electric field (arrow) at 0.4 volts FB (illum.) w/ BSF.

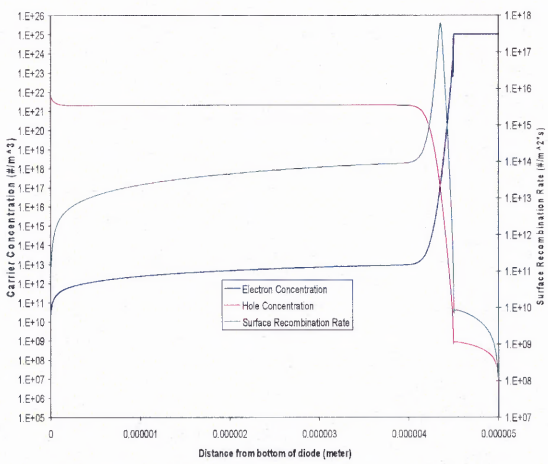

$5x10^{10}$ cm^{-2} Surface Charge on Right Side

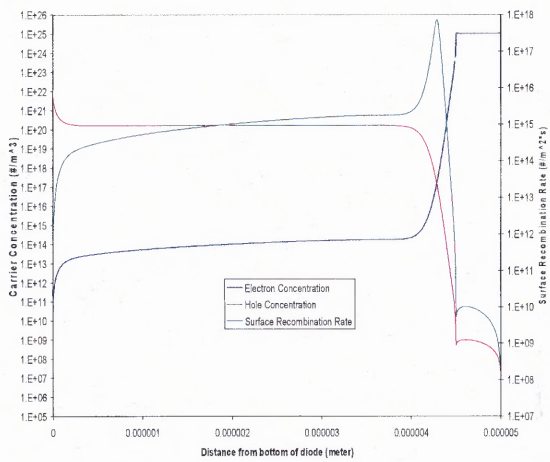

$1.25x10^{11}$ cm^{-2} Surface Charge on Right Side

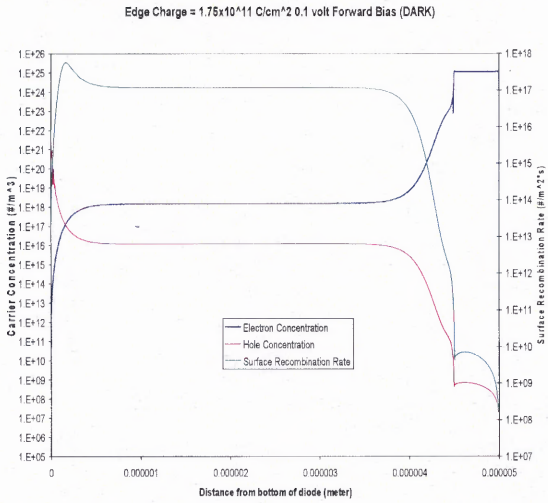

$1.75x10^{11}$ cm^{-2} Surface Charge on Right Side

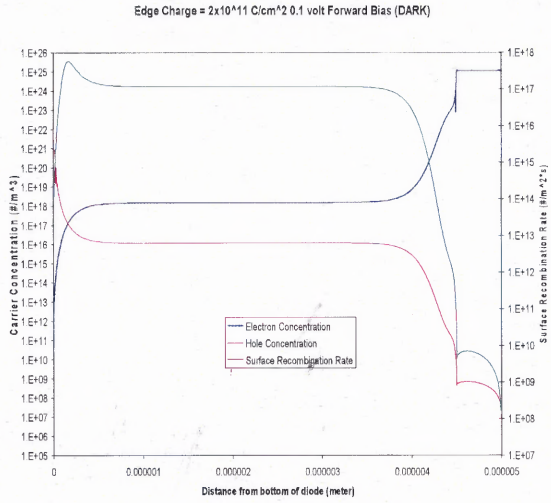

$2x10^{11}$ cm^{-2} Surface Charge on Right Side

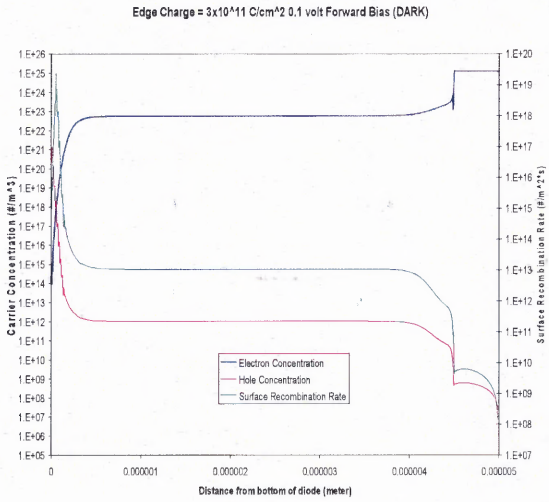

$3x10^{11}$ cm^{-2} Surface Charge on Right Side

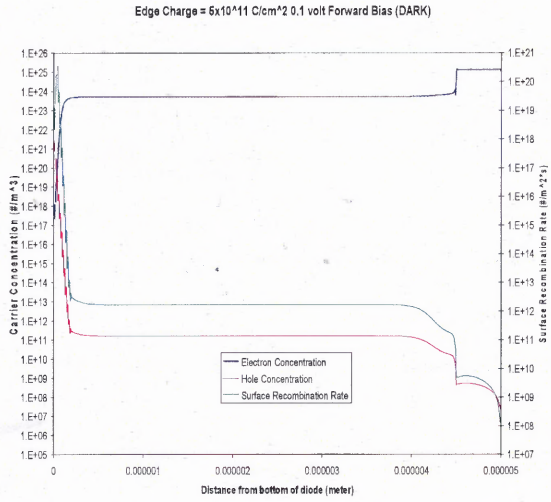

$5x10^{11}$ cm^{-2} Surface Charge on Right Side

Figure A.33 Surface recombination rate, electron & hole concentration 0.1 volts FB.

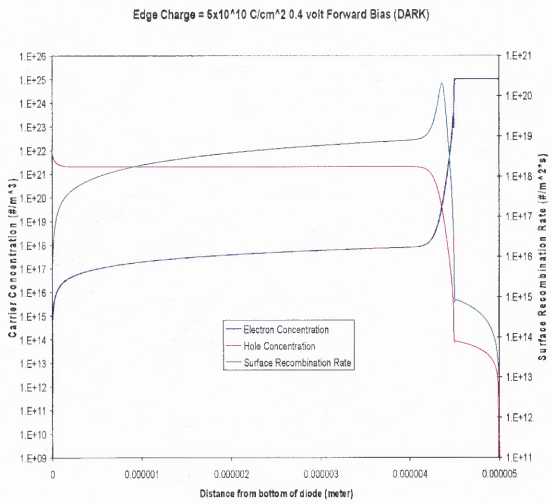

$5x10^{10}$ cm^{-2} Surface Charge on Right Side

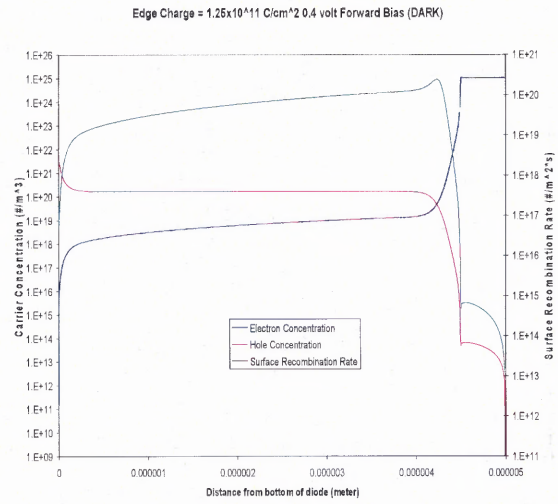

$1.25x10^{11}$ cm^{-2} Surface Charge on Right Side

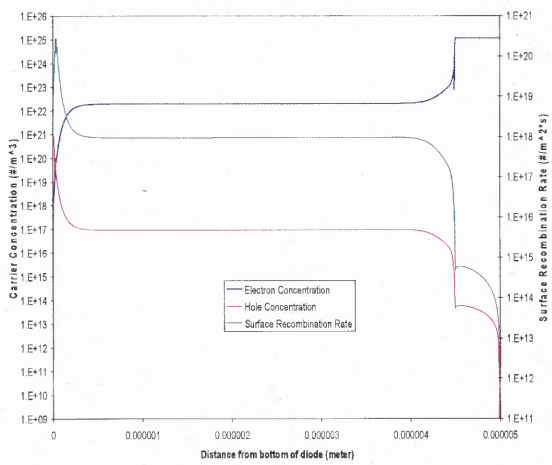

$1.75x10^{11}$ cm^{-2} Surface Charge on Right Side

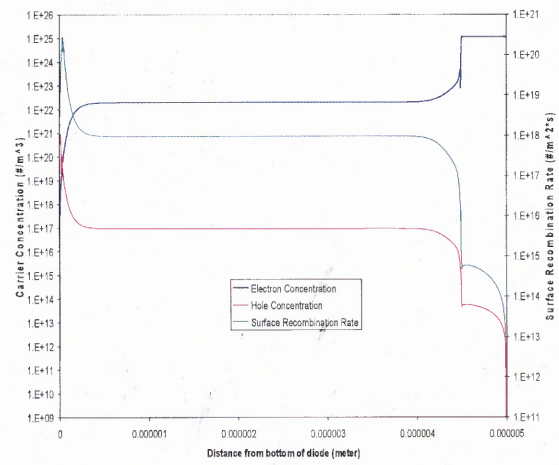

$2x10^{11}$ cm^{-2} Surface Charge on Right Side

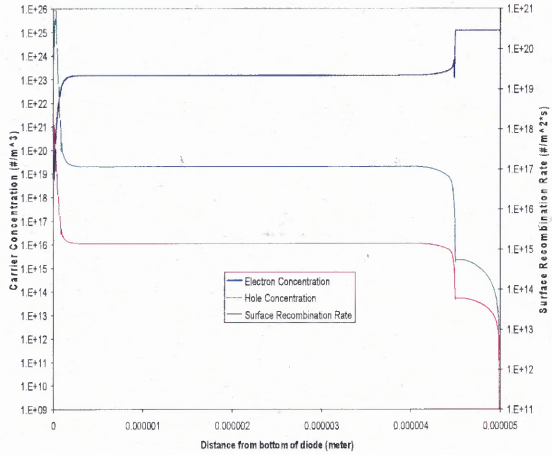

$3x10^{11}$ cm^{-2} Surface Charge on Right Side

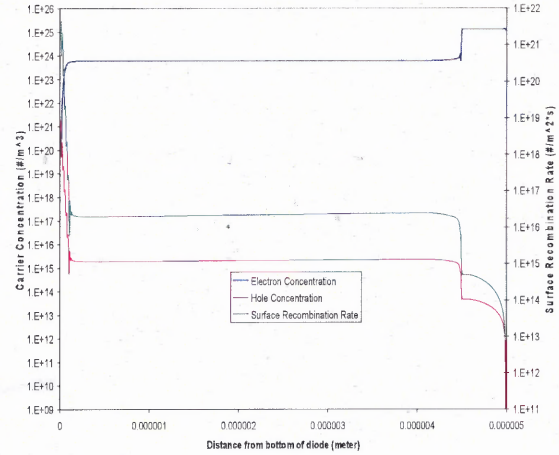

$5x10^{11}$ cm^{-2} Surface Charge on Right Side

Figure A.34 Surface recombination rate, electron & hole concentration 0.4 volts FB.

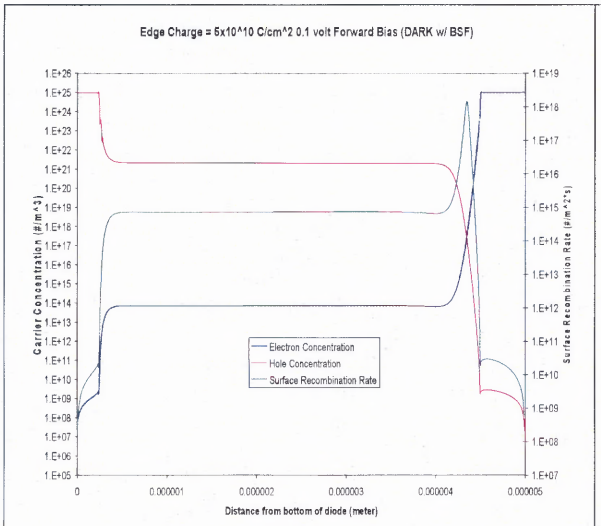

$5x10^{10}$ cm^{-2} Surface Charge on Right Side

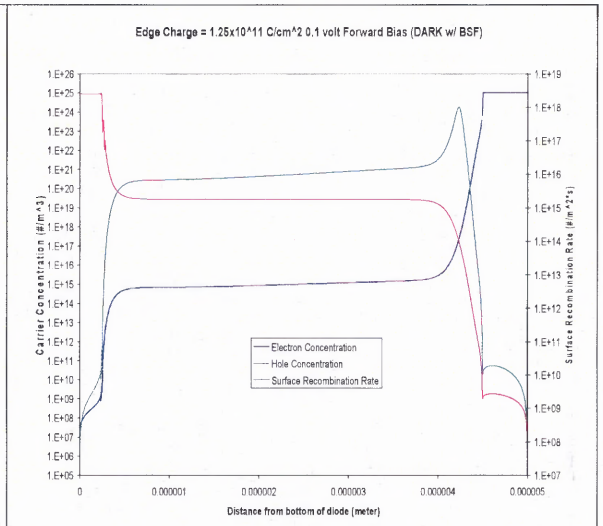

$1.25x10^{11}$ cm^{-2} Surface Charge on Right Side

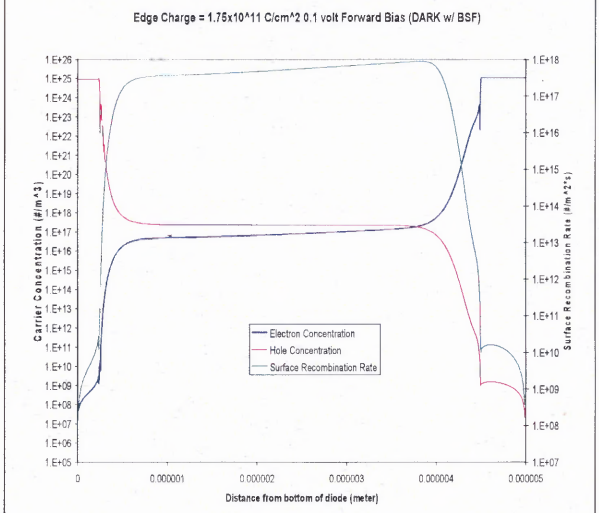

$1.75x10^{11}$ cm^{-2} Surface Charge on Right Side

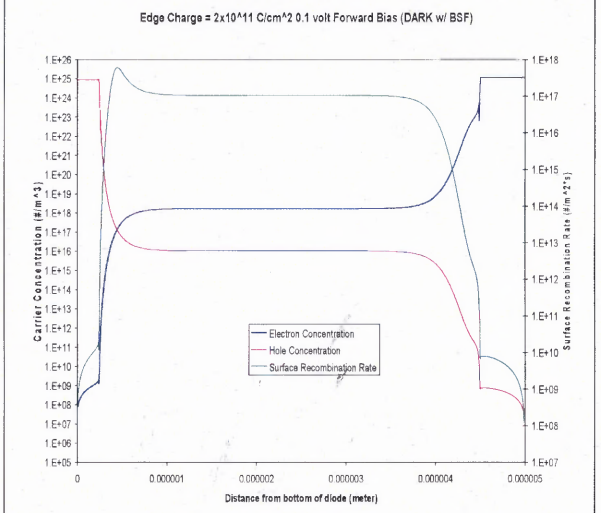

$2x10^{11}$ cm^{-2} Surface Charge on Right Side

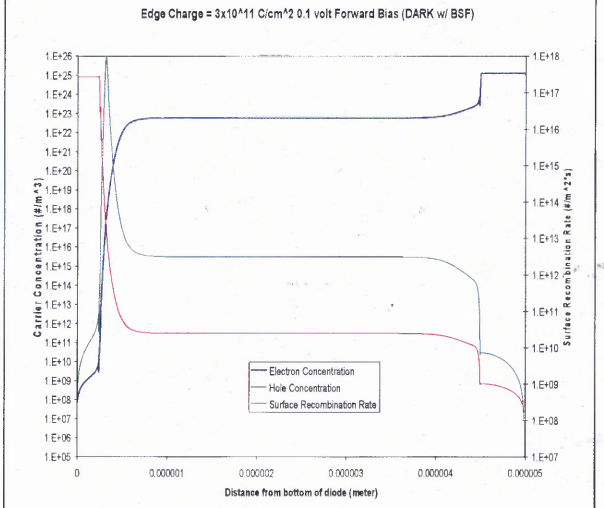

$3x10^{11}$ cm^{-2} Surface Charge on Right Side

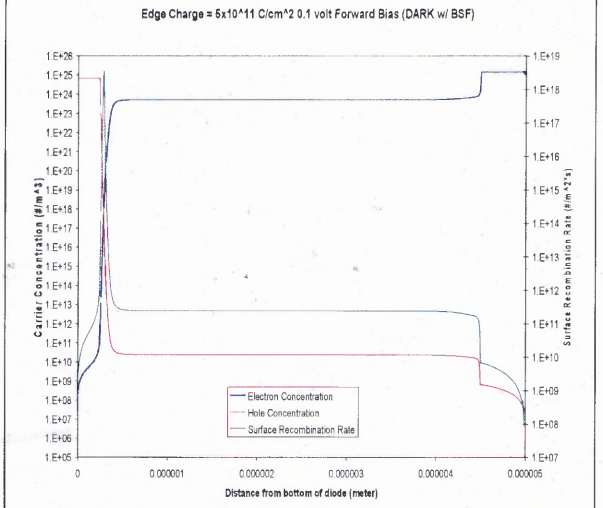

$5x10^{11}$ cm^{-2} Surface Charge on Right Side

Figure A.35 Surface recombination rate, electron & hole conc. 0.1 volts FB w/ BSF.

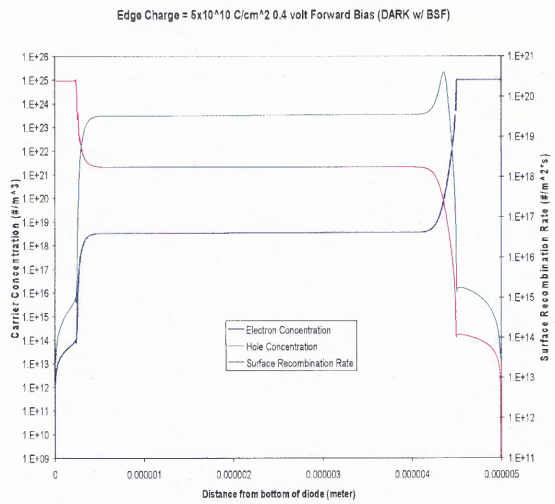

$5x10^{10}$ cm^{-2} Surface Charge on Right Side

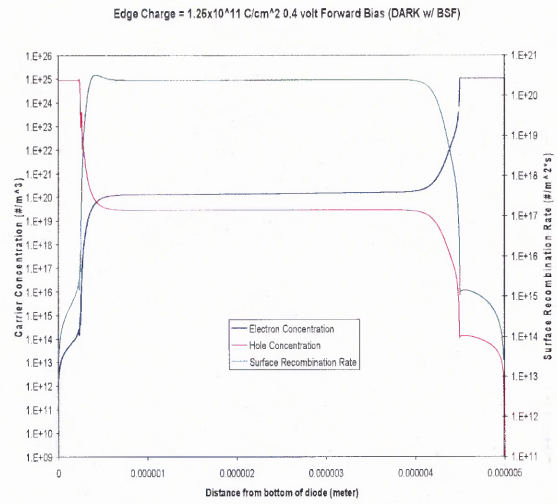

$1.25x10^{11}$ cm^{-2} Surface Charge on Right Side

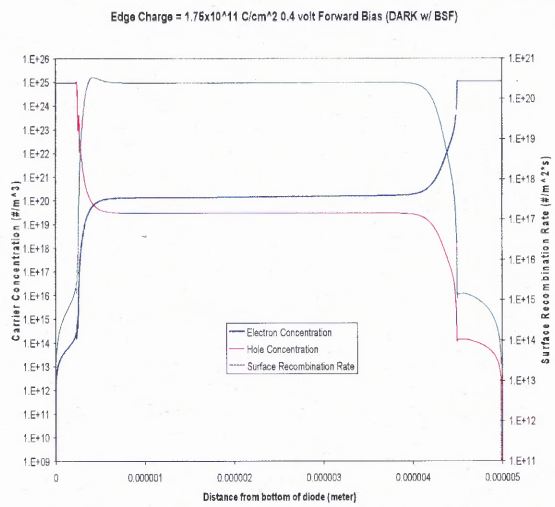

$1.75x10^{11}$ cm^{-2} Surface Charge on Right Side

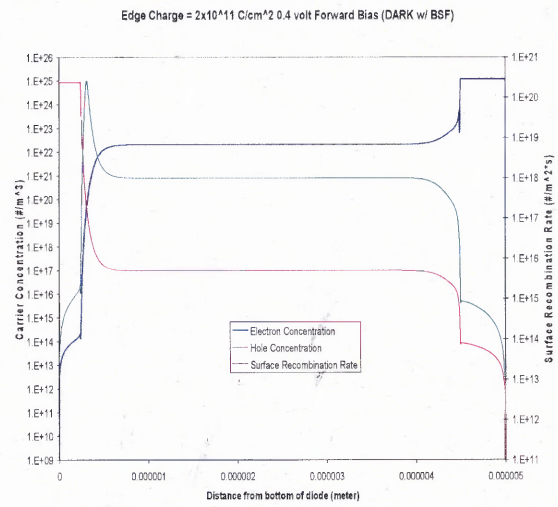

$2x10^{11}$ cm^{-2} Surface Charge on Right Side

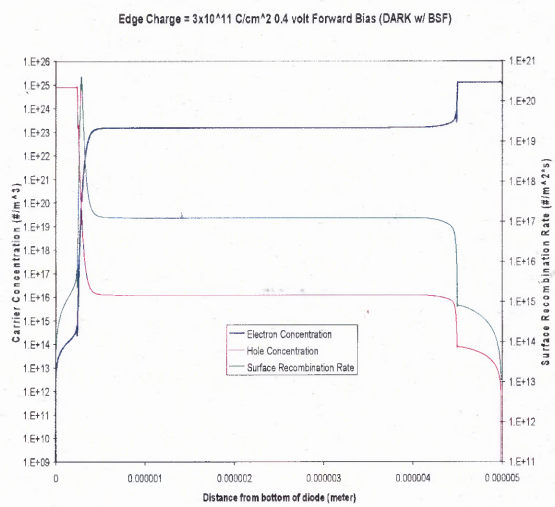

$3x10^{11}$ cm^{-2} Surface Charge on Right Side

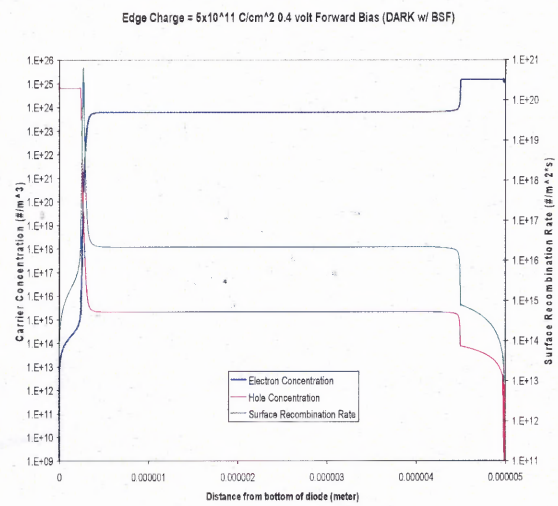

$5x10^{11}$ cm^{-2} Surface Charge on Right Side

Figure A.36 Surface recombination rate, electron & hole conc. 0.4 volts FB w/ BSF.

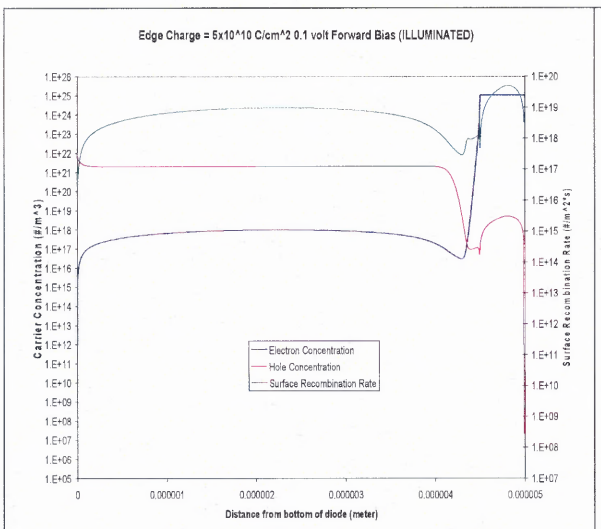

$5x10^{10}$ cm^{-2} Surface Charge on Right Side

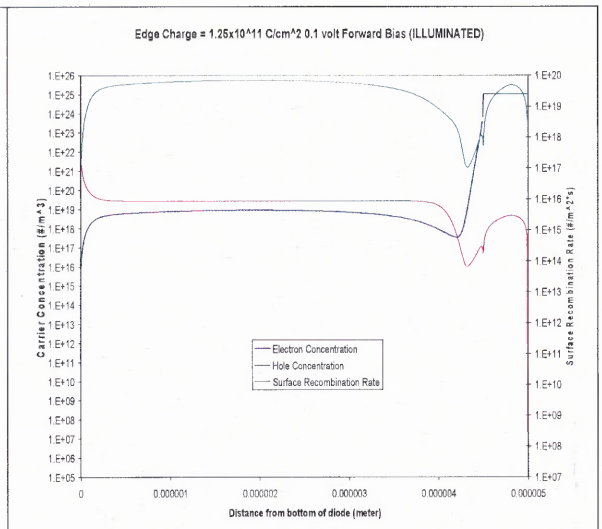

$1.25x10^{11}$ cm^{-2} Surface Charge on Right Side

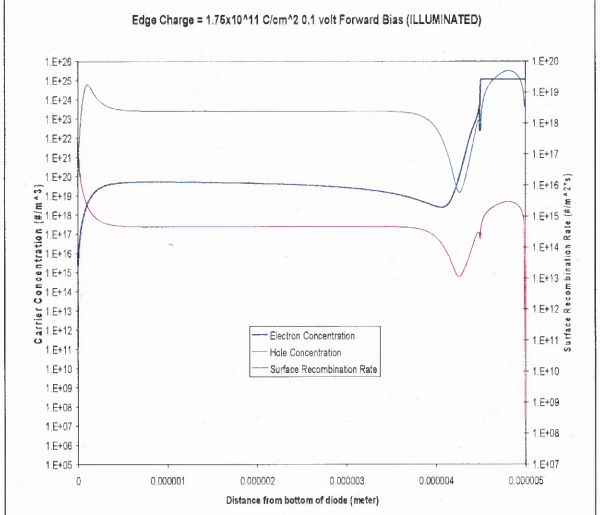

$1.75x10^{11}$ cm^{-2} Surface Charge on Right Side

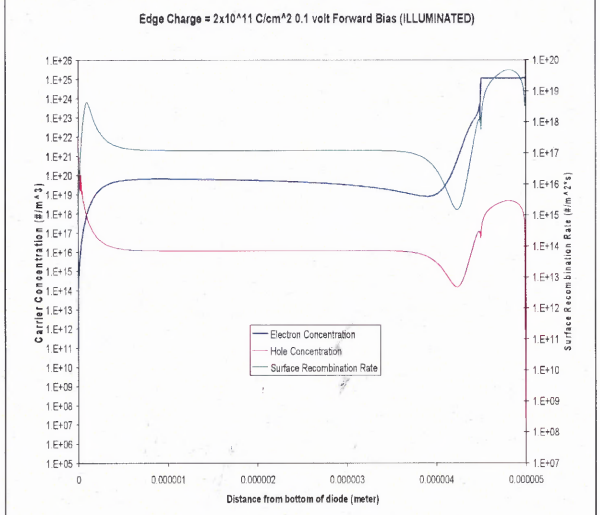

$2x10^{11}$ cm^{-2} Surface Charge on Right Side

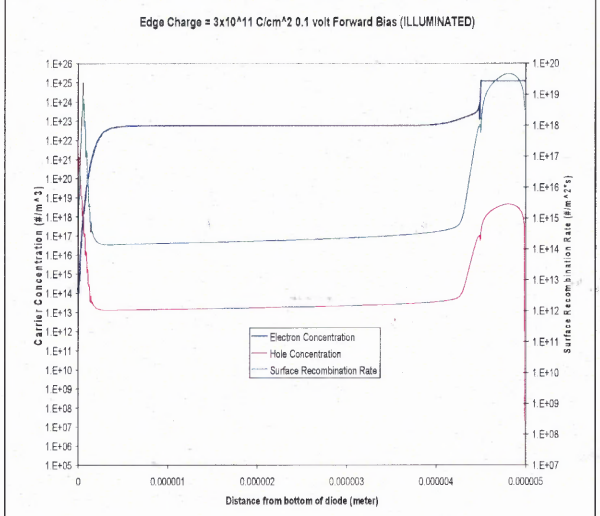

$3x10^{11}$ cm^{-2} Surface Charge on Right Side

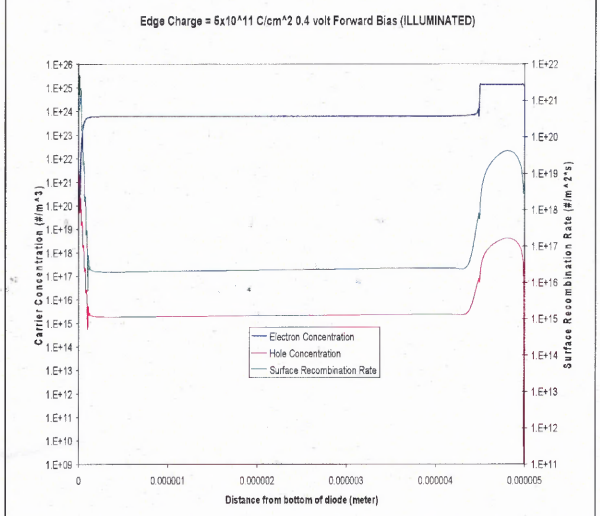

$5x10^{11}$ cm^{-2} Surface Charge on Right Side

Figure A.37 Surface recombination rate, electron & hole conc. 0.1 volts FB (illum.).

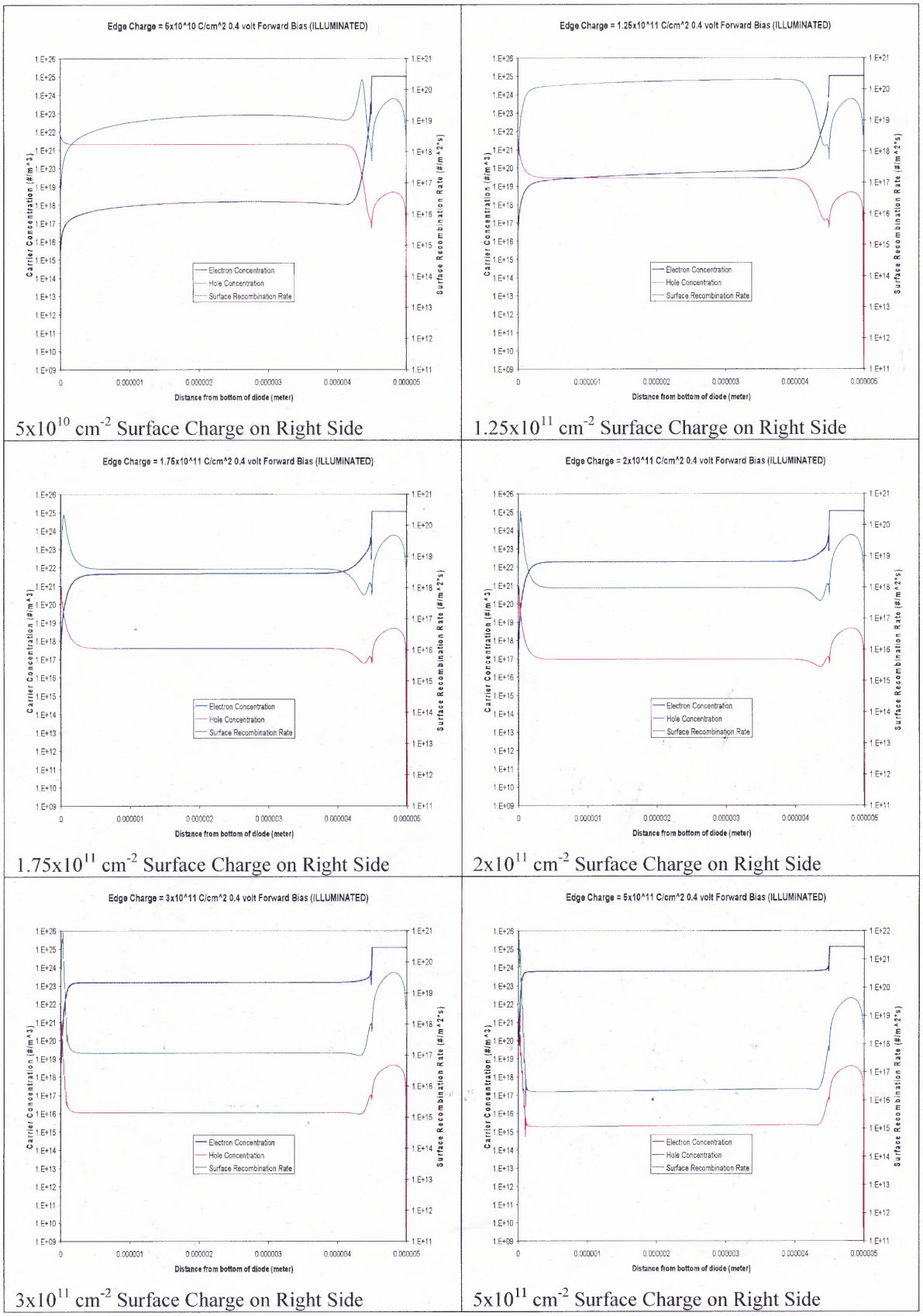

Figure A.38 Surface recombination rate, electron & hole conc. 0.4 volts FB (illum.).

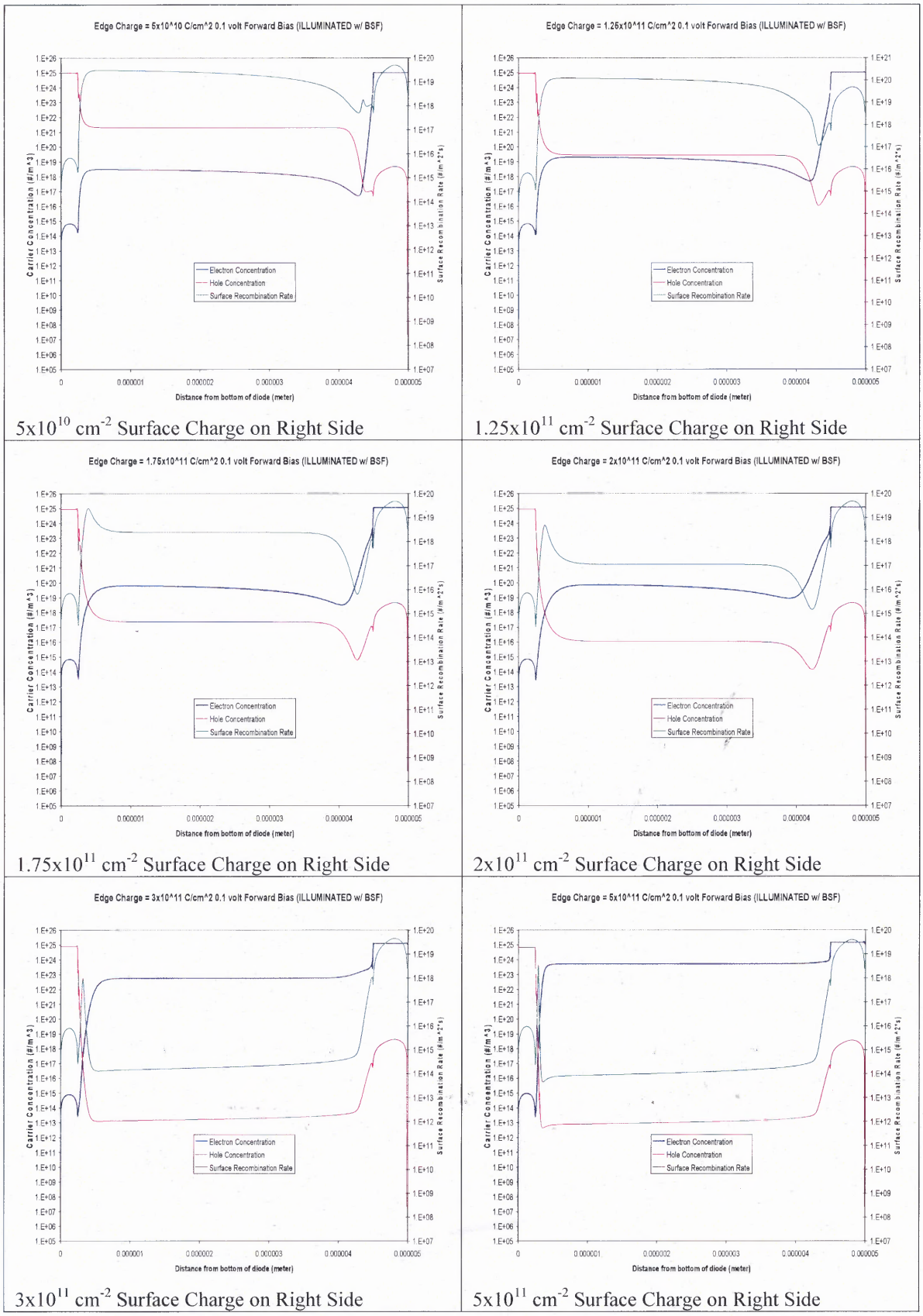

$5x10^{10}$ cm^{-2} Surface Charge on Right Side

$1.25x10^{11}$ cm^{-2} Surface Charge on Right Side

$1.75x10^{11}$ cm^{-2} Surface Charge on Right Side

$2x10^{11}$ cm^{-2} Surface Charge on Right Side

$3x10^{11}$ cm^{-2} Surface Charge on Right Side

$5x10^{11}$ cm^{-2} Surface Charge on Right Side

Figure A.39 Surface recomb. rate, electron & hole conc. 0.1 volts FB (illum. w/ BSF).

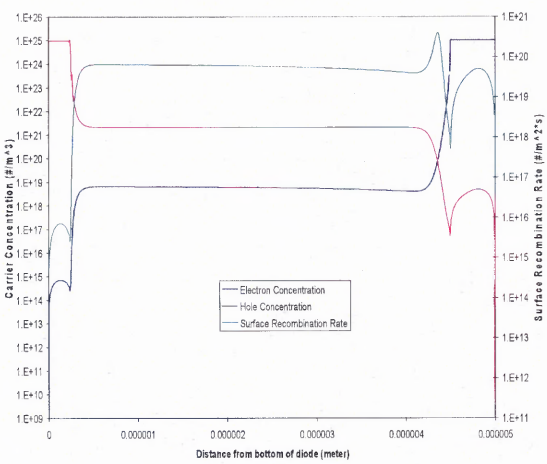

$5x10^{10}$ cm^{-2} Surface Charge on Right Side

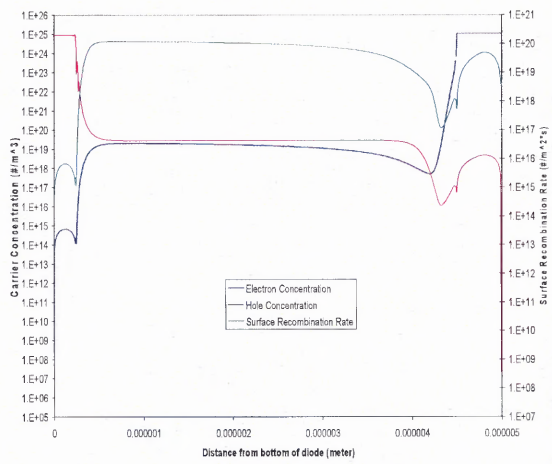

$1.25x10^{11}$ cm^{-2} Surface Charge on Right Side

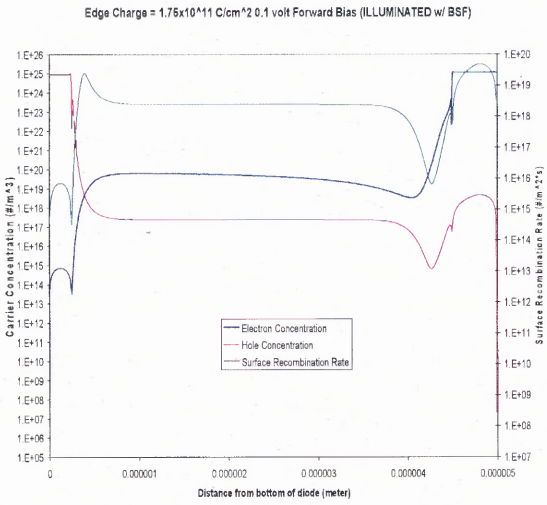

$1.75x10^{11}$ cm^{-2} Surface Charge on Right Side

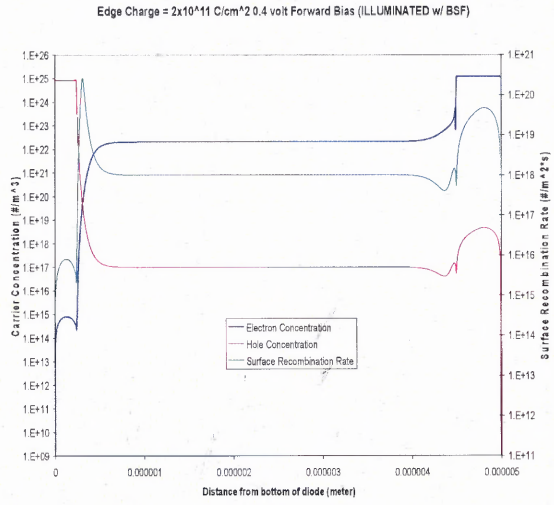

$2x10^{11}$ cm^{-2} Surface Charge on Right Side

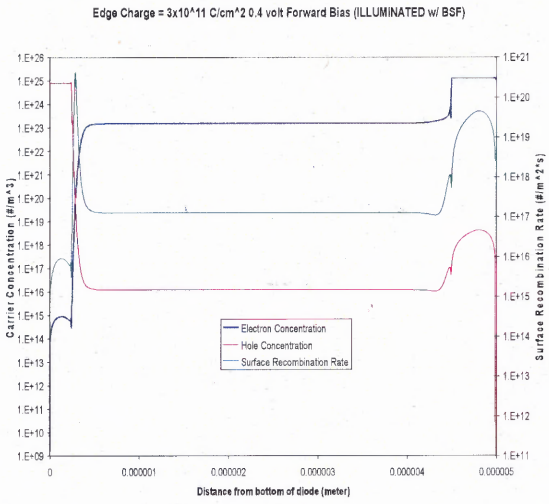

$3x10^{11}$ cm^{-2} Surface Charge on Right Side

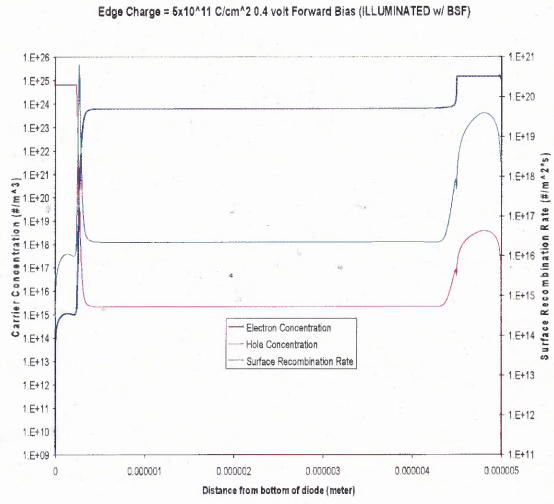

$5x10^{11}$ cm^{-2} Surface Charge on Right Side

Figure A.40 Surface recomb. rate, electron & hole conc. 0.4 volts FB (illum. w/ BSF).

REFERENCES

1. Tim Jackson and Mark Oliver, *Energy Policy* **28**, 983-988 (2000).

2. Arnulf Jager-Waldau, *Renewable & Sustainable Energy Reviews* **11**, 1414-1437 (2007).

3. Staffan Jacobsson and Volkmar Lauber, *Energy Policy* **34**, 256-276 (2006).

4. Tariq Muneer, Muhammad Asif, and Saima Munawwar, *Renewable & Sustainable Energy Reviews* **9**, 444-473 (2005).

5. Ray Boyer *et al. Annual Energy Review 2006* **DOE/EIA-0384**, (2007).

6. Peter Woditsch and Wolfgang Koch *Solar Energy Materials & Solar Cells* **72**, 11-26 (2002).

7. Bhushan Sopori, in *16th Workshop on Crystalline Silicon Solar Cells and Modules: Materials and Processes*, Denver, United States of America, 2006, p. 1.

8. J. Degoulange, I. Perichaud, C. Trassy, and S. Martinuzzi, *Solar Energy Materials & Solar Cells* (2008), doi:10.1016/j.solmat.2008.04.20.

9. W.G.J.H.M. van Sark, G.W. Brandsen, M. Fleuster, and M.P. Hekkert, *Energy Policy* **35**, 3121-3125 (2007).

10. Alvin D. Compaan, *Solar Energy Materials & Solar Cells* **90**, 2170-2180 (2006).

11. Lawrence L. Kazmerski, *Journal of Electron Spectroscopy and Related Phenomena* **150**, 105-135 (2006).

12. Andrea Feltrin and Alex Freundlich, *Renewable Energy* **33**, 180-185 (2008).

13. Jack Hanoka, in *16th Workshop on Crystalline Silicon Solar Cells and Modules: Materials and Processes*, Denver, United States of America, 2006, pp. 123-124.

14. K. Bilen *et al.*, *Renewable & Sustainable Energy Reviews* **12**, 1529-1561 (2008).

15. Martin A. Green, *Solar Cells: Operating Principles, Technology and Applications* (The University of New South Wales, Kensington, 1998), p. 43.

16. Ben G. Streetman and Sanjay Banerjee, *Solid State Electronics*, 5th ed. (Prentice Hall, Inc., Upper Saddle River, 2000), p. 109.

17. Ben G. Streetman and Sanjay Banerjee, *Solid State Electronics*, 5th ed. (Prentice Hall, Inc., Upper Saddle River, 2000), pp. 159-160.

18. Martin A. Green, *Silicon Solar Cells: Advanced Principles & Practice*, Centre for Photovoltaic Devices and Systems University of New South Wales, Sydney, 1995), pp. 205-236.

19. Ben G. Streetman and Sanjay Banerjee, *Solid State Electronics*, 5th ed. (Prentice Hall, Inc., Upper Saddle River, 2000), pp. 159-176.

20. Martin A. Green, *Solar Cells: Operating Principles, Technology and Applications* (The University of New South Wales, Kensington, 1998), p. 76.

21. Martin A. Green, *Solar Cells: Operating Principles, Technology and Applications* (The University of New South Wales, Kensington, 1998), pp. 54-58.

22. Martin A. Green, *Solar Cells: Operating Principles, Technology and Applications* (The University of New South Wales, Kensington, 1998), p. 164.

23. C. Zechner, P. Fath, G. Willeke, and E. Bucher, *Solar Energy Materials & Solar Cells* **51**, 255-267 (1998).

24. Dieter K. Schroder, *Semiconductor Material and Device Characterization*, 3rd ed. (John Wiley & Sons, Inc., Hoboken, 2006), pp. 389-401.

25. Dieter K. Schroder, *Semiconductor Material and Device Characterization*, 3rd ed. (John Wiley & Sons, Inc., Hoboken, 2006), pp. 391-392.

26. R.N. Hall, *Physical Review* **87**, 387 (1952).

27. W. Shockley and W.T. Read, Jr., *Physical Review* **87** (5), 835-842 (1952).

28. Ben G. Streetman and Sanjay Banerjee, *Solid State Electronics*, 5th ed. (Prentice Hall, Inc., Upper Saddle River, 2000), pp. 117-120.

29. Dieter K. Schroder, *Semiconductor Material and Device Characterization*, 3rd ed. (John Wiley & Sons, Inc., Hoboken, 2006), p. 391.

30. A.S. Grove, B.E. Deal, E.H. Snow and C.T. Sah, *Solid-State Electronics* **8**, 145-163 (1965).

31. D.J. Fitzgerald and A.S. Grove, *Surface Science* **9**, 347-369 (1968).

32. Armin G. Aberle *et al.*, *Journal of Applied Physics* **77** (7), 3491-3504 (1995).

33. M. Kunst, O. Abdallah, and F. Wunsch, *Solar Energy Materials & Solar Cells* **72**, 335-341 (2002).

34. Jed Brody and Ajeet Rohatgi, *Solid-State Electronics* **45**, 1549-1557 (2001).

35. B. Ba, M. Kane, and J. Sarr, *Solar Energy Materials & Solar Cells* **80**, 143-154 (2003).

36. Wyatt K. Metzger, *Solar Energy Materials & Solar Cells* **92**, 1123-1135 (2008).

37. Dragica Vasileska and Stephen M. Goodnick, *Computational Electronics* (Morgan & Claypool Publishers, United States of America, 2006), pp. 16-35.

38. S.J. Robinson, S.R. Wenham, P.P. Altermatt, A.G. Aberle, G. Heiser, and M.A. Green, *Journal of Applied Physics* **78** (7), 4740-4754 (1995).

39. H.K. Gummel, *IEEE Transactions on Electron Devices* **11**, 455-465 (1964).

40. Robert McConnell, *reFocus* "Concentrator Photovoltaic Technologies: Review and Market Prospects" **July/August**, 35-39 (2005).

41. P. Manshandan and L.J. Geerligs, in *20th European Photovoltaic Solar Energy Conference and Exhibition*, Barcelona, Spain, 2005.

42. K. Mahfoud, B. Pivac, and J.C. Muller, *Solar Energy Materials and Solar Cells* **46**, 123-131 (1997).

43. P. Rupnowski and B. Sopori, in *33rd IEEE Photovoltaic Specialists Conference*, San Diego, United States of America, 2008, pp. 1-4.

44. A. Buczkowski, G. Rozgonyi, and F. Shimura, *Journal of the Electrochemical Society* **140** (11), 3240-3245 (1993).

45. B.L. Sopori, *Applied Physics Letters* **52** (20), 1718-1720 (1988).

46. Dieter K. Schroder, *Semiconductor Material and Device Characterization*, 3rd ed. (John Wiley & Sons, Inc., Hoboken, 2006), pp. 416-417.

47. T. Buonassisi, *et al.*, *Applied Physics Letters* **87**, 044101-1 – 3 (2005).

48. Bhushan Sopori, Chuan Li, S. Narayanan, and D, Carlson, in *MRS 2005 Spring Symposium Proceedings: Symposium E: Semiconductor Defect Engineering – Materials, Synthetic Structures and Devices*, San Francisco, United States of America, pp. 233-240.

49. J.Lagowski, P. Edelman, M. Dexter, and W. Henley, *Semiconductor Science and Technology* **7**, A185-A192 (1992).

50. J. Tousek, S. Dolhov, and J. Touskova, *Solar Energy Materials & Solar Cells* **76**, 205-210 (2003).

51. J. Tousek, D. Kindl, J. Touskova, S.Dolhov, *Solar Energy Materials & Solar Cells* **69**, 297-302 (2001).

52. J.A. Eikelboom, C. Leguijt, C.F.A. Frumau, and A.R. Burgers, *Solar Energy Materials & Solar Cells* **36**, 169-185 (1995).

53. G. Citarella, S. von Aichberger, and M. Kunst, *Materials Science & Engineering B* **B91-92**, 224-228 (2002).

54. Michio Tajima, Hiroki Sugimoto, Masaaki Inoue, and Kiyoto Araki, in *16th Workshop on Crystalline Silicon Solar Cells and Modules: Materials and Processes*, Denver, United States of America, 2006, pp. 58-66.

55. H.Z. Song, *Solid State Communications* **12** (11), 813-816 (1997).

56. R. Bruggemann and S. Reynolds, *Journal of Non-Crystalline Solids* **352**, 1888-1891 (2006).

57. Ronald A. Sinton and Andreas Cuevas, *Applied Physics Letters* **69** (17), 2510-2512 (1996).

58. J. Gervais, O. Palais, L. Clerc, and S. Martinuzzi, *Review of Scientific Instruments* **70** (10), 4044-4046 (1999).

59. Dieter K. Schroder, *Semiconductor Material and Device Characterization*, 3rd ed. (John Wiley & Sons, Inc., Hoboken, 2006), p. 417.

60. O. Palais, E. Yakimov, and S. Martinuzzi, *Materials Science& Engineering B* **B91-92**, 216-219 (2002).

61. B.L. Sopori, *Journal of Applied Physics* **64** (10), 5264-5266 (1988).

62. P.A. Tove, *Journal of Physics D: Applied Physics* **15** (4), 517-536 (1982).

63. W. Shockley, W.W. Hooper, H.J. Queisser, and W. Schroen, *Surface Science* **2**, 277-287 (1964).

64. Ben G. Streetman and Sanjay Banerjee, *Solid State Electronics*, 5th ed. (Prentice Hall, Inc., Upper Saddle River, 2000), pp. 255-316.

65. P.A. Tove, S.A. Hyder, and G. Susila, *Solid-State Electronics* **16**, 513-521 (1973).

66. Andrey Kamarou, Alexander Komarov, Pawel Zukowski, *Vacuum Surface Engineering, Surface Instrumentation & Vacuum Technology* **63**, 609-612 (2001).

67. P.A. Stolk, *et al.*, *Applied Physics Letters* **68** (1), 51-53 (1996).

68. Scott A. McHugo, *et al.*, *Journal of Applied Physics* **89** (8), 4282-4288 (2001).

69. M.D. Negoita and T.Y. Tan, *Journal of Applied Physics* **94** (8), 5064-5070 (2003).

70. R. Hall and J.P. White, *Solid-State Electronics* **8**, 211-226 (1965).

71. J.C. Manifacier, P. Parot, and J.P. Fillard, *Journal of Electrostatics* **3**, 203-212 (1977).

72. C.Y. Chang and S.M. Sze, *Solid-State Electronics* **13**, 727-740 (1970).

73. A.Y.C. Yu and E.H. Snow, *Journal of Applied Physics* **39** (7), 3008-3016 (1968).

74. F. Conti and M. Conti, *Solid-State Electronics* **15**, 93-105 (1972).

75. M.M. Atalla, A.R. Bray, and R. Linder, in *International Convention on Transistors and Associated Semiconductor Devices, 25th May, 1959*, London, England, 1960, pp. 1130-1137.

76. Ernst L. Wall, *Solid-State Electronics* **19**, 389-396 (1976).

77. A.J. Willis, *Solid-State Electronics* **33** (5), 531-536 (1990).

78. O. Militaru, *Nuclear Instruments & Methods in Physics Research Section A* **A 439**, 262-269 (2000).

79. J.L. Saltich and L.E. Clark, *Solid-State Electronics* **13**, 857-863 (1970).

80. Ming L. Tarng and Jacques I. Pankove, in *IEEE Transactions on Electron Devices* **ED-26** (11), 1728-1734 (1979).

81. Bhushan Sopori (private communication, 2007).

82. Charles Kittel, *Introduction to Solid State Physics*, 7th ed. (John Wiley & Sons, Inc., New York, 1996), pp. 647-651.

83. Dragica Vasileska and Stephen M. Goodnick, *Computational Electronics* (Morgan & Claypool Publishers, United States of America, 2006), pp. 191-197.

84. Donald A. McQuarrie, *Statistical Mechanics* (University Science Books, Sausalito, 2000), p. 411.

85. Martin A. Green, *Silicon Solar Cells: Advanced Principles & Practice*, Centre for Photovoltaic Devices and Systems University of New South Wales, Sydney, 1995), p. 66.

86. A.S. Grove, *Physics and Technology of Semiconductor Devices* (John Wiley & Sons, Inc., New York, 1967), pp. 129-140.

87. Daniel Macdonald and Andres Cuevas, *Physical Review B* **67**, 075203-1 – 7 (2003).

88. Martin A. Green, *Silicon Solar Cells: Advanced Principles & Practice*, Centre for Photovoltaic Devices and Systems University of New South Wales, Sydney, 1995), pp. 166-179.

89. Ben G. Streetman and Sanjay Banerjee, *Solid State Electronics*, 5th ed. (Prentice Hall, Inc., Upper Saddle River, 2000), p. 87.

90. Erik Danielson, *et al.*, *COMSOL Multiphysics Model Library*, 3.2 ed. (COMSOL AB, Burlington, 2005), pp. 402-417.

91. Martin A. Green, *Silicon Solar Cells: Advanced Principles & Practice*, Centre for Photovoltaic Devices and Systems University of New South Wales, Sydney, 1995), pp. 57-61.

92. B. Sopori, J. Madjdpour, Y. Zhang, and W. Chen, in *Electrochemical Society International Symposium*, Seattle, United State of America, 1999, pp. 1-9.

93. Bhushan Sopori, computer code PV Optics version 2 (National Renewable Energy Laboratory, Golden, CO, 1999).

94. Stephen Wolfram, computer code Mathematica 4.1.1.0 (Wolfram Research, Champaign, IL, 2000).

95. COMSOL AB, computer code COMSOL Multiphysics version 3.4 (COMSOL AB, Burlington, MA, 2007).

96. Anastasis C. Polycarpou, *Introduction to the Finite Element Method in Electromagnetics* (Morgan & Claypool Publishers, United States of America, 2006), p. ix.

97. Anastasis C. Polycarpou, *Introduction to the Finite Element Method in Electromagnetics* (Morgan & Claypool Publishers, United States of America, 2006), pp. 7-12.

98. Anastasis C. Polycarpou, *Introduction to the Finite Element Method in Electromagnetics* (Morgan & Claypool Publishers, United States of America, 2006), pp. 29-48.

99. COMSOL AB, *COMSOL Multiphysics Modeling Guide*, 3.2 ed. (COMSOL AB, Burlington, 2005), pp. 262-268.

100. COMSOL AB, *COMSOL Multiphysics User's Guide*, 3.2 ed. (COMSOL AB, Burlington, 2005), p. 521.

101. COMSOL AB, *COMSOL Multiphysics User's Guide*, 3.2 ed. (COMSOL AB, Burlington, 2005), pp. 326-327.

102. James F. Epperson, *An Introduction to Numerical Methods and Analysis* (John Wiley & Sons, Inc., New York, United States of America, 2002), pp. 447-450.

103. Dragica Vasileska and Stephen M. Goodnick, *Computational Electronics* (Morgan & Claypool Publishers, United States of America, 2006), p. 43.

104. Anastasis C. Polycarpou, *Introduction to the Finite Element Method in Electromagnetics* (Morgan & Claypool Publishers, United States of America, 2006), p. 72.

105. Ralph Kuhn, Peter Fath, and Ernst Bucher, in *Proceedings of the 28th IEEE Photovoltaic Specialists Conference*, Anchorage, United States of America, 2000, pp. 116-119.

106. Pietro P. Altermatt, Armin G. Aberle, Jianhua Zhao, Aihua Wang, and Gernot Heiser, *Solar Energy Materials & Solar Cells* **74**, 165-174 (2002).

107. R. Kuhn, A. Boueke, M. Wibral, C. Zechner, P. Fath, G. Willeke, and E. Bucher, in *2nd World Conference and Exhibition on Photovoltaic Solar Energy Conversion*, Vienna, Austria, 1998, pp. 1390-1393.

108. M. Hermle, J. Dicker, W. Warta, S.W. Glunz, and G. Willeke, in *3rd World Conference on Photovoltaic Energy Conversion*, Osaka, Japan, 2003, pp. 1009-1012.

109. Raymond A. Serway, *Physics for Scientists & Engineers*, 3rd ed. (Saunders College Publishing, Philadelphia, 1992), Vol. II, p. 692.

110. Bhushan Sopori, U.S. Patent No. 5,406,367 (11 April, 1995).

111. E. Tran, E.S. Kim, and S.Y. Lee, *Journal of Micromechanics and Microengineering* **5**, 251-256 (1995).

112. Raymond A. Serway, *Physics For Scientists & Engineers*, 3rd ed. (Saunders College Publishing, Philadelphia, 1992), Vol. II, pp. 626-701.